

A multi-objective optimization procedure for locally adaptive time-frequency analysis with application in EEG signal processing

Jurdana, Vedran

Doctoral thesis / Disertacija

2023

Degree Grantor / Ustanova koja je dodijelila akademski / stručni stupanj: **University of Rijeka, Faculty of Engineering / Sveučilište u Rijeci, Tehnički fakultet**

Permanent link / Trajna poveznica: <https://um.nsk.hr/um:nbn:hr:190:267373>

Rights / Prava: [Attribution 4.0 International](#) / [Imenovanje 4.0 međunarodna](#)

Download date / Datum preuzimanja: **2024-07-24**



Repository / Repozitorij:

[Repository of the University of Rijeka, Faculty of Engineering](#)



UNIVERSITY OF RIJEKA
FACULTY OF ENGINEERING

Vedran Jurdana

**A MULTI-OBJECTIVE OPTIMIZATION
PROCEDURE FOR LOCALLY ADAPTIVE
TIME-FREQUENCY ANALYSIS WITH
APPLICATION IN EEG SIGNAL
PROCESSING**

DOCTORAL DISSERTATION

Rijeka, 2023.

UNIVERSITY OF RIJEKA
FACULTY OF ENGINEERING

Vedran Jurdana

**A MULTI-OBJECTIVE OPTIMIZATION
PROCEDURE FOR LOCALLY ADAPTIVE
TIME-FREQUENCY ANALYSIS WITH
APPLICATION IN EEG SIGNAL
PROCESSING**

DOCTORAL DISSERTATION

Supervisor: Prof. D. Sc. Miroslav Vrankić

Rijeka, 2023.

SVEUČILIŠTE U RIJECI
TEHNIČKI FAKULTET

Vedran Jurdana

VIŠECILJNI OPTIMIZACIJSKI
POSTUPAK ZA LOKALNO ADAPTIVNU
VREMENSKO-FREKVENCIJSKU
ANALIZU S PRIMJENOM U OBRADI
EEG SIGNALA

DOKTORSKI RAD

Mentor: prof. dr. sc. Miroslav Vrankić

Rijeka, 2023.

Doctoral dissertation supervisor: Prof. D. Sc. Miroslav Vrankić, University of Rijeka,
Faculty of Engineering, Croatia

The doctoral dissertation was defended on _____ at the University
of Rijeka, Faculty of Engineering, Croatia, in front of the following Evaluation
Committee:

1. Prof. D. Sc. Saša Vlahinić, University of Rijeka, Faculty of Engineering,
Croatia - Committee Chair
2. Prof. D. Sc. Damir Seršić, University of Zagreb, Faculty of Electrical Engi-
neering and Computing, Croatia
3. Prof. D. Sc. Davor Petrinović, University of Zagreb, Faculty of Electrical
Engineering and Computing, Croatia

To my wife, Sara

ACKNOWLEDGMENTS

First, I wish to acknowledge my doctoral dissertation supervisor, Prof. D. Sc. Miroslav Vrankić, in the most sincere way possible. I am truly grateful for the trust he placed in me and for his unwavering instructions and support throughout my doctoral studies. In the crucial moments of my research, he provided invaluable encouragement and expert insight, always finding time to answer my questions. This dissertation owes its completion to the invaluable mentorship provided by Prof. D. Sc. Miroslav Vrankić.

I want to express my heartfelt appreciation to the members of the evaluation committee, Prof. D. Sc. Saša Vlahinić, Prof. D. Sc. Damir Seršić, and Prof. D. Sc. Davor Petrinović, for their invaluable time and insightful suggestions, which greatly contributed to the quality and refinement of this dissertation.

Furthermore, I want to express my appreciation to Prof. D. Sc. Viktor Sučić and Assist. Prof. D. Sc. Ivan Volarić for their valuable time, numerous discussions, and guidance in both scientific and teaching activities that I will incorporate and carry in my future academic endeavors.

My family and friends deserve my sincere appreciation for their unwavering love, support, and understanding throughout this demanding journey.

Lastly, I owe my deepest indebtedness to my wife, Sara, whose unconditional love and support have been the cornerstone of my success. From the first day, her belief in my abilities has been a driving force, and her understanding and encouragement have sustained me through the challenges. I am enormously privileged to have her by my side, and I look forward to sharing many more achievements together.

To everyone mentioned above and to all those who have contributed to my academic journey, directly or indirectly, I extend my heartfelt thanks.

Author

ABSTRACT

This dissertation addresses the challenges in the spectral representation of non-stationary signals using joint time-frequency distributions (TFDs). Heuristic time-frequency methods introduce additional interfering energy clusters, while the wrong choice of parameters in advanced methods may lead to the loss of useful components, thus restricting their practical use.

Existing concentration and entropy measures, along with their optimization methods, are appropriate when the structure of the useful components is preserved. However, these methods lack local positional information on the useful components, thereby making it difficult to account for the possible undesired loss of such components. The absence of a suitable criterion and optimization procedure for advanced methods, such as the compressive sensing (CS) method, has led to an experimental selection of the method's parameters, which requires specialist knowledge and increases the unreliability of its application for a wide range of signals.

To surmount these challenges, this dissertation proposes performance criteria based on the localized Rényi entropy (LRE) and the estimated instantaneous frequencies and group delays, formulated as objective functions of multi-objective meta-heuristic optimization algorithms. Two methods are also proposed to further improve the TFD reconstruction method: a locally adaptive sparse reconstruction algorithm based on the LRE and an improved selection of the CS area. The here-proposed methods are tested on synthetic and real-life signals, with a focus on their application in electroencephalogram signal analysis. The obtained results show improvements compared with the existing state-of-the-art concentration measures, optimization procedures, and TFD reconstruction algorithms.

Keywords: Time-frequency signal analysis, localized Rényi entropy, multi-objective meta-heuristic optimization, compressive sensing, ambiguity function, instantaneous frequency, data clustering, electroencephalogram.

PROŠIRENI SAŽETAK

Analiza korisnih informacija iz signala od velike je važnosti u raznim primjenama u praksi. Korištenje klasične Fourierove transformacije (FT) pokazalo se neefikasno za nestacionarne signale čiji frekvencijski spektar pokazuje ovisnost o vremenu. Njihova analiza zahtijeva korištenje napredne tehnike prikaza signala u zajedničkoj vremensko-frekvencijskoj (VF) domeni. Unatoč brojnih prednosti VF analize signala u odnosu na klasični pristup, neizvedivo je postići savršenu lokalizaciju energije u idealnoj vremensko-frekvencijskoj distribuciji (VFD) signala u stvarnim primjenama.

Linearne VFD, poput kratkotrajne FT, računski su jednostavne, ali ograničene su kompromisom između vremenske i frekvencijske razlučivosti. Kvadratne VFD (KVFD) češće se koriste u praksi, ali njihova kvadratna priroda uvodi neželjene među-članove, posebno kada signal posjeduje više od jedne komponente ili barem jednu nelinearnu frekvencijski moduliranu komponentu. Iako dvodimenzionalni niskopropusni filter u domeni neodređenosti (DN) može filtrirati među-članove, time se neželjeno smanjuje koncentracija korisnih informacija (auto-članova). Spomenuti kompromis, koji još uvijek predstavlja izazov u ovom području, potaknuo je razvoj raznih naprednih metoda.

Od posebnog interesa u ovom doktorskom radu je napredna metoda koja koristi svojstva komprimiranog uzorkovanja (KU) i prorijedenosti signala, čija su svojstva omogućila rekonstrukciju VFD signala iz komprimiranih uzoraka domene neodređenosti. Kako bi se nadoknadio nezaobilazni gubitak razlučivosti auto-članova, u ovoj metodi koriste se rekonstrukcijski algoritmi koji su pokazali poboljšanu učinkovitost u odnosu na razmatrane klasične i napredne VF metode. No, VFD rekonstrukcijska metoda zahtijeva veću računalnu složenost i složeniju uporabu za korisnika. Naime, ulazni parametri ove metode moraju biti pažljivo određeni s obzirom na dani signal, što se u dosadašnjim istraživanjima obično odradilo eksperimentalnim putem, pritom smanjujući pouzdanost metode. Odabir njenog regulacijskog parametra posebno je ključan, jer neispravan odabir dovodi do neželjenog gubitka auto-članova, što nije bio problem kod klasičnih VF metoda. Najčešće korištene globalne mjere koncentracije i entropijske mjere učinkovite su za procjenu klasičnih VF metoda koji balansiraju isključivo kompromis između rezolucije auto-članova i kvalitete suzbijanja među-članova. Međutim, spomenute mjere pokazale su se neprikladnim za otkrivanje potencijalno izgubljenih auto-članova VFD rekonstrukcijske metode. Razlog

tome je u nedostatku lokalne pozicijske informacije o auto-članovima signala čiji gubitak postojeće mjere ocjenjuju poželjnim, jednako kao i gubitak među-članova. Također, trenutno ne postoji dostupan optimizaciji pristup za automatski odabir parametara VFD rekonstrukcijske metode bez prethodnog znanja o signalu, s obzirom da minimizacijom ili maksimizacijom postojećih mjera optimizacija konvergira ka praznoj rekonstruiranoj VFD.

U svrhu prevladavanja navedenog problema, u ovom doktorskom radu predloženi su odgovarajući kriteriji učinkovitosti VFD bazirani na lokaliziranoj Rényijevoj entropiji (LRE) te procijenjenim trenutnim frekvencijama i spektralnim pomacima. Predloženi kriteriji implementirani su u objektne funkcije višeciljnih meta-heurističkih optimizacijskih algoritama za automatsku optimizaciju parametara VFD rekonstrukcijske metode bez potrebe za bilo kakvim predznanjem od korisnika. U tu svrhu, istraženi su nedostaci postojećeg lokalizacijskog pristupa isključivo kroz vremenske isječke, na temelju čega je predložena kombinirana lokalizacija koja ciljano koristi vremenske i frekvencijske isječke. S ciljem daljnjeg poboljšanja performansi VFD rekonstrukcijske metode, u ovom doktorskom radu predložene su dodatne dvije metode. Prva metoda je rekonstrukcijski algoritam čiji je operator sažimanja informacija baziran na LRE, dok druga metoda unapređuje odabir KU područja adaptivnim prilagođavanjem na korisne uzorke u DN. Opisane metode testirane su na sintetičkim i stvarnim signalima iz prakse, pri čemu je naglasak na primjeni u području analize elektroencefalogram (EEG) signala. U ovom doktorskom radu, od značajnog interesa su EEG signali napadaja epilepsije. Njihova nestacionarnost i više-komponentnost sa sinusnim i impulsnim karakteristikama predstavlja značajan izazov za VF metode, čiji bi doprinos pomogao u daljnjem razvoju alata za analizu signala napadaja. Dobiveni rezultati pokazuju poboljšanja u usporedbi s najsuvremenijim postojećim mjerama koncentracije i optimizacijskim procedurama, te algoritmima VFD rekonstrukcije.

Ključne riječi: Vremensko-frekvencijska analiza signala, lokalizirana Rényijeva entropija, višeciljna meta-heuristička optimizacija, komprimirano uzorkovanje, domena neodređenosti, trenutna frekvencija, grupiranje podataka, elektroencefalogram.

TABLE OF CONTENTS

ACKNOWLEDGMENTS	I
ABSTRACT	III
PROŠIRENI SAŽETAK	V
1 INTRODUCTION	1
1.1 Motivation	1
1.2 Objectives and Scientific Contributions	2
1.3 Organization of the Doctoral Dissertation	4
2 TIME-FREQUENCY SIGNAL ANALYSIS	7
2.1 Fundamental Time-Frequency Concepts	7
2.1.1 Time-Domain and Frequency-Domain Representations of Stationary and Non-Stationary Signals	7
2.1.2 Analytic Signals	10
2.1.3 Ideal Joint Time-Frequency Representation	11
2.2 Short-Time Fourier Transform and Spectrogram	13
2.3 Quadratic Time-Frequency Distributions	14
2.3.1 Wigner-Ville Distribution	14
2.3.2 Ambiguity Function and Cross-Term Filtration	14
2.4 Adaptive Time-Frequency Distribution	18
2.5 Global Concentration Measures for Time-Frequency Distributions	20
2.6 Summary	21
3 TIME-FREQUENCY SIGNAL ANALYSIS USING COMPRESSIVE SENSING	23
3.1 Sparse Time-Frequency Distribution Reconstruction	23
3.1.1 Problem Formulation	24
3.1.2 Problem Solution	25
3.2 Limitations of the Existing Measurement Criteria When Selecting the Optimal Regularization Parameter λ	28
3.2.1 Single Objective Meta-Heuristic Approach	31
3.3 Summary	31
4 PERFORMANCE CRITERIA FOR TIME-FREQUENCY DISTRI- BUTIONS BASED ON THE LOCALIZED RÉNYI ENTROPY	33

4.1	The Localized Rényi Entropy	33
4.1.1	Limitations of the Existing Methods	34
4.1.2	The Narrow-Band Rényi Entropy	35
4.2	Performance Criteria Based on the Localized Rényi Entropy: Definition and Evaluation Performance	38
4.3	A Multi-Objective Meta-Heuristic Optimization Approach	42
4.3.1	Problem Definition	42
4.3.2	Pareto Optimal Solutions	42
4.3.3	Multi-Objective Meta-Heuristic Optimization Algorithms	44
4.4	Evaluating Optimization Performance: Results	45
4.5	Summary	50
5	ADVANCEMENTS IN COMPRESSIVE SENSING-BASED SIGNAL ANALYSIS	51
5.1	The Rényi Entropy-Based Shrinkage Sparse Reconstruction Algorithm . . .	51
5.1.1	Simulation Results	58
5.1.2	Sensitivity to Noise	62
5.2	Parametrized Compressive Sensing Area Selection	66
5.2.1	Ambiguity Function Thresholding	66
5.2.2	Extraction of Signal Samples From the Ambiguity Function Using Density-Based Spatial Clustering	67
5.2.3	Simulation Results: Synthetic Signal	71
5.2.4	Simulation Results: Real-Life Gravitational Signal	73
5.2.5	Sensitivity to Noise	76
5.3	Summary	78
6	PERFORMANCE CRITERIA FOR TIME-FREQUENCY DISTRI- BUTIONS BASED ON THE INSTANTANEOUS FREQUENCY AND GROUP DELAY ESTIMATION	81
6.1	Component Alignment Towards Time or Frequency Axis Detection Using the Local Rényi Entropy	82
6.1.1	Component Extraction and Estimation of the Local Number of Components	86
6.2	Strategy for Mutual Estimation of Instantaneous Frequency and Group Delay	89
6.2.1	Image-Based and Blind Source Separation Instantaneous Frequency Estimation Methods	91
6.2.2	Method for Automatic Estimation of Instantaneous Frequency and Group Delay	92
6.2.3	Simulation Results	93
6.3	Performance Criteria Based on the Instantaneous Frequency and Group Delay Estimation	98
6.3.1	Validation of Criteria for Reconstructed TFD Evaluation	102
6.3.2	Evaluating Optimization Performance: Results	106
6.4	Renyi Entropy-Based Algorithm Enhancement	107

6.5	Summary	110
7	TIME-FREQUENCY ANALYSIS OF ELECTROENCEPHALOGRAM SEIZURE SIGNALS	111
7.1	EEG Database Description	112
7.1.1	EEG Seizure Signal: Mathematical Model	113
7.2	Evaluating Instantaneous Frequency and Group Delay Estimation Performance: Results	115
7.3	Evaluating TFD Reconstruction Performance: Results	121
7.4	Summary	125
8	CONCLUSIONS AND FUTURE WORK	127
8.1	Conclusions	127
8.2	Future Research Directions	129
	BIBLIOGRAPHY	131
	LIST OF ABBREVIATIONS	143
	LIST OF SYMBOLS	145
	LIST OF FIGURES	151
	LIST OF TABLES	159
	APPENDICES	163
A	PSEUDOCODE OF MULTI-OBJECTIVE META-HEURISTIC ALGORITHMS	165
B	RESULTS OF THE HYPERVOLUME TEST ON META-HEURISTIC ALGORITHMS IN CHAPTER 4	167
C	RESULTS OF THE PARETO FRONT IN CHAPTER 4	169
D	RESULTS OF THE OPTIMIZED COMPRESSIVE SENSING AREAS IN CHAPTER 5	171
E	RESULTS OF THE RECONSTRUCTED TFDS OPTIMIZED WITH THE IF/GD-BASED CRITERIA IN CHAPTER 6	173
F	RESULTS OF THE OPTIMIZED COMPRESSIVE SENSING AREAS IN CHAPTER 6	175
	CURRICULUM VITAE	177
	LIST OF PUBLICATIONS	179

CHAPTER 1

INTRODUCTION

1.1 Motivation

In numerous real-life situations, mere observation of a signal's behavior over time proves insufficient to comprehend the underlying phenomenon. Understanding its frequency content becomes imperative in such cases. While the Fourier transform has been conventionally employed for this purpose, it falls short for non-stationary signals featuring time-dependent frequency content as the time properties of the signal are disregarded. In this circumstances, the joint time-frequency (TF) domain emerges as the preferred observation domain for non-stationary signals, as it allows for a comprehensive depiction of signal energy conjointly in relation to both time and frequency. Nonetheless, it is practically infeasible to attain an exceptional localization of energy in the ideal time-frequency distribution (TFD) in real-world applications, given inherent practical constraints [14, 113].

The short-time Fourier transform, which falls under the linear class of TFDs, exhibits a restricted resolution and necessitates the compromise between its quality in time or frequency [14, 29]. In contrast, the quadratic class of TFDs (QTFD) is widely utilized, but its quadratic attribute initiates unwanted cross-terms, particularly in scenarios characterized by the existence of multiple signal components or a minimum of one non-linear frequency modulated component [14, 29]. While the two-dimensional low-pass filter in the ambiguity function (AF) can filter out cross-terms, it also diminishes the concentration of auto-terms. This trade-off, which still presents a challenge in this field, has inspired the growth of a number of advanced methods [14, 29, 44, 91, 113].

Of particular interest in this dissertation is an advanced method based on compressive sensing (CS), a rapidly expanding research area in signal analysis using time-frequency methods with numerous applications [37, 89, 96, 107, 108, 114, 115, 127, 134, 136, 140]. Specifically, the CS-based approach is utilized for TF signal analysis to reconstruct a signal's TFD from a small subset of auto-term-related samples selected from the AF, thus

forming the CS-AF area. To overcome the inherent loss of auto-term concentration, sparse reconstruction algorithms are employed, which have demonstrated superior performance compared to classical and advanced TF methods [107, 108, 127, 131].

Despite the superior performance of the CS-based method for TF signal analysis, it incurs increased computational complexity and a more complex user experience. The method's input parameters must be defined carefully, usually through experimental selection, which may compromise the sparse TFD reconstruction's reliability. The selection of the regularization parameter is particularly crucial, as an incorrect choice may lead to the loss of auto-terms, which is not a concern in classical TF methods [37, 127]. The state-of-the-art global concentration measures are effective for evaluating classical TF methods, which control auto-term resolution and cross-term suppression. However, these measures are inadequate for detecting missing auto-terms in CS-based methods and may even artificially enhance their values as the number of samples decreases. Currently, there is no optimization approach available to select the CS-based method's parameters lacking in any former comprehension regarding the signal.

The above-mentioned limitations indicate a need for further improvement of the underlying algorithms of the CS-based method. First, the thresholding procedure with the regularization parameter, which relies only on the amplitude difference in favor of auto-terms compared to cross-terms, may not always be reliable. Second, the selection of the CS-AF area using geometrically strict rectangles [37, 127, 131] around the AF origin may include unnecessary samples for auto-term reconstruction, noise, and cross-term-related samples that have not been properly avoided.

The primary real-life signal example investigated in this dissertation is the non-stationary electroencephalogram (EEG) seizure signal comprising multiple components [17, 59, 60, 62, 86]. This signal has remained a challenging task for proper representation in the TF domain due to its sinusoidal and spike characteristics. The ability to detect and comprehend the underlying mechanisms of seizures is of paramount importance to neuroscience, as it has significant implications for the development of more efficacious treatments for neurological conditions [31, 36, 62, 63, 66, 85, 86, 124].

1.2 Objectives and Scientific Contributions

Based on the scientific motivation outlined above, the primary objective of the research presented in this dissertation is to establish proper criteria for assessing the performance of reconstructed TFDs. Specifically, the here-presented criteria should effectively address the loss of auto-terms and be suitable for implementation as objective functions within an automatic, multi-objective optimization approach that avoids convergence to an empty TFD, as occurs with existing methods. Therefore, our first hypothesis is that incorporating

information about the number and local behavior of signal's components in a TFD, which can be derived using the localized Rényi entropy (LRE) [120, 121], can overcome these limitations. To overcome the one-dimensional (1-D) nature of LRE information, the development of a 2-D performance criteria established on the concepts of instantaneous frequency (IF) and group delay (GD) will be explored.

As the LRE is an important part of this research, its potential shortcomings will be thoroughly addressed. In particular, its estimation reliability of the local number of components using time slices diminishes as signal's components diverge from the method's reference signal, which aligns with the time axis. Consequently, our second hypothesis is that more precise estimations may be achieved for certain signals by considering frequency slices and calculating the local number of components in frequency bins. In this dissertation, the shortcomings of using localization explicitly in time slices in several applications will be addressed, and the need for both localization approaches will be carefully analyzed.

The secondary aim of the research outlined in this dissertation is to enhance the CS-based method. Our third hypothesis posits that auto-terms exhibit higher local surfaces than cross-terms in each time or frequency slice of a filtered TFD. As such, the simple thresholding operator with the regularization parameter should be replaced with a more sophisticated operator that considers not only amplitude but also the number and position of auto-terms. This may result in increased detection and maintenance of auto-terms in the reconstructed TFD. Furthermore, the parametrization of the existing CS-AF area will be analyzed, which may be optimized with a clustering method to abandon its strict rectangular shape and allow the selection of samples that follow the trajectory of auto-terms in the AF. Excluding noise or cross-term-related samples using this approach will prevent their reappearance in the reconstructed TFD, while the inclusion of more auto-term-related samples will enhance the concentration of the reconstructed TFD.

Taken together, achieving these objectives in this dissertation will enhance the overall efficacy of the CS-based method across various signals. The proposed multi-objective optimization approach will reduce the need for signal specialists to intervene and ensure automatic convergence to a resulting TFD with preserved auto-terms, high resolution, and suppressed cross-terms. Importantly, beyond the scope of this dissertation, the presented multi-objective optimization approach holds tremendous potential for a wide range of applications across various methods.

Therefore, the novel scientific contributions introduced in this dissertation are concisely outlined into four points as follows:

1. Optimization of TFDs using multi-objective meta-heuristic algorithms (Sections 4.2 and 6.3).
2. A shrinkage algorithm for sparse TFD reconstruction based on the one-dimensional localized Rényi entropies (Section 5.1).

3. An algorithm for adaptive selection of the parametrized CS area in the ambiguity domain using the data clustering method to improve the concentration of useful components and suppress interference and noise in the reconstructed TFD (Section 5.2).
4. A method for automatic estimation of the instantaneous frequency and group delay for EEG seizure signals analysis (Sections 6.1, 6.2, and 7.2).

1.3 Organization of the Doctoral Dissertation

This dissertation comprises a total of eight chapters and six appendices in its organizational structure, offering a methodical and comprehensive presentation of the conducted research. A succinct overview of the dissertation chapters is presented below for the reader's perusal.

- **Chapter 1** provides a scientific motivation for the presented research and delineates the primary objectives and contributions of the dissertation. Additionally, this chapter furnishes a succinct outline of the dissertation structure.
- **Chapter 2** presents an overview of time-frequency signal processing, emphasizing the benefits of utilizing a two-dimensional approach compared to traditional one-dimensional methods in the time and frequency domains. The chapter reviews classical and advanced numerical techniques for computing TFDs and assesses the trade-off between auto-term resolution and cross-term removal for the quadratic class of TFDs and TFDs with adaptive directional kernels utilizing state-of-the-art global concentration measures. The efficacy of these TFDs is evaluated using a synthetic signal.
- **Chapter 3** gives an exposition of compressive sensing methodology utilizing the ambiguity function to enhance TFD concentration. Advanced sparse reconstruction algorithms based on the ℓ_1 norm are presented. Additionally, the chapter addresses the challenges related to the selection and assessment of the regularization parameter and demonstrates its effect on the reconstruction algorithms' performance applied to synthetic signals in the presence of noise.
- **Chapter 4** presents the original scientific contribution of this dissertation. The chapter begins with an outline of the localized Rényi entropy, highlighting its limitations. Subsequently, an alternative method for computing the localized Rényi entropy is introduced and discussed, leading to the definition of TFD performance criteria. A multi-objective optimization approach is examined, succeeded by the formalization of the objective functions. The efficacy of the proposed criteria in terms

of reconstructed TFD evaluation and optimization is evaluated through experiments conducted on synthetic signals in the presence of noise.

- **Chapter 5** unveils two original scientific contributions of this dissertation, focusing on the enhancement of the compressive sensing approach. It introduces a sparse reconstruction algorithm founded on the localized Rényi entropy, as well as an algorithm for adaptively determining the compressive sensing region, taking into account explicitly auto-terms of the signal within the parameterized ambiguity function. The efficacy of the here-proposed methods is evaluated through experiments conducted on both synthetic and real-life signals in the presence of noise.
- **Chapter 6** presents the original scientific contribution of this dissertation. The chapter outlines a novel method for automatic detection of time-frequency regions requiring different localization approaches. The proposed method is employed in a strategy for combined IF and GD estimation, as well as in the enhancement of sparse reconstruction described in Chapter 5 and in the definition of performance criteria based on the estimated IFs and GDs. The effectiveness of each implementation is comprehensively evaluated through experiments conducted on both synthetic and real-life signals in the presence of noise.
- **Chapter 7** involves the time-frequency analysis of EEG seizure signals using the contributions of this dissertation. The chapter commences with a brief introduction to EEG signals, after which a detailed exposition of the database and the illustrative EEG signal employed in this dissertation is provided. The performances of combined IF and GD estimation, as presented in Chapter 6, and sparse reconstruction, utilizing the methods proposed in Chapter 5, are thoroughly examined.
- **Chapter 8** summarizes the fundamental conclusions derived from this dissertation. It also delves into potential avenues for future research, building upon the insights and outcomes presented in the dissertation.

The experimental simulations of this dissertation have been performed in MathWorks MATLAB¹ programming language and numerical computing software. The base toolbox used in the research is the Time-Frequency Toolbox². The simulations were executed on a PC with the AMD RyzenTM 9 5900X @ 3.70 GHz processor and 32GB of RAM.

¹Available at: <https://www.mathworks.com/products/matlab.html>

²Available at: <https://tftb.nongnu.org/>

CHAPTER 2

TIME-FREQUENCY SIGNAL ANALYSIS

In this chapter, an in-depth exploration is undertaken to examine the benefits of time-frequency representations over time- or frequency-only representations. It reviews fundamental time-frequency notions, including analytic signals, instantaneous frequency and group delay, and the ambiguity function. The properties of an ideal TFD and conventional TFD calculation approaches, including the short-time Fourier transform and the Wigner-Ville distribution, are discussed, as is an advanced TFD approach based on adaptive kernel design.

The performance evaluation of TFDs is also addressed, and state-of-the-art performance measures are introduced. Synthetic signals are used as examples to demonstrate the effectiveness of these methods.

2.1 Fundamental Time-Frequency Concepts

2.1.1 Time-Domain and Frequency-Domain Representations of Stationary and Non-Stationary Signals

A *signal* refers to a time-varying quantity that carries valuable information regarding a physical process or phenomenon. In many applications, signals are measured and represented as functions of time, t , denoted as $z(t)$. This time-domain signal representation allows us to observe the amplitude variation of the signal over time or the dispersion of signal energy over time, which can be represented as $|z(t)|^2$ [14, 29].

Apart from the time domain, signals may be effectively characterized in the frequency domain, which provides valuable details about the signal's spectral properties. The frequency-domain representation of a signal, denoted as $Z(f)$, is obtained through *Fourier*

transform (FT), which states that any limited signal satisfying Dirichlet conditions is expressed as a summation of sinusoids and cosinusoids (or complex exponentials) in distinct frequencies, f :

$$Z(f) = \mathcal{F}_{t \rightarrow f}\{z(t)\} = \int_{-\infty}^{\infty} z(t)e^{-j2\pi ft} dt, \quad (2.1)$$

where j is the imaginary unit. The FT provides a unique representation of a signal in terms of its frequency components, allowing us to identify important features such as frequency content, bandwidth, and phase information. The squared magnitude spectrum, denoted as $|Z(f)|^2$, represents the energy spectrum of a signal, which expresses the dispersion of signal energy over the frequency domain [14, 29].

On the other hand, the *inverse Fourier transform* (IFT) allows us to recover a signal from its frequency-domain representation. The IFT is given as:

$$z(t) = \mathcal{F}_{t \leftarrow f}^{-1}\{Z(f)\} = \int_{-\infty}^{\infty} Z(f)e^{j2\pi ft} df. \quad (2.2)$$

The tools discussed here are particularly useful in the analysis of *stationary signals*, which are portrayed by a constant frequency spectrum [14, 29]. A synthetic stationary signal example and its corresponding time and frequency domain representations are depicted in Figure 2.1. The time-domain representation of the instantaneous power $|z(t)|^2$, illustrated in Figure 2.1a, clearly indicates that the signal's energy remains constant over time. Furthermore, the frequency-domain representation in the form of the energy spectrum $|Z(f)|^2$, depicted in Figure 2.1b, confirms that the FT is an appropriate tool for stationary signals, as it accurately captures their constant frequency content.

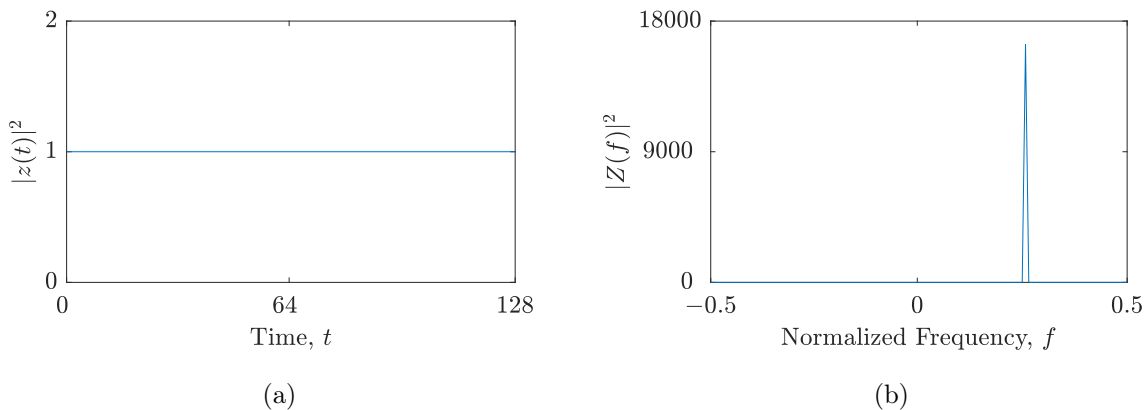


Figure 2.1 Example of a stationary signal $z(t)$ with a constant frequency spectrum: (a) the signal's instantaneous power, $|z(t)|^2$; (b) the signal's energy spectrum, $|Z(f)|^2$.

In practical applications, most signals are *non-stationary* and exhibit a time-varying frequency spectrum [14, 113]. In such cases, traditional representations in the time and frequency domain alone are insufficient, as they fail to provide information on the number of signal components, their frequency modulations, and time supports. Specifically, while

the frequency-domain representation conveys the frequency components that exist within a signal, it fails to offer any details on their time localization.

Furthermore, non-stationary signals are often *multi-component*, with their individual components exhibiting different linear or non-linear frequency modulations and having distinct time supports. Additionally, signals may be corrupted by noise in practice, which further limits the usefulness of the FT. A multi-component signal is expressed as the sum of two or more *mono-component* signals, mathematically written in the form of an analytic associate, $z(t)$, as:

$$z(t) = \sum_{i=1}^{NC} a_i(t)e^{j\phi_i(t)}, \quad (2.3)$$

where $\phi_i(t)$ and $a_i(t)$ denote the instantaneous phase and amplitude of the i -th component of the signal, respectively, while NC represents the overall number of signal components [14, 29].

The limitations of one-dimensional signal representations are evidenced through the analysis of a synthetic multi-component non-stationary signal, denoted as $z_{\text{SINLFM}}(t)$. This signal contains one linear frequency modulated (LFM) component and one sinusoidal FM component, and its corresponding time and frequency domain representations are depicted in Figure 2.2. The inadequacy of the one-dimensional representations becomes apparent as neither representation alone can distinguish between the two components or accurately depict their frequency content.

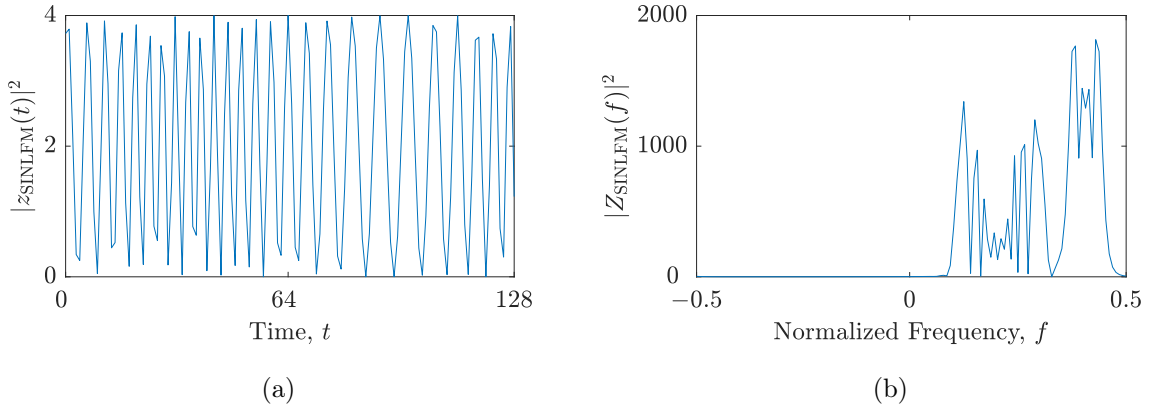


Figure 2.2 Example of a two-component non-stationary signal $z_{\text{SINLFM}}(t)$ with a linear and sinusoidal frequency modulated component: (a) the signal's instantaneous power, $|z_{\text{SINLFM}}(t)|^2$; (b) the signal's energy spectrum, $|Z_{\text{SINLFM}}(f)|^2$.

In light of the aforementioned shortcomings of analyzing non-stationary signals in disjoint time and frequency domains, it becomes necessary to employ more sophisticated methods that can simultaneously represent signals in both domains. *Time-frequency distributions* (TFDs) have been developed to address this need by representing the signal energy dispersion in relation to both time and frequency. In that manner, joint signal

representations can be obtained in the two-dimensional time-frequency plane [14, 29, 44, 91, 113].

2.1.2 Analytic Signals

To understand time-frequency analysis, we should review the theory of the *analytic signal*, denoted by $z(t)$, or the analytic associate. A real signal is characterized by its Hermitian symmetry, which mathematically describes the relationship between its components at positive and negative frequencies [14, 29]:

$$S(-f) = S^*(f), \quad (2.4)$$

where $S(f)$ represents FT of the real signal $s(t)$.

Equation (2.4) implies that no information is lost if the negative-frequency components are discarded, i.e., $Z(f) = 0$, $f < 0$. This approach offers several advantages, such as enabling sampling with half of the usual Nyquist rate, or the interference removal between the signal's positive and negative components in the time-frequency representation [14, 29].

By incorporating a *Hilbert transform*, denoted as $\mathcal{H}\{s(t)\}$, into the imaginary component, the analytic signal can be acquired from a real signal $s(t)$ as [14, 29]:

$$z(t) = s(t) + j\mathcal{H}\{s(t)\}. \quad (2.5)$$

The Hilbert transform can be mathematically expressed as [14, 29]:

$$\mathcal{H}\{s(t)\} = \mathcal{F}^{-1}_{t \leftarrow f} \left\{ (-j \operatorname{sgn}(f)) \mathcal{F}_{t \rightarrow f} \{s(t)\} \right\} = s(t) * \frac{1}{\pi t}, \quad (2.6)$$

where $*$ signifies convolution, while the signum function, $\operatorname{sgn}(\zeta)$, is given as:

$$\operatorname{sgn}(\zeta) = \begin{cases} -1, & \zeta < 0 \\ 0, & \zeta = 0, \\ 1, & \zeta > 0. \end{cases} \quad (2.7)$$

The analytic signal is a valuable resource for conducting time-frequency analysis given its ability to involve both the original signal and its Hilbert transform. This feature enables the simultaneous extraction of amplitude and phase information, thereby enhancing the analytical capabilities of the signal. Henceforth, the analytical associate of all signals in the continuation of this dissertation will be used.

2.1.3 Ideal Joint Time-Frequency Representation

At any specific time, the ideal TFD, represented as $\hat{\rho}(t, f)$, is characterized by a Dirac delta function positioned at the *instantaneous frequency* (IF), $f_{0_i}(t)$, of the i -th component [14, 29]:

$$\hat{\rho}(t, f) = \sum_{i=1}^{NC} a_i^2(t) \delta(f - f_{0_i}(t)), \quad (2.8)$$

$$f_{0_i}(t) = \frac{1}{2\pi} \frac{d}{dt} [\arg(z(t))] = \frac{1}{2\pi} \frac{d\phi_i(t)}{dt}, \quad (2.9)$$

signifying the prominent frequency of the signal's i -th component at a particular time point.

The dual of the IF is the *spectral delay* (SD), $\tau_{d_i}(f)$, of the i -th component, revealing the prominent time when an assigned frequency appears [14, 29]:

$$\tau_{d_i}(f) = -\frac{1}{2\pi} \frac{d}{df} [\arg(Z(f))] = -\frac{1}{2\pi} \frac{d\varphi_i(f)}{df}, \quad (2.10)$$

where $\varphi_i(t)$ is the signal's i -th component phase of the FT of $z(t)$. The SD and *group delay* (GD) are related to each other with the same equation as (2.10), although they have different physical interpretations. The SD is associated with an impulse, in contrast to the GD, which pertains to the envelope of a narrow-band signal [14, 29].

Figure 2.3 displays the ideal TFDs of the stationary and non-stationary signals under consideration. As illustrated in Figure 2.3a, the joint TF representation of the stationary signal did not reveal any new information beyond that conveyed by the classical FT, which is shown in Figure 2.1. In contrast, the ideal TFD of the non-stationary signal $z_{\text{SINLFM}}(t)$ provides valuable insights into the signal's components, their IF laws, and the time and frequency supports.

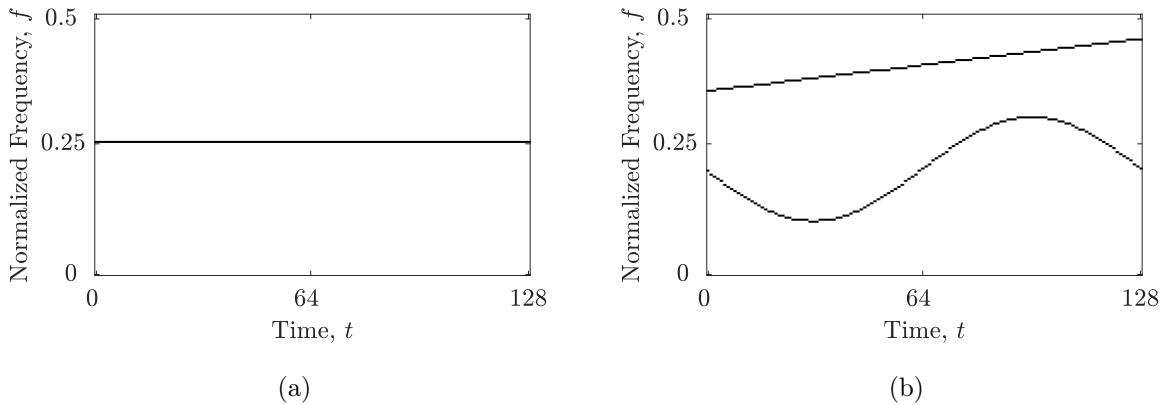


Figure 2.3 Ideal TFDs of the considered examples of: (a) a stationary signal; (b) a non-stationary signal with a linear and sinusoidal frequency modulated component, $z_{\text{SINLFM}}(t)$.

Numerical methods are commonly used for calculating TFDs in practical applications due to the difficulty of obtaining analytical forms of signals [14, 29, 44, 91, 113]. However, the accuracy and usefulness of TFDs depend on their properties, which must be carefully considered when selecting a method for signal analysis. Desirable properties of TFDs that are widely used in signal processing include [14]:

1. Realness and non-negativity – TFD is real and non-negative $\forall t, f$:

$$\hat{\rho}(t, f) \in \mathbb{R}, \quad (2.11)$$

$$\hat{\rho}(t, f) \geq 0. \quad (2.12)$$

2. Time- and frequency-shift invariances – any time or frequency shift in the signal leads to a corresponding time or frequency shift in the TFD:

$$z(t - t_0) \iff Z(f)e^{-j2\pi t_0 f} \Rightarrow \hat{\rho}(t - t_0, f), \quad (2.13)$$

$$z(t)e^{j2\pi f_0 t} \iff Z(f - f_0) \Rightarrow \hat{\rho}(t, f - f_0). \quad (2.14)$$

3. Time and frequency marginals – instantaneous power, $|z(t)|^2$, and energy spectrum, $|Z(f)|^2$, are derived by integrating the TFD over frequency and time, respectively:

$$\int_{-\infty}^{\infty} \hat{\rho}(t, f) df = |z(t)|^2, \quad (2.15)$$

$$\int_{-\infty}^{\infty} \hat{\rho}(t, f) dt = |Z(f)|^2. \quad (2.16)$$

4. Total energy – total energy, E_z , is calculated by integrating the TFD over the whole (t, f) domain and is equal to the energy calculated with Parseval's theorem:

$$E_z = \int_{-\infty}^{\infty} |z(t)|^2 dt = \int_{-\infty}^{\infty} |Z(f)|^2 df = \int_{-\infty}^{\infty} \int_{-\infty}^{\infty} \hat{\rho}(t, f) dt df. \quad (2.17)$$

5. Instantaneous frequency – instantaneous frequency is determined as the first moment of the TFD with respect to frequency:

$$\frac{\int_{-\infty}^{\infty} f \hat{\rho}(t, f) df}{\int_{-\infty}^{\infty} \hat{\rho}(t, f) df} = \frac{1}{2\pi} \frac{d}{dt} [\arg(z(t))]. \quad (2.18)$$

6. Spectral delay – spectral delay is determined as the first moment of the TFD with respect to time:

$$\frac{\int_{-\infty}^{\infty} t \hat{\rho}(t, f) dt}{\int_{-\infty}^{\infty} \hat{\rho}(t, f) dt} = -\frac{1}{2\pi} \frac{d}{df} [\arg(Z(f))]. \quad (2.19)$$

7. Time and frequency supports – the TFD $\hat{\rho}(t, f) = 0$ for $t \in [t_1, t_2]$ or $f \in [f_1, f_2]$ if $s(t) = 0$ or $S(f) = 0$ over equal time or frequency interval, respectively.
8. Reduced interference – the TFD is free of interference terms.

2.2 Short-Time Fourier Transform and Spectrogram

The *short-time Fourier transform* (STFT) is a widely used linear time-frequency distribution that gives a combined time-frequency depiction of a signal [2, 14, 29]. The STFT is obtained by multiplying a signal $z(\tau)$ by a window function, denoted with $w(\tau)$, centered at time $\tau = t$, followed by the computation of the FT of each resulting windowed signal. The STFT, $F_z(t, f)$, is given analytically as [2]:

$$F_z(t, f) = \int_{-\infty}^{\infty} z(\tau)w(\tau - t)e^{-j2\pi f\tau} d\tau. \quad (2.20)$$

The compromise between the time and frequency resolution of the STFT depends on the window length and shape. Employing shorter windows leads to an amelioration in time resolution but a decline in frequency resolution, whereas employing longer windows offers heightened frequency resolution at the cost of sacrificing time resolution. Commonly used window functions include the Rectangular, Triangular, Hanning, Hamming, among others [14, 29, 113].

With the intention of obtaining the energy dispersion of the signal in time and frequency jointly, the squared magnitude of the STFT is used. This representation is commonly referred to as the *spectrogram* (SPEC), $S_z(t, f)$, and is defined as [14, 29, 113]:

$$S_z(t, f) = |F_z(t, f)|^2 = \left| \int_{-\infty}^{\infty} z(\tau)w(\tau - t)e^{-j2\pi f\tau} d\tau \right|^2. \quad (2.21)$$

The spectrogram is a powerful tool used to analyze signals with varying spectral content and is widely applied in signal processing, speech and audio analysis, and image processing [14, 44, 91, 113]. However, it is important to note that the spectrogram is influenced by the *Heisenberg uncertainty principle*, which signifies that there is a fundamental trade-off between time and frequency resolution. In other words, any attempt to enhance one resolution at the expense of the other will be subject to this limit [14, 38].

The choice of window function and length, denoted as N_w , plays a crucial role in balancing time and frequency resolutions in spectrogram analysis. For instance, short windows are often used to analyze transient signals with abrupt changes in time, while longer windows are more appropriate for signals with slowly varying frequency content. The selection of window function and length relies on the specific application and the desired balance between time and frequency resolution [14, 44, 91, 113].

2.3 Quadratic Time-Frequency Distributions

Linear TFDs have limitations and drawbacks that make them unsuitable for certain types of signals and applications. For example, they may not be able to accurately represent signals with non-stationary or time-varying spectral content, or may suffer from poor resolution given the inherent compromise between time and frequency resolution. To overcome these issues, a class of time-frequency distributions called *quadratic time-frequency distributions* (QTFD) has been developed [14, 29, 113].

2.3.1 Wigner-Ville Distribution

The *Wigner-Ville distribution* (WVD) is a primary member of the QTFD class [126, 137]. QTFDs acquire the time dependency of the signal by multiplying the signal $z\left(t + \frac{\tau}{2}\right)$ shifted in time with the lag variable, denoted with τ , with its time-shifted complex conjugated copy $z^*\left(t - \frac{\tau}{2}\right)$, known as the *instantaneous auto-correlation function* (IACF), $K_z(t, \tau)$ [14, 29]:

$$K_z(t, \tau) = z\left(t + \frac{\tau}{2}\right) z^*\left(t - \frac{\tau}{2}\right). \quad (2.22)$$

The WVD, $W_z(t, f)$, is defined as the FT of the IACF as [14, 29]:

$$W_z(t, f) = \int_{-\infty}^{\infty} z\left(t + \frac{\tau}{2}\right) z^*\left(t - \frac{\tau}{2}\right) e^{-j2\pi f\tau} d\tau. \quad (2.23)$$

The WVD delivers an almost perfect representation for mono-component LFM signals [14, 29]. However, for multi-component signals, the WVD is accompanied by *cross-terms* that emerge as a mathematical artifact given the quadratic nature of the IACF between each pair of components at their midpoints. They manifest as oscillations in the time-frequency domain that are directly commensurate with the spatial separation between the interfering components and exhibit a perpendicular orientation to the linear trajectory connecting the components. In contrast, *auto-terms* provide valuable information about the energy of the components [14, 29].

2.3.2 Ambiguity Function and Cross-Term Filtration

The cross-terms usually create a visual understanding of the TFD challenging. Hence, in order to obtain interpretable time-frequency representations, the unwanted cross-terms need to be attenuated. The attenuation of the cross-terms is possible by smoothing the WVD in the Doppler-lag (ν, τ) domain, known as the *ambiguity function* (AF) [14, 29]:

$$A_z(\nu, \tau) = \int_{-\infty}^{\infty} \int_{-\infty}^{\infty} W_z(t, f) e^{j2\pi(f\tau - \nu t)} dt df, \quad (2.24)$$

by a simple multiplication with the two-dimensional low-pass filters, also known as *kernels*, $g(\nu, \tau)$ [14, 29]:

$$\mathcal{A}_z(\nu, \tau) = g(\nu, \tau)A_z(\nu, \tau). \quad (2.25)$$

Low-pass filtration is a viable technique due to the slow variation of auto-terms, which are situated near the origin of the Doppler-lag domain. Conversely, the rapid variation of cross-terms places them farther from the origin [14, 29]. Nevertheless, this filtration leads to the partial loss of the auto-terms, resulting in a decrease in their concentration in the TF domain. Balancing cross-term suppression and auto-term concentration is a crucial challenge in TF signal processing, which leads to the establishment of the QTFD class, $\rho(t, f)$, mathematically defined as the forward and inverse two-dimensional FT of the AF [14, 29]:

$$\rho(t, f) = \mathcal{F}_{\tau \rightarrow f} \{ \mathcal{F}_{t \leftarrow \nu}^{-1} \{ \mathcal{A}_z(\nu, \tau) \} \} = \int_{-\infty}^{\infty} \int_{-\infty}^{\infty} \mathcal{A}_z(\nu, \tau) e^{j2\pi(\nu t - f\tau)} d\nu d\tau. \quad (2.26)$$

Equation (2.26) indicates duality among $\rho(t, f)$ and $\mathcal{A}_z(\nu, \tau)$, which gives the possibility for a kernel design in either domain [14, 29]:

$$\mathcal{A}_z(\nu, \tau) = g(\nu, \tau)A_z(\nu, \tau) \iff \rho(t, f) = \underset{t}{\gamma}(t, f) \underset{f}{**} W_z(t, f), \quad (2.27)$$

where $\gamma(t, f)$ denotes the smoothing kernel in the TF domain.

For example, examine a multi-component signal consisting of two tones with frequencies f_1 and f_2 :

$$z(t) = e^{j2\pi f_1 t} + e^{j2\pi f_2 t}. \quad (2.28)$$

Signal kernel, $K_z(t, \tau)$, is calculated as:

$$\begin{aligned} K_z(t, \tau) &= z\left(t + \frac{\tau}{2}\right) z^*\left(t - \frac{\tau}{2}\right) \\ &= e^{j2\pi f_1 \tau} + 2 \cos[2\pi(f_1 - f_2)t] e^{j2\pi \frac{f_1 + f_2}{2} \tau} + e^{j2\pi f_2 \tau}, \end{aligned} \quad (2.29)$$

while the WVD follows as $\mathcal{F}_{\tau \rightarrow f} \{ K_z(t, \tau) \}$:

$$W_z(t, f) = \underbrace{\delta(f - f_1)}_{\text{auto-term}} + \underbrace{2 \cos[2\pi(f_1 - f_2)t] \delta\left(f - \frac{f_1 + f_2}{2}\right)}_{\text{cross-term}} + \underbrace{\delta(f - f_2)}_{\text{auto-term}}. \quad (2.30)$$

Finally, the signal's AF is calculated as:

$$\begin{aligned} A_z(\nu, \tau) &= \underbrace{e^{j2\pi f_1 \tau} \delta(\nu)}_{\text{auto-term}} + \underbrace{e^{j\pi(f_1 + f_2)\tau} \delta(\nu - (f_1 - f_2))}_{\text{cross-term}} + \\ &+ \underbrace{e^{j\pi(f_1 + f_2)\tau} \delta(\nu + (f_1 - f_2))}_{\text{cross-term}} + \underbrace{e^{j2\pi f_2 \tau} \delta(\nu)}_{\text{auto-term}}. \end{aligned} \quad (2.31)$$

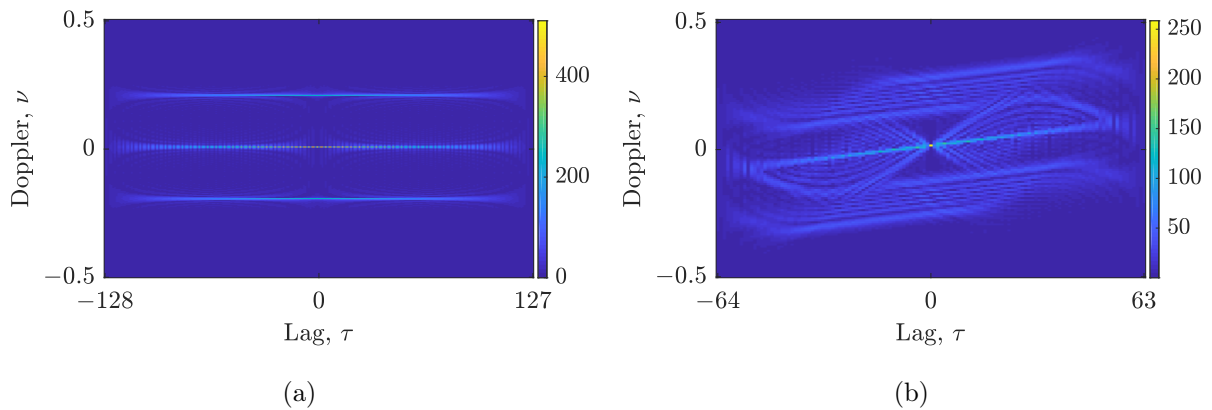


Figure 2.4 Ambiguity function of the considered examples of: (a) a stationary signal with two constant frequency modulated components; (b) a non-stationary signal with a linear and sinusoidal frequency modulated component, $z_{\text{SINLFM}}(t)$.

The magnitude plot of the AF is commonly used to represent the auto-terms and cross-terms, as demonstrated in Figure 2.4. For the signal's AF calculated in (2.31), the auto-term trajectories of both tones pass through the AF origin and do not intersect with the cross-terms, as illustrated in Figure 2.4a. However, for the signal $z_{\text{SINLFM}}(t)$ depicted in Figure 2.4b, the cross-terms intersect with the sinusoidal component, presenting a more challenging task for kernel design.

Numerous QTFDs have been designed with varying levels of compromise between the concentration of auto-terms and the suppression of cross-terms [14, 44, 91, 113]. Table 2.1 lists the most frequently utilized QTFDs alongside their kernels in the time-lag and Doppler-lag domains. Figure 2.5 demonstrates the chosen QTFDs and the SPEC achieved for the signal $z_{\text{SINLFM}}(t)$.

Notably, the WVD and SPEC exhibit entirely different performance characteristics. Specifically, the WVD (shown in Figure 2.5a) provides superior auto-term resolution while being heavily influenced by cross-terms, whereas the SPEC (shown in Figure 2.5b) does not experience any cross-terms but exhibits the poorest auto-term resolution. Other QTFDs fall somewhere between these two extremes, with the EMBD emerging as the TFD that achieves the optimal balance between auto-term resolution quality and cross-term suppression, as shown in Figure 2.5f. Additionally, we can identify two categories of cross-terms: the inner-terms resulting from non-linear frequency modulation of the signal component and the outer-terms arising from the interaction between the signal components. Both cross-term categories, particularly when superimposed with noise, may diminish the interpretation of the TFD in practice.

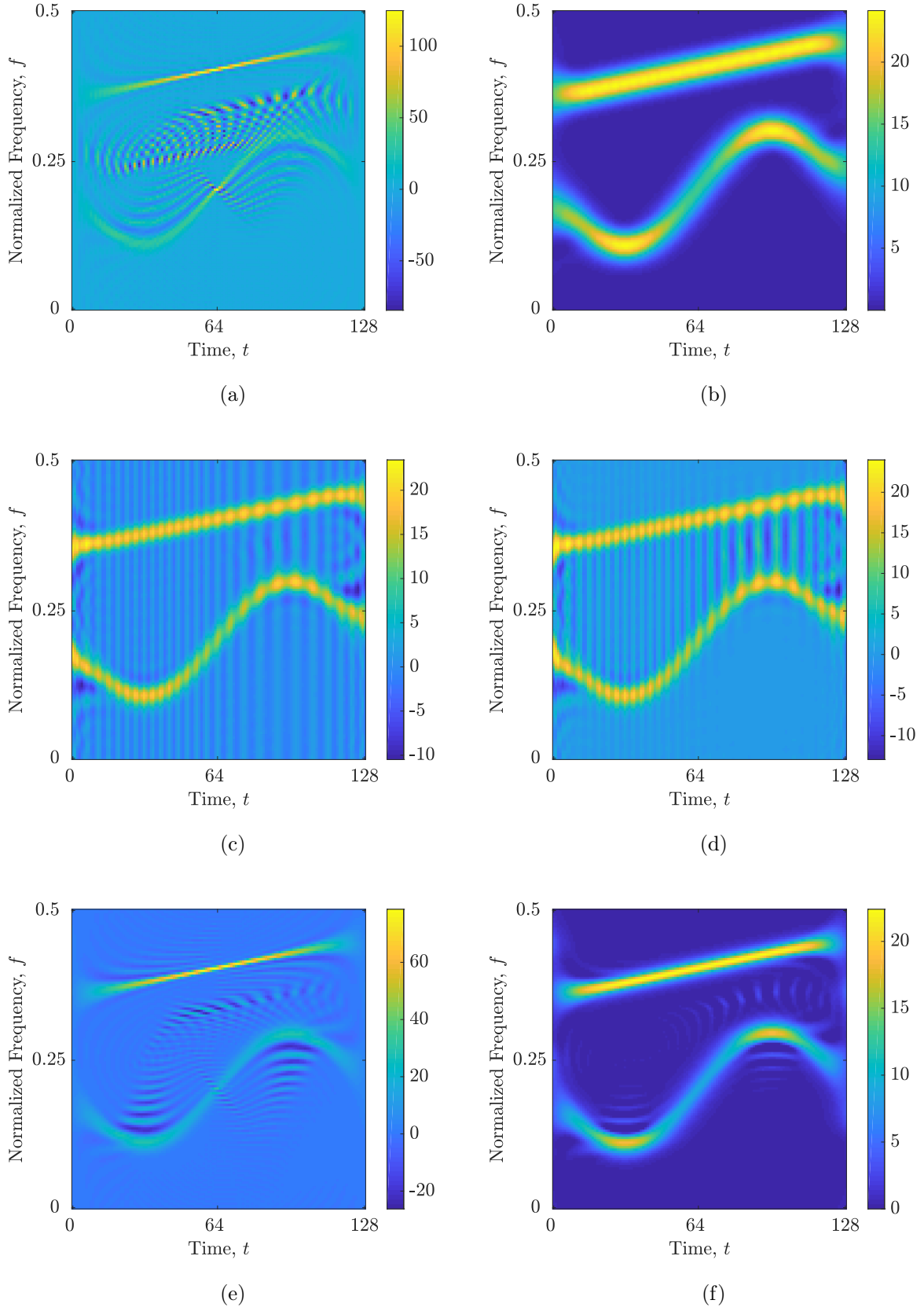


Figure 2.5 Considered QTFDs of the signal $z_{\text{SINLFM}}(t)$: (a) WVD; (b) SPEC (*Hamming*, $N_w = 32$); (c) CWD ($\sigma_{\text{CW}} = 1$), (d) BJD ($\alpha_{\text{BJ}} = 0.4$), (e) MBD ($\beta_{\text{MB}} = 0.2$); (f) EMBD ($\alpha_{\text{EMB}} = 0.3, \beta_{\text{EMB}} = 0.12$.)

Table 2.1 Time-lag and Doppler-lag selected QTFD kernels.

Distribution	Kernel	
	$G(t, \tau)$	$g(\nu, \tau)$
Wigner-Ville [126, 137]	$\delta(t)$	1
Choi-Williams (CWD) [27]	$\frac{\sqrt{\pi\sigma_{CW}}}{ \tau } e^{-\pi^2\sigma_{CW}t^2/\tau^2}$	$e^{-\nu^2\tau^2/\sigma_{CW}}$
Born-Jordan (BJD) [22]	$\frac{1}{ 2\alpha_{BJ}\tau } \text{rect} \frac{t}{2\alpha_{BJ}\tau}$	$\text{sinc}(2\alpha_{BJ}\nu\tau)$
Modified B (MBD) [48]	$\frac{\cosh^{-2\beta_{MB}} t}{\int_{-\infty}^{\infty} \cosh^{-2\beta_{MB}} \xi d\xi}$	$\frac{ \Gamma(\beta_{MB} + j\pi\nu) ^2}{\Gamma^2(\beta_{MB})}$
Extended Modified B (EMBD) [18]	$\frac{ \Gamma(\alpha_{EMB} + j\pi\tau) ^2 \cosh^{-2\beta_{EMB}} t}{\Gamma^2(\alpha_{EMB}) \int_{-\infty}^{\infty} \cosh^{-2\beta_{EMB}} \xi d\xi}$	$\frac{ \Gamma(\beta_{EMB} + j\pi\nu) ^2}{\Gamma^2(\beta_{EMB})} \frac{ \Gamma(\alpha_{EMB} + j\pi\tau) ^2}{\Gamma^2(\alpha_{EMB})}$

2.4 Adaptive Time-Frequency Distribution

However, despite the advantages of QTFDs, they suffer from an inability to perfectly concentrate the energy of signal auto-terms while suppressing cross-terms. To address this issue, adaptive directional filtering has been used to achieve a better compromise between the resolution of auto-terms and the suppression of cross-terms [59, 64, 68]. Conventional filtering methods employ a uniform directional kernel across all points within a TFD without making local adaptations. However, these techniques prove inadequate for signals exhibiting energy distribution in multiple directions. To address these limitations, an adaptive directional TFD (ADTFD) approach was introduced [64], which dynamically fine-tunes the orientation of the smoothing kernel at every point within the TFD, as [64]:

$$\rho_{(ad)}(t, f) = \rho(t, f) \underset{t}{*} \underset{f}{*} \gamma_{\theta}(t, f), \quad (2.32)$$

where $\gamma_{\theta}(t, f)$ is the adaptive directional kernel, whose orientation is regulated by the parameter θ . The adaptive directional kernel may be applied to various TFDs with the goal of further improving its performance. However, it has been shown that the WVD is not suitable when analyzing noisy signals or signals with non-LFM components [59, 64, 68]. Instead, the EMBD has been selected as an underlying QTFD for the study in this dissertation, as in [59, 64, 65, 67, 68].

The double-derivative directional Gaussian filter (DGF), which satisfies the required properties of the adaptive directional kernel, has been selected as $\gamma_{\theta}(t, f)$ [64, 78]:

$$\gamma_{\theta}(t, f) = \frac{ab}{2\pi} \frac{d^2}{df_{\theta}^2} e^{-a^2 t_{\theta}^2 - b^2 f_{\theta}^2}, \quad (2.33)$$

where $f_{\theta} = -t \sin(\theta) + f \cos(\theta)$ and $t_{\theta} = t \cos(\theta) + f \sin(\theta)$, while the smoothing degree along the time and frequency axes is governed by parameters a and b , respectively.

The local orientation angle of $\gamma_\theta(t, f)$ is dynamically adjusted for every TF point by optimizing the correlation between TF ridges and the $\gamma_\theta(t, f)$, as [64]:

$$\theta(t, f) = \arg \max_{\theta} \left| \left| \rho(t, f) \right| *_t *_f \gamma_\theta(t, f) \right|, \quad -\pi/2 \leq \theta \leq \pi/2. \quad (2.34)$$

Previous investigations [64, 68] have proposed that designating a small value to parameter a facilitates pronounced smoothing along the major axis, while an increase in the parameter b value impedes the consolidation of closely proximate components. To provide accurate guidelines, it is recommended to set a within the range of [2,3], and b within the range of [5,30]. Furthermore, besides the smoothing parameters a and b , the window length, denoted with WL , of $\gamma_\theta(t, f)$ plays a crucial role. A smaller WL inadequately resolves closely located components and eliminates cross-terms, while preserving the energy of short-duration components. Contrarily, an augmented WL brings about the inverse outcome [64, 68].

The exhaustive search with all (a, b, WL) combinations is computationally demanding; thus, an automatically optimized version of the ADTFD, specifically the locally adaptive ADTFD (LO-ADTFD)¹, denoted as $\rho_{(lo)}(t, f)$, was used in this dissertation [87]. The LO-ADTFD is derived by selecting TF points with the minimum value from a predetermined set of ADTFDs. In this dissertation, the parameter values (a, b) were chosen from the set $\{(2, 20), (2, 30), (3, 6), (3, 8)\}$, while the WL was optimized for every (a, b) combination using the evaluation metric given in [116]. The optimization was performed within the range of $[N_t/4 : 4 : 3N_t/8]$ for the combination $\{(3, 8), (2, 30)\}$ and $[N_t/8 : 4 : N_t/4]$ for the combination $\{(3, 6), (2, 20)\}$, as recommended in [87]. Here, N_t denotes the number of time samples. An example of LO-ADTFD for the signal $z_{\text{SINLFM}}(t)$ is depicted in Figure 2.6, showing high auto-term resolution and cross-term suppression.

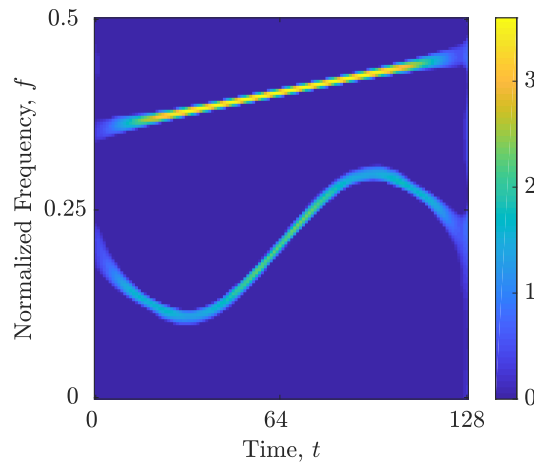


Figure 2.6 LO-ADTFD of the signal $z_{\text{SINLFM}}(t)$.

¹Available at: <https://github.com/mokhtarmohammadi/Locally-Optimized-ADTFD>

2.5 Global Concentration Measures for Time-Frequency Distributions

Due to the absence of a universally optimal kernel suitable for all applications, there has been a demand for an unbiased method to evaluate the performance of TFDs [14]. One such approach is to quantify the concentration of the auto-terms and the quality of cross-term suppression by computing the TFD complexity. In this section, the state-of-the-art global concentration measures are reviewed that consider the TFD as a whole and produce a single numerical value. First, Jones and Park introduced a concentration measure [50], known as the *ratio-of-norms*, M^{RN} , which is computed as follows [50]:

$$M^{\text{RN}} = \frac{\int_{-\infty}^{\infty} \int_{-\infty}^{\infty} \rho^4(t, f) dt df}{\left(\int_{-\infty}^{\infty} \int_{-\infty}^{\infty} \rho^2(t, f) dt df \right)^2}. \quad (2.35)$$

A high value of M^{RN} indicates a high TFD concentration, and vice versa. However, this measure can produce misleading results when signal components have varying amplitudes. Given that the sparsity complexity requirement is met by TFD, the *Hoyer measure* can be employed, which is expressed as [47]:

$$M^{\text{H}} = \left(\sqrt{H} - \frac{\int_{-\infty}^{\infty} \int_{-\infty}^{\infty} |\rho(t, f)| dt df}{\sqrt{\int_{-\infty}^{\infty} \int_{-\infty}^{\infty} |\rho(t, f)|^2 dt df}} \right) (\sqrt{H} - 1)^{-1}, \quad (2.36)$$

where $H = N_t \times N_f$ is the total size of the TFD (N_f being the number of frequency bins). A larger M^{H} value signifies a more condensed and preferable TFD, and vice versa. An alternative method for assessing the TFD effectiveness is by quantifying its region of support, defined as [116]:

$$M^{\text{S}} = \frac{1}{N_t N_f} \left[\int_{-\infty}^{\infty} \int_{-\infty}^{\infty} \left| \frac{\rho(t, f)}{\int_{-\infty}^{\infty} \int_{-\infty}^{\infty} \rho(t, f) dt df} \right|^{\frac{1}{p_s}} dt df \right]^{p_s}, \quad p_s > 1 \in \mathbb{N}, \quad (2.37)$$

where $p_s = 2$ has been recommended [116]. A lower M^{S} value indicates a higher TFD concentration, and vice versa. Finally, given that TFD signifies a pseudo-energy density in the TF domain, the *Rényi entropy*, denoted as R , may be used to quantify TFD complexity, given as [3, 8, 138]:

$$R = \frac{1}{1 - \alpha_{\text{R}}} \log_2 \int_{-\infty}^{\infty} \int_{-\infty}^{\infty} \left(\frac{\rho(t, f)}{\int_{-\infty}^{\infty} \int_{-\infty}^{\infty} \rho(t, f) dt df} \right)^{\alpha_{\text{R}}} dt df, \quad \alpha_{\text{R}} > 2 \in \mathbb{N}. \quad (2.38)$$

Table 2.2 Concentration measures of the considered QTFDs, SPEC and LO-ADTFD for the signal $z_{\text{SINLFM}}(t)$. Values in bold indicate the best-performing TFD according to the respective measure.

TFD	$z_{\text{SINLFM}}(t)$			
	$M^{\text{RN}} \times 10^4$	M^{H}	M^{S}	R
WVD	6.8591	0.4414	2.9010	9.3291
SPEC	3.4575	0.4804	0.4199	12.0026
CWD	4.4747	0.4143	1.1001	11.2507
BJD	4.2860	0.4435	0.9202	11.2052
MBD	16.0	0.5501	0.9722	9.9678
EMBD	6.8768	0.5606	0.3807	11.4196
LO-ADTFD	19.0	0.7597	0.0840	9.7773

In practical applications, $\alpha_{\text{R}} = 3$ is usually used [3, 8, 138], as in this dissertation. When α_{R} takes on an odd number value, the cross-terms are eliminated, and the Rényi entropy solely captures information from the auto-terms. As M^{S} , a lower R value represents a more desirable TFD, and vice versa.

Using $p_s = 2$ and $\alpha_{\text{R}} = 3$, concentration measures were computed for the chosen QTFDs of the signal $z_{\text{SINLFM}}(t)$. The results are provided in Table 2.2, utilizing the measures given by (2.35), (2.36), (2.37), and (2.38). Since the Rényi entropy only considers the auto-terms and disregards cross-terms, the TFD with the most concentrated auto-terms, in this case the WVD, is deemed the best-performing one. However, the other three concentration measures select LO-ADTFD as the optimal choice. Among the concentration measures considered, M^{S} and R have been widely utilized in numerous studies, to name a few [14, 44, 91, 113, 127, 131].

2.6 Summary

This chapter has demonstrated the benefits of the combined time-frequency signal representation compared to the disjoint time and frequency signal representations. It has examined the desirable properties of an ideal TFD and compared conventional numerical methods for TFD computation with the adaptive directional TFD. The superior performance of the advanced, adaptive directional TFD has been evaluated with state-of-the-art global TFD performance measures, evidencing feasibility in dealing with the compromise between auto-term resolution and cross-term suppression.

CHAPTER 3

TIME-FREQUENCY SIGNAL ANALYSIS USING COMPRESSIVE SENSING

This chapter presents the compressive sensing-based method as an advanced approach to enhance TFD concentration. It investigates the application of sparse reconstruction techniques employing ℓ_0 , ℓ_1 , and ℓ_2 norm-based regularization functions and evaluates the efficacy of state-of-the-art algorithms in achieving improved TFD concentration. Additionally, the chapter critically examines the influence of selecting suitable regularization parameters on the reconstructed TFD's quality, raising concerns about the appropriateness of employing global concentration measures introduced in the preceding chapter.

3.1 Sparse Time-Frequency Distribution Reconstruction

The notion of computing sparse TFDs bears resemblance to the cross-term filtering technique employed in QTFD. The QTFD methodology entails assigning weights to every auto-term sample in accordance with its proximity to the AF origin. Conversely, the sparse TFD method entails the selection of a limited number of auto-terms samples through a technique named as *compressive sensing* (CS). The remaining points are then calculated in order to produce the TFD with the fewest non-zero values, thereby achieving sparsity [37, 108, 114, 127, 131].

3.1.1 Problem Formulation

In matrix form, the AF filtering described by (2.25), results in the observation matrix, or the CS-AF [108, 127, 131]:

$$\mathbf{A}_z^M(\nu, \tau) = \begin{cases} \mathbf{A}_z(\nu, \tau), & (\nu, \tau) \in C_\Omega, \\ 0, & \text{otherwise,} \end{cases} \quad (3.1)$$

where $\mathbf{A}_z(\nu, \tau)$ is the matrix representation of the discrete AF in (2.24), while C_Ω is the index set of the (ν, τ) area around the AF origin. It is essential to clarify that the approach presented in (3.1) diverges from the conventional CS technique that seeks the reconstruction of the original signal. Instead, the objective is to reconstruct a TFD that is devoid of cross-terms. Consequently, the selection of the CS-AF area cannot be a random process. The AF samples must be selected purposefully to guarantee that they solely correspond to the auto-terms.

To achieve a cross-terms-free TFD through sparse reconstruction, an adaptive rectangular CS-AF area of size $N'_\tau \times N'_\nu$ has been proposed [127, 131], where N'_ν and N'_τ represent the numbers of Doppler and lag bins, respectively. The CS-AF area, fixed adjacent to the initial pair of cross-terms, is usually centered around the origin. The selection of the parameters N'_τ and N'_ν is determined by matching the Doppler and lag distance between the first pair of cross-terms and the AF domain origin. To accomplish this, the method examines zero-lag ($A_z(\nu, 0)$) and the zero-Doppler ($A_z(0, \tau)$) slices, searching for the initial spike of energy located away from the origin [127, 131]. By enlarging the size of this area compared to the static $\sqrt{N_t} \times \sqrt{N_t}$ area used in [21, 37, 114, 123], with cardinality $\text{card}(\mathbf{A}_z^M(\nu, \tau)) \cong N_t$, the CS-AF area contains more samples related to auto-terms, while simultaneously reducing the demands of the reconstruction algorithm [127, 131].

The difference between the static $\sqrt{N_t} \times \sqrt{N_t}$ and adaptive $N'_\tau \times N'_\nu$ CS-AF areas is illustrated in Figure 3.1 for the signal $z_{\text{SINLFM}}(t)$ and signal $z_{\text{LFM}}(t)$ consisting of four LFM components with varying amplitudes embedded in additive white Gaussian noise (AWGN) with the signal-to-noise ratio $\text{SNR} = 5$ dB. From the visual observation of both CS-AF areas, the $N'_\tau \times N'_\nu$ area selected more auto-term-related samples while avoiding cross-terms, compared to the $\sqrt{N_t} \times \sqrt{N_t}$. The importance of selecting the appropriate CS-AF area will be further discussed in this dissertation.

The relation between the sparse TFD, denoted as $\Upsilon_z(t, f)$, and $\mathbf{A}_z^M(\nu, \tau)$ is given as follows [108, 127, 131, 147]:

$$\Upsilon_z(t, f) = \Psi^H \cdot \mathbf{A}_z^M(\nu, \tau), \quad (3.2)$$

where Ψ^H denotes the Hermitian transpose of a domain transformation matrix portraying

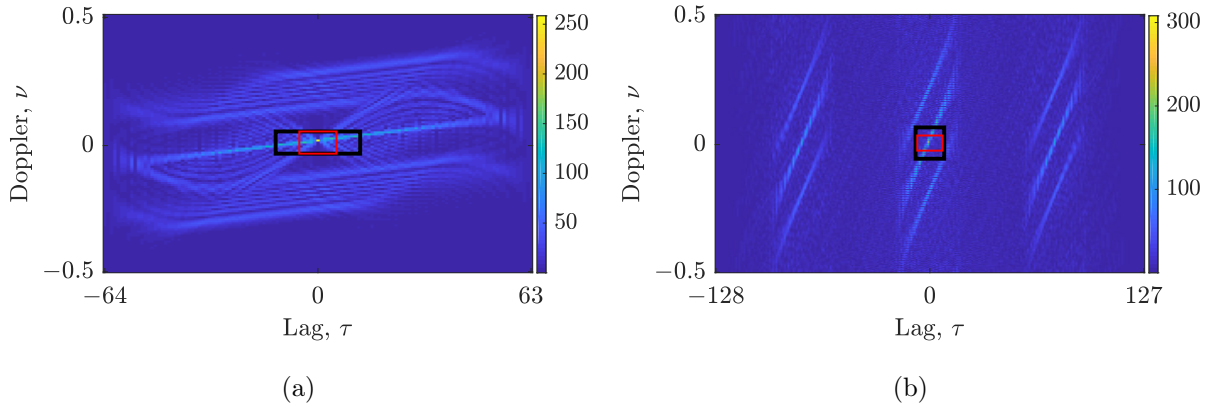


Figure 3.1 Ambiguity functions with the static CS-AF area, $\sqrt{N_t} \times \sqrt{N_t}$, (red rectangle) versus the automatically obtained adaptive CS-AF area, N'_τ and N'_ν , (black rectangle): (a) $z_{\text{SINLFM}}(t)$, $\sqrt{N_t} \cong 11$ (static), $N'_\tau = 25, N'_\nu = 11$ (adaptive); (b) $z_{\text{LFM}}(t)$, $\sqrt{N_t} \cong 15$ (static), $N'_\tau = 17, N'_\nu = 31$ (adaptive).

the 2D FT analogue to (2.24). In contrast to the conventional CS formulation, the objective in (3.2) is to determine the optimal solution for $\Upsilon_z(t, f)$ using the information provided by $\mathbf{A}_z^M(\nu, \tau)$. Due to the significantly smaller number of samples present in $\mathbf{A}_z^M(\nu, \tau)$ ($N'_\tau \times N'_\nu$) compared to the desired high-resolution TFD $\Upsilon_z(t, f)$ ($N_t \times N_f$), that is, $\text{card}(\mathbf{A}_z^M(\nu, \tau)) \ll \text{card}(\Upsilon_z(t, f))$ there exists no unique solution for (3.2) [108, 127, 131]. As a result, a regularization function is given to highlight the desired attributes of the solution, serving as the objective function to be minimized. Essentially, it leads to an unconstrained optimization problem expressed as follows [1, 13, 108, 127, 139, 147]:

$$\hat{\Upsilon}_z(t, f) = \arg \min_{\Upsilon_z(t, f)} \frac{1}{2} \|\Upsilon_z(t, f) - \Psi^H \mathbf{A}_z^M(\nu, \tau)\|_2^2 + \lambda c(\Upsilon_z(t, f)), \quad (3.3)$$

where $c(\Upsilon_z(t, f)) : \mathbb{R}^2 \rightarrow \mathbb{R}$ is the regularization function, and $\lambda > 0$ is the regularization parameter. To attain a sparse solution, the regularization function must promote sparsity, $\hat{\Upsilon}_z(t, f)$. In pursuit of that, the ℓ_q -norm with $0 \leq q \leq 2$ has been investigated in previous studies [21, 37, 39, 42, 113, 114, 127, 128, 130, 131, 147]. However, the ℓ_2 norm, which measures signal energy, is not a sparsity-inducing function. As demonstrated in [127], reconstruction based on the ℓ_2 norm yields poor auto-term resolution and filters out a significant number of auto-terms.

3.1.2 Problem Solution

When solving the sparse TFD reconstruction problem using regularization functions based on either ℓ_0 or ℓ_1 norms, the optimization problem described in (3.3) can be restated

as follows [94, 127, 147]:

$$\mathbf{Y}_z^{\ell_0,1}(t, f) = \arg \min_{\mathbf{Y}_z(t, f)} \|\mathbf{Y}_z(t, f)\|_{0,1}, \quad \text{s.t.} \quad \|\mathbf{Y}_z(t, f) - \mathbf{\Psi}^H \mathbf{A}_z^M(\nu, \tau)\|_2^2 \leq \epsilon, \quad (3.4)$$

where ϵ is a predefined solution tolerance. The resulting sparse TFD is obtained when the ϵ is met or until the user-defined maximum number of iterations, N_{it} , is achieved. In this dissertation, $\epsilon = 10^{-3}$ and $N_{it} = 100$ are used as in [127, 128, 129, 130, 131]. Closed-form solutions exist for the minimization problem (3.4) when using ℓ_0 and ℓ_1 norms. Specifically, for the ℓ_0 norm, the solution is expressed as [127]:

$$\mathbf{Y}_z^{\ell_0}(t, f) = \text{hard}_{\sqrt{2\lambda}}\{\mathbf{Y}_z(t, f)\}, \quad (3.5)$$

where $\text{hard}_{\sqrt{2\lambda}}\{\mathbf{Y}_z(t, f)\}$ denotes a hard-thresholding function, which is mathematically expressed as [127]:

$$\text{hard}_{\sqrt{2\lambda}}\{\mathbf{Y}_z(t, f)\} = \begin{cases} \mathbf{Y}_z(t, f), & \mathbf{Y}_z(t, f) \geq \sqrt{2\lambda}, \\ 0, & \text{otherwise.} \end{cases} \quad (3.6)$$

Similarly, for the ℓ_1 norm, the closed-form solution is expressed as [127]:

$$\mathbf{Y}_z^{\ell_1}(t, f) = \text{soft}_{\lambda}\{\mathbf{Y}_z(t, f)\}, \quad (3.7)$$

where $\text{soft}_{\lambda}\{\mathbf{Y}_z(t, f)\}$ represents a soft-thresholding function, which is given as follows [127]:

$$\text{soft}_{\lambda}\{\mathbf{Y}_z(t, f)\} = \text{sgn}(\mathbf{Y}_z(t, f)) \max(|\mathbf{Y}_z(t, f)| - \lambda, 0). \quad (3.8)$$

While the ℓ_0 norm is known to be the most effective in inducing sparsity, minimizing it necessitates exploring all potential aggregations of non-zero elements in a given matrix. This process is computationally expensive and NP-hard. Therefore, the ℓ_0 minimization is often approximated iteratively using greedy or hard-thresholding-based algorithms [7, 37, 94, 127, 143]. Additionally, the ℓ_0 norm is sensitive to noise due to its reliance on counting the number of non-zero elements, which can readily increase in the presence of noise.

The ℓ_1 norm is a widely used regularization function due to its convexity and ease of global minimum identification [7, 108, 127]. Although reconstruction algorithms based on the ℓ_1 norm generally require more computation time than those based on the ℓ_0 norm, a study [127] has demonstrated that ℓ_1 norm-based reconstructed TFDs outperform TFDs reconstructed using classical filtering, as well as those based on the ℓ_2 and ℓ_0 norms.

Therefore, the reconstruction algorithms used in this dissertation and listed below are based on the ℓ_1 norm, which were carefully selected based on their performance in past

studies [108, 127, 128, 130, 131].

The two-step iterative shrinkage/thresholding (TwIST) algorithm is a high-performing algorithm where the solution of the $(n + 1)$ -th iteration depends on solutions from the previous two iterations, given as [13, 127]:

$$\begin{aligned} [\mathbf{r}_z^{\ell_1}(t, f)]^{[n+1]} &= (1 - \alpha_{\text{TwIST}}) [\mathbf{r}_z^{\ell_1}(t, f)]^{[n-1]} + (\alpha_{\text{TwIST}} - \beta_{\text{TwIST}}) [\mathbf{r}_z^{\ell_1}(t, f)]^{[n]} + \\ &+ \beta_{\text{TwIST}} \text{soft}_\lambda \left\{ [\mathbf{r}_z^{\ell_1}(t, f)]^{[n]} + \Psi^H \left(\mathbf{A}_z^M(\nu, \tau) - \Psi [\mathbf{r}_z^{\ell_1}(t, f)]^{[n]} \right) \right\}, \end{aligned} \quad (3.9)$$

where $\alpha_{\text{TwIST}} \in \langle 0, 1 \rangle$ and $\beta_{\text{TwIST}} \in \langle 0, 2\alpha_{\text{TwIST}} \rangle$, $\alpha_{\text{TwIST}}, \beta_{\text{TwIST}} \in \mathbb{R}$, are the relaxation parameters.

The sparse reconstruction by separable approximation (SpaRSA) framework systematically reduces a thresholding parameter throughout algorithm iterations at two levels, namely the outer and inner iterations, as [127, 139]:

$$[\alpha_{\text{SpaRSA}}]^{[n+1]} = \frac{\left([\mathbf{r}_z^{\ell_1}(t, f)]^{[n]} - [\mathbf{r}_z^{\ell_1}(t, f)]^{[n-1]} \right)^T \left(\nabla f \left([\mathbf{r}_z^{\ell_1}(t, f)]^{[n]} \right) - \nabla f \left([\mathbf{r}_z^{\ell_1}(t, f)]^{[n-1]} \right) \right)}{\left([\mathbf{r}_z^{\ell_1}(t, f)]^{[n]} - [\mathbf{r}_z^{\ell_1}(t, f)]^{[n-1]} \right)^T \left([\mathbf{r}_z^{\ell_1}(t, f)]^{[n]} \right) - \left([\mathbf{r}_z^{\ell_1}(t, f)]^{[n-1]} \right)}, \quad (3.10a)$$

$$[\mathbf{r}_z^{\ell_1}(t, f)]^{[n+1]} = \text{soft}_{\frac{\lambda}{[\alpha_{\text{SpaRSA}}]^{[n+1]}}} \left\{ [\mathbf{r}_z^{\ell_1}(t, f)]^{[n]} - \frac{1}{[\alpha_{\text{SpaRSA}}]^{[n+1]}} \nabla f \left([\mathbf{r}_z^{\ell_1}(t, f)]^{[n]} \right) \right\}, \quad (3.10b)$$

where $\nabla f \left([\mathbf{r}_z^{\ell_1}(t, f)]^{[n+1]} \right)$ is the gradient of error estimation function, while $[\alpha_{\text{SpaRSA}}]^{[n+1]}$ in each iteration is decreased with the parameter $\beta_{\text{SpaRSA}} < 1$.

The split augmented Lagrangian shrinkage algorithm (SALSA) converts the unconstrained optimization problem (3.4) into a constrained optimization problem with equivalence through variable splitting: $[\mathbf{r}_z^{\ell_1}(t, f)]^{[n]} = [\mathbf{a}(t, f)]^{[n]} + [\mathbf{b}(t, f)]^{[n]}$, based on which the SALSA algorithm is defined as [1, 127]:

$$[\mathbf{r}_z^{\ell_1}(t, f)]^{[n+1]} = \Psi^H \left(\mathbf{A}_z^M(\nu, \tau) - \Psi \left([\mathbf{v}(t, f)]^{[n]} + [\mathbf{b}(t, f)]^{[n]} \right) \right), \quad (3.11a)$$

$$[\mathbf{a}(t, f)]^{[n+1]} = \text{soft}_\lambda \left\{ [\mathbf{r}_z^{\ell_1}(t, f)]^{[n+1]} - [\mathbf{b}(t, f)]^{[n]} \right\}, \quad (3.11b)$$

$$[\mathbf{b}(t, f)]^{[n+1]} = [\mathbf{b}(t, f)]^{[n]} - \left([\mathbf{r}_z^{\ell_1}(t, f)]^{[n+1]} - [\mathbf{a}(t, f)]^{[n+1]} \right). \quad (3.11c)$$

The your augmented Lagrangian algorithm for ℓ_1 (YALL1), similarly to the SALSA algorithm, is given as [127, 143]:

$$[\mathbf{y}(\nu, \tau)]^{[n+1]} = \alpha_{\text{YALL}} \Psi [\mathbf{z}(t, f)]^{[n]} - \beta_{\text{YALL}} \left(\Psi [\mathbf{r}_z^{\ell_1}(t, f)]^{[n]} - \mathbf{A}_z^M(\nu, \tau) \right), \quad (3.12a)$$

$$[\mathbf{z}(t, f)]^{[n+1]} = \text{soft}_{\frac{\lambda}{\mu_{\text{YALL}}}} \left\{ \Psi^H [\mathbf{y}(\nu, \tau)]^{[n+1]} + \frac{1}{\mu_{\text{YALL}}} [\mathbf{r}_z^{\ell_1}(t, f)]^{[n]} \right\}, \quad (3.12b)$$

$$[\mathbf{r}_z^{\ell_1}(t, f)]^{[n+1]} = [\mathbf{r}_z^{\ell_1}(t, f)]^{[n]} + \gamma_{\text{YALL}}\mu_{\text{YALL}} \left(\Psi^H [\mathbf{y}(\nu, \tau)]^{[n+1]} - [\mathbf{z}(t, f)]^{[n+1]} \right), \quad (3.12c)$$

where $\mu_{\text{YALL}} > 0$ is the penalty parameter, while the parameters α_{YALL} , β_{YALL} and γ_{YALL} are calculated as: $\gamma_{\text{YALL}} \in [0, (1 + \sqrt{5})/2]$, $\alpha_{\text{YALL}} = \mu_{\text{YALL}}/(\mu_{\text{YALL}} + (1/2\lambda))$, and $\beta_{\text{YALL}} = 1/(\mu_{\text{YALL}} + (1/2\lambda))$.

3.2 Limitations of the Existing Measurement Criteria When Selecting the Optimal Regularization Parameter λ

Many previous studies, including [7, 37, 46, 108, 123, 127], emphasized the significance of the parameter λ , which must be carefully chosen to achieve good reconstruction performance. Setting λ too low may fail to remove cross-terms, while setting it too high may remove auto-term samples as well. However, the optimal value of λ is dependent on the signal, the reconstruction algorithm, and the specific use case, because of which in many studies λ has been chosen experimentally [37, 46, 108, 123, 127, 130, 131]. Experimental selection of λ can be time-consuming and requires expertise from the user.

Sorting TFD samples based on their amplitude has also been proposed [123], but this approach may not work well for signals with components of varying amplitudes, and it was shown to be dependent on the number of total components and level of noise, which are not often available in practice.

Several studies [46, 123] have proposed feasible ranges for λ based on their extensive research. For example, $\lambda \in [0.001, 10]$ and $\lambda \in [0.001, 40]$ have been proposed in [46] for CS-based methods that do not use the WVD and AF as in this dissertation. However, these ranges proved to be method-specific and cannot be used for different CS-based methods.

To illustrate the effect of parameter λ on reconstruction performance, two low values, $\lambda = 0.01$ and $\lambda = 1$, and one high value $\lambda = 15$, were arbitrarily selected and tested on the considered reconstruction algorithms and the signals $z_{\text{SINFM}}(t)$ and $z_{\text{LFM}}(t)$. Figure 3.2 depicts the obtained reconstructed TFDs. On the one hand, it is to be observed that by setting λ parameter too high, a partial or complete lack of auto-terms appears in a reconstructed TFD, as shown with $\lambda = 15$ in Figures 3.2a, 3.2e and 3.2g. On the other hand, too low λ parameter causes the reconstruction of cross-terms with blurred auto-terms, as shown in Figures 3.2b, 3.2d, 3.2f and 3.2h.

Moreover, the λ performance dependency on the reconstruction algorithm is evident from the reconstructed TFDs shown in Figures 3.2a and 3.2c, where for the same $\lambda = 15$, the SALSA algorithm achieves significantly better preservation of auto-terms than the TwIST algorithm.

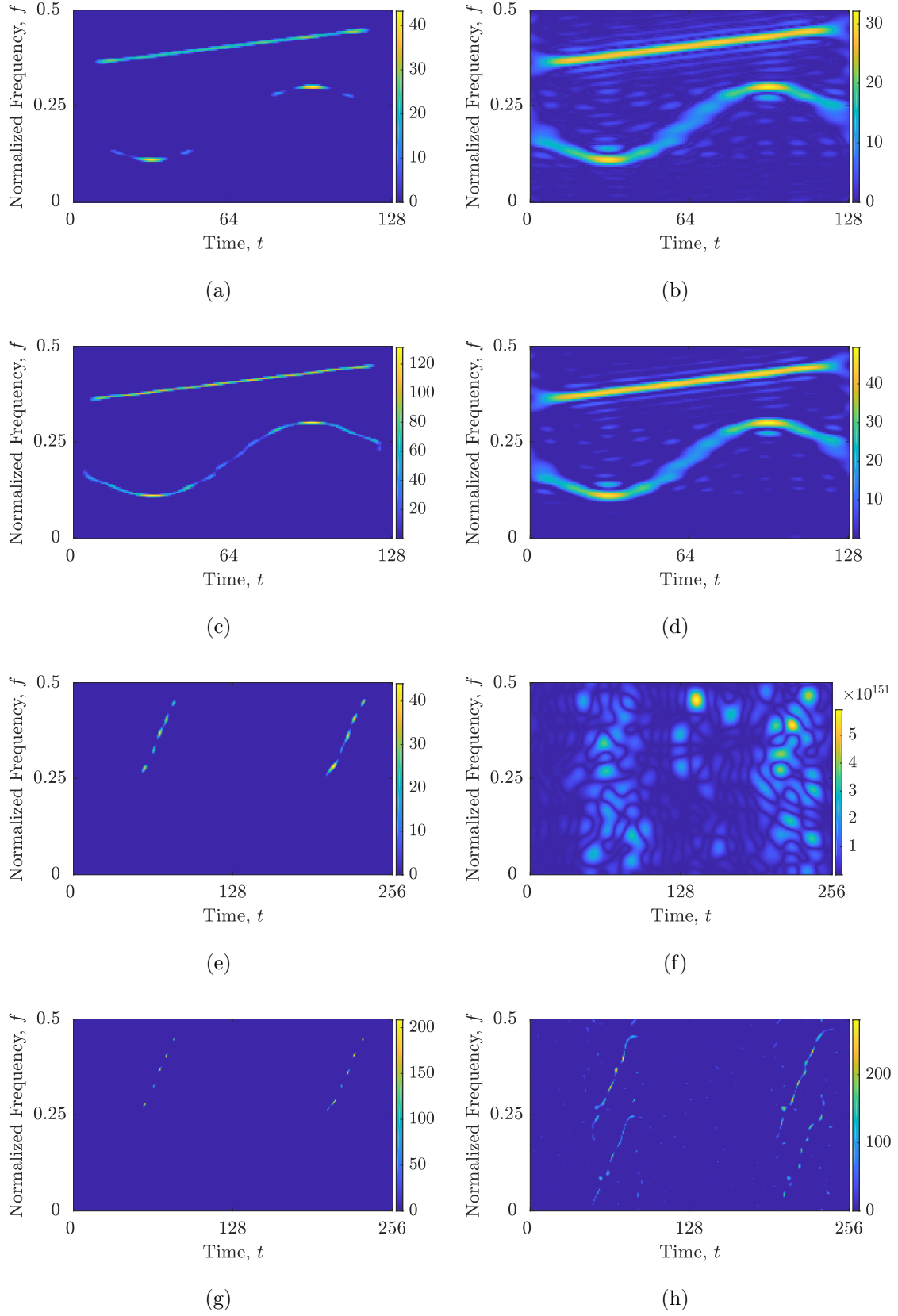


Figure 3.2 Reconstructed TFDs for the following signal, reconstruction algorithm and parameter λ : (a) $z_{\text{SINFM}}(t)$, TwIST, $\lambda = 15$; (b) $z_{\text{SINFM}}(t)$, TwIST, $\lambda = 0.01$; (c) $z_{\text{SINFM}}(t)$, SALSA, $\lambda = 15$; (d) $z_{\text{SINFM}}(t)$, SALSA, $\lambda = 1$; (e) $z_{\text{LFM}}(t)$, SpARSA, $\lambda = 15$; (f) $z_{\text{LFM}}(t)$, SpARSA, $\lambda = 0.01$; (g) $z_{\text{LFM}}(t)$, YALL1, $\lambda = 15$; (h) $z_{\text{LFM}}(t)$, YALL1, $\lambda = 1$.

Table 3.1 Performance measures of the considered ℓ_1 norm-based reconstruction algorithms with an arbitrarily chosen regulation parameter λ . According to the respective measure, values in bold indicate the best-performing reconstruction algorithm for the signals $z_{\text{SINLFM}}(t)$ and $z_{\text{LFM}}(t)$.

$z_{\text{SINLFM}}(t)$				
	TwIST	TwIST	SALSA	SALSA
	$\lambda = 15$	$\lambda = 0.01$	$\lambda = 15$	$\lambda = 1$
R	8.3191	11.5049	8.4739	10.9909
M^{S}	0.0253	0.5069	0.0416	0.2846
$M^{\text{RN}}(\times 10^4)$	42.0741	6.9837	39.0077	8.2131
M^{H}	0.8617	0.5389	0.8529	0.6259
$z_{\text{LFM}}(t)$				
	SpaRSA	SpaRSA	YALL1	YALL1
	$\lambda = 15$	$\lambda = 0.01$	$\lambda = 15$	$\lambda = 1$
R	8.0075	13.9955	5.6745	9.2696
M^{S}	0.0054	0.6635	0.0011	0.0182
$M^{\text{RN}}(\times 10^4)$	55.1245	NaN	277.1471	31.0014
M^{H}	0.9382	0.4336	0.9746	0.8981

Additionally, it is important to address the numerical evaluation of reconstructed TFDs. A number of previous studies, involving [127, 130, 131], have relied on global concentration measures, such as M^{S} and R , which produce a single numerical value for a TFD and do not consider the local positional information of individual samples. This simplicity can result in the misclassification of oversparse or completely empty TFDs. Indeed, reconstructed TFDs may be compared with an ideal version of the signal’s TFD, but finding a suitable metric that does not necessitate any a priori information about the signal remains an open research direction.

To demonstrate the limitations of global measures, the reconstructed TFDs were evaluated using metrics from the previous chapter, and the results are given in Table 3.1. All considered metrics highlight the TwIST algorithm with $\lambda = 15$ for $z_{\text{SINLFM}}(t)$ and the YALL1 algorithm with $\lambda = 15$ for $z_{\text{LFM}}(t)$ as the best-performing TFDs, despite their relatively low number of TF samples. Therefore, it should be mentioned that the absence of crucial auto-terms in these TFDs contributes to artificially improved performance.

Overall, it may be concluded that for advanced methods in TF signal analysis, a suitable measure should include information about the number of components, their time and frequency supports, and the quality of auto-term preservation. The use of such a measure should accompany or replace state-of-the-art performance measures to obtain more reliable and accurate results.

3.2.1 Single Objective Meta-Heuristic Approach

Commonly employed optimization techniques for optimizing QTFDs include conventional gradient-based methods such as the gradient descent method (GDM) [4, 14, 113]. However, these methods possess inherent limitations that diminish their suitability for this particular task. GDM, for instance, exhibits strong dependence on the initial parameter values, necessitating prior knowledge regarding the TFD and the signal being analyzed. Furthermore, GDM generates only a single point at each iteration, potentially leading to an extensive number of iterations, without guaranteeing convergence to a global minimum or maximum for non-convex functions. An alternative optimization algorithm, often utilized in derivative-free optimization, is the classical Nelder-Mead algorithm [88], yet its performance is contingent upon the precise selection of initial parameters.

The limitations described above have been effectively mitigated in a prior research effort [4] through the introduction of a hybrid genetic algorithm (HGA) for the QTFD optimization [122]. The HGA combined the strengths of both genetic algorithms (GAs) and classical gradient-based optimization techniques. The GA was used to perform global search, while gradient-based optimization was used for local search. The hybrid approach presents an automated framework for optimizing QTFDs while simultaneously minimizing the concentration measure M^S [4].

However, the aforementioned optimization techniques, which employ a single objective, face the challenge of converging towards oversparse or completely empty reconstructed TFDs. Because of the limitations of the global concentration measures discussed before, every attempt to optimize reconstruction algorithm parameters converges to an empty TFD with a too high λ parameter and $M^S = 0$.

3.3 Summary

This chapter introduced a compressive sensing-based method for enhancing TFD concentration, along with a review of state-of-the-art sparse reconstruction algorithms based on the ℓ_1 norm, which will be utilized throughout the dissertation. One concern raised was the regularization parameter in sparse reconstruction, whereby it was demonstrated that setting the parameter too high leads to the loss of auto-terms. Another concern was the suitability of performance measures for evaluating reconstructed TFDs, which were found to be inadequate due to their lack of local positional information about signal components, leading to the incorrect identification of TFDs without auto-terms as the best-performing ones. These issues serve as motivation for further investigation in subsequent chapters of this dissertation.

CHAPTER 4

PERFORMANCE CRITERIA FOR TIME-FREQUENCY DISTRIBUTIONS BASED ON THE LOCALIZED RÉNYI ENTROPY

This chapter examines the benefits and drawbacks of the short-term Rényi entropy, followed by an introduction to the narrow-band Rényi entropy. To evaluate TFDs based on the localized Rényi entropies, a set of performance criteria is proposed and applied as a metric in the TFD reconstruction method.

Additionally, this chapter delves into a discussion on multi-objective optimization and provides a succinct outline of the state-of-the-art meta-heuristic algorithms. A multi-objective optimization problem is formulated for sparse reconstruction algorithms, along with the objective functions used as previously defined performance criteria. The proposed optimization approach and performance criteria are tested on synthetic signals with and without noise, and the results are compared with global concentration measures and the single-objective optimization approach provided in Chapter 3. The research of this chapter is published by the author in international peer-reviewed journals and conference proceedings [53, 55, 56].

4.1 The Localized Rényi Entropy

The enumerating characteristics of the Rényi entropy were effectively leveraged to modify the global Rényi entropy measure presented in (2.38) and obtain the instantaneous number of signal components [120, 121]. To achieve this, a localized approach is employed, namely the *localized Rényi entropy* (LRE), where the Rényi entropy is calculated for each

time slice of the TFD, $t = t_0$, in its proximity. Subsequently, the obtained entropy value is compared with the entropy of a reference TFD that possesses an established number of components, which yields the instantaneous number of signal components, $NC_t(t_0)$, namely the *short-term Rényi entropy* (STRE), as [120, 121]:

$$NC_t^{\rho(t,f)}(t_0) = 2^{R(\Delta_{t_0}\{\rho(t,f)\}) - R(\Delta_{t_0}\{\rho_{\text{ref}}(t,f)\})}, \quad (4.1)$$

where t_0 refers to the extracted time slice, while $\rho_{\text{ref}}(t, f)$ and $\rho(t, f)$ represent the reduced-interference distributions (RIDs) of the reference signal and the signal under consideration, respectively. For a valid comparison, an equal RID kernel has to be employed in order to compute $\rho_{\text{ref}}(t, f)$ and $\rho(t, f)$ [120, 121].

In the time-localization operator, Δ_{t_0} , the subscript t_0 denotes that all TFD samples, except those in the proximity of the extracted time slice, are set to zero. This is given as follows [120, 121]:

$$\Delta_{t_0}\{\rho(t, f)\} = \begin{cases} \rho(t, f), & t \in \left[t_0 - \frac{\Theta_t}{2}, t_0 + \frac{\Theta_t}{2} \right], \\ 0, & \text{otherwise,} \end{cases} \quad (4.2)$$

where Θ_t the localization parameter that specifies the length of the extracted time interval. Note that Θ_t has been set for each signal according to the recommendation in [103, 105]. In (4.1), the reference signal serves the purpose of supplying a reference energy level for a component in every time slice. To achieve the most convenient outcome, a cosine signal exhibiting a normalized frequency of 0.1 and an amplitude of unity is commonly used as the reference signal [120, 121]. The STRE has demonstrated utility across diverse fields. To name a few, it has been utilized for analyzing jamming signals in global navigation satellite systems [135], characterizing EEG signals [10, 71, 72, 73], extracting information content from noisy signals [102, 103, 105], and optimizing QTFDs [104].

In [101], an iterative approach for estimating the number of components that exhibit significantly diverse spectral amplitudes was presented. The method utilizes an iterative procedure to filter out the most prominent spectral components and highlight weaker ones. At each iteration, the local number of components, $NC_t(t)$, is computed. For time slices where $NC_t(t) \geq 1$, the highest amplitude component is excluded and the local number of components counter is incremented by 1. The iterative process continues until no components are identified based on the entropy criterion in the TF plane [101].

4.1.1 Limitations of the Existing Methods

This iterative method has been used in the automatic extraction of the dominant signal component [71, 73], where it was observed that the estimated local number of components

can exhibit significant variability when a different threshold is applied to the signal. This indicates that the iterative method may misclassify a cross-term or noise sample as an auto-term when the TFD is not completely cross-term-free or when it is corrupted by noise. In addition, the presence of imperfections in the component removal process can lead to inconsistent estimations. In [104], it was shown that this method can be repurposed to estimate the complete count of energy regions by equalizing the significance of signal auto-terms and cross-terms.

Due to the aforementioned inconsistencies with the iterative method and the specific use case in this dissertation, which requires robust estimation of only auto-terms, the original non-iterative method given in (4.1) will be used throughout this dissertation.

Recently, an approach for the extraction of useful components has been in development, which involves computing entropy over 2-D TF regions instead of 1-D time slices [32, 70, 132, 133]. Given that the entropy is calculated multiple times for each TF point, the algorithm's computational complexity is significant, scaling as $\mathcal{O}(N_t^5)$. Consequently, its applicability is limited in some practical applications where the original STRE method is still preferred, as highlighted in [103]. In the context of this dissertation, where multiple calculations of LRE in an optimization environment will be required, the original STRE remains a more practical choice.

The STRE method has been demonstrated to achieve highly accurate results when processing signals with components that are aligned to the reference signal. Nevertheless, its performance declines when processing signals with non-parallel components. For instance, when analyzing a signal $\delta(t - t_0)$, the expected local number of components at time slice t_0 is 1. Nevertheless, since the energy of the impulse is larger than that of the reference signal in the proximity of t_0 , the local number of components becomes significantly greater than 1, i.e., $NC_t(t_0) \gg 1$.

To demonstrate this limitation, the STRE method has been applied to the signal $z_{\text{LFM}}(t)$, which all four components exhibit significant deviation from the reference signal. Figure 4.1 shows an arbitrarily selected time slice at $t_0 = 71$ and reveals that the components extracted from $z_{\text{LFM}}(t)$ exhibit much higher entropy than those extracted from the reference signal. As a result, an inaccurate estimation of the local number of components is produced, as evidenced with $NC_t(71) = 6.1777 \gg 2$.

4.1.2 The Narrow-Band Rényi Entropy

To address the limitation of the STRE approach for signals with components significantly deviating from the reference signal, it is necessary to introduce additional localized information. This entails computing the LRE in narrower frequency intervals, which leads us to the explanation of the *narrow-band Rényi entropy* (NBRE). The determination of the quantity of data points within a particular frequency slice, $NC_f(f_0)$, is calculated

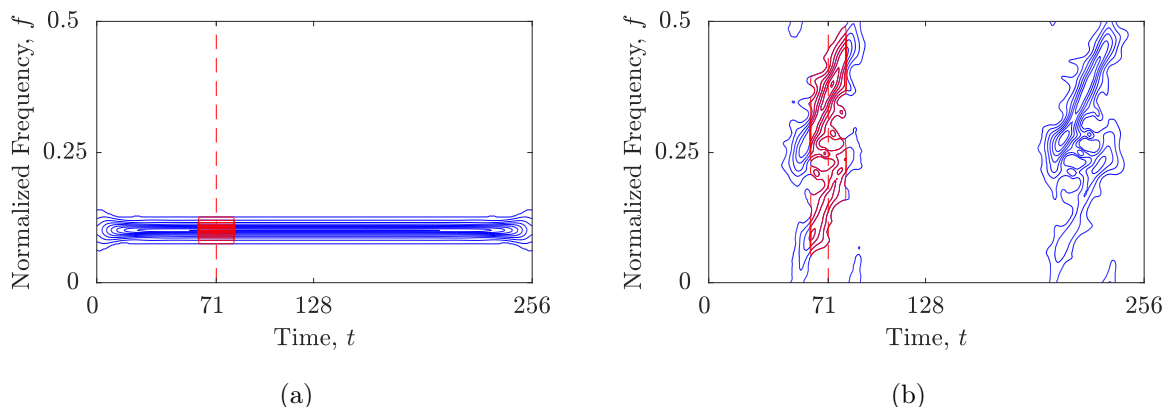


Figure 4.1 Extracted components (in red) taken at time slice $t_0 = 71$: (a) the STRE method's reference signal; (b) the signal $z_{\text{LFM}}(t)$, $NC_t(71) = 6.1777 \gg 2$.

using the frequency-localization operator, Δ_{f_0} , analogous to (4.1) [55]:

$$\Delta_{f_0}\{\rho(t, f)\} = \begin{cases} \rho(t, f), & f \in \left[f_0 - \frac{\Theta_f}{2}, f_0 + \frac{\Theta_f}{2} \right], \\ 0, & \text{otherwise,} \end{cases} \quad (4.3)$$

where f_0 represents the targeted frequency slice, while Θ_f corresponds to the localization parameter that governs the size of the extracted frequency interval. Compared to the STRE, which uses a constant frequency reference signal, the NBRE approach employs a reference signal that is aligned to the frequency axis, consisting of a time-localized impulse located at $t = 15$. This reference signal provides a more appropriate energy reference for certain signals, allowing for improved accuracy in estimating the number of components.

Figure 4.2 demonstrates an application of the NBRE method using an arbitrarily-chosen frequency slice at $f_0 = 200$ on the signal $z_{\text{LFM}}(t)$. The extracted reference signal using the NBRE method shows a significantly improved suitability for the signal $z_{\text{LFM}}(t)$, leading to an almost ideal estimation of $NC_f(200) = 1.9058 \approx 2$ for this frequency slice.

The results of the STRE and NBRE methods for estimating the local number of components for signals $z_{\text{SINLFM}}(t)$ and $z_{\text{LFM}}(t)$ are presented in Figure 4.3. It is noteworthy that for the sake of practical interpretation or application purposes, the estimated local numbers of components are typically rounded to the nearest integer [118, 120, 121].

For $z_{\text{SINLFM}}(t)$, the STRE estimation provided results that were consistent with the ideal, as depicted in Figure 4.3a, indicating the presence of two distinct components. Conversely, the NBRE estimation illustrated in Figure 4.3b exhibited significant inaccuracies due to the alignment of the components with the time axis.

For the signal $z_{\text{LFM}}(t)$, the STRE estimation demonstrated significant inaccuracies, as shown in Figure 4.3c. In contrast, the NBRE approach resulted in a more accurate estimation, with the estimated $NC_f(f)$ values being much closer to the ideal, as shown

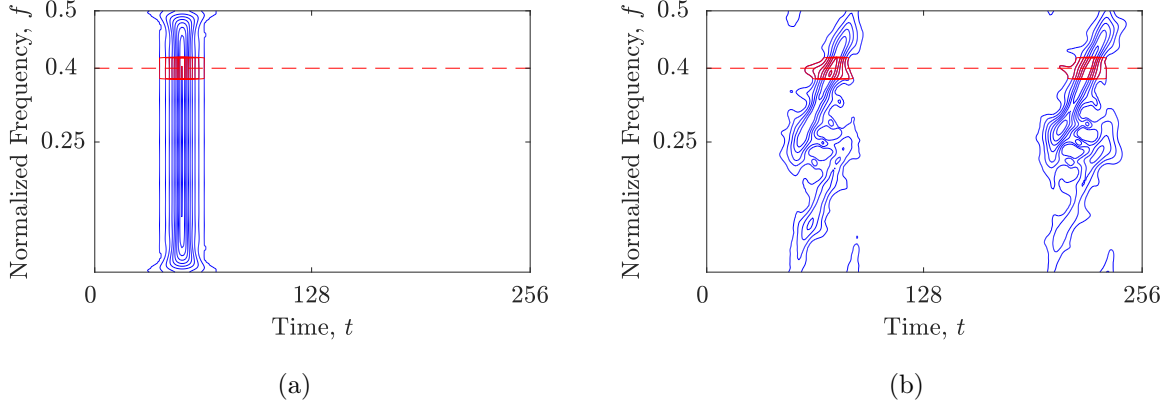


Figure 4.2 Extracted components (in red) taken at frequency slice $f_0 = 200$ of: (a) the NBRE method's reference signal; (b) the signal $z_{\text{LFM}}(t)$, $NC_f(200) = 1.9058 \approx 2$.

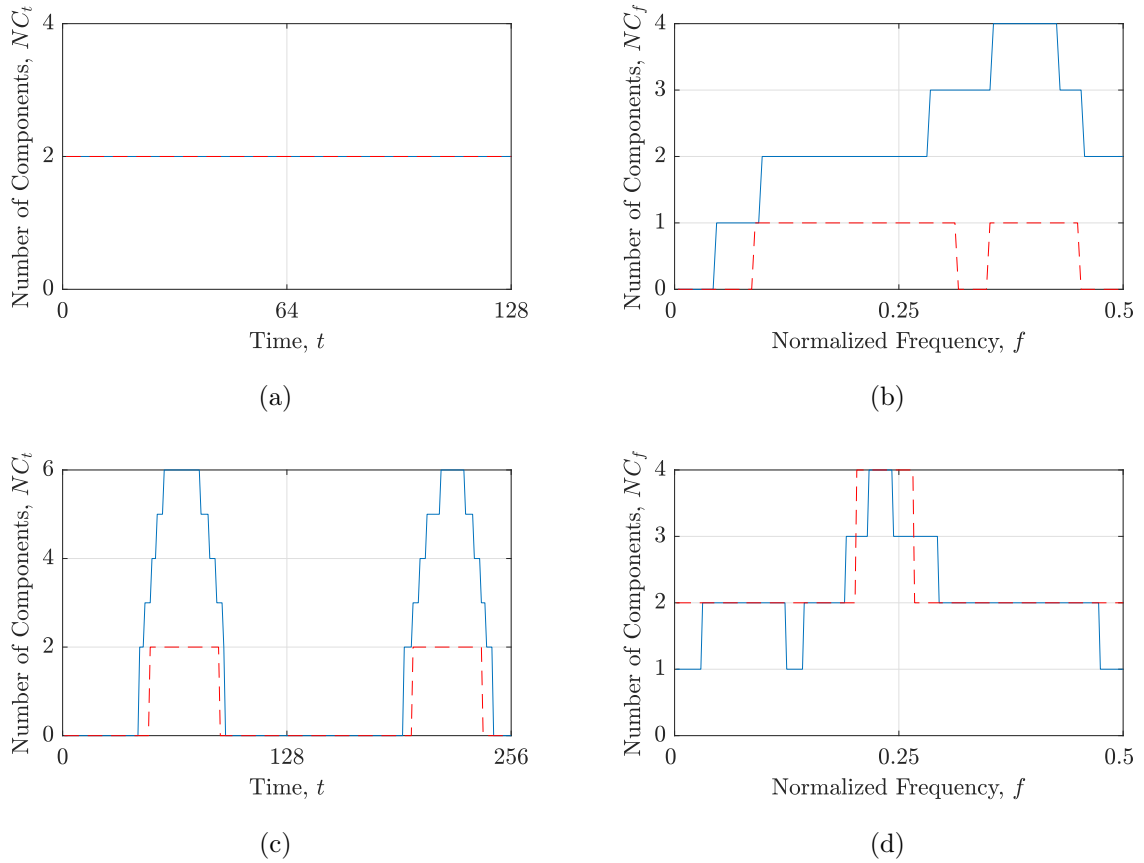


Figure 4.3 The ideal (red dashed line) and obtained (blue solid line) local numbers of components for the considered signals: (a, b) $z_{\text{SINLFM}}(t)$ with $\alpha_R = 3$ and $\Theta_t = \Theta_f = 5$; (c, d) $z_{\text{LFM}}(t)$ with $\alpha_R = 3$ and $\Theta_t = \Theta_f = 11$.

in Figure 4.3d. These observations highlight the need for the NBRE approach in certain applications. Furthermore, its usefulness in conjunction with the STRE will be thoroughly emphasized in this dissertation.

4.2 Performance Criteria Based on the Localized Rényi Entropy: Definition and Evaluation Performance

The study presented in [104] proposed an optimization approach to construct an optimized TFD. This procedure involved the meticulous selection of the optimal TFD for each time slice, chosen from a collection of randomly generated TFDs. The selection process relied on evaluating the local number of components and entropy values using the STRE criterion. Specifically, the time slice inserted into the final TFD is extracted from a TFD from the input set that exhibits the minimal entropy value and the lowest local number of components. This ensures that each time slice is composed of auto-terms with high resolution.

However, when applied in the circumstances of sparse reconstruction, this approach has several limitations. Primarily, it necessitates the inclusion of at least one TFD within the chosen set that is devoid of any cross-terms for every time slice. For the use case in this dissertation, this requirement translates to the preservation of auto-terms in every time slice of the reconstructed TFDs within the designated set. Nevertheless, this dissertation revealed that the arbitrary selection of parameters for the reconstruction may result in the exclusion of crucial components in the resulting TFDs. Consequently, the optimization procedure delineated in [104] could erroneously designate a time slice of a reconstructed TFD comprising incongruous components as the optimal choice.

Second, the large number of parameters involved in CS-based methods renders generating a significant number of reconstructed TFDs impractical and requires substantial time and memory resources. Therefore, the optimization scheme in [104] may not be feasible in practice, and alternative approaches are necessary to address the difficulties involved with the sparse reconstruction of TFDs.

To address limitations mentioned above, the criteria presented here evaluate a TFD based on the information about auto-terms derived from the starting signal before performing sparse reconstruction. Two mean squared errors (MSEs) are formulated to assess the dissimilarity between the local number of components in the starting, $\rho(t, f)$, and reconstructed TFD, $\Upsilon_z^{\ell_1}(t, f)$, acquired from the STRE (subscript t) and NBRE (subscript f), as [55]:

$$\text{MSE}_t = \frac{1}{N_t} \sum_{t=1}^{N_t} \left(\frac{NC_t^{\rho(t,f)}(t) - NC_t^{\Upsilon_z^{\ell_1}(t,f)}(t)}{\max \left(NC_t^{\rho(t,f)}(t), NC_t^{\Upsilon_z^{\ell_1}(t,f)}(t) \right)} \right)^2, \quad (4.4a)$$

$$\text{MSE}_f = \frac{1}{N_f} \sum_{f=1}^{N_f} \left(\frac{NC_f^{\rho(t,f)}(f) - NC_f^{\Upsilon_z^{\ell_1}(t,f)}(f)}{\max \left(NC_f^{\rho(t,f)}(f), NC_f^{\Upsilon_z^{\ell_1}(t,f)}(f) \right)} \right)^2, \quad (4.4b)$$

$$\text{MSE}_{t,f} = \frac{\text{MSE}_t + \text{MSE}_f}{2}. \quad (4.4c)$$

By normalizing the local number of signal components, a standardized and unbiased comparison of the MSE values is achieved, ensuring fairness across different signal samples. A high MSE value indicates either an oversparse TFD with inconsistent auto-terms or a TFD with low-resolution auto-terms and cross-terms. Note that the local numbers of components in the reconstructed TFDs were calculated based on the ideal reference signals in both, the STRE and NBRE.

To comprehensively evaluate the performance of the reconstructed TFD and validate the MSE values, supplementary performance metrics have been employed. Namely, the mean absolute error (MAE) and the maximum absolute error (MAX) are utilized as [55]:

$$\text{MAE}_t = \frac{1}{N_t} \sum_{t=1}^{N_t} \left| \frac{NC_t^{\rho(t,f)}(t) - NC_t^{\Upsilon_z^{\ell_1}(t,f)}(t)}{\max \left(NC_t^{\rho(t,f)}(t), NC_t^{\Upsilon_z^{\ell_1}(t,f)}(t) \right)} \right|, \quad (4.5a)$$

$$\text{MAE}_f = \frac{1}{N_f} \sum_{f=1}^{N_f} \left| \frac{NC_f^{\rho(t,f)}(f) - NC_f^{\Upsilon_z^{\ell_1}(t,f)}(f)}{\max \left(NC_f^{\rho(t,f)}(f), NC_f^{\Upsilon_z^{\ell_1}(t,f)}(f) \right)} \right|, \quad (4.5b)$$

$$\text{MAE}_{t,f} = \frac{\text{MAE}_t + \text{MAE}_f}{2}, \quad (4.5c)$$

$$\text{MAX}_t = \max_{t=1, \dots, N_t} \left(\left| \frac{NC_t^{\rho(t,f)}(t) - NC_t^{\Upsilon_z^{\ell_1}(t,f)}(t)}{\max \left(NC_t^{\rho(t,f)}(t), NC_t^{\Upsilon_z^{\ell_1}(t,f)}(t) \right)} \right| \right), \quad (4.6a)$$

$$\text{MAX}_f = \max_{f=1, \dots, N_f} \left(\left| \frac{NC_f^{\rho(t,f)}(f) - NC_f^{\Upsilon_z^{\ell_1}(t,f)}(f)}{\max \left(NC_f^{\rho(t,f)}(f), NC_f^{\Upsilon_z^{\ell_1}(t,f)}(f) \right)} \right| \right), \quad (4.6b)$$

$$\text{MAX}_{t,f} = \frac{\text{MAX}_t + \text{MAX}_f}{2}. \quad (4.6c)$$

The effectiveness of the performance criteria is demonstrated through an assessment of a blurred and an oversparse reconstructed TFD obtained using the TwIST algorithm exhibiting different values of λ (specifically, $\lambda = 15$ and $\lambda = 0.01$) for the signal $z_{\text{SINLFM}}(t)$. The discrepancies shown in Figure 4.4 between the local number of components in the starting and reconstructed TFD provide insights into the nature of the reconstructed TFD, indicating whether it is oversparse or blurred. Specifically, an augmentation in the local number of components in the reconstructed TFD suggests that artifacts or low-resolution

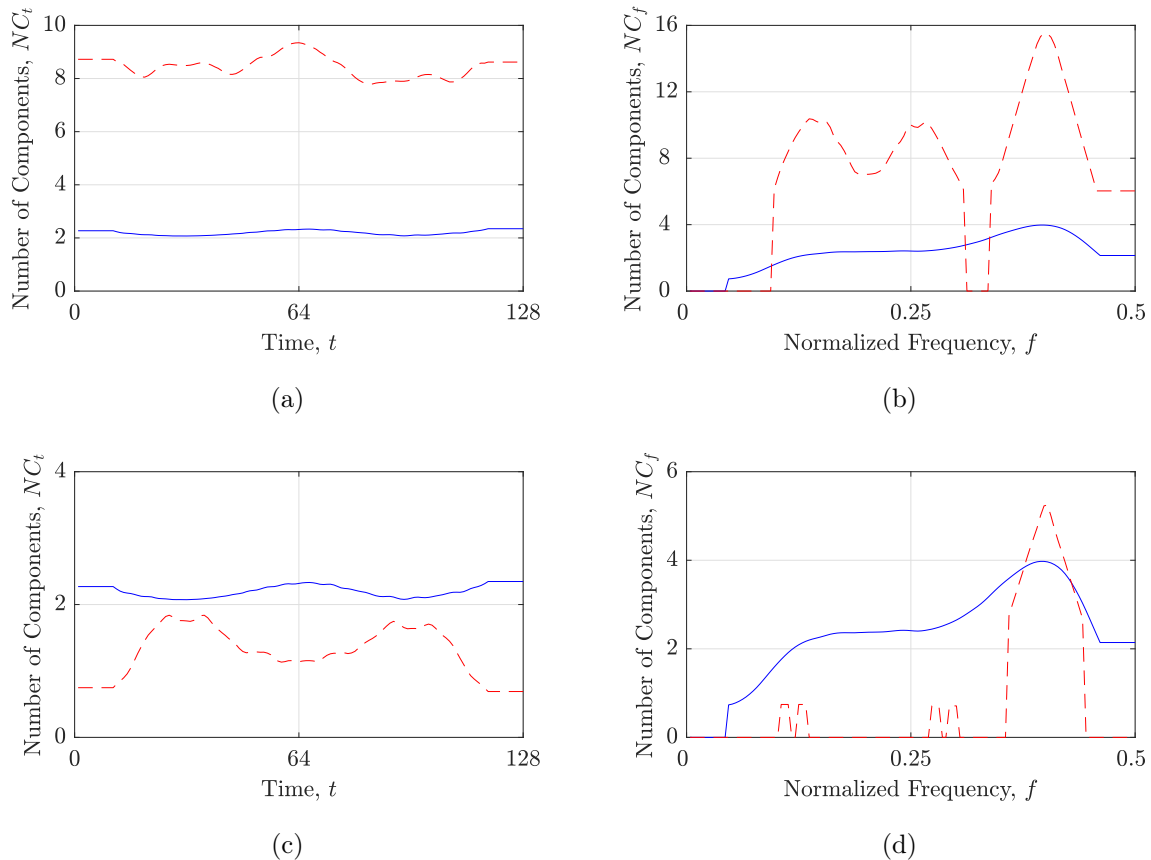


Figure 4.4 The local numbers of components in starting (depicted with a solid blue line) and reconstructed TFD obtained by the TwIST algorithm (depicted with a dashed red line) for the signal $z_{\text{SINLFM}}(t)$ with: (a, b) $\lambda = 15$; (c, d) $\lambda = 0.01$.

auto-terms are present, as depicted in Figures 4.4a and 4.4b. Conversely, a decrease in the local number of components indicates an oversparse TFD with missing components, as demonstrated in Figures 4.4c and 4.4d. Furthermore, a rapid decrease to zero in the local number of components signifies the specific time or frequency slices in which a complete absence of components has occurred, as evidenced in Figure 4.4d.

However, the LRE-metrics do not account for the connectivity of signal components across diverse slices. Therefore, a global performance metric, denoted as N_r , is introduced that assesses the number of TFD regions that exhibit continuous connectivity among neighboring samples. Each sample at location (z, q) is required to maintain connectivity with at least one of its eight nearest neighbors: $\{(z-1, q-1), (z-1, q), (z-1, q+1), (z, q-1), (z, q+1), (z+1, q-1), (z+1, q), (z+1, q+1)\}$. The objective is to obtain a reconstructed TFD with components that form smooth, uninterrupted IF trajectories. A lower N_r value indicates higher component consistency, which is desirable. Additionally, fewer interference samples in the reconstructed TFD also result in a lower N_r value.

While it would be ideal for N_r to match the total number of components in the TFD, it is typically not the case in practice. Therefore, the N_r metric should be interpreted as a

Table 4.1 LRE-based metrics, MSE_t , MSE_f , and N_r of the considered ℓ_1 norm-based reconstruction algorithms with arbitrarily chosen regulation parameter λ . According to the respective measure, values in bold indicate the best-performing reconstruction algorithm for the signals $z_{\text{SINLFM}}(t)$ and $z_{\text{LFM}}(t)$.

	$z_{\text{SINLFM}}(t)$				$z_{\text{LFM}}(t)$			
	TwIST		SALSA		SpaRSA		YALL1	
λ	15	0.01	15	1	15	0.01	15	1
MSE_t	0.1629	0.4469	0.1130	0.4063	0.1606	0.2481	0.2387	0.1392
MSE_f	0.1807	0.1759	0.1703	0.1911	0.2577	0.3840	0.3236	0.2320
$MSE_{t,f}$	0.1718	0.3114	0.1417	0.2987	0.2092	0.3161	0.2812	0.1856
N_r	6	43	2	36	8	54	10	48
MAE_t	0.3638	0.6674	0.3241	0.6365	0.2596	0.3897	0.3051	0.2564
MAE_f	0.3597	0.3581	0.3448	0.3633	0.4625	0.5961	0.5443	0.4609
MAX_t	0.7058	0.7520	0.5018	0.6993	0.9989	0.8914	1.0	0.8676
MAX_f	0.8722	0.7839	0.7585	0.8072	1.0	0.8873	1.0	0.8676

supplementary measure to the MSE_t and MSE_f values rather than a direct measure of the global number of components.

Table 4.1 presents the numerical outcomes for the reconstructed TFDs depicted in Figure 3.2, using LRE-based and N_r metrics for the signals $z_{\text{SINLFM}}(t)$ and $z_{\text{LFM}}(t)$. The LRE parameters have been set as $\alpha_R = 3$, while $\Theta_t = \Theta_f = 5$ and $\Theta_t = \Theta_f = 11$ have been used for the signals $z_{\text{SINLFM}}(t)$ and $z_{\text{LFM}}(t)$, respectively. The LRE has been calculated using the EMBD, which parameters have been optimized using the M^S measure and chosen as $\alpha_{\text{EMB}} = 0.06$, $\beta_{\text{EMB}} = 0.15$ and $\alpha_{\text{EMB}} = 0.09$, $\beta_{\text{EMB}} = 0.12$ for the signals $z_{\text{SINLFM}}(t)$ and $z_{\text{LFM}}(t)$, respectively.

As illustrated in Table 3.1, the deficiency of predefined upper or lower limits for global measures M^S , R , M^{RN} , and M^{H} , leads to the erroneous classification of oversparse TFDs as high-performing. This limitation is solved by a raise in the values of MSE_t , MSE_f , and N_r , thereby effectively penalizing the unwanted oversparsity. These measures also appropriately account for the presence of artifacts in low-resolution TFDs, which are typically correctly identified by M^S , R , M^{RN} , and M^{H} .

Note that the LRE-based metrics correctly identify the reconstructed TFD obtained using the SALSA with $\lambda = 15$ and YALL1 algorithms with $\lambda = 1$ as the best-performing among the given TFDs for the signals $z_{\text{SINLFM}}(t)$ and $z_{\text{LFM}}(t)$, respectively. Also note that the high N_r value obtained for the YALL1 algorithm with $\lambda = 1$ indicates reconstructed TFD with low auto-term consistency and/or reconstruction of cross-terms and noise, whereas the low N_r value for the SALSA algorithm with $\lambda = 15$ confirms its good performance. The robustness of these findings is supported by additional performance indicators: MAE_t , MAE_f , MAX_t , and MAX_f .

4.3 A Multi-Objective Meta-Heuristic Optimization Approach

4.3.1 Problem Definition

In the circumstances of the multi-objective meta-heuristic optimization approach, the primary objective is to identify a compilation of optimal solutions that effectively balance and optimize multiple conflicting objective functions. These functions push the process towards a reconstructed TFD that exhibits superior performance characteristics. This entails enhancing the resolution and preservation of auto-terms, while mitigating the presence of cross-terms and noise-related TF samples.

In this chapter, two objective function formulations based on the LRE metrics are considered. The first formulation combines the LRE-based metric with the M^S global measure used in a previous study [4] as a standalone measure. This formulation is expressed as $(M^S, \text{MSE}_t, \text{MSE}_f)$, where M^S ensures high auto-term resolution and cross-term suppression, and MSE_t and MSE_f ensure auto-term preservation in the reconstructed TFD.

The second formulation considers the N_r measure in conjunction with MSE_t and MSE_f , expressed as $(N_r, \text{MSE}_t, \text{MSE}_f)$. In this formulation, the MSE_t and MSE_f metrics are used to detect missing or low-resolution auto-terms and unwanted reconstruction of cross-terms without the need for the M^S measure. The N_r measure ensures auto-term consistency across the entire TFD.

Therefore, a multi-objective optimization problem may be established in the context of sparse TFD reconstruction for the TwIST algorithm as follows:

$$\begin{aligned} & \text{minimize: } M^S/N_r, \text{MSE}_t, \text{MSE}_f(\alpha_{\text{TwIST}}, \beta_{\text{TwIST}}, \lambda), \\ & \text{subject to: } \alpha_{\text{TwIST}} \in \langle 0, 1 \rangle, \beta_{\text{TwIST}} \in \langle 0, 2\alpha \rangle, \lambda \in \langle 0, 100 \rangle. \end{aligned} \tag{4.7}$$

Note that in order to ensure an unbiased comparison, all parameters involved in the state-of-the-art algorithms, which are used for comparison throughout this dissertation, undergo optimization in a consistent manner.

4.3.2 Pareto Optimal Solutions

In a multi-objective optimization environment, contradictory objectives are often encountered. Enhancing one objective can result in the deterioration of another objective, and this holds true for the introduced objective functions in this study as well. Specifically, improving $M^S \rightarrow 0$ or $N_r \rightarrow 0$ will degrade the MSE_t and MSE_f metrics. Therefore, the aim is to identify a collection of solutions that achieve a balance between the conflicting

objectives, indicated as the *Pareto optimal set*. The Pareto front is obtained by mapping the Pareto optimal set using the objective functions. [28].

The Pareto optimal set comprises solutions that that are non-improvable on one objective without degrading another objective. These remedies, known as Pareto optimal or non-dominated solutions, are determined based on the dominance relationship. In particular, if two reconstructed TFDs are denoted as solutions \mathbf{x} and \mathbf{y} , a solution \mathbf{x} is stated to dominate another solution \mathbf{y} , $\mathbf{x} \preceq \mathbf{y}$, if and only if the stated conditions are satisfied:

$$\begin{aligned} \forall \text{ objectives: } & \text{MSE}_t(\mathbf{x}) \leq \text{MSE}_t(\mathbf{y}), \text{MSE}_f(\mathbf{x}) \leq \text{MSE}_f(\mathbf{y}), M^S/N_r(\mathbf{x}) \leq M^S/N_r(\mathbf{y}), \\ \exists \text{ objectives: } & \text{MSE}_t(\mathbf{x}) < \text{MSE}_t(\mathbf{y}), \text{MSE}_f(\mathbf{x}) < \text{MSE}_f(\mathbf{y}), \text{ or } M^S/N_r(\mathbf{x}) < M^S/N_r(\mathbf{y}). \end{aligned} \quad (4.8)$$

The Pareto optimal set can take on a variety of shapes, such as convex, concave, or non-convex, depending on the optimization problem and the nature of the objective functions [25, 45, 76, 99, 110, 144]. In this study, due to the presence of a large number of reconstruction parameters and multiple local optima in the objective function landscape, the Pareto optimal set is not obligatory convex.

To assess the quality of the Pareto front, an efficient Monte Carlo approximation of the hypervolume, referred to as *HV*, has been employed. This method involves randomly inserting a total of $N_{\text{tot}} = 10^5$ solutions into a hypercuboid and computing the percentage of dominated solutions, denoted as N_{dom} . The calculation of *HV* is performed according to the following formula [5]:

$$HV = \frac{N_{\text{dom}}}{N_{\text{tot}}} \cdot 100\%. \quad (4.9)$$

For a minimization problem with three objective functions, such as the one addressed in this dissertation, the hypercuboid used for calculating the hypervolume is a cube. The cube's vertices are defined as $[0, 0, 0]$, representing the origin, and the coordinates of the maximum values of the Pareto front are given by $[M^{S, (\text{max})}$ or $N_r^{(\text{max})}$, $\text{MSE}_t^{(\text{max})}$, and $\text{MSE}_f^{(\text{max})}]$. A larger hypervolume indicates that the Pareto front dominates over more solutions and is therefore preferred [5]. It should be noted that in the following simulations, the random behavior of this measure has been minimized over 1000 runs.

Decision-Making: The Fuzzy Satisfying Method

Decision-making approaches refer to a set of methods that help choose the most suitable solution from a given set of options. In multi-objective optimization, decision-making approaches are used to identify a preferred solution from the Pareto optimal set, which represents the trade-off between multiple conflicting objectives. In this dissertation, the fuzzy satisfying method (FSM) has been used due to its ability to handle vagueness and uncertainty in the decision-making approach, its low computational complexity, and its

ease of implementation [112].

The FSM evaluates each solution with respect to each criterion using a fuzzy membership function that appoints a degree of membership to every solution based on how well it satisfies the criterion. To calculate the linear membership function for the k -th solution of the j -th objective function, the following equation is used [112]:

$$\xi_j^k = \begin{cases} 1, & v_j^k \leq v_j^{\min}, \\ \frac{v_j^{\max} - v_j^k}{v_j^{\max} - v_j^{\min}}, & v_j^{\min} < v_j^k < v_j^{\max} \\ 0, & v_j^k \geq v_j^{\max}, \end{cases} \quad (4.10)$$

where v_j^{\min} and v_j^{\max} denote the minimum and maximum values of the j -th objective function, respectively, with $k = 1, 2, \dots, N_{\text{par}}$ and $j = 1, 2, \dots, N_{\text{obj}}$ (where N_{par} and N_{obj} represent the numbers of Pareto optimal solutions and objective functions, respectively).

Next, the membership function for each Pareto optimal solution k is determined using the following expression [112]:

$$\xi^k = \min(\xi_1^k, \xi_2^k, \dots, \xi_{N_{\text{obj}}}^k). \quad (4.11)$$

Ultimately, the most convenient solution is identified by selecting the solution with the weakest maximum membership function as follows [112]:

$$\xi^{\text{best}} = \max(\xi^1, \xi^2, \dots, \xi^{N_{\text{par}}}). \quad (4.12)$$

In this dissertation, the objective function formulation considers $N_{\text{obj}} = 3$.

4.3.3 Multi-Objective Meta-Heuristic Optimization Algorithms

The utilization of meta-heuristic optimization algorithms in this dissertation serves the purpose of efficiently exploring the non-convex Pareto optimal set and obtaining a varied range of solutions that capture the trade-offs between conflicting objectives. Meta-heuristic algorithms are a popular choice for addressing non-linear optimization problems due to their ability to handle non-continuous, non-differentiable, and non-convex objective functions. In this study, various meta-heuristic algorithms have been incorporated, which have proven to be effective in tackling a wide range of multi-objective optimization problems encountered in real-world scenarios, as evidenced by recent research [25, 45, 76, 99, 110, 144], while also exhibiting computational efficiency.

One of the algorithms considered in this dissertation is the multi-objective particle swarm optimization (MOPSO), which is an continuation of the particle swarm optimization (PSO) algorithm [34]. MOPSO has been developed to handle multiple objectives by using

Table 4.2 Fixed parameters for the MOPSO, NSGA-III and MOWCA meta-heuristic optimization algorithms.

Number of iterations, denoted with T_{\max} : 100		
Population size, denoted with N_{pop} : 100		
N_{par} : 50		
MOPSO	NSGA-III	MOWCA
$w = 0.9, m_r = 0.1$	$m_r = 0.1$	$d_{\max} = 10^{-4}$
$c_1 = c_2 = 2$	$p_c = 0.5, p_m = 0.5$	$N_{sr} = 5$

a Pareto dominance approach to compare and evaluate solutions. The algorithm iteratively updates the velocity and position of a swarm of particles in a search space, aiming to converge towards a set of Pareto optimal solutions.

Another algorithm employed is the non-dominated sorting genetic algorithm III (NSGA-III), a variant of the well-known GA [30]. NSGA-III converges towards a set of well-dispersed Pareto optimal solutions with good coverage of the Pareto front, and it can handle a large number of objectives. The non-domination sorting and reference point selection strategies employed by NSGA-III promote diversity in the population, which is particularly useful for identifying a diverse set of high-quality solutions that capture the balances between conflicting objectives.

The multi-objective water cycle algorithm (MOWCA) is the last algorithm considered in this dissertation [97, 98]. It is based on the water cycle algorithm, which mimics the natural process of the water cycle in nature. MOWCA generates a diverse set of Pareto optimal solutions that span the entire trade-off surface by using a Pareto dominance approach to evaluate and compare solutions.

Table 4.2 reports the meta-heuristic algorithms' parameters that have been used in this dissertation based on the recommended values in literature [12, 26, 43, 77, 97, 98], which pseudocodes are given in Appendix A. The NSGA-III showed the best performance based on the hypervalue analysis given in Appendix B, and it will be used throughout the whole dissertation.

Note that providing a detailed review of the numerous available optimization algorithms falls beyond the scope of this dissertation. The focus of this study has been to properly define the objective function, which may be used in a variety of existing and future meta-heuristic optimization algorithms.

4.4 Evaluating Optimization Performance: Results

This section presents reconstructed TFDs obtained using TwIST, SpARSA, SALSA and YALL1 algorithms, optimized with given objective functions, namely $(M^S, \text{MSE}_t, \text{MSE}_f)$ and $(N_r, \text{MSE}_t, \text{MSE}_f)$, for the signals $z_{\text{SINLFM}}(t)$ and $z_{\text{LFM}}(t)$. The LRE parameters and

Table 4.3 Performance comparison of the reconstructed TFDs obtained using the TwIST, SpaRSA, SALSA and YALL1 algorithms optimized with $(M^S, \text{MSE}_t, \text{MSE}_f)$ versus $(N_r, \text{MSE}_t, \text{MSE}_f)$ objective functions for the signal $z_{\text{SINLFM}}(t)$. Values in bold indicate the best-performing and the fastest algorithm.

		$z_{\text{SINLFM}}(t)$							
		TwIST		SpaRSA		SALSA		YALL1	
Objectives	M^S	N_r	M^S	N_r	M^S	N_r	M^S	N_r	
	MSE_t	MSE_t	MSE_t	MSE_t	MSE_t	MSE_t	MSE_t	MSE_t	
	MSE_f	MSE_f	MSE_f	MSE_f	MSE_f	MSE_f	MSE_f	MSE_f	
λ^+	7.947	6.711	9.262	6.541	13.217	11.706	5.561	1.480	
MSE_t	0.0269	0.0221	0.1234	0.0153	0.1024	0.0299	0.4954	0.3770	
MSE_f	0.0658	0.0620	0.1765	0.0687	0.1301	0.0654	0.2978	0.2351	
M^S	0.0485	0.0535	0.0297	0.0472	0.0392	0.0458	0.0119	0.0167	
N_r	3	3	6	2	3	2	21	12	
MAE_t	0.1492	0.1445	0.3361	0.1122	0.2830	0.1645	0.6991	0.6122	
MAE_f	0.2055	0.2012	0.3538	0.2057	0.3010	0.2068	0.5097	0.4465	
MAX_t	0.2466	0.2214	0.5430	0.1988	0.5184	0.2787	0.9877	0.9055	
MAX_f	0.4961	0.4853	0.8446	0.5382	0.7133	0.4987	0.8873	0.8871	
$t[\text{s}]$	0.142	0.139	0.031	0.022	0.188	0.152	0.887	0.742	

reconstruction parameters have been kept consistent with Table 4.1, while the NSGA-III parameters have been set as in Table 4.2.

For the signal $z_{\text{SINLFM}}(t)$, the reconstructed TFDs in Figure 4.5 show that both optimizations solve the limitations of existing approaches and present TFDs with both components preserved. However, the optimization using the N_r objective function has a slight advantage in better preserving the sinusoidal FM component, as is particularly evident in the SpaRSA algorithm result shown in Figure 4.5c.

This observation is supported by the numerical results shown in Table 4.3. The quality of auto-term preservation is higher when optimizing with the N_r objective function, resulting in lower MSE_t and MSE_f values for all reconstruction algorithms compared to optimizing with the M^S objective. As evident by the visual observation, the SpaRSA algorithm attains the most notable enhancement in MSE_t and MSE_f values, by 87.60% and 61.08%, respectively. Using the M^S objective function resulted in a higher optimal λ^+ parameter for all reconstruction algorithms ($\{\cdot\}^+$ denotes the optimal value), indicating more thresholding, which has led to the partial absence of auto-terms. Overall, the TwIST algorithm achieves the best MSE_t and MSE_f values, while the lowest execution time is achieved by the SpaRSA algorithm. The YALL1 algorithm achieves the highest auto-term resolution, but its poor consistency significantly increases MSE_t and MSE_f values.

In the case of the signal $z_{\text{LFM}}(t)$, both optimizations yield almost identical results,

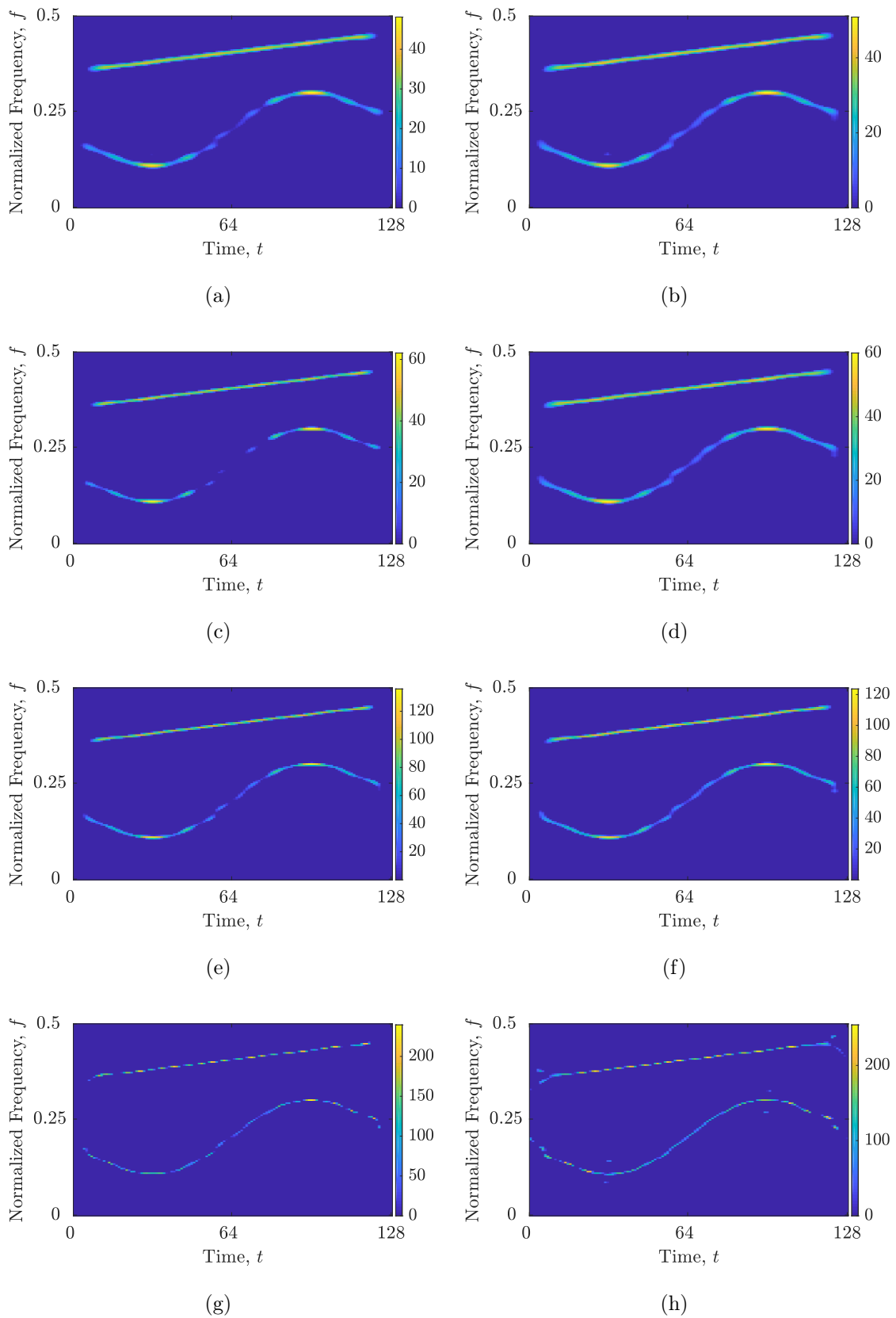


Figure 4.5 Reconstructed TFDs for the signal $z_{\text{SINLFM}}(t)$ optimized with two objective function formalizations: (a) TwIST, M^S ; (b) TwIST, N_r ; (c) SpARSA, M^S ; (d) SpARSA, N_r ; (e) SALSA, M^S ; (f) SALSA, N_r ; (g) YALL1, M^S ; (h) YALL1, N_r .

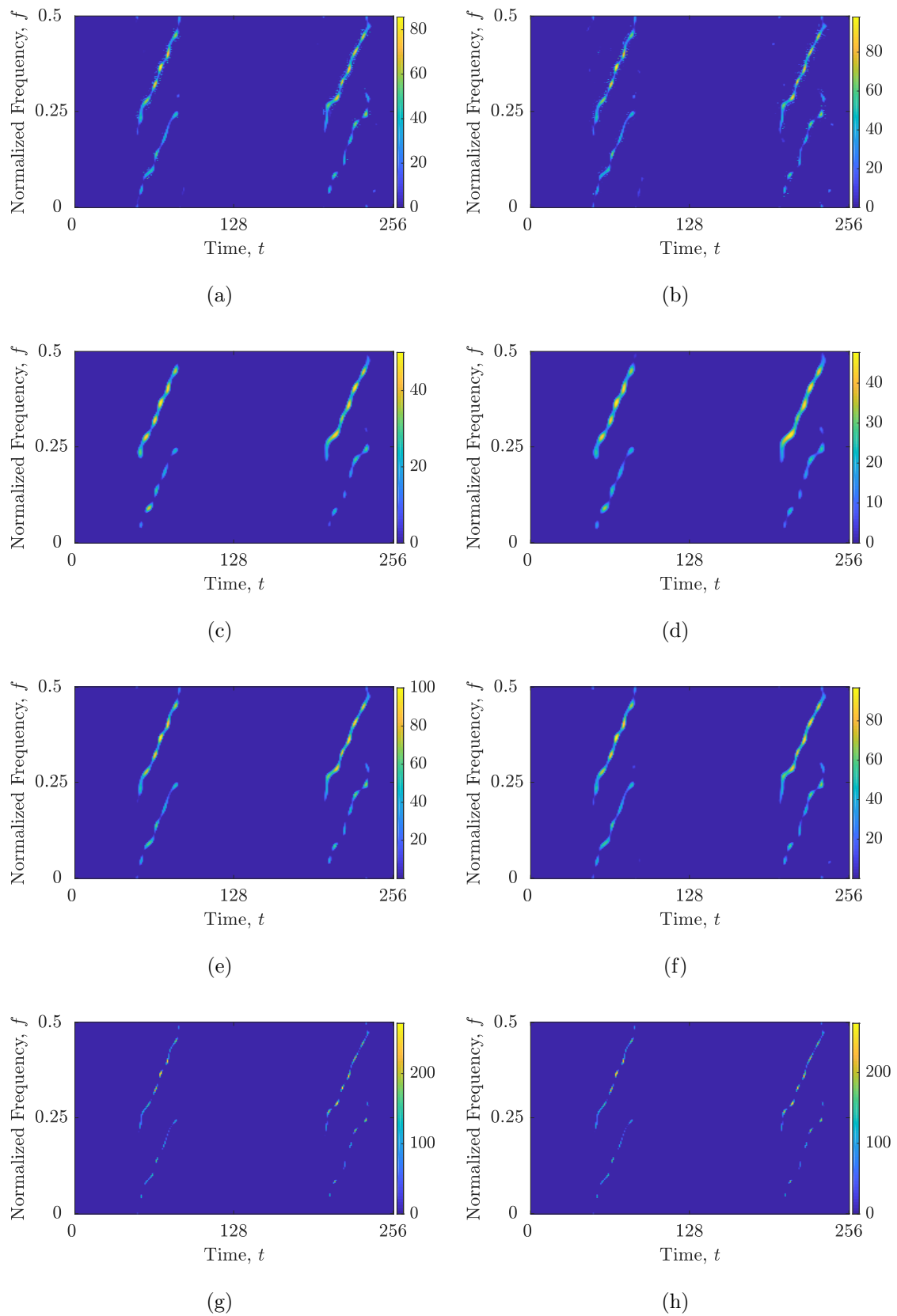


Figure 4.6 Reconstructed TFDs for the signal $z_{\text{LFM}}(t)$ optimized with two objective function formalizations: (a) TwIST, M^S ; (b) TwIST, N_r ; (c) SpARSA, M^S ; (d) SpARSA, N_r ; (e) SALSA, M^S ; (f) SALSA, N_r ; (g) YALL1, M^S ; (h) YALL1, N_r .

Table 4.4 Performance comparison of the reconstructed TFDs obtained using the TwIST, SpaRSA, SALSA and YALL1 algorithms optimized with $(M^S, \text{MSE}_t, \text{MSE}_f)$ versus $(N_r, \text{MSE}_t, \text{MSE}_f)$ objective functions for the signal $z_{\text{LFM}}(t)$. Values in bold indicate the best-performing and the fastest algorithm.

		$z_{\text{LFM}}(t)$							
		TwIST		SpaRSA		SALSA		YALL1	
Objectives	M^S	N_r	M^S	N_r	M^S	N_r	M^S	N_r	
	MSE_t	MSE_t	MSE_t	MSE_t	MSE_t	MSE_t	MSE_t	MSE_t	
	MSE_f	MSE_f	MSE_f	MSE_f	MSE_f	MSE_f	MSE_f	MSE_f	
λ^+	2.701	2.081	6.145	5.390	13.941	12.180	4.001	3.931	
MSE_t	0.0197	0.0142	0.0229	0.0317	0.0181	0.0198	0.1379	0.1380	
MSE_f	0.0342	0.0386	0.0630	0.0639	0.0484	0.0378	0.2222	0.2201	
M^S	0.0258	0.0267	0.0221	0.0276	0.0396	0.0448	0.0063	0.0064	
N_r	22	14	12	9	12	11	25	19	
MAE_t	0.0817	0.0645	0.0841	0.1086	0.0691	0.0817	0.236	0.2362	
MAE_f	0.1408	0.1590	0.2251	0.2282	0.1756	0.1623	0.4492	0.4487	
MAX_t	0.4557	0.4229	0.4942	0.3943	0.4786	0.4269	1.0	1.0	
MAX_f	0.5385	0.5020	0.5038	0.4132	0.5451	0.4908	0.8497	0.8487	
$t[\text{s}]$	0.214	0.184	0.119	0.116	0.596	0.537	5.010	4.380	

resulting in visually indistinguishable reconstructed TFDs, as depicted in Figure 4.6. The numerical analysis presented in Table 4.4 confirms this observation, with competitive MSE_t and MSE_f values achieved by both M^S and N_r objectives, depending on the reconstruction algorithm employed. As with the signal $z_{\text{SINLFM}}(t)$, the optimal value of λ^+ is lower when using the M^S objective for all reconstruction algorithms. Similar to the previous signal example, the TwIST and SALSA algorithms achieve the best MSE_t and MSE_f values, while the SpaRSA is the fastest. Moreover, the YALL1 algorithm provides the highest auto-term resolution with the worst consistency, as evidenced by high MSE_t and MSE_f values. Supporting graphical representations of several arbitrarily selected Pareto fronts are visualized in Appendix C.

In conclusion, it can be inferred that both formulations of the objective function have surpassed the constraints of optimization using global concentration measures, and have demonstrated highly competitive performance. Notably, the use of the M^S objective function tends to result in slightly higher component resolution in the reconstructed TFDs, albeit at the cost of losing a small proportion of auto-term samples. Conversely, the use of the N_r objective function may be preferred due to its higher ability to preserve component connectivity while maintaining high resolution in the reconstructed TFDs.

4.5 Summary

In this chapter, it has been demonstrated that the localization in frequency slices using the narrow-band Rényi entropy has achieved higher accuracy than the STRE in providing the local number of components for signals whose components diverge significantly from the time axis. The combination of both approaches has been used to define performance criteria based on the LRE, which serves as the mean squared error between the local numbers of components in the starting and reconstructed TFDS. The presented LRE-based metric has been shown to surpass the drawbacks of global concentration measures and properly penalize the loss of auto-terms, as demonstrated by the reconstructed TFDS obtained in the previous chapter.

Furthermore, the LRE-based metrics have been formalized with two different measures as objective functions for multi-objective optimization. The first measure has been the global concentration measure M^S , and the second measure has been presented here, N_r , which measures the number of continuously-connected samples in a TFD. The results have evidenced that both objective function combinations have overcome the limitations of existing optimization approaches and provided high-performing reconstructed TFDS with preserved auto-terms. A slight advantage has been given to the optimization with the N_r measure, which has achieved better preservation of auto-terms with competitive auto-term resolution and cross-term suppression when using the M^S measure.

CHAPTER 5

ADVANCEMENTS IN COMPRESSIVE SENSING-BASED SIGNAL ANALYSIS

This chapter introduces two approaches aimed at enhancing the performance of sparse TFD reconstruction. The first method is the reconstruction algorithm, in which the original thresholding operator is substituted with the shrinkage operator based on the localized Rényi entropy information. The goal of the presented shrinkage operator in this context is to detect and concentrate a TFD filtered by the CS-AF only on auto-terms, as well as reduce the incidence of oversparsity in the final reconstructed TFD.

The second method parameterizes the original CS-AF area from the literature and extracts the magnitude-significant auto-term-related samples. The aim of the presented method is to include additional auto-term-related samples in the CS-AF area while discarding the cross-term- and noise-related ones that may be present in the non-parameterized CS-AF area. The methods introduced in this study are assessed using synthetic and real-life gravitational signals, both with and without noise. The obtained results are compared to those achieved by state-of-the-art reconstruction algorithms and the existing CS-AF area selection approach. The methods presented in this chapter are published by the author in international peer-reviewed journals and conference proceedings [52, 53, 54, 55].

5.1 The Rényi Entropy-Based Shrinkage Sparse Reconstruction Algorithm

In this section, an alternative method for TFD shrinkage is presented that utilizes the numbers of local components derived from the STRE and NBRE, NC_t and NC_f , respectively. The commonly used $\text{hard}_{\sqrt{2\lambda}}\{\cdot\}$ and $\text{soft}_{\lambda}\{\cdot\}$ operators are not suitable as classifiers since the maxima of cross-terms may exceed those of auto-terms. This necessitates an increase in the λ parameter, resulting in the loss of some auto-terms. To

address this issue, a new classifier is presented that identifies TF points as auto-terms based on the assumption that auto-terms possess a more prominent non-negative TFD energy surface. This assumption is justified by the prior application of the CS-AF filter, which emphasizes energy surfaces corresponding to auto-terms, given that the majority of samples within the CS-AF area are related to auto-terms.

The algorithm initiates by applying a thresholding operation to set all negative values in the TFD to zero:

$$\Upsilon_z(t, f) = \text{hard}_0\{\Upsilon_z(t, f)\}, \quad (5.1)$$

as negative samples are predominantly associated with the cross-terms. The subsequent step involves analyzing 1-D time or frequency slices, which are composed of multiple local maxima corresponding to auto-terms or cross-terms. To differentiate between these two types of maxima, a surface area is assigned to each local maximum by calculating the sum of all samples enclosed between the adjacent minima to the right and left of the maximum value. Subsequently, the largest surface areas are associated with the local number of components derived from either the STRE or NBRE, NC_t or NC_f , respectively. This is done in a new time or frequency slice that contains only auto-term-related samples.

The quantity of transferred samples is regulated by the supplementary parameters δ_t and δ_f , in time and frequency slices, respectively, where $\delta_t, \delta_f \in [0, 1], \delta_t, \delta_f \in \mathbb{R}$. The aforementioned procedure is iteratively applied to all remaining time and frequency slices within the TFD. The pseudocode of the algorithm is provided in Algorithm 1 [55]. It should be emphasized that the complexity of the presented algorithm, $\mathcal{O}(n^2)$, is equivalent to that of the original thresholding operator.

Algorithm 1 Pseudocode of the shrinkage operator

```

1: Function shrink( $\varsigma'_z(tf, ft), \delta_{t,f}, NC_{t,f}$ ):
2:  $\text{hard}_0\{\varsigma'_z(tf, ft)\}$ ;
3: for  $i \leftarrow 1$  to  $\text{length}(\varsigma'_z(:, ft))$  do
4:    $\text{slice}(\cdot) \leftarrow \varsigma'_z(i, \cdot)$ ;
5:    $\text{max}_{ind}(\cdot) \leftarrow$  indexes of slice local maxima;
6:   for  $j \leftarrow 1$  to  $\text{length}(\text{max}_{ind})$  do
7:      $\text{surf}(j, 3) = \text{max}_{ind}(j)$ ;
8:      $\text{surf}(j, 2) \leftarrow$  local minima to the left;
9:      $\text{surf}(j, 1) \leftarrow$  local minima to the right;
10:     $\text{surf}(j, 0) \leftarrow$  sum of samples from  $\text{surf}(j, 2)$  to  $\text{surf}(j, 1)$ ;
11:   end for
12:    $\text{surf} \leftarrow$  ascendantly sort w.r.t. the  $\text{surf}(:, 0)$ ;
13:   for  $j \leftarrow 1$  to  $NC_{t,f}(i)$  do
14:     for  $k \leftarrow \text{surf}(j, 2)$  to  $\text{surf}(j, 1)$  do
15:       if  $\text{slice}(k) \geq \delta_{t,f} \cdot \text{surf}(j, 3)$  then
16:          $\varsigma_z(i, k) = \text{slice}(k)$ ;
17:       end if
18:     end for
19:   end for
20: end for
21: return  $\varsigma_z(tf, ft)$ 

```

The presented shrinkage operator has been implemented in the TwIST algorithm because of its high performance, low execution time, and simplicity over other considered reconstruction algorithms. To formally establish the presented algorithm inside the TwIST framework, the argument of the soft-thresholding operator in (3.9) is denoted as $\zeta'_z(t, f)$, while the outcome of the soft-thresholding operation is represented as $\zeta_z(t, f)$. Thus, we have the following relationship [55]:

$$[\zeta'_z(t, f)]^{[n+1]} = [\Upsilon_z^{\ell_1}(t, f)]^{[n]} + \Psi^H \left(\mathbf{A}'_z(\nu, \tau) - \Psi [\Upsilon_z^{\ell_1}(t, f)]^{[n]} \right), \quad (5.2a)$$

$$[\zeta_z(t, f)]^{[n+1]} = \text{soft}_\lambda \left\{ [\zeta'_z(t, f)]^{[n+1]} \right\}. \quad (5.2b)$$

In the presented algorithm, (5.2b) was substituted with the following expression [55]:

$$[\zeta_z^{t,f}(t, f)]^{[n+1]} = \text{shrink}_{t,f} \left\{ [\zeta'_z(t, f)]^{[n+1]} \right\}, \quad (5.3)$$

where $\text{shrink}_{t,f}\{\cdot\}$ represents the algorithm outlined in Algorithm 1. The notation t, f represents the application of shrinkage on time or frequency slices using the STRE or NBRE method, respectively. In the subsequent step, $\zeta_z^f(t, f)$ and $\zeta_z^t(t, f)$ are merged by using their weighted average to be utilized as an input for (3.9) [55]:

$$[\zeta_z(t, f)]^{[n+1]} = p \cdot [\zeta_z^t(t, f)]^{[n+1]} + (1 - p) \cdot [\zeta_z^f(t, f)]^{[n+1]}, \quad (5.4)$$

where $p \in [0, 1], p \in \mathbb{R}$ is the weighting parameter supplied by the user. The complete algorithm for sparse TFD reconstruction with shrinkage is presented in Algorithm 2 [55].

Algorithm 2 Pseudocode of the sparse TFD reconstruction algorithm

Require: $\mathbf{A}'_z(\nu, \tau), \Psi, \Psi^H, NC_t, NC_f, \alpha_{\text{TwIST}}, \beta_{\text{TwIST}}, \epsilon, N_{it}, p, \delta_t, \delta_f$.

Ensure: Reconstructed sparse TFD, $\Upsilon_z(t, f)$.

- 1: $[\Upsilon_z(t, f)]^{[-1]}, [\Upsilon_z(t, f)]^{[0]} \leftarrow \Psi^H \mathbf{A}'_z(\nu, \tau)$;
 - 2: **while** $((c \geq \epsilon)$ **and** $(n \leq N_{it}))$ **do**
 - 3: Solve (5.2a);
 - 4: $\zeta_z^t(t, f) \leftarrow \text{shrink}(\zeta'_z(t, f), \delta_t, NC_t)$;
 - 5: $\zeta_z^f(t, f) \leftarrow \text{shrink}(\zeta'_z(t, f)^T, \delta_f, NC_f)$;
 - 6: Solve (5.4);
 - 7: Solve (3.9);
 - 8: $\epsilon \leftarrow$ stopping criterion;
 - 9: $n \leftarrow n + 1$;
 - 10: **end while**
-

Figures 5.1 and 5.2 illustrate a single iteration of the presented algorithm. Figure 5.1 shows the TFDs obtained after the CS-AF filtration step, which precedes the application of the shrinkage operator. The obtained TFDs exhibit prominent auto-terms compared to cross-terms. However, the resolution of the auto-terms is limited because the CS-AF area covers only a fraction of their samples from the AF. The presented algorithm addresses this issue by identifying and selecting the largest surface areas in each time or frequency

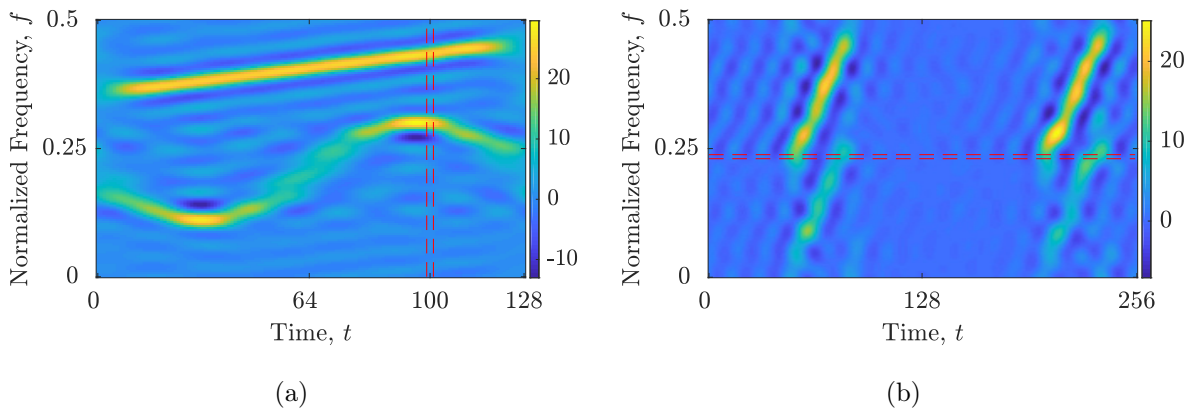


Figure 5.1 The obtained TFDs from the filtered AFs with the CS-AF area for the considered signals: (a) $z_{\text{SINLFM}}(t)$; (b) $z_{\text{LFM}}(t)$. Red dashed lines represent an arbitrarily chosen time slice at sample $t = 100$ for the signal $z_{\text{SINLFM}}(t)$ in (a), and a frequency slice at frequency bin $f = 120$ for the signal $z_{\text{LFM}}(t)$ in (b).

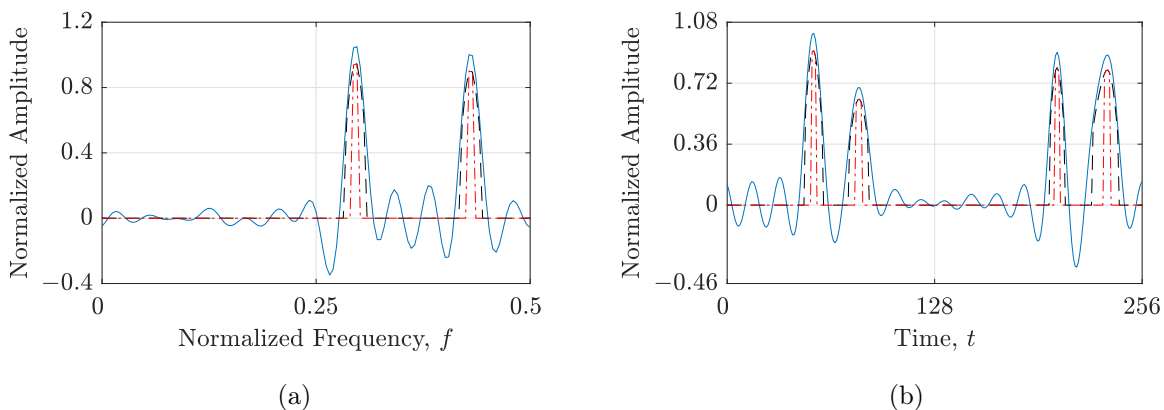


Figure 5.2 (a) A time slice at sample $t_0 = 100$ for the signal $z_{\text{SINLFM}}(t)$ with $p = 0.9$ and $NC_t(t_0) = 2$; (b) a frequency slice at frequency bin $f_0 = 120$ for the signal $z_{\text{SINLFM}}(t)$ with $p = 0.1$ and $NC_f(f_0) = 4$. The RTwIST parameters $\delta_t = \delta_f$ have been randomly set to 0.5 (black dashed line) and 0.95 (red dashed line).

slice based on the number of components, $NC_t(t)$ or $NC_f(f)$, as shown in Figure 5.2. The spread of each surface, measured in the number of samples along the time or frequency axis, is adjusted by modifying the signal-dependent parameters δ_t and δ_f . Increasing these parameters reduces the number of samples in each surface, as depicted in Figure 5.2 for $\delta_t = \delta_f = 0.95$ compared to $\delta_t = \delta_f = 0.5$. The impact of the signal-dependent parameters p , δ_t , and δ_f on the performance of the presented algorithm is discussed separately.

Influence of the parameter p

It is of importance to comprehend the significance of the parameter p and its impact on the overall performance of the algorithm. Equation (5.4) indicates that the algorithm uses the STRE exclusively when $p = 1$, the NBRE exclusively when $p = 0$, or a weighted

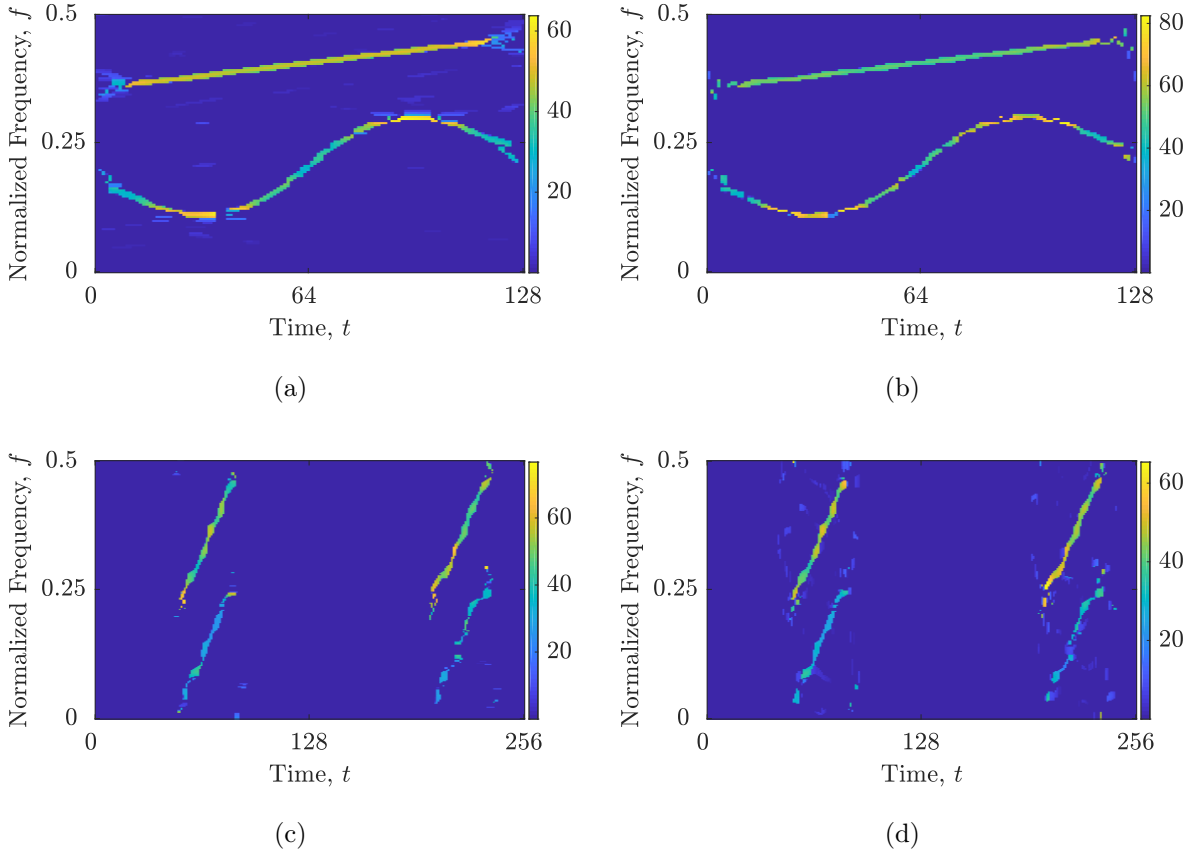


Figure 5.3 Reconstructed TFDs obtained using the RTwIST algorithm with parameters $\alpha_{\text{TwIST}} = 0.91$, $\beta_{\text{TwIST}} = 0.8$ and $\delta_t = \delta_f = 0.85$: (a) signal $z_{\text{SINLFM}}(t)$ with $p = 0.1$; (b) signal $z_{\text{SINLFM}}(t)$ with $p = 0.9$; (c) signal $z_{\text{LFM}}(t)$ with $p = 0.1$; (d) signal $z_{\text{LFM}}(t)$ with $p = 0.9$.

combination of both when $0 < p < 1$. Both the STRE and NBRE are essential, as the previous chapters have demonstrated, to cover a significantly wider range of signals. An incorrect number of local components can misclassify cross-terms or noise-related surfaces as auto-terms, making the inclusion of both approaches necessary. Figure 5.3 provides a clear representation of the RTwIST algorithm’s reconstruction performance for signals $z_{\text{SINLFM}}(t)$ and $z_{\text{LFM}}(t)$ using mostly the STRE ($p = 0.9$) and NBRE ($p = 0.1$). It is worth noting that the other RTwIST parameters, including δ_t and δ_f , were randomly selected and kept constant to highlight the effect of parameter p .

For the signal $z_{\text{SINLFM}}(t)$, the incorrect numbers of local components obtained from the NBRE misclassify cross-terms as auto-terms in the shrinkage operator, leading to their inevitable reconstruction, as shown in Figure 5.3a. Similar consequences are observed for the signal $z_{\text{LFM}}(t)$, but for a different value of p . Since the NBRE provides a more precise estimate of the number of local components for this signal, utilizing the STRE in the reconstruction adds unwanted cross-terms to the reconstructed TFD, as demonstrated in Figure 5.3d.

Table 5.1 Performance comparison of the RTwIST algorithm with different parameters p selection for the signals $z_{\text{SINLFM}}(t)$ and $z_{\text{LFM}}(t)$. Bold values indicate the superior performing algorithm.

RTwIST with parameters $\alpha_{\text{TwIST}} = 0.91$, $\beta_{\text{TwIST}} = 0.8$ and $\delta_t = \delta_f = 0.85$				
	$z_{\text{SINLFM}}(t)$		$z_{\text{LFM}}(t)$	
	$p = 0.1$	$p = 0.9$	$p = 0.1$	$p = 0.9$
MSE_t	0.0342	0.0041	0.0266	0.0398
MSE_f	0.0359	0.0312	0.0435	0.0474
N_r	13	8	19	54

Table 5.1 displays the numerical confirmation of the reconstruction performance for various p parameters using the Rényi entropy-based metric presented in the previous chapter. Reconstructing cross-terms increased the inaccuracy within the MSE_t and MSE_f metrics by 88.01% for the signal $z_{\text{SINLFM}}(t)$ and 33.17% for the signal $z_{\text{LFM}}(t)$, as well as the number of regions with continuously-connected TFD samples by 38.46% for the signal $z_{\text{SINLFM}}(t)$ and 64.81% for the signal $z_{\text{LFM}}(t)$. This validated the visual assessment that $p \rightarrow 1$ should be employed to the signal $z_{\text{SINLFM}}(t)$ and $p \rightarrow 0$ to the signal $z_{\text{LFM}}(t)$.

Incorrect parameter selection for p can result in both the loss of auto-terms in the reconstructed TFD, as well as the undesired reconstruction of cross-terms. This issue can arise due to several reasons. Firstly, when analyzing signals with components whose amplitudes differ significantly, incomplete $NC_t(t)$ or $NC_f(f)$ values may become apparent. In such cases, it is advised for the user to emphasize proper selection of the underlying RID in the original STRE and NBRE methods, or to use an iterative LRE approach. Secondly, if an unsuitable axis is used for slice localization on signal components that deviate from it, shrinkage operations may miss the true component, as illustrated in Figure 5.3a for the sinusoidal component. Therefore, careful parameter selection is essential to ensure accurate and complete reconstruction of the TFD.

Influence of the parameters δ_t and δ_f

After selecting the appropriate parameter p for a given signal, it is important to properly consider the values of δ_t and δ_f . For the signals $z_{\text{SINLFM}}(t)$ and $z_{\text{LFM}}(t)$, p values of 0.9 and 0.1 respectively were found to be more suitable in the previous simulation. In this simulation, the influence of varying the parameters δ_t and δ_f was investigated by examining lower values ($\delta_t = \delta_f = 0.5$) and higher values ($\delta_t = \delta_f = 0.95$). The results are given in Table 5.2 and depicted in Figure 5.4.

The results of the simulations signifies that the choice of suitable values for δ_t and δ_f carries a crucial role in determining the resolution quality of the reconstructed TFD. The analysis of signals $z_{\text{SINLFM}}(t)$ and $z_{\text{LFM}}(t)$, demonstrated in Figure 5.4, shows that

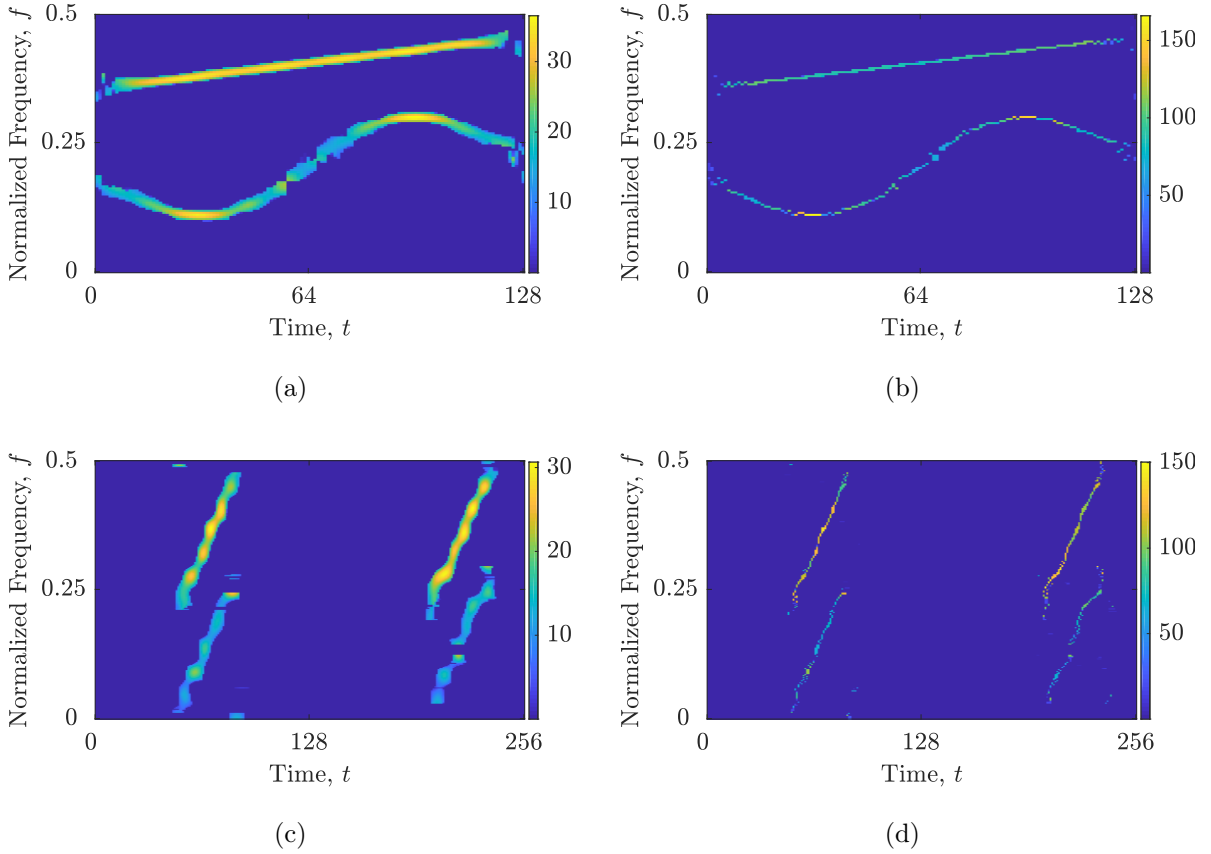


Figure 5.4 Reconstructed TFDs obtained using the RTwIST algorithm with parameters $\alpha_{\text{EMB}} = 0.91$, $\beta_{\text{EMB}} = 0.8$: (a) signal $z_{\text{SINLFM}}(t)$, $p = 0.9$ and $\delta_t = \delta_f = 0.5$; (b) signal $z_{\text{SINLFM}}(t)$, $p = 0.9$ and $\delta_t = \delta_f = 0.95$; (c) signal $z_{\text{LFM}}(t)$, $p = 0.1$ and $\delta_t = \delta_f = 0.5$; (d) signal $z_{\text{LFM}}(t)$, $p = 0.1$ and $\delta_t = \delta_f = 0.95$.

the resolution of the reconstructed TFD is in direct correlation to the values of δ_t and δ_f . Higher values of δ_t and δ_f (i.e., stronger shrinkage) lead to an improvement in the resolution of the reconstructed TFD, whereas lower values (i.e., less shrinkage) result in a reduction in resolution.

It should be emphasized that excessively large values of δ_t and δ_f may result in the absence of samples related to auto-terms, particularly for signals with weaker components, such as the two LFM components in the signal $z_{\text{LFM}}(t)$. Furthermore, reconstructing non-LFM components, as in the case of the signal $z_{\text{SINLFM}}(t)$ shown in Figure 5.4b, may result in a loss of auto-terms in the non-linear portion of the components, which usually have lower amplitude as well. The underlying cause for this is that auto-term-related surfaces with low amplitude are more likely to be misclassified as cross-terms, making it more difficult for the shrinkage operator to maintain the successful identification of such auto-terms over its iterations.

Upon examining the numerical values presented in Table 5.2, the earlier visual observations are corroborated. In both signal examples, a lower reconstructed TFD resolution

Table 5.2 Performance of the RTwIST algorithm with different parameters δ_t and δ_f selection for the signals $z_{\text{SINLFM}}(t)$ and $z_{\text{LFM}}(t)$. Bold values indicate the superior performing algorithm.

RTwIST with parameters $\alpha_{\text{TwIST}} = 0.91, \beta_{\text{TwIST}} = 0.8$				
	$z_{\text{SINLFM}}(t)$ with $p = 0.9$		$z_{\text{LFM}}(t)$ with $p = 0.1$	
	$\delta_t = \delta_f = 0.5$	$\delta_t = \delta_f = 0.95$	$\delta_t = \delta_f = 0.5$	$\delta_t = \delta_f = 0.95$
MSE_t	0.2783	0.2011	0.1187	0.0455
MSE_f	0.1036	0.1302	0.1685	0.0811
N_r	3	7	16	18

increased the MSE_t and MSE_f values because each time or frequency slice generated higher entropy than the reference one. However, the difference in MSE_t and MSE_f values between reconstructed TFDs with lower and higher resolution is not as significant as it was in the previous simulation of different parameters p .

Interestingly, in the case of the signal $z_{\text{SINLFM}}(t)$, the MSE_f is even lower for the low-resolution TFD with $\delta_t = \delta_f = 0.5$ than with a higher $\delta_t = \delta_f = 0.95$. This is because, as previously indicated, an increase in δ_t and δ_f values may result in the partial loss of auto-terms, which in turn increases the MSE_t and MSE_f values. Furthermore, this increase is reflected in a higher N_r value, indicating greater discontinuity in the reconstructed TFD components.

Although $\delta_t = \delta_f = 1$ theoretically provides the highest possible TFD resolution reconstruction, practical imperfections in the methods or the complexity of the signal itself may prevent the ideal outcome. Extensive usage and research findings indicate that it is not advisable to select this value for every signal in practice. Instead, a range of $\delta_t, \delta_f \in [0.6, 1]$ achieves an optimal compromise between auto-term resolution and retention.

5.1.1 Simulation Results

The optimal values for the presented RTwIST parameters for the signals $z_{\text{SINLFM}}(t)$ and $z_{\text{LFM}}(t)$ are found by formalizing a multi-objective optimization problem as:

$$\begin{aligned}
 &\text{minimize: } M^S/N_r, \text{MSE}_t, \text{MSE}_f(\alpha_{\text{TwIST}}, \beta_{\text{TwIST}}, p, \delta_t, \delta_f), \\
 &\text{subject to: } \alpha_{\text{TwIST}} \in \langle 0, 1 \rangle, p \in [0, 1], \beta_{\text{TwIST}} \in \langle 0, 2\alpha \rangle, \delta_t, \delta_f \in [0.6, 1].
 \end{aligned} \tag{5.5}$$

The results of the performance of the RTwIST algorithm optimized with two different objective function combinations, $(M^S, \text{MSE}_t, \text{MSE}_f)$ and $(N_r, \text{MSE}_t, \text{MSE}_f)$, are shown in Figure 5.5 and given in Table 5.3. The LRE, reconstruction algorithm, and NSGA-III parameters have been kept equal as in the previous simulations, considering signals $z_{\text{SINLFM}}(t)$ and $z_{\text{LFM}}(t)$.

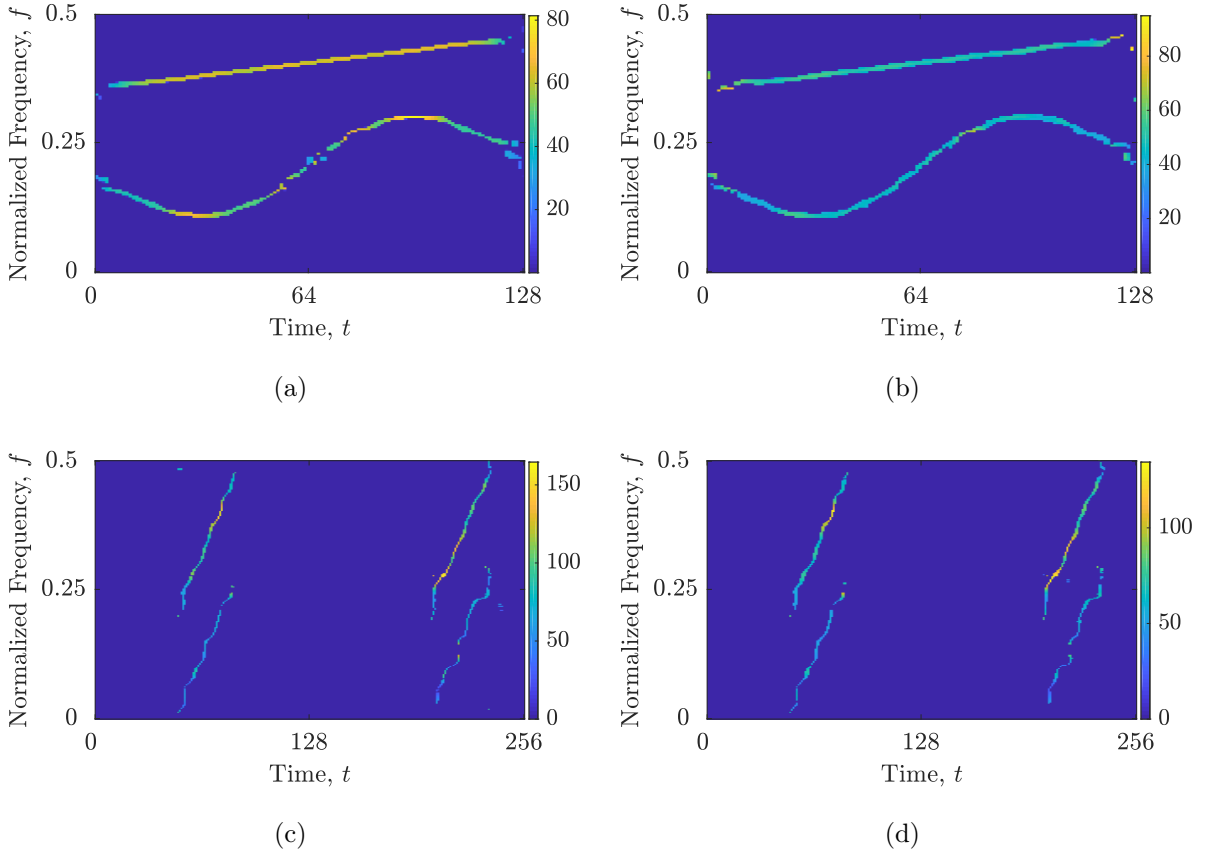


Figure 5.5 Reconstructed TFDs obtained by the RTwIST algorithm with objective functions formalized as MSE_t, MSE_f and: (a) signal $z_{\text{SINLFM}}(t), M^S$; (b) signal $z_{\text{SINLFM}}(t), N_r$; (c) signal $z_{\text{LFM}}(t), M^S$; (d) signal $z_{\text{LFM}}(t), N_r$.

Visually, both optimization approaches result in reconstructed TFDs with successfully suppressed cross-terms and retained auto-terms. While the difference in performance of the obtained reconstructed TFDs for the signal $z_{\text{LFM}}(t)$ is difficult to discuss from visual observation, we can observe in Figures 5.5a and 5.5b for the signal $z_{\text{SINLFM}}(t)$ that the reconstructed TFD optimized with measure N_r achieves better preservation of the auto-terms, while the reconstructed TFD optimized with measure M^S achieves slightly better concentration.

Using the numerical results from Table 5.3, we can expand on the visual observations. Despite the 15.32% increase in MSE_t for the signal $z_{\text{SINLFM}}(t)$ when optimizing with the N_r measure, an overall reduction is present in both, MSE_t and MSE_f , by 30.87% to 34.89%, respectively, for both signals $z_{\text{SINLFM}}(t)$ and $z_{\text{LFM}}(t)$. This confirms the observations that an optimization procedure using the M^S measure can exclude some auto-terms in favor of higher concentration. Note that for both signal examples, higher optimal δ_t^+ and δ_f^+ parameters result in higher concentration. Furthermore, the obtained reconstructed TFDs achieve better M^S and N_r values when these measures are included as objective functions compared to when they are not. This is expected and consistent with the conclusions

Table 5.3 Performance of the RTwIST algorithm optimized with the NSGA-III and objective functions formalized as (MSE_t, MSE_f, M^S) versus (MSE_t, MSE_f, N_r) for the signals $z_{\text{SINLFM}}(t)$ and $z_{\text{LFM}}(t)$. Bold values indicate the superior performing algorithm.

	$z_{\text{SINLFM}}(t)$		$z_{\text{LFM}}(t)$	
(α^+, β^+)	(0.92, 0.86)	(0.99, 0.80)	(0.89, 0.87)	(0.90, 0.92)
$(p^+, \delta_t^+, \delta_f^+)$	(1, 0.93, 0.91)	(1, 0.84, 0.88)	(0, 0.97, 0.96)	(0, 0.84, 0.95)
Objectives	M^S		M^S	
	MSE_t, MSE_f	N_r MSE_t, MSE_f	MSE_t, MSE_f	N_r MSE_t, MSE_f
MSE_t	0.0124	0.0143	0.0171	0.0118
MSE_f	0.0617	0.0405	0.0149	0.0103
M^S	0.0328	0.0408	0.0154	0.0171
N_r	5	2	11	8
MAE_t	0.0937	0.1437	0.0647	0.0531
MAE_f	0.1812	0.1565	0.1067	0.0849
MAX_t	0.2015	0.2460	0.5358	0.5024
MAX_f	0.6468	0.4855	0.2389	0.2055
$t[s]$	0.312	0.289	0.931	0.888

given in the previous chapter. The remaining performance indices support the MSE_t and MSE_f results.

Furthermore, the RTwIST algorithm’s performance has been compared to other reconstruction algorithms considered in the dissertation, whose results are provided in Tables 4.3 and 4.4 for the signals $z_{\text{SINLFM}}(t)$ and $z_{\text{LFM}}(t)$, respectively. The findings illustrate that the RTwIST algorithm surpasses all considered algorithms in terms of both MSE_t and MSE_f . Specifically, for the signal $z_{\text{SINLFM}}(t)$, the RTwIST algorithm achieves a 6.54% improvement in MSE_t over SpARSA, up to a 97.50% improvement over YALL1, and a 0.48% improvement in MSE_f over TwIST, up to an 82.77% improvement over YALL1, when both objective function formulations are considered. Similarly, for the signal $z_{\text{LFM}}(t)$, the RTwIST algorithm achieves a 13.20% improvement in MSE_t over TwIST, up to a 91.45% improvement over YALL1, and a 72.75% improvement in MSE_f over TwIST, up to a 95.32% improvement over YALL1, considering both objective function formulations.

When optimizing with the N_r measure, the RTwIST algorithm is competitive with the best algorithms in terms of component connectivity (SpARSA and SALSA), achieving $N_r = 2$ for the signal $z_{\text{SINLFM}}(t)$ and reducing N_r by one more than SpARSA exhibits for the signal $z_{\text{LFM}}(t)$. However, when optimizing with the M^S measure, the practical imperfection of the RTwIST’s shrinkage operator with particularly high $\delta_{t,f}$ may induce a small bias to the auto-term samples of non-LFM components, which slightly decreases component connectivity. The results also show that the M^S value is the lowest for the YALL1 algorithm in all simulations, indicating that the YALL1 achieves the best component concentration.

Table 5.4 Hypervolume values (best, average, worst) of five reconstruction algorithms, including RTwIST, TwIST, SALSA, SpaRSA, and YALL1, for the signals $z_{\text{SINLFM}}(t)$ and $z_{\text{LFM}}(t)$ with objective functions using the M^S or N_r measures. Values in bold indicate the best-performing algorithm with the highest hypervolume values.

Objectives	$z_{\text{SINLFM}}(t)$				$z_{\text{LFM}}(t)$			
	M^S		N_r		M^S		N_r	
	MSE _t , MSE _f	Rank	MSE _t , MSE _f	Rank	MSE _t , MSE _f	Rank	MSE _t , MSE _f	Rank
RTwIST	63.4587	1.	75.4444	1.	94.6665	1.	93.8877	1.
	61.5476		73.4121		92.9561		91.5503	
	59.8788		71.8871		90.1145		88.9634	
TwIST	55.3698	2.	74.1287	2.	89.5478	2.	84.1124	2.
	53.1436		73.0080		87.0559		82.7896	
	51.1245		70.0014		84.7896		81.1478	
SpaRSA	44.5687	4.	73.7778	3.	77.4568	4.	79.3698	4.
	42.6156		71.9287		75.7616		78.9316	
	39.6547		69.8878		71.6987		75.7899	
SALSA	49.8887	3.	70.5554	4.	86.5111	3.	83.8987	3.
	47.1472		68.7837		84.0811		82.7047	
	45.8111		66.8788		82.2247		80.4444	
YALL1	38.1478	5.	42.0014	5.	72.2258	5.	73.3214	5.
	35.4417		39.4470		69.6930		70.9316	
	32.1487		37.1879		65.1789		67.9878	

Finally, the RTwIST algorithm is slower than the SpaRSA, TwIST, and SALSA algorithms, but significantly faster than the YALL1 algorithm.

To further demonstrate the superiority of the presented RTwIST algorithm, a hypervolume analysis has been conducted for all considered reconstruction algorithms, including RTwIST, TwIST, SALSA, SpaRSA, and YALL1. The results are summarized in Table 5.4. To ensure a fair comparison, all reconstruction algorithms were optimized using the NSGA-III algorithm with the same parameters provided in Table 4.2. The optimization was performed independently 1000 times to minimize its stochastic nature. The resulting Pareto fronts from all algorithms were stored in a single repository, and the maximum values of the objective functions represented the vertices of the cube for the measure.

The results present that the RTwIST algorithm generates the best-performing Pareto front. More precisely, its best hypervolume value ranges from 63.4587 to 94.6665, with an average range from 61.5476 to 92.9561, and the worst range from 59.8788 to 90.1145 when considering all objective function formulations and both signals, $z_{\text{SINLFM}}(t)$ and $z_{\text{LFM}}(t)$. This represents an improvement of up to 44.33%, 46.27% and 46.31% for the best, average, and worst hypervolume values compared to the worst-performing algorithm (YALL1). It

is noteworthy that the second-best-performing algorithm in this analysis is TwIST, which further validates its selection as the underlying algorithm in RTwIST.

5.1.2 Sensitivity to Noise

To assess the performance of the presented RTwIST algorithm in the presence of noise, a numerical analysis has been conducted by adding synthetic signals to AWGN with SNRs ranging from 1 to 9. Then, the reconstructed TFDs of the noisy signals were compared with those of the noise-free signals using machine learning evaluation metrics [41]. To facilitate the use of these metrics in this dissertation, the noise-free and noisy reconstructed TFDs were transformed into a binary classification problem. The *positive class* (P) represents signal samples in the reconstructed TFD, while the *negative class* (N) represents reconstructed TFD samples where no signal is present.

The noise-free TFD comprises actual or true samples that should be retained at their exact positions (and positive or negative class) in the noisy TFD. Therefore, the following indices were used to measure the number of samples in a noisy reconstructed TFD that are equivalent to or distinct from the actual, noise-free TFD [41]:

- true positives (TP) – samples erroneously categorized in the positive class,
- true negatives (TN) – samples erroneously categorized in the negative class,
- false positives (FP) – samples erroneously categorized in the positive class,
- false negatives (FN) – samples erroneously categorized in the negative class.

Noise is anticipated to increase the FP and FN indices. A high FP value indicates the reconstruction of noise and/or cross-term-related samples, whereas a high FN value indicates the absence of true signal samples in a noisy TFD reconstruction.

The provided indices are visually represented in the *confusion matrix* [9, 41]. In this dissertation, each row of the confusion matrix represents the samples belonging to a noise-free (or true) TFD, whereas each column represents the samples belonging to a noisy TFD. Consequently, the cells on the major diagonal of the confusion matrix, where the positive and negative classes from the noise-free and noisy TFD align, show the correct reconstruction classifications, TN and TP. Other matrix cells, however, show inaccurate classifications, namely the FN and FP. It is worth noting that the confusion matrix for our classification problem has a 2×2 dimension. Using the aforementioned confusion matrix and its indices, several statistical measures are defined. First, the classification *accuracy* is expressed as the portion of correct samples in a noisy TFD (both TP and TN) among the whole TFD ($N_t \cdot N_f$) [41]:

$$\text{Accuracy} = \frac{\text{TP} + \text{TN}}{\text{TP} + \text{TN} + \text{FP} + \text{FN}} = \frac{\text{TP} + \text{TN}}{N_t \cdot N_f}. \quad (5.6)$$

Next, the *specificity*, also called the *true negative rate*, measures the reconstruction algorithm's ability to retain TN as [41]:

$$\text{Specificity} = \frac{\text{TN}}{\text{TN} + \text{FP}}. \quad (5.7)$$

In order to measure the amount of correct samples belonging to a signal in a noisy TFD among all samples reconstructed in the positive class, the *precision*, also called the *positive predictive value*, is used, defined as [41]:

$$\text{Precision} = \frac{\text{TP}}{\text{TP} + \text{FP}}. \quad (5.8)$$

The precision is commonly combined with the *recall* measure, also known as the *true positive rate* or *sensitivity*, which represents the number of correct signal samples in a noisy TFD in comparison to the true number of signal samples in a noise-free TFD [41]:

$$\text{Recall} = \frac{\text{TP}}{\text{TP} + \text{FN}}. \quad (5.9)$$

The balance of both measures, precision and recall, is combined in the *F1 score* measure as a single metric value, representing the harmonic mean of their values [41]:

$$\text{F1} = 2 \cdot \frac{\text{Precision} \cdot \text{Recall}}{\text{Precision} + \text{Recall}} = \frac{2 \cdot \text{TP}}{2 \cdot \text{TP} + \text{FP} + \text{FN}}. \quad (5.10)$$

Note that all the aforementioned statistical metrics are inside the range $[0, 1]$, where a higher value is preferred.

As previously stated, the evaluation metrics treat given reconstructed TFDs as binary images; that is, signal samples (regarding the amplitude value) are set to ones. To account for TFD amplitudes, the 2-D MSE with a scaled and squared *Frobenius norm* between the noisy and noise-free reconstructed TFDs has been used:

$$\text{F-norm} = \frac{1}{N_t N_f} \|\rho(t, f) - \rho^{(\text{noise})}(t, f)\|_F^2 = \frac{1}{N_t N_f} \sum_{t=1}^{N_t} \sum_{f=1}^{N_f} |\rho(t, f) - \rho^{(\text{noise})}(t, f)|^2. \quad (5.11)$$

The confusion matrices and the corresponding statistical measures obtained by the RTwIST algorithm when comparing its performance in the presence of AWGN in different SNRs are given in Tables 5.5 and 5.6. Note that in this test and throughout the dissertation, when noise is considered, the obtained results have been averaged over 1000 independent noise realizations in order to minimize its random behavior. As seen in Table 5.5, the presence of noise increased the FN and FP values. A significant increase in the FN and FP, with a drop in the TN and TP values, is evident when both signals $z_{\text{SINLFM}}(t)$ and $z_{\text{LFM}}(t)$ are embedded in AWGN in $\text{SNR} = 1$ dB.

Table 5.5 Confusion matrices for evaluating the RTwIST algorithm’s sensitivity to noise for SNR = (1, 3, 5, 7, 9) dB for the signals $z_{\text{SINLFM}}(t)$ and $z_{\text{LFM}}(t)$. Values in bold indicate the true negative and true positive indices.

SNR		1 dB		5 dB		9 dB		
		Noisy TFD		Noisy TFD		Noisy TFD		
		N	P	N	P	N	P	
$z_{\text{SINLFM}}(t)$	True TFD	N	14908	678	15328	258	15421	165
			P	529	141	170	500	141
$z_{\text{LFM}}(t)$	True TFD	N	63323	1065	64112	258	64161	198
			P	617	275	209	701	186

This behavior is also shown with the statistical measures in Table 5.6. The F1 score may be highlighted, which is decreased by 23.77% and 14.88% in the signals $z_{\text{SINLFM}}(t)$ and $z_{\text{LFM}}(t)$, respectively, going from SNR = 9 dB to SNR = 3 dB, compared with a further decrease by 67.97% and 63.49% in the signals $z_{\text{SINLFM}}(t)$ and $z_{\text{LFM}}(t)$, respectively, when SNR = 1 dB. The precision, recall, and F-norm measures also confirm this behavior.

Note that the accuracy and specificity measures have not shown themselves to be reliable, since they remained high for all SNRs. The reason behind this is the large difference between a number of auto-term samples and the size of the whole TFD, where a portion of incorrect signal samples does not greatly affect the accuracy and specificity measures. Therefore, it can be concluded that the RTwIST algorithm is suitable for use in noisy environments with SNR > 1 dB, which corresponds with the noise sensitivity of the STRE [118, 120, 121] and NBRE methods.

Examples of reconstructed TFDs for both signals $z_{\text{SINLFM}}(t)$ and $z_{\text{LFM}}(t)$ embedded in AWGN with SNR = (1, 3) dB are depicted in Figure 5.6. For SNR = 3 dB, the reconstructed TFDs, shown in Figures 5.6b and 5.6d, are competitive with the ones in Figure 5.5. However, a more significant drop in performance, also detected by the statistical measures, is visible for SNR = 1 dB in Figures 5.6a and 5.6c. The drop in performance is mainly attributed to two factors. The decline in performance may be primarily attributed to two factors. Firstly, the high noise levels cause an increase in the values of $NC_t(t)$ and $NC_f(f)$, which in turn causes the shrinkage operator to include a greater number of surfaces than there are auto-terms. Secondly, it is possible for noise to surpass certain auto-terms with low amplitude, leading to their erroneous identification as auto-terms across the entire time-frequency distribution. This involves another difficulty in the reconstruction since the desired auto-term may be replaced with noise or a cross-term.

Table 5.6 Statistical measures for evaluating the RTwIST algorithm’s sensitivity to noise for SNR = (1, 3, 5, 7, 9) dB for the signals $z_{\text{SINLFM}}(t)$ and $z_{\text{LFM}}(t)$.

$z_{\text{SINLFM}}(t)$						
	Accuracy	Specificity	Precision	Recall	F1	F-norm
1 dB	0.9258	0.9565	0.1722	0.2104	0.1894	235.1081
3 dB	0.9635	0.9774	0.5493	0.6403	0.5913	73.4112
5 dB	0.9737	0.9834	0.6596	0.7463	0.7003	58.1807
7 dB	0.9785	0.9874	0.7245	0.7731	0.7480	42.2222
9 dB	0.9812	0.9894	0.7622	0.7896	0.7757	38.7343
$z_{\text{LFM}}(t)$						
	Accuracy	Specificity	Precision	Recall	F1	F-norm
1 dB	0.9742	0.9835	0.2052	0.3083	0.2464	147.3097
3 dB	0.9899	0.9944	0.6539	0.6973	0.6749	36.3391
5 dB	0.9928	0.9960	0.7310	0.7703	0.7501	16.9878
7 dB	0.9937	0.9967	0.7742	0.7835	0.7788	13.2328
9 dB	0.9941	0.9969	0.7878	0.7980	0.7929	11.1238

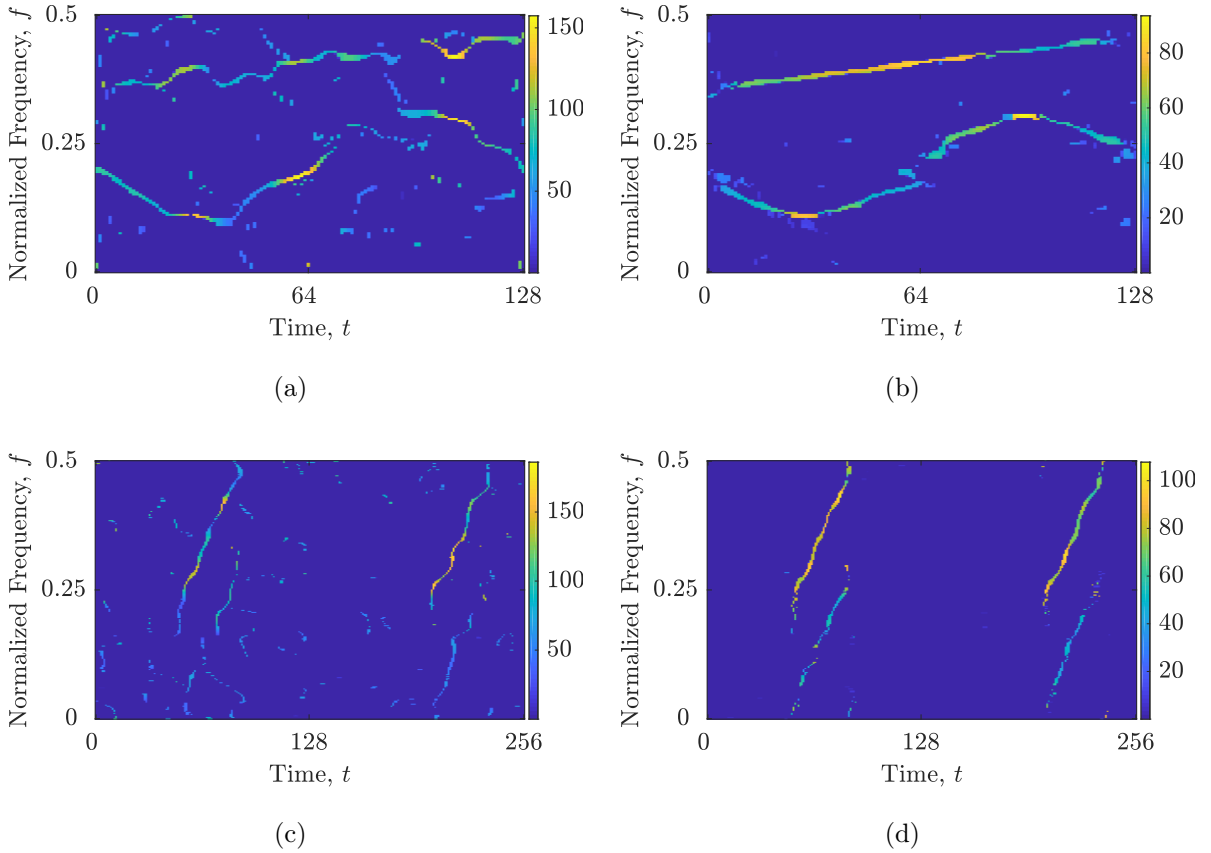


Figure 5.6 Reconstructed TFDs obtained by the RTwIST algorithm for the considered signals embedded in AWGN: (a) $z_{\text{SINLFM}}(t)$, SNR = 1 dB; (b) $z_{\text{SINLFM}}(t)$, SNR = 3 dB; (c) $z_{\text{LFM}}(t)$, SNR = 1 dB; (d) $z_{\text{LFM}}(t)$, SNR = 3 dB.

5.2 Parametrized Compressive Sensing Area Selection

5.2.1 Ambiguity Function Thresholding

The choice of the CS-AF area significantly impacts the outcome of sparse TFD reconstruction. Insufficient sampling in the CS-AF area hampers TF resolution and prevents the reconstruction of low-amplitude, higher-polynomial FM signal components. Using an excessive number of samples, on the other hand, leads to an undesirable reconstruction of the cross-terms [37, 127, 131]. In addition, this issue is exacerbated by the RTwIST algorithm, as the improper CS-AF area can reduce the classification reliability of the shrinkage operator. In other words, the shrinkage operator may incorrectly include cross-term-related samples as part of the auto-term-related components, while rejecting samples related to the auto-terms. The whole $N'_\tau \times N'_\nu$ area is limited by two constraints. First, its adaptive size captures only the linear phenomenon of auto-terms, potentially degrading the accuracy of higher polynomial FM component trajectories in the filtered TFD. Second, it is constrained by its rigid rectangular form, which may contain AF samples associated with noise or inner-terms (produced by non-LFM components) as N'_τ and N'_ν increase. All of the aforementioned cases diminish the overall performance of reconstruction.

To address the limitations described above, a method for selecting the CS-AF is now presented. The underlying premise is that the performance of the reconstruction may be significantly enhanced by selectively choosing the most salient samples within the CS-AF area, $N'_\tau \times N'_\nu$, further denoted with $\mathbf{A}_{z_T}(\nu, \tau)$. Furthermore, the method allows for the incorporation of additional external samples from the wider AF region, referred to as $\mathbf{A}_{z_\Lambda}(\nu, \tau)$, if deemed beneficial. Therefore, the matrix form of the (ν, τ) area, $\mathbf{\Omega}$, is constructed with AF samples as follows [53]:

$$\mathbf{\Omega} = \begin{cases} \mathbf{A}_z(\nu, \tau), & |\mathbf{A}_{z_T}(\nu, \tau)| \geq \Gamma \cup |\mathbf{A}_{z_\Lambda}(\nu, \tau)| \geq \Lambda, \\ 0, & \text{otherwise,} \end{cases} \quad (5.12)$$

where $\Gamma, \Lambda \in [0, 1]$, $\Gamma, \Lambda \in \mathbb{R}$ parameters define the minimal normalized magnitude of the AF sample chosen from $\mathbf{A}_{z_T}(\nu, \tau)$ and $\mathbf{A}_{z_\Lambda}(\nu, \tau)$, respectively. Notably, it has been ensured that auto-terms and cross-terms satisfy the essential AF properties [15, 20]:

1. Auto-terms demonstrate a densely concentrated distribution along trajectories that traverse the origin of the AF, adhering to the IF law of the components.
2. The auto-term magnitude peaks at the AF origin and then gradually diminishes.
3. Auto-terms and cross-terms may cross each other within the AF.

The rationale behind the incorporation of the parameter Γ in $\mathbf{A}_{z_T}(\nu, \tau)$ is discussed first. In this area, the majority of samples are essential to the TFD reconstruction since

that area is centered around the AF origin, where the majority of auto-terms are expected to reside. However, due to the rigorous rectangular structure of the $\mathbf{A}_{z_\Gamma}(\nu, \tau)$, it often includes low-magnitude samples that are unrelated to the auto-terms. These samples may be unnecessary for reconstruction, or worse, they may be associated with noise or inner-terms due to the non-linear auto-term behavior. Therefore, the purpose of parameter Γ in this area is to effectively decrease the CS-AF and exclude undesirable AF samples. Note that for $\Gamma = 0$, $\mathbf{A}_{z_\Gamma}(\nu, \tau)$ equals the original $N'_\tau \times N'_\nu$ area, while for $\Gamma = 1$ only the sample at the AF origin is considered. Moreover, it is recommended to employ a relatively small Γ value to mitigate the potential inclusion of low-magnitude auto-terms.

Conversely, the objective of incorporating $\mathbf{A}_{z_\Lambda}(\nu, \tau)$ is to enlarge the CS-AF area by including auto-term-related samples, thereby providing additional insights into the missing auto-term characteristics, particularly those exhibiting non-linear behavior. By virtue of the second property outlined earlier, the cross-terms within $\mathbf{A}_{z_\Lambda}(\nu, \tau)$ can possess magnitudes that surpass those of the auto-terms. Consequently, the utilization of a low Γ value in $\mathbf{A}_{z_\Gamma}(\nu, \tau)$ is insufficient to remove the cross-term-related samples, which validates the need for a second parameter and presented AF segmentation. To ensure the sole incorporation of auto-term-related samples, it is advisable to employ a larger Λ value.

Note that the parameters $\Gamma, \Lambda \in [0, 1], \Gamma, \Lambda \in \mathbb{R}$ will be included in the optimization process because they are also signal-dependent and that for $(\Gamma = 0, \Lambda = 1)$, the CS-AF region fully corresponds to the original $N'_\tau \times N'_\nu$ area.

Excluding AF samples with the presented parameters Γ and Λ is to selectively exclude AF samples, aiming to reduce the sample density between the auto-term and cross-term regions. This selective exclusion assists in minimizing the overall cardinality of Ω while retaining a significant portion of the auto-terms. Note that in cases where the cross-terms have pronounced magnitudes, it may not be possible to completely remove them before constructing Ω . Therefore, one more step has been included in the proposed algorithm to further improve Ω by utilizing the clustering algorithm to make the final classification decision and extract only auto-term-related samples from Ω .

5.2.2 Extraction of Signal Samples From the Ambiguity Function Using Density-Based Spatial Clustering

In the ultimate stage, the objective is to identify a single cluster, denoted as C_Ω , within Ω that aligns with the specified properties of auto-terms. To achieve this, the acquired Ω is utilized as input for a data clustering endeavor. Considering the requirement of retrieving a single cluster located exactly at the AF origin based on the known auto-term properties, the density-based spatial clustering in applications with noise (DBSCAN) algorithm has been utilized. Unlike other clustering methods, DBSCAN does not rely on a predefined number of clusters, which is advantageous in this context [35, 100, 106]. Additionally,

DBSCAN offers flexibility in terms of cluster shape and size, which is crucial for identifying signals with diverse auto-term directions. The above mentioned benefits, coupled with the reduced computational complexity and the capability to eliminate anomalous data points, highlight the superiority of DBSCAN over partitioning and hierarchical approaches in our specific scenario [40, 141, 142, 148].

The DBSCAN algorithm strives to identify clusters within Ω based on the minimum density criterion, where clusters are distinguished by regions with lower sample density [49, 92, 106, 111, 145]. The DBSCAN is influenced by two distinct parameters. The first parameter is the ε radius, which defines the ε -neighborhood of the AF sample $\mathbf{A}_z(\nu_p, \tau_p)$:

$$\mathcal{N}_\varepsilon(\mathbf{A}_z(\nu_p, \tau_p)) = \{\mathbf{A}_z(\nu_q, \tau_q) \in \Omega \mid d(\mathbf{A}_z(\nu_p, \tau_p), \mathbf{A}_z(\nu_q, \tau_q)) \leq \varepsilon\}, \quad (5.13)$$

where $\mathbf{A}_z(\nu_q, \tau_q)$ represents an AF sample within the ε -neighborhood of the $\mathbf{A}_z(\nu_p, \tau_p)$, and the Euclidean distance is given by:

$$d(\mathbf{A}_z(\nu_p, \tau_p), \mathbf{A}_z(\nu_q, \tau_q)) = \sqrt{(\nu_p - \nu_q)^2 + (\tau_p - \tau_q)^2}. \quad (5.14)$$

The second parameter, denoted as *minPts*, specifies the minimum cardinality of samples required within the ε -neighborhood of an observed AF sample.

The DBSCAN parameter values have been fixed for our clustering task at *minPts* = 4 and ε = 3 in accordance with the recommended guidelines provided in [100, 106]. To ensure a more cohesive cluster, border samples were combined with core samples, aligning with the principles of a density level set [24, 106]. For specific data structures, the computing efficiency of DBSCAN is $\mathcal{O}(n^2)$ or $\mathcal{O}(n \cdot \log n)$. In order to increase computing performance, DBSCAN avoids computing density between individual points and instead clusters all data points located within the ε -neighborhood of a core data point [106].

CS-AF Area Selection

The efficacy of the presented CS-AF area is shown on a synthetic signal, $z_{\text{PFM}}(t)$, with $N_t = 256$ samples consisted of two parabolic FM (PFM) components embedded in AWGN with SNR = 6 dB, and the real-life gravitational signal¹, $z_{\text{grav}}(t)$ [79, 80, 81, 82]. This gravitational signal includes 3441 data samples. Prior to the analysis, the signal $z_{\text{grav}}(t)$ was downsampled by a factor of 16, resulting in $N_t = 216$ samples. Note that the acquired 216 samples correspond to a signal duration between 0.25 and 0.45 seconds with a frequency in the range of [0, 500] Hz. The WVDs of the signals under consideration and their AFs with the automatically selected $N'_\tau \times N'_\nu$ areas are depicted in Fig. 5.7.

¹This research has made use of data, software and/or web tools obtained from the LIGO Open Science Center (<https://losc.ligo.org>), a service of LIGO Laboratory and the LIGO Scientific Collaboration. LIGO is funded by the U.S. National Science Foundation.

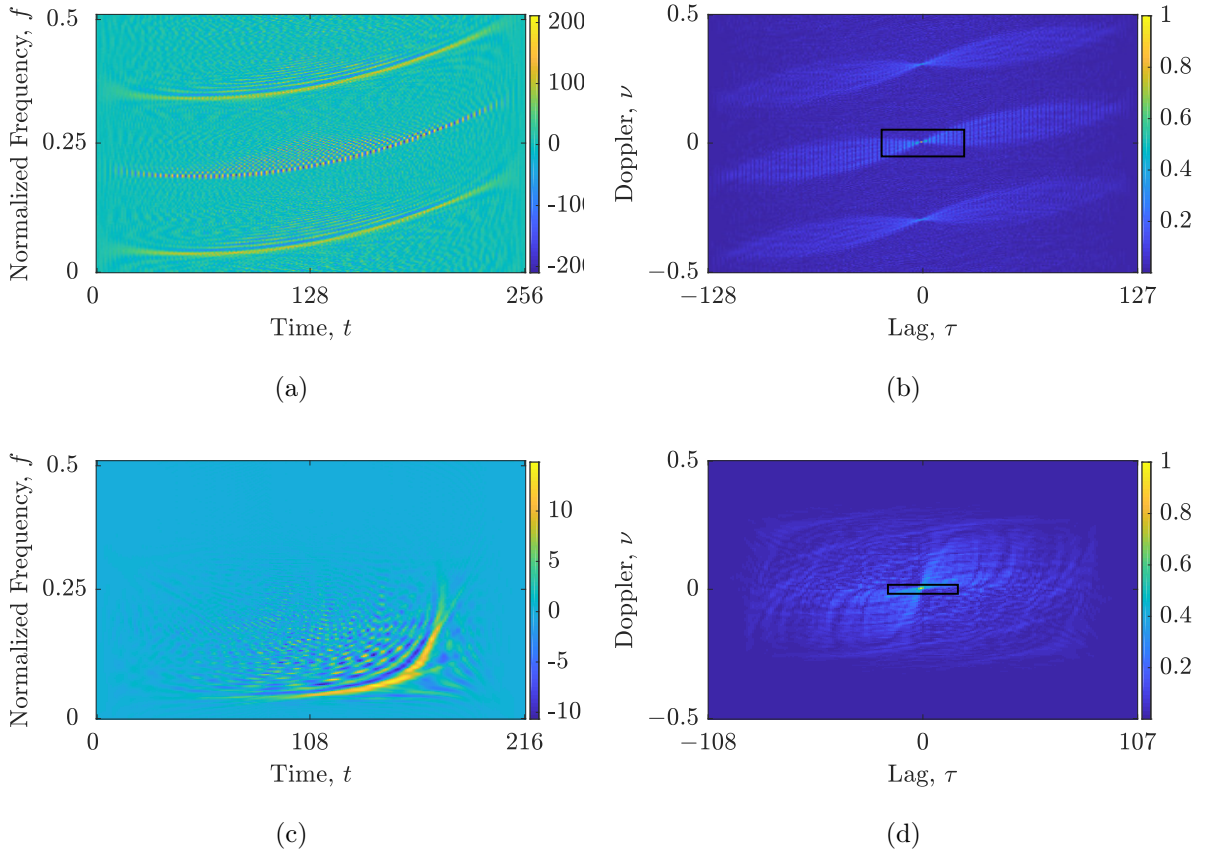


Figure 5.7 (a) the WVD of $z_{\text{PFM}}(t)$; (b) the AF of $z_{\text{PFM}}(t)$, $N'_\tau \times N'_\nu = 49 \times 53$; (c) the WVD of $z_{\text{grav}}(t)$; (d) the AF of $z_{\text{grav}}(t)$, $N'_\tau \times N'_\nu = 35 \times 15$. The automatically selected $N'_\tau \times N'_\nu$ area is marked by the rectangle.

Figure 5.8 depicts the clustered CS-AF areas derived utilizing the presented CS-AF area selection technique. Figure 5.8a reveals, for the signal z_{PFM} , that the C_Ω may be

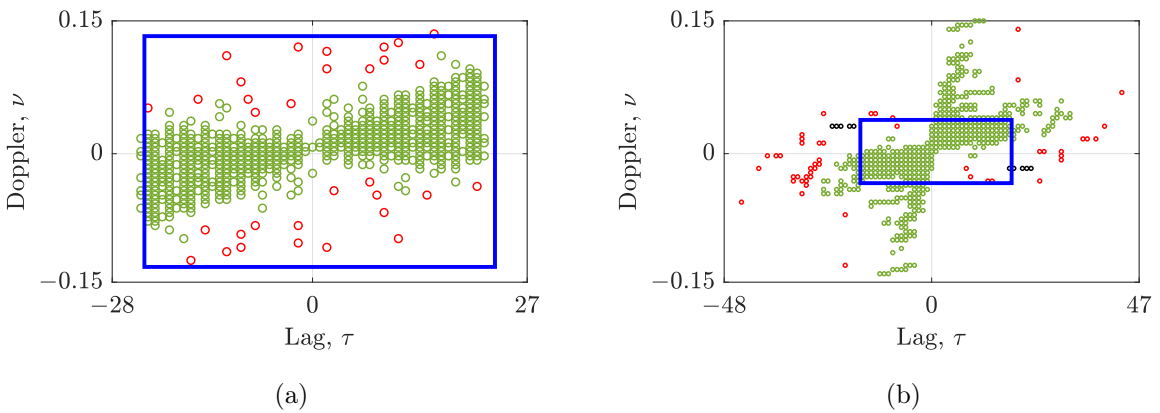


Figure 5.8 Clustered CS-AF area, denoted as C_Ω , for: (a) signal $z_{\text{PFM}}(t)$, with $(\Gamma, \Lambda) = (0.06, 0.5)$; (b) signal $z_{\text{grav}}(t)$ with $(\Gamma, \Lambda) = (0.15, 0.18)$. The green circles represent the samples within the cluster, while the red circles indicate the outlier samples. The blue rectangle corresponds to the automatically selected $N'_\tau \times N'_\nu$ area.

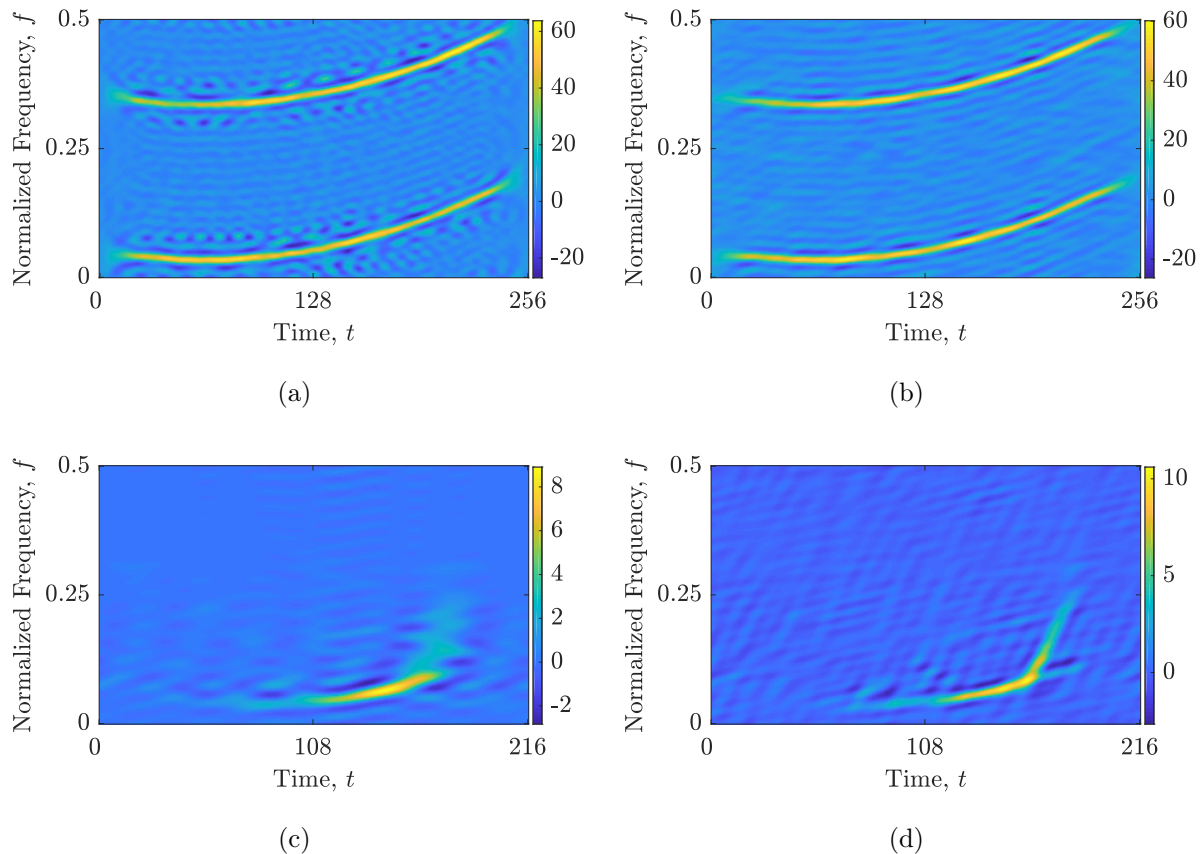


Figure 5.9 TFDs obtained from filtered AFs for: (a) signal $z_{\text{PFM}}(t)$ with a full $N'_\tau \times N'_\nu$ area; (b) signal $z_{\text{PFM}}(t)$ with the presented CS-AF area, $(\Gamma, \Lambda) = (0.06, 0.5)$; (c) signal $z_{\text{grav}}(t)$ with a full $N'_\tau \times N'_\nu$ area; (d) signal $z_{\text{grav}}(t)$ with the presented CS-AF area, $(\Gamma, \Lambda) = (0.15, 0.18)$.

decreased from the $N'_\tau \times N'_\nu$ area by concentrating on the AF samples correlated solely with the auto-terms when using the presented approach. Additionally, Figure 5.8b illustrates the ability of DBSCAN to accurately generate the C_Ω area by incorporating additional AF samples beyond the boundaries of the $N'_\tau \times N'_\nu$ area, thereby highlighting the hyperbolic nature of the signal $z_{\text{grav}}(t)$. Notably, the DBSCAN successfully classifies AF samples that deviate from the auto-term trajectories as outliers or noise, resulting in their exclusion from the final C_Ω . Also note that the given parameters Γ and Λ are not necessarily the optimal parameters for the signal examples under consideration. They were chosen to illustrate the effectiveness of the presented CS-AF area selection method.

Figure 5.9 presents a comparative analysis between the TFDs obtained by applying AF filtering using a full $N'_\tau \times N'_\nu$ rectangular region (i.e., $\Gamma = 0, \Lambda = 1$) and the presented CS-AF area method with the specified Γ and Λ parameters. In the case of the signal $z_{\text{PFM}}(t)$, the utilization of the presented method (shown in Figure 5.9b) decreased the number of artifacts composed of superimposed cross-terms and noise, particularly in the vicinity of its auto-terms with non-linear behavior, while maintaining the resolution of

the auto-terms. A notable improvement in both the resolution of the auto-terms and the depiction of their hyperbolic behavior for the signal $z_{\text{grav}}(t)$, as observed in Figure 5.9d, is achieved, compared with the original TFD depicted in Figure 5.9c. These enhancements will result in higher performance of the shrinkage and thresholding operators of the reconstruction algorithms. Moreover, considering the strong reliance of the RTwIST algorithm on accurately distinguishing the bandwidth, duration and amplitude of the auto-terms from the cross-terms, an improvement in its classification effectiveness and, ultimately, the overall reconstruction performance is expected.

5.2.3 Simulation Results: Synthetic Signal

In the succeeding simulations, the performances of the CS-AF area selection with static geometric as in [127, 131] and the presented adaptive CS-AF area with optimal (Γ^+, Λ^+) are compared and shown on the TwIST, SALSA, SpaRSA, and RTwIST algorithms. Note that for the CS-AF area with rigid geometry, parameters have been preset to $\Gamma = 0, \Lambda = 1$, while for the presented selection method, they have been included in optimization. The NSGA-III and reconstruction algorithms' parameters have been set as in the previous examples. The LRE has been defined with $\alpha_R = 3$ and $\Theta_t = \Theta_f = 11$, whereas the underlying EMBD parameters have been optimized using the M^S measure and set to $\alpha_{\text{EMB}} = 0.09, \beta_{\text{EMB}} = 0.18$ and $\alpha_{\text{EMB}} = 0.12, \beta_{\text{EMB}} = 0.13$ for the signals $z_{\text{PFM}}(t)$ and $z_{\text{grav}}(t)$, respectively.

For the signal $z_{\text{PFM}}(t)$, the obtained reconstructed TFDs are illustrated in Figure 5.10, while the numerical results are given in Table 5.7. Upon visual inspection, it becomes apparent that the reconstructed TFDs generated using the parametrized CS-AF area exhibit fewer interference terms in the vicinity of auto-terms compared to the TFDs obtained using the full $N'_\tau \times N'_\nu$ area. Quantitatively, the presented CS-AF area's advantage is reflected in all considered reconstruction algorithms. The RTwIST algorithm, employing the presented CS-AF area, demonstrates a significant improvement in comparison to the same algorithm with the full $N'_\tau \times N'_\nu$ area, particularly for N_r and MSE_t , which are lowered by 59.10% and 49.17%, respectively. Further metrics, including the global concentration measures, also validate this enhancement.

The SpaRSA algorithm yields the most substantial visual and numerical improvement, as shown in Figures 5.10f and 5.10e. Specifically, the values of N_r , MSE_t , and MSE_f are lowered by 98.38%, 70.44%, and, 59.39%, respectively, which is evident since the reconstructed TFD when using the original $N'_\tau \times N'_\nu$ area yields heavily discontinuous and low-resolution auto-terms. Moreover, the significance of N_r is apparent in the SALSA algorithm outcome. Despite a modest raise in MSE_f of 5.29% due to slightly reduced auto-term resolution, the presented CS-AF area achieves a considerable decrease in N_r of 93.33%, demonstrating greater component coherence with reduced artifact samples.

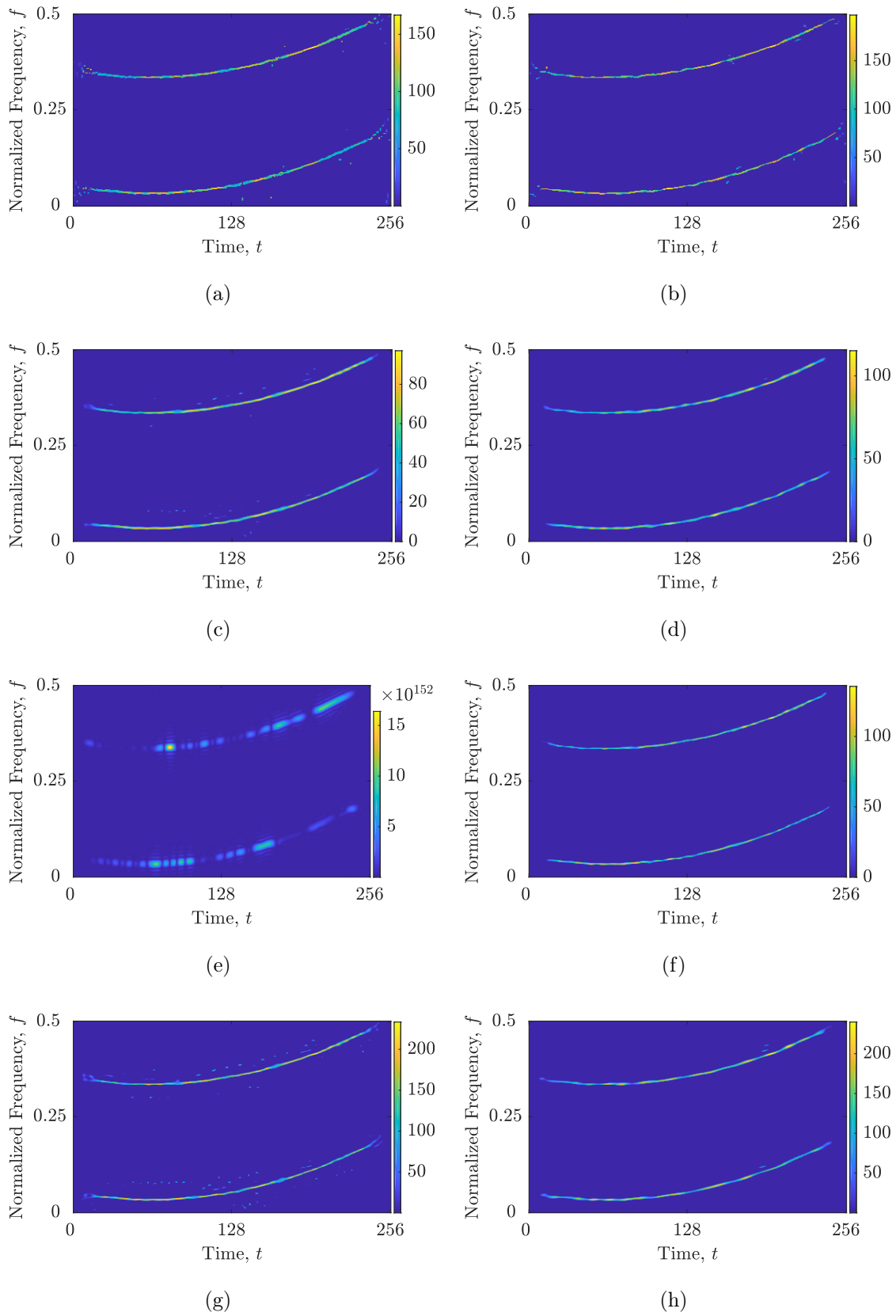


Figure 5.10 Reconstructed TFDs obtained using the following reconstruction algorithm and CS-AF area with (Γ, Λ) for the signal $z_{\text{PFM}}(t)$: (a) RTwIST, $(0, 1)$; (b) RTwIST, $(0.046, 0.426)$; (c) TwIST, $(0, 1)$; (d) TwIST, $(0.043, 0.520)$; (e) SpARSA, $(0, 1)$; (f) SpARSA, $(0.029, 0.515)$; (g) SALSA, $(0, 1)$; (h) SALSA, $(0.070, 0.350)$.

Table 5.7 Performance comparison of considered reconstruction algorithms using the full $N'_\tau \times N'_\nu$ area ($(\Gamma, \Lambda) = (0, 1)$) versus the presented CS-AF area with optimized (Γ^+, Λ^+) for the signal $z_{\text{PFM}}(t)$. Bold values represent the best-performing or the fastest algorithm.

	$z_{\text{PFM}}(t)$							
	RTwIST		TwIST		SpaRSA		SALSA	
	$\Gamma = 0$	$\Gamma^+ =$ 0.046	$\Gamma = 0$	$\Gamma^+ =$ 0.043	$\Gamma = 0$	$\Gamma^+ =$ 0.029	$\Gamma = 0$	$\Gamma^+ =$ 0.070
	$\Lambda = 1$	$\Lambda^+ =$ 0.426	$\Lambda = 1$	$\Lambda^+ =$ 0.520	$\Lambda = 1$	$\Lambda^+ =$ 0.515	$\Lambda = 1$	$\Lambda^+ =$ 0.350
$\text{card}(C_\Omega)$	2597	883	2597	1009	2597	1617	2597	531
MSE_t	0.0179	0.0091	0.0597	0.0378	0.1029	0.0253	0.0159	0.0117
MSE_f	0.0178	0.0158	0.0207	0.0187	0.0904	0.0248	0.0189	0.0199
N_τ	22	9	35	3	186	3	75	5
MAE_t	0.1141	0.0780	0.2344	0.1738	0.2866	0.0847	0.1054	0.0928
MAE_f	0.0769	0.0735	0.0886	0.0792	0.2240	0.091	0.0742	0.0778
MAX_t	0.3192	0.2654	0.5791	0.6475	0.5833	0.7890	0.6804	0.2983
MAX_f	0.5334	0.6170	0.4897	0.5411	0.9411	0.6762	0.6820	0.6112
R	10.33	9.97	10.47	10.28	11.44	9.94	10.22	10.14
M^S	0.0269	0.0195	0.0278	0.0237	0.3690	0.0185	0.0405	0.0431
$M^{\text{RN}}(\cdot 10^3)$	0.89	1.13	0.92	1.21	0.03	1.30	1.11	1.22
M^H	0.8607	0.8781	0.8516	0.8611	0.6578	0.8771	0.8631	0.8672
$t[s]$	0.747	0.726	0.231	0.233	0.465	0.117	0.467	0.385

Finally, among the considered reconstruction algorithms, the RTwIST algorithm demonstrates the best MSE_t and MSE_f values. This further corroborates the conclusions given in the previous section for different signal examples, considering the RTwIST's improved performance over the existing algorithms.

It is important to highlight the significant reduction achieved in the size of the CS-AF area, ranging from 37.75% (SpaRSA algorithm) to 79.54% (SALSA algorithm). This indicates that a considerable portion of the AF samples within the entire $N'_\tau \times N'_\nu$ rectangle are unrelated to the auto-terms, as demonstrated in Appendix D. Furthermore, it is noteworthy that the utilization of the presented CS-AF area, along with the obtained Γ^+ and Λ^+ values, does not lead to an increase in the runtime of the reconstruction algorithms.

5.2.4 Simulation Results: Real-Life Gravitational Signal

The presented CS-AF area's performance is further shown on the signal $z_{\text{grav}}(t)$. Given the numerical results provided in Table 5.8 and shown in Figure 5.11, significant reductions are achieved in MSE_t and MSE_f values by up to 90.41% and 73.95%, respectively, in the considered reconstruction algorithms with the presented CS-AF area. These findings

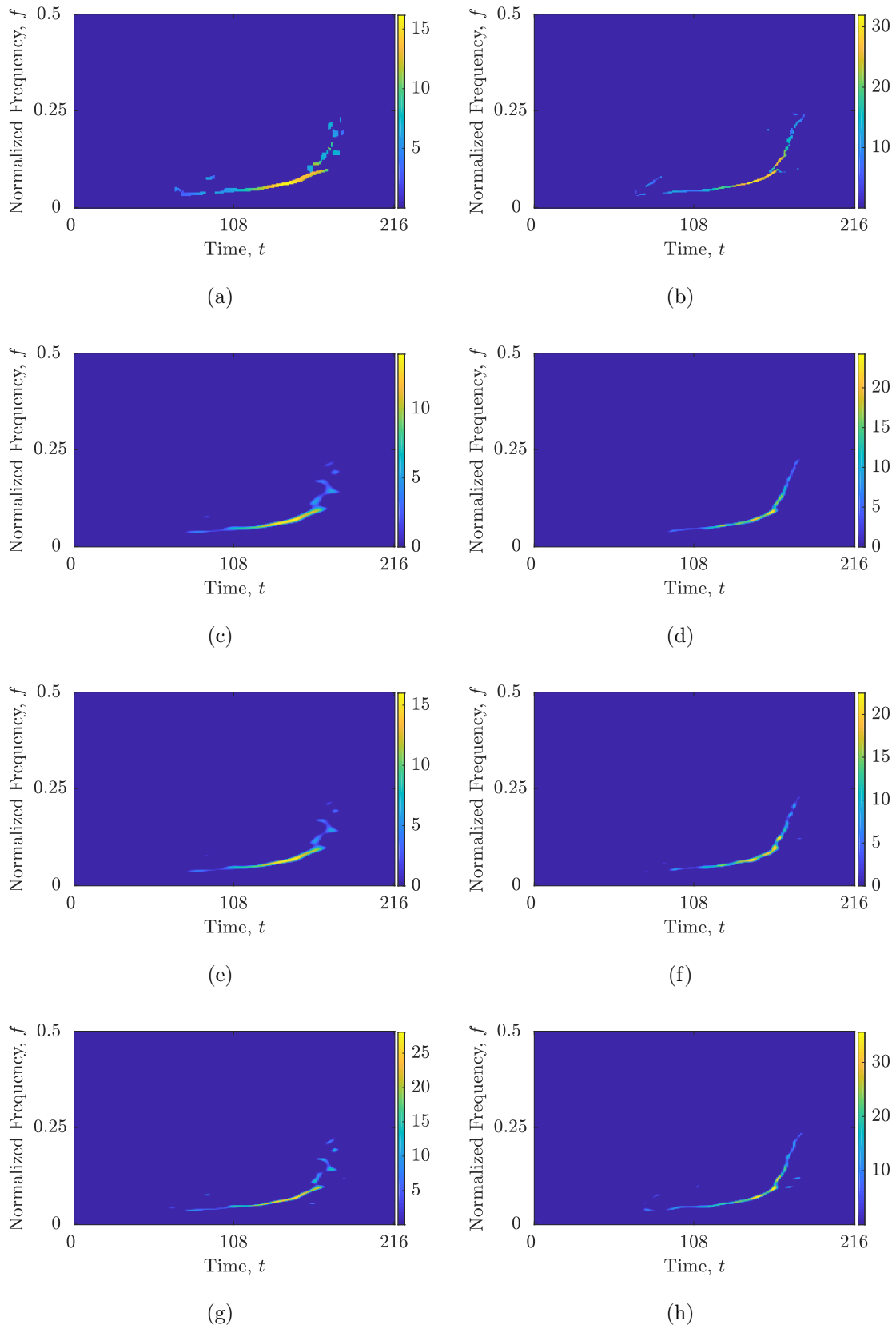


Figure 5.11 Reconstructed TFDs obtained using the following reconstruction algorithm and CS-AF area with (Γ, Λ) for the signal $z_{\text{grav}}(t)$: (a) RTwIST, $(0, 1)$; (b) RTwIST, $(0.142, 0.189)$; (c) TwIST, $(0, 1)$; (d) TwIST, $(0.300, 0.179)$; (e) SpaRSA, $(0, 1)$; (f) SpaRSA, $(0.080, 0.195)$; (g) SALSA, $(0, 1)$; (h) SALSA, $(0.098, 0.195)$.

Table 5.8 Performance comparison of considered reconstruction algorithms using the full $N'_\tau \times N'_\nu$ area ($(\Gamma, \Lambda) = (0, 1)$) versus the presented CS-AF area with optimized (Γ^+, Λ^+) for the signal $z_{\text{grav}}(t)$. Values in bold represent the best-performing or the fastest algorithm.

		$z_{\text{grav}}(t)$							
		RTwIST		TwIST		SpaRSA		SALSA	
		$\Gamma = 0$	$\Gamma^+ =$	$\Gamma = 0$	$\Gamma^+ =$	$\Gamma = 0$	$\Gamma^+ =$	$\Gamma = 0$	$\Gamma^+ =$
			0.142		0.130		0.080		0.098
		$\Lambda = 1$	$\Lambda^+ =$	$\Lambda = 1$	$\Lambda^+ =$	$\Lambda = 1$	$\Lambda^+ =$	$\Lambda = 1$	$\Lambda^+ =$
			0.189		0.179		0.195		0.195
card(C_Ω)		525	441	525	505	525	505	525	456
MSE _t	0.0386	0.0037	0.0404	0.0268	0.0356	0.0286	0.0155	0.0151	
MSE _f	0.0357	0.0093	0.0280	0.0200	0.0245	0.0197	0.0209	0.0144	
N_r	9	10	4	2	4	4	7	7	
MAE _t	0.1375	0.0332	0.1221	0.1084	0.1192	0.1128	0.0733	0.0773	
MAE _f	0.1119	0.0510	0.1002	0.0820	0.0952	0.0807	0.0845	0.0627	
MAX _t	0.5148	0.2061	0.5371	0.5191	0.5212	0.5531	0.4898	0.4511	
MAX _f	0.5566	0.5092	0.5538	0.6227	0.513	0.5747	0.6683	0.6087	
R	8.82	8.01	8.61	8.03	8.38	8.12	8.14	8.13	
M^S	0.0134	0.0070	0.0131	0.0078	0.0109	0.0085	0.0344	0.0473	
$M^{\text{RN}}(\cdot 10^3)$	2.91	5.22	4.12	5.53	4.62	5.23	5.74	5.61	
M^H	0.9024	0.9272	0.9075	0.9261	0.9152	0.9232	0.9231	0.9221	
$t[s]$	0.203	0.331	0.133	0.250	0.060	0.050	0.162	0.137	

are consistent with the observations made in the preceding signal $z_{\text{PFM}}(t)$. Specifically, the RTwIST algorithm exhibits the highest efficacy, whereas the SpaRSA algorithm demonstrates the fastest runtime.

In addition, by reducing the CS-AF samples by up to 16%, all reconstruction algorithms produce superior results. Notice that the decrease in the CS-AF area is not as large as in the preceding signal. This is attributed to the optimized CS-AF areas in this case encompassing supplemental auto-term-related samples outside the $N'_\tau \times N'_\nu$ area, as shown in Appendix D. Note that the deterioration of the hyperbolic IF seen in Figure 5.9d when employing the original $N'_\tau \times N'_\nu$ rectangle leads to the same degradation in the reconstructed TFD obtained with all reconstructed algorithms, as shown in Figures 5.11a, 5.11c, 5.11e and 5.11g. The presented CS-AF area substantially enhances the concentration of components along the hyperbolic IF in all reconstructed TFDs depicted in Figures 5.11b, 5.11d, 5.11f and 5.11h.

The obtained R values for the SALSA algorithm with both CS-AF areas and the SpaRSA algorithm using the presented CS-AF area demonstrate nearly identical outcomes. This observation highlights two limitations of the global Rényi entropy [93] for the use case

in this research. First, its insensitivity to minor deviations in the TFDs may not produce values that will distinguish two similarly-performed TFDs. Secondly, the permutation of values within the distribution has no impact on the entropy value, meaning that the same R value can be obtained for two different TFDs. Once more, the global concentration metrics inaccurately suggest that SALSA with $(\Gamma, \Lambda) = (0, 1)$ outperforms SALSA with $(\Gamma^+, \Lambda^+) = (0.098, 0.195)$ and more preserved auto-terms. This highlights the significance of harnessing the characteristics of the auto-terms acquired through the localized approach $(N_r, \text{MSE}_t, \text{MSE}_f)$ as opposed to the global approach when assessing TFDs.

5.2.5 Sensitivity to Noise

Finally, Table 5.9 gives the results obtained for the signal $z_{\text{PFM}}(t)$ embedded in AWGN with three distinct SNRs. Overall, the results show that the reconstruction performance with the presented CS-AF area experiences a smaller increase in the MSE_t , MSE_f , and N_r values as the SNR decreases than with the full $N'_\tau \times N'_\nu$ area, indicating that the Γ parameter's capability to exclude noise-related samples lowers the CS-AF area's sensitivity to noise. However, noise still influences the presented CS-AF area selection for low SNRs, despite the fact that the sensitivity to noise has been reduced. This is also expected given that, as noise increases, the noise-related samples in the AF may become indistinguishable from the auto-term-related samples when comparing their magnitudes, particularly when dealing with nonlinear auto-terms of low magnitude.

Note that the presented CS-AF area selection outperforms the original $N'_\tau \times N'_\nu$ area selection by the greatest margin at the lowest SNR of 1 dB. Specifically, the MSE_t , MSE_f , and N_r values are lowered by 41.99%, 37.40%, and 34.88%, respectively. This can be attributed to the fact that as the noise level increases, a greater number of noise-related samples are present within the $N'_\tau \times N'_\nu$. Furthermore, observe that the Γ^+ value increases as the SNR decreases. This indicates that the magnitude of the noise-related samples increases, necessitating a larger Γ value for their removal.

Table 5.9 Comparison of the performance between the RTwIST algorithm using the full $N'_\tau \times N'_\nu$ area $((\Gamma, \Lambda) = (0, 1))$ and the presented CS-AF area (Γ^+, Λ^+) for the signal $z_{\text{PFM}}(t)$ in the presence of noise at various SNR levels.

	$z_{\text{PFM}}(t)$					
	1 dB		5 dB		9 dB	
Γ	0	0.082	0	0.047	0	0.038
Λ	1	0.482	1	0.448	1	0.414
MSE_t	0.0381	0.0221	0.0168	0.0107	0.0105	0.0088
MSE_f	0.0385	0.0241	0.0196	0.0167	0.0138	0.0121
N_r	43	28	26	15	19	11

Table 5.10 Confusion matrices and statistical measures for evaluating the RTwIST algorithm’s sensitivity to noise for SNR = (1, 5, 9) dB with the full $N'_\tau \times N'_\nu$ area versus the presented CS-AF area selection (Γ^+, Λ^+) for the signal $z_{\text{PFM}}(t)$. Values in bold indicate the true negative and true positive indices.

			$z_{\text{PFM}}(t)$					
			1 dB		5 dB		9 dB	
			Noisy	TFD	Noisy	TFD	Noisy	TFD
$N'_\tau \times N'_\nu$	True TFD	N	P	N	P	N	P	
		63522	917	64071	302	64098	252	
		620	221	211	691	182	748	
(Γ^+, Λ^+)	True TFD	N	P	N	P	N	P	
		63632	867	64084	278	65130	221	
		480	301	188	730	158	771	
		$N'_\tau \times N'_\nu$	(Γ^+, Λ^+)	$N'_\tau \times N'_\nu$	(Γ^+, Λ^+)	$N'_\tau \times N'_\nu$	(Γ^+, Λ^+)	
F-norm		168.1897	81.1123	55.0087	35.7789	24.7896	21.0243	
Accuracy		0.9765	0.9794	0.9921	0.9929	0.9934	0.9942	
Specificity		0.9858	0.9866	0.9953	0.9957	0.9961	0.9966	
Precision		0.1942	0.2577	0.6959	0.7242	0.7480	0.7772	
Recall		0.2628	0.3854	0.7661	0.7952	0.8043	0.8299	
F1		0.2233	0.3089	0.7293	0.7580	0.7751	0.8027	

Additional metrics (TP, TN, FP, FN) and their statistical measures derived from the confusion matrices given in Table 5.10 for the signal $z_{\text{PFM}}(t)$ support the aforementioned results and their discussion. The F1 score may be highlighted, which is consistently improved by 38.33%, 3.94%, 3.56% for SNR = (1, 5, 9), respectively.

In order to confirm the conclusions in this study, the confusion matrices and statistical measures have been calculated for two additional signals, as previously used in this dissertation: $z_{\text{SINLFM}}(t)$ and $z_{\text{LFM}}(t)$. The obtained results are given in Tables 5.11 and 5.12, which provide a comprehensive overview of the performance metrics for the signals under consideration.

We may observe significant improvements in the F1 score for both signals. Specifically, the F1 score is improved by 50.63%, 6.50%, 2.45% for the signal $z_{\text{SINLFM}}(t)$ and by 34.25%, 5.60%, 3.15% for the signal $z_{\text{LFM}}(t)$ for SNR = (1, 5, 9), respectively. Upon comparing the outcomes presented in Table 5.6, one can infer that using the presented CS-AF area selection, all evaluation metrics and statistical measures are improved for all considered signals and SNR levels.

Table 5.11 Confusion matrices for evaluating the RTwIST algorithm’s sensitivity to noise for SNR = (1, 5, 9) dB with the presented CS-AF area selection (Γ^+ , Λ^+) for the signals $z_{\text{SINLFM}}(t)$ and $z_{\text{LFM}}(t)$. Values in bold indicate the true negative and true positive indices.

			1 dB		5 dB		9 dB	
			Noisy TFD		Noisy TFD		Noisy TFD	
			N	P	N	P	N	P
$z_{\text{SINLFM}}(t)$	True TFD	N	14988	583	15368	218	15443	145
		P	474	211	142	528	132	536
$z_{\text{LFM}}(t)$	True TFD	N	63398	902	64144	220	64183	174
		P	607	373	171	745	164	759

Table 5.12 Statistical measures for evaluating the RTwIST algorithm’s sensitivity to noise for SNR = (1, 5, 9) dB with the presented CS-AF area selection (Γ^+ , Λ^+) for the signals $z_{\text{SINLFM}}(t)$ and $z_{\text{LFM}}(t)$.

$z_{\text{SINLFM}}(t)$						
	Accuracy	Specificity	Precision	Recall	F1	F-norm
1 dB	0.9350	0.9693	0.2657	0.3080	0.2853	180.1487
5 dB	0.9779	0.9860	0.7078	0.7881	0.7458	39.6697
9 dB	0.9830	0.9907	0.7871	0.8024	0.7947	21.1121
$z_{\text{LFM}}(t)$						
	Accuracy	Specificity	Precision	Recall	F1	F-norm
1 dB	0.9860	0.9769	0.2925	0.3806	0.3308	98.5656
5 dB	0.9940	0.9966	0.7720	0.8133	0.7921	10.1888
9 dB	0.9948	0.9973	0.8135	0.8223	0.8179	6.2356

5.3 Summary

In this chapter, two methods have been introduced with the objective of augmenting the performance of sparse TFD reconstruction have been presented. The primary method involves using the shrinkage operator instead of the thresholding operator in the TwIST algorithm, which uses information from localized Rényi entropies to preserve auto-terms while reconstructing high-resolution TFDs. The obtained results have shown that the here-presented RTwIST algorithm outperforms all considered reconstruction algorithms with respect to the performance measures proposed in Chapter 4, providing high-resolution reconstructed TFD with high auto-term preservation for a wide range of signals (ensured with the inclusion of both, the STRE and NBRE). Furthermore, noise tests have revealed that the RTwIST method follows the noise sensitivity of the STRE and NBRE methods. The second method presents the extraction of the magnitude-significant auto-term-related

samples from the AF by using two independent parameters and the AF segmentation defined using the original CS-AF area from the literature. The obtained results show that the presented CS-AF area is able to reject unwanted AF samples within the rectangular CS-AF segment, and include auto-term-related samples from the rest of the AF with an arbitrary shape. This has led to an improvement in the performance of the reconstructed TFDs. Moreover, the presented CS-AF area has been used in conjunction with the reconstruction algorithms to further increase reconstructed TFDs' performance in the existence of noise, as confirmed by the obtained results in this chapter.

CHAPTER 6

PERFORMANCE CRITERIA FOR TIME-FREQUENCY DISTRIBUTIONS BASED ON THE INSTANTANEOUS FREQUENCY AND GROUP DELAY ESTIMATION

This chapter focuses on the development of performance measure criteria for evaluating the quality of auto-term consistency, resolution, and cross-term suppression in the 2-D TF plane based on estimated IFs and GDs. It also introduces a technique for automatic component alignment preference towards the time or frequency axis, due to the unsuitability of localization in time slices with IF estimation for certain signals. The chapter explains how component alignment information is utilized in component extraction from TFD, combined IF and GD estimation strategy, and modification of the RTwIST algorithm. The presented methods are evaluated on synthetic and real-life gravitational signals with and without noise used throughout the dissertation, and the results of the combined IF and GD estimation are compared to the IF estimation alone. Additionally, the performance measure presented is compared to the 1-D measure based on the LRE, presented in Chapter 4. The research presented in this chapter has been published by the author in the international peer-reviewed journal [57].

6.1 Component Alignment Towards Time or Frequency Axis Detection Using the Local Rényi Entropy

In this section, a method is presented for automatically detecting TFD regions that require a specific localization approach in either time or frequency slices. The detection of these TFD regions is accomplished by utilizing the STRE and NBRE methods. This method leverages the estimation errors obtained when applying these techniques to signal components that deviate from their reference components. By exploiting the resulting raise in the local number of components, it becomes possible to identify TFD regions where a different localization approach is needed.

To determine the most suitable localization approach for a previously detected TFD region, the quality of IF and GD estimations is evaluated using the N_r measure. It has been noticed that an inappropriate localization approach results in discontinuous IF or GD estimations and the addition of irrelevant samples to the auto-terms, which increases the N_r value. To illustrate the method's steps, a synthetic signal denoted as $z_{\text{mix}}(t)$ is employed. This signal is generated with $N_t = 256$ samples and comprises two constant FM components and four non-LFM components. These components exhibit diverse directions and have distinct time and frequency supports.

The presented method involves the following steps:

1. First, the algorithm generates two TFDS by applying the shrinkage operator, presented in the previous chapter, to an input TFD as follows [57]:

$$\rho^t(t, f) = \text{shrink}_t\{\rho(t, f)\}\big|_{\delta_t=1}, \quad \rho^f(t, f) = \text{shrink}_f\{\rho(t, f)\}\big|_{\delta_f=1}, \quad (6.1)$$

where $\rho^t(t, f)$ and $\rho^f(t, f)$ denote the shrunken TFDS using time and frequency slices, respectively. By setting $\delta_t = \delta_f = 1$, only the local maxima of signal components (in the amount detected by the STRE and NBRE) are left in $\rho^t(t, f)$ and $\rho^f(t, f)$, which define estimated IFs and GDs (or ridges) of signal components, respectively.

Figure 6.1 depicts the signal's LO-ADTFD and its shrunken TFDS, $\rho_{(lo)}^f(t, f)$ and $\rho_{(lo)}^t(t, f)$. Observe that the acquired $\rho_{(lo)}^f(t, f)$ and $\rho_{(lo)}^t(t, f)$ manifest dissimilarities in the precision of signal component estimation. Notably, Figure 6.1b vividly illustrates fragmented non-LFM components within $\rho_{(lo)}^t(t, f)$, where their alignment diverges from the t axis. Figure 6.1c for $\rho_{(lo)}^f(t, f)$ demonstrates the same phenomenon, but with opposite outcomes. Now, the same non-LFM components whose alignment diverges from the time axis exhibit better preservation than constant FM components that are completely coaxial with the t axis.

2. In this step, the quantities $N_r\{\rho^t(t, f)\}$ and $N_r\{\rho^f(t, f)\}$ are computed. If $N_r\{\rho^t(t, f)\} \leq N_r\{\rho^f(t, f)\}$, it is inferred that the signal components are predominantly aligned

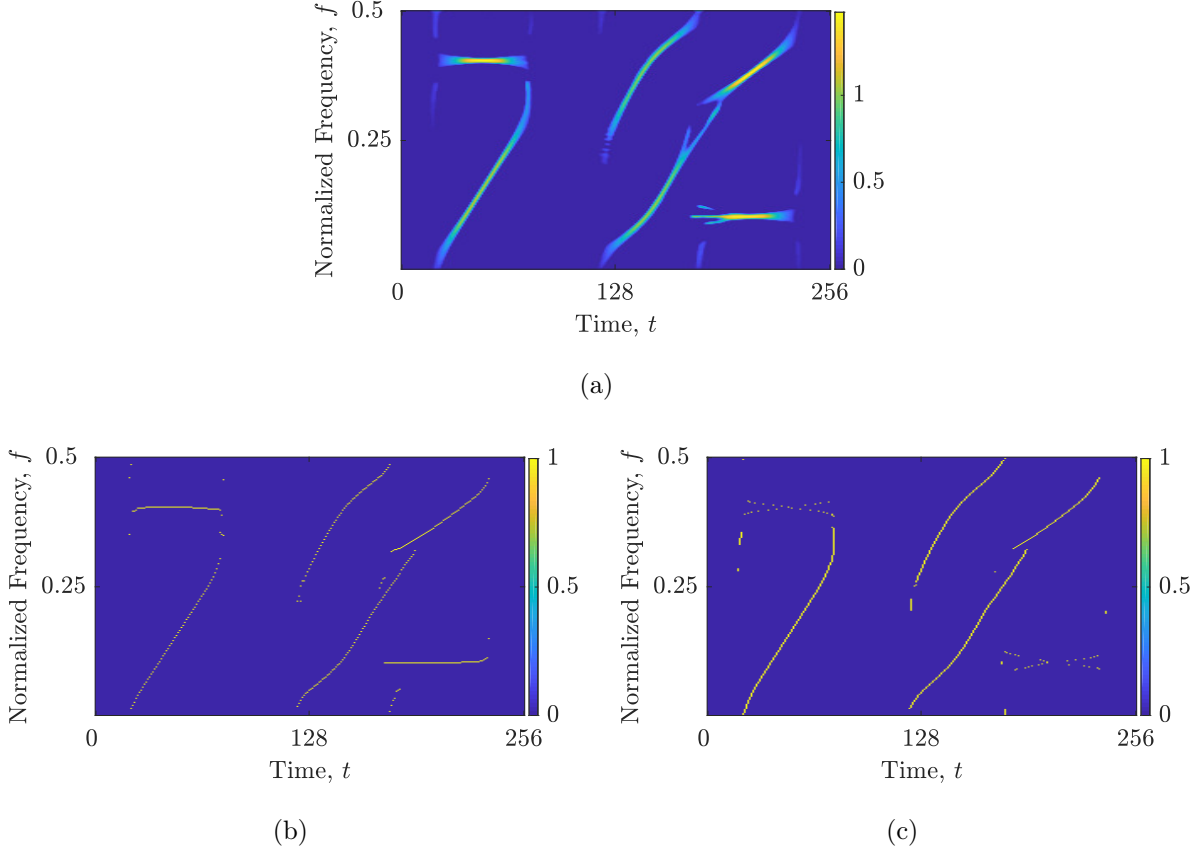


Figure 6.1 Considering the signal $z_{\text{mix}}(t)$: (a) $\rho_{(l_0)}(t, f)$; (b) the estimated IFs (yellow) in $\rho_{(l_0)}^t(t, f)$; (c) the estimated GDs (yellow) in $\rho_{(l_0)}^f(t, f)$.

with the time axis globally. Consequently, the component alignment map, denoted as $C_M(t, f)$, is generated with values of one. Moreover, the local behavior of components is examined using the STRE method. Likewise, if $N_r\{\rho^t(t, f)\} > N_r\{\rho^f(t, f)\}$, the $C_M(t, f)$ is generated with zeros, and the initial localization approach is determined utilizing the NBRE technique with $NC_f(f)$.

3. The $NC_t(t)$ or $NC_f(f)$ is examined to identify any prominent localized maxima that may reveal an unsatisfactory component alignment for the considered NBRE or STRE method. The identification of all localized maxima saturated in $NC_t(t)$ (or $NC_f(f)$) is performed, and the distinction in the number of local components, symbolized as ΔNC , among the inspected maximum and the adjacent minima on both sides is computed. Intervals with $\Delta NC \geq 1.50$ are classified as "suspicious" and necessitate further investigation. In this dissertation, ΔNC value has been set to 1.50 because it is desired that the algorithm recognizes components that diverge significantly from the respective time or frequency axis compared to a reference LFM component, which has a normalized frequency starting at 0 and stopping at 0.5. This reference LFM component is deemed reasonably suitable for both the STRE and NBRE approaches with $\frac{1}{N_t} \sum_{t=1}^{N_t} NC_t(t) \cong \frac{1}{N_f} \sum_{f=1}^{N_f} NC_f(f) \cong 1.48$. If every

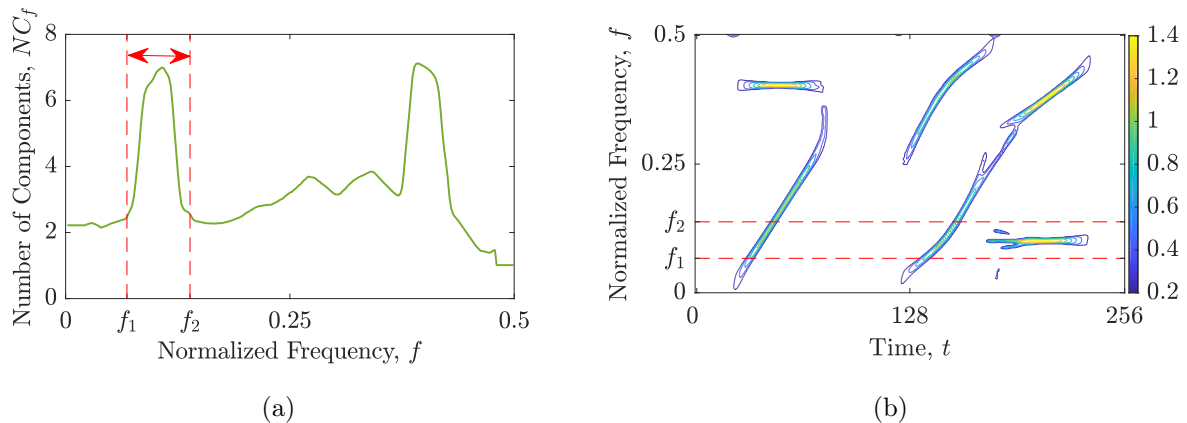


Figure 6.2 Considering the signal $z_{\text{mix}}(t)$: (a) the local number of components, $NC_f(f)$; (b) LO-ADTFD. The red dashed lines delineate the initial segment $[f_1, f_2]$ chosen from $NC_f(f)$, where a substantial augmentation in $NC_f(f)$ is observed.

$\Delta NC < 1.50$, the algorithm terminates, and the $C_M(t, f)$ containing only ones or zeros is output. If not, the algorithm advances to the following step.

4. The algorithm identifies a contiguous segment from $NC_t(t)$ (or $NC_f(f)$) based on the presence of local minima satisfying the condition $\Delta NC \geq 1.50$. Figure 6.2a showcases an instance of $NC_f(f)$ for the signal $z_{\text{mix}}(t)$, in which the initial division is pointed out by red dashed lines at the frequency bins f_1 and f_2 . Subsequently, a TFD is partitioned with the same division, in which an inappropriate component for the present localization procedure can exist. An exemplification of this scenario is presented in Figure 6.2b, displaying $\rho_{(lo)}(t, f)$ with the segment confined by the previously identified f_1 and f_2 , where the constant FM component necessitates further detection in the subsequent steps of the algorithm.
5. In this step, an additional localization process takes place within the extracted TFD by calculating the opposite LRE used in the previous step, i.e., $NC_f(f)$ if $N_r\{\rho^t(t, f)\} \leq N_r\{\rho^f(t, f)\}$, or $NC_t(t)$ if $N_r\{\rho^t(t, f)\} > N_r\{\rho^f(t, f)\}$. The protocol follows a similar approach as the preceding steps. Firstly, all localized minima and maxima with discrepancies in the number of components exceeding the ΔNC of 1.50 are identified. Subsequently, segments satisfying the condition $\Delta NC \geq 1.50$ are detected, delineating 2-D TF regions within $\rho^f(t, f)$ and $\rho^t(t, f)$ which are questioned based on the N_r value. If a TF block within $\rho^t(t, f)$ exhibits lower N_r value than in $\rho^f(t, f)$, it indicates that the localization in time slices is more appropriate, and the corresponding $C_M(t, f)$ positions are set to 1. All estimated signal components within minima with $\Delta NC < 1.50$ are considered to pertain to the present localization approach, and the relevant TFD blocks within the output $C_M(t, f)$ experience a change in values $0 \leftrightarrow 1$. Lastly, a comparison is made between the N_r values obtained

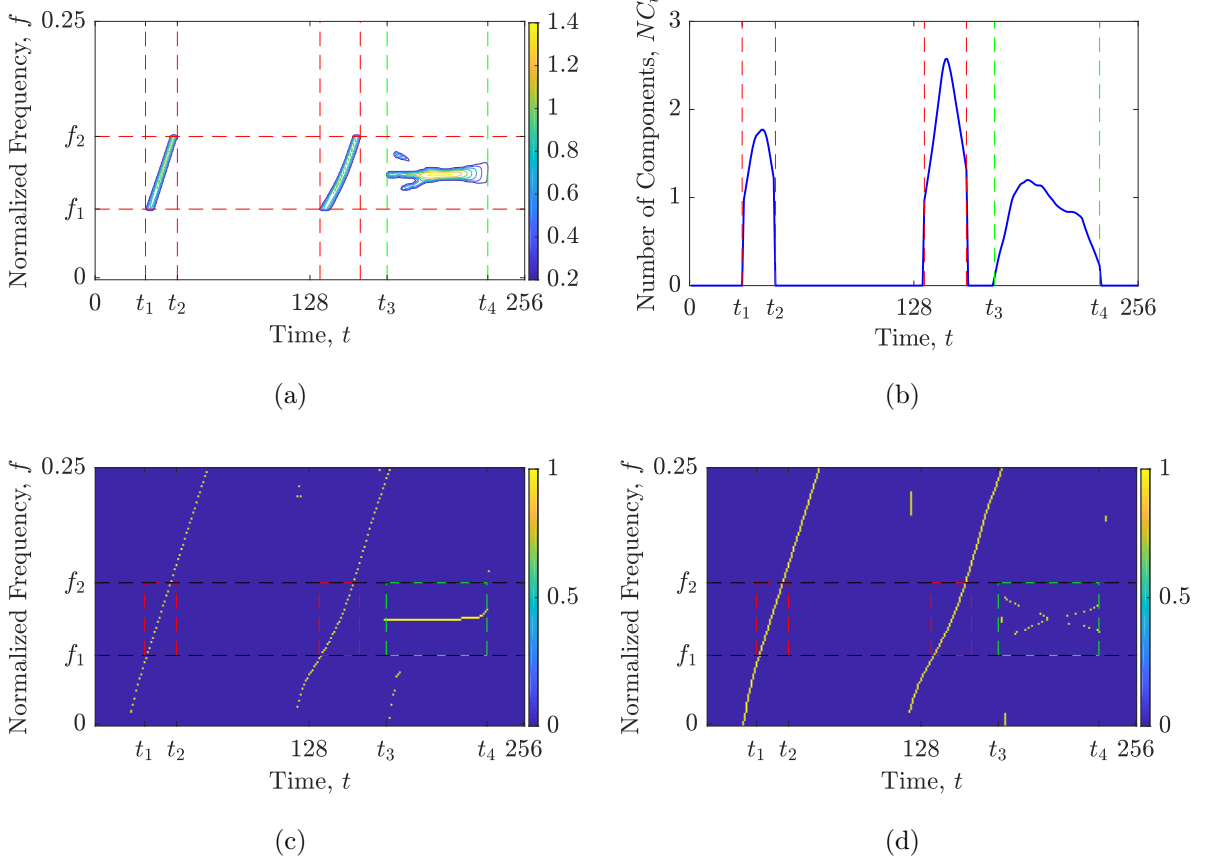


Figure 6.3 Considering the signal $z_{\text{mix}}(t)$: (a) detected components in extracted LO-ADTFD; (b) the $NC_t(t)$ calculated on extracted LO-ADTFD; (c) $\rho_{(lo)}^t(t, f)$; (d) $\rho_{(lo)}^f(t, f)$. Detected segments, evaluated using the N_r measure in $\rho_{(lo)}^t(t, f)$ and $\rho_{(lo)}^f(t, f)$, are indicated by red dashed lines. A segment that contains components suitable for the current time localization approach is highlighted by green dashed lines.

from $\rho^t(t, f)$ and $\rho^f(t, f)$ for samples where no component has been uncovered. Based on this comparison, the $C_M(t, f)$ is assigned a value of 0 or 1, depending on the lower N_r .

This step is demonstrated in Figure 6.3. First, Figure 6.3a depicts the extracted TFD segment bounded in range $[f_1, f_2]$ on which an opposite LRE approach, in this case the STRE, is applied to obtain the $NC_t(t)$, as depicted in Figure 6.3b. Note that the extracted segment from LO-ADTFD with red dashed lines utilizing the $NC_t(t)$ defines a TFD region $(t_1 : t_2, f_1 : f_2)$ of interest in $\rho_{(lo)}^t(t, f)$ and $\rho_{(lo)}^f(t, f)$ depicted in Figures 6.3c and 6.3d, respectively. It is evident that the estimated GDs within the TFD regions enclosed by the red dashed lines exhibit better connectivity compared to the estimated IFs, which leads to the fact that the $C_M(t_1 : t_2, f_1 : f_2)$ does not change the initial values from zero. Conversely, the constant FM component identified within the region marked by the green dashed lines does not introduce discrepancies in the calculation of $NC_t(t)$, as evident from Figure 6.3b, thus, $C_M(t_3 : t_4, f_1 : f_2) = 1$.

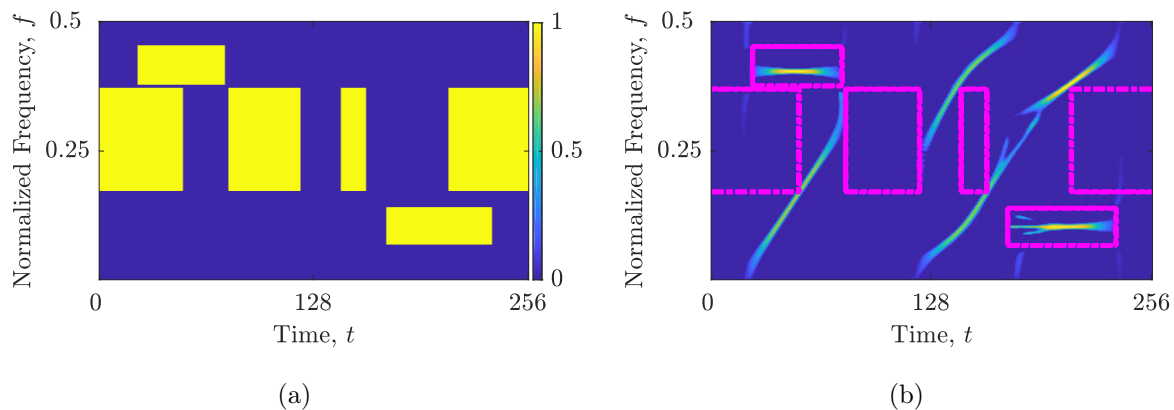


Figure 6.4 Considering the signal $z_{\text{mix}}(t)$: (a) $C_M(t, f)$; (b) LO-ADTFD with $C_M(t, f)$. The yellow and dash-dotted pink rectangles highlight the specific regions within the TFD that are suitable for analysis using time slices. The remaining portion of the TFD, indicated by the blue color, should be analyzed using frequency slices.

6. The preceding two steps are repeated for all identified segments in the input $NC_t(t)$ (or $NC_f(f)$), that is, until all ΔNC are analyzed. The output of the presented algorithm is the binary map $C_M(t, f)$. This map consists of ones and zeros, serving as indicators to identify the regions within the TFD that are suitable for either a time or frequency localization approach, respectively.

Finally, Figure 6.4 shows that both constant FM components are effectively labeled in the obtained $C_M(t, f)$ for the time localization approach. Furthermore, the presented method has been utilized on a real-life gravitational signal $z_{\text{grav}}(t)$ with a characteristic hyperbolic component that is vertical to both time and frequency axes. The results show that separate IF and GD estimations exhibit significant inaccuracies when the signal's component is completely vertical to the applied localization approach, as shown in Figures 6.5a and 6.5b. Despite these challenges, Figures 6.5c and 6.5d demonstrate that the presented method successfully detects appropriate localization approaches for certain component parts.

6.1.1 Component Extraction and Estimation of the Local Number of Components

The resulting $C_M(t, f)$ supplies the means to retrieve signal components from the TFD. This process does not necessitate the extraction of each component separately, but rather entails the identification of components in two sets: one set determined for localization via time slices, and another set determined for localization via frequency slices. This can be easily achieved by element-wise multiplication between the $C_M(t, f)$ and the TFD. For which purpose, η operator is introduced in two distinct forms. Precisely, by employing

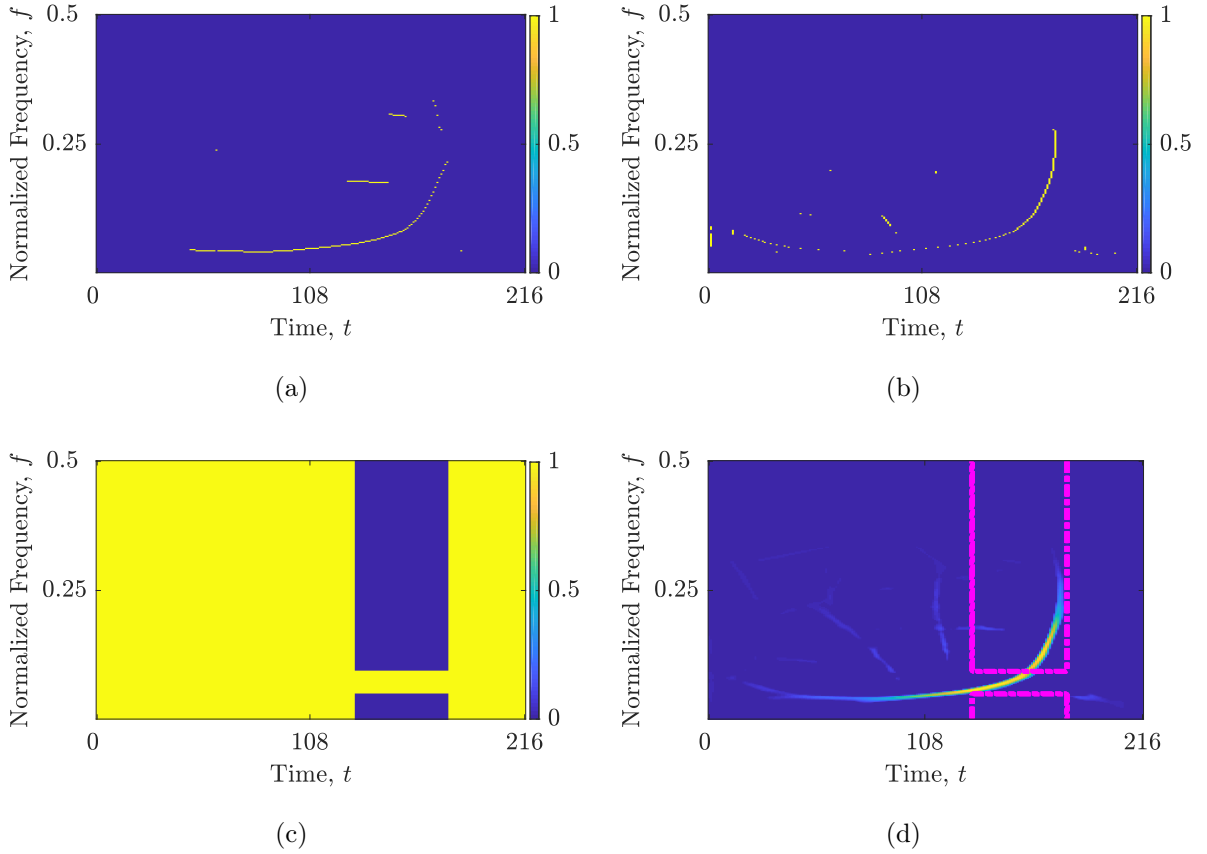


Figure 6.5 Considering the real-life gravitational signal $z_{\text{grav}}(t)$: (a) $\rho_{(lo)}^t(t, f)$; (b) $\rho_{(lo)}^f(t, f)$; (c) $C_M(t, f)$; (d) LO-ADTFD with $C_M(t, f)$. The yellow and dashed red rectangles highlight the specific regions within the TFD that are suitable for analysis using time slices. In contrast, the remaining portion of the TFD, indicated by the blue color, should be analyzed using frequency slices.

the operator η_t , it becomes possible to deduce the signal components that align with the localization procedure through time slices [57]:

$$\eta_t\{\rho(t, f)\} = \begin{cases} \rho(t, f), & C_M(t, f) = 1, \\ 0, & C_M(t, f) = 0, \end{cases} \quad (6.2)$$

where the multiplication of the $C_M(t, f)$ map and the TFD retains those TF blocks that are represented by ones in $C_M(t, f)$. In a similar way, the TFD blocks defined by zeros in $C_M(t, f)$ may be preserved utilizing the operator η_f [57]:

$$\eta_f\{\rho(t, f)\} = \begin{cases} \rho(t, f), & C_M(t, f) = 0, \\ 0, & C_M(t, f) = 1. \end{cases} \quad (6.3)$$

As a result, if $\min\{C_M(t, f)\} = 0$ and $\max\{C_M(t, f)\} = 1$, the considered TFD can be divided into two TFDs: $\eta_f\{\rho(t, f)\}$ and $\eta_t\{\rho(t, f)\}$. These TFDs encapsulate the signal

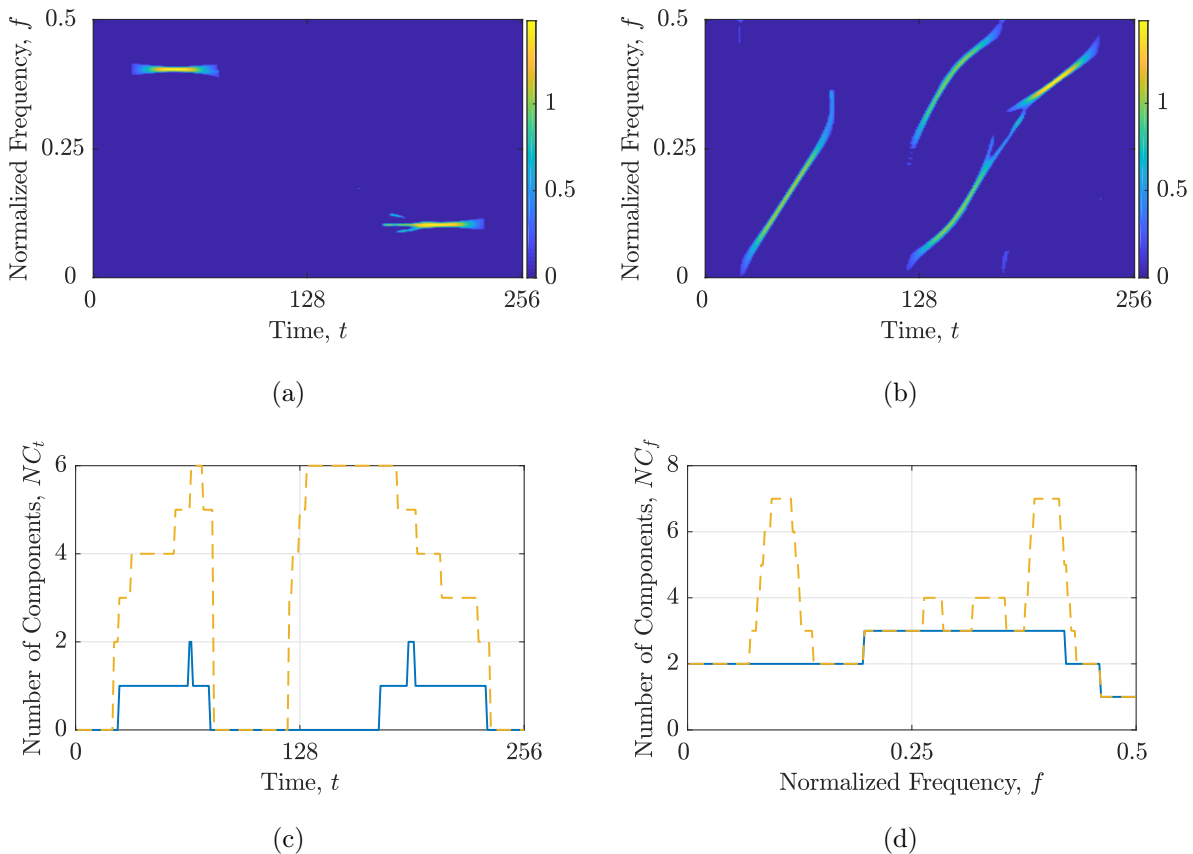


Figure 6.6 Considering the signal $z_{\text{mix}}(t)$: (a) $\eta_t\{\rho_{(lo)}(t, f)\}$; (b) $\eta_f\{\rho_{(lo)}(t, f)\}$; (c) the $NC_t(t)$ estimates obtained utilizing the STRE in starting TFD and $\eta_t\{\rho_{(lo)}(t, f)\}$; (d) the $NC_f(f)$ estimates obtained utilizing the NBRE in starting TFD and $\eta_f\{\rho_{(lo)}(t, f)\}$. The estimates are represented with yellow dashed lines for starting TFD, and blue solid lines for $\eta_t\{\rho_{(lo)}(t, f)\}$ and $\eta_f\{\rho_{(lo)}(t, f)\}$.

components that align with the chosen localization approaches through time slices and frequency bins, respectively. By employing these TFDS, a more precise assessment of the local number of components can be achieved utilizing the NBRE and STRE, respectively. This refined estimation is anticipated to yield superior accuracy compared to the initial TFD-based estimates. The outcomes obtained by employing the operators η_t and η_f to the signals' $z_{\text{mix}}(t)$ and $z_{\text{grav}}(t)$ LO-ADTFDs are shown in Figures 6.6 and 6.7.

First, we may observe that $\eta_t\{\rho_{(lo)}(t, f)\}$ and $\eta_f\{\rho_{(lo)}(t, f)\}$ contain appropriate components for the considered localization approach for the signal $z_{\text{mix}}(t)$ (shown in Figures 6.6a and 6.6b) or component parts for the signal $z_{\text{grav}}(t)$ (shown in Figures 6.7a and 6.7b). This is also validated by the $NC_t(t)$ and $NC_f(f)$ calculations in $\eta_t\{\rho_{(lo)}(t, f)\}$ and $\eta_f\{\rho_{(lo)}(t, f)\}$, which exhibit minimal occurrence of erroneous local maxima, and are overall significantly more accurate than the estimations in the starting TFD, as shown in Figures 6.6c and 6.6d for the signal $z_{\text{mix}}(t)$, and 6.7c and 6.7d for the signal $z_{\text{grav}}(t)$. It is imperative to acknowledge that the updated assessments of the local number of

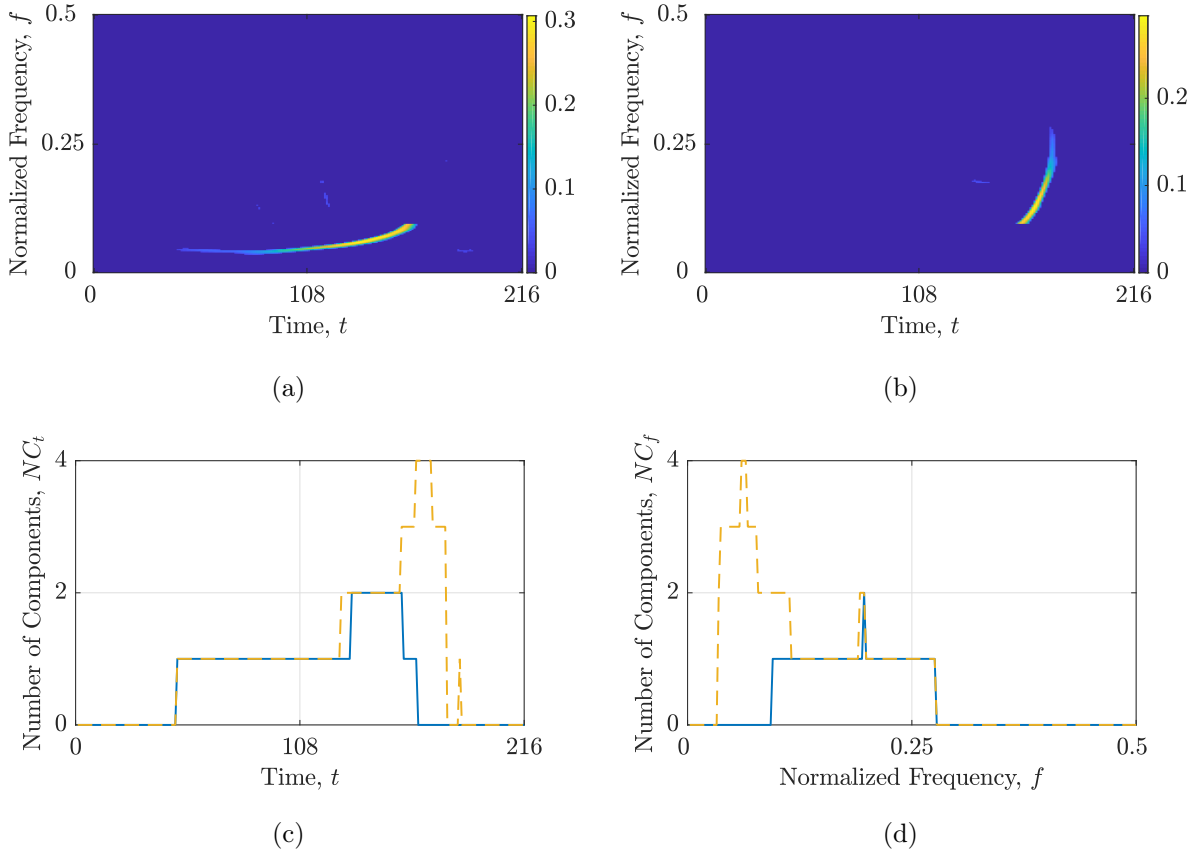


Figure 6.7 Considering the signal $z_{\text{grav}}(t)$: (a) $\eta_t\{\rho_{(lo)}(t, f)\}$; (b) $\eta_f\{\rho_{(lo)}(t, f)\}$; (c) the $NC_t(t)$ estimates obtained utilizing the STRE in starting TFD and $\eta_t\{\rho_{(lo)}(t, f)\}$; (d) the $NC_f(f)$ estimates obtained utilizing the NBRE in starting TFD and $\eta_f\{\rho_{(lo)}(t, f)\}$. The estimates are represented with red dashed lines for starting TFD, and blue solid lines for $\eta_t\{\rho_{(lo)}(t, f)\}$ and $\eta_f\{\rho_{(lo)}(t, f)\}$.

components need to be interpreted in conjunction with the $C_M(t, f)$ map, as they pertain exclusively to specific TFD regions demarcated by $C_M(t, f)$ rather than encompassing the entirety of the TFD. Also, throughout this chapter and subsequent analyses, the calculations of the LRE have been performed using the LO-ADTFD as the underlying TFD. This decision aligns with the adoption of LO-ADTFD for the calculation of the $C_M(t, f)$ and its subsequent applications throughout the remainder of this chapter.

6.2 Strategy for Mutual Estimation of Instantaneous Frequency and Group Delay

The presented $C_M(t, f)$ map is used to estimate TFD ridges in this section. As previously demonstrated, one possible way to estimate the IFs and GDs of a signal is by employing the operator $\text{shrink}_{t,f}\{\cdot\}$ and considering only local maxima (by setting the parameters $\delta_t = 1$ or $\delta_f = 1$) in (6.1). The binary TFD, denoted as $B^{(\text{shrink})}(t, f)$,

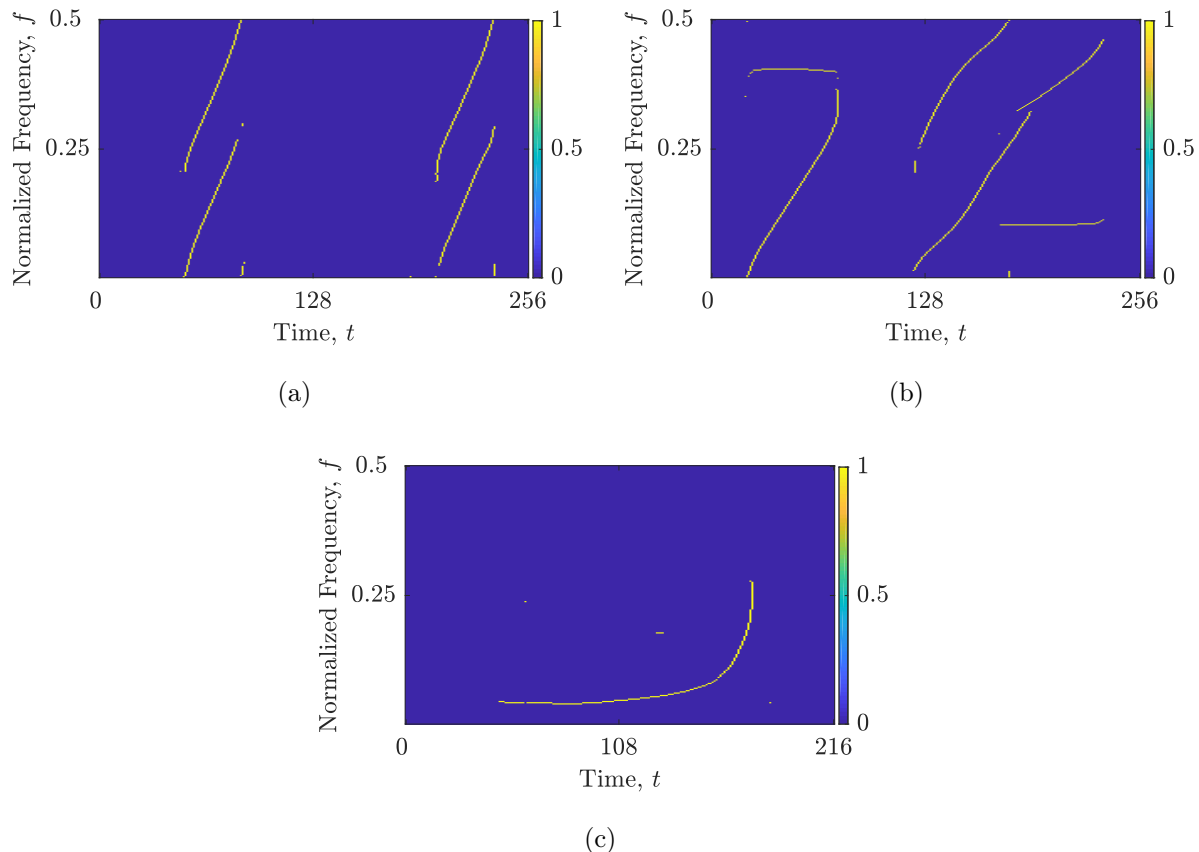


Figure 6.8 $B^{(\text{shrink})}(t, f)$ with IF and GD estimations (in yellow) utilizing the shrinkage operator for the signals: (a) $z_{\text{LFM}}(t)$; (b) $z_{\text{mix}}(t)$; (c) $z_{\text{grav}}(t)$.

which contains estimation of TFD ridges, is therefore accomplished by combining both estimations, $\rho^t(t, f)$ and $\rho^f(t, f)$, together as [57]:

$$B^{(\text{shrink})}(t, f) = \eta_t\{\rho^t(t, f)\} + \eta_f\{\rho^f(t, f)\}, \quad (6.4)$$

where $C_M(t, f)$ determines the TFD regions that will select $\rho^t(t, f)$ or $\rho^f(t, f)$. The $B^{(\text{shrink})}(t, f)$ performance is shown in Figure 6.8 for the signals $z_{\text{LFM}}(t)$, $z_{\text{mix}}(t)$ and $z_{\text{grav}}(t)$. For all signal examples, the estimated component ridges in the TFD are found to exhibit high connectivity and to belong to the signal's true components.

In addition, the $C_M(t, f)$ map has been utilized to improve the considered IF estimation methods. Specifically, IF estimation algorithms that make efficient use of the STRE method are considered for the purposes of this dissertation. Knowing the number of components and the time support related with each component provides a significant competitive advantage over algorithms that do not use this information and, as a result, require significantly more user input. Given that the objective is to create an environment that does not require the participation of a user other than a signal, the use of IF estimation algorithms without STRE information is not considered in this dissertation.

6.2.1 Image-Based and Blind Source Separation Instantaneous Frequency Estimation Methods

The initial method employed in this dissertation for estimating the IF is a technique based on image processing, as proposed in [95]. This method utilizes the first and second derivatives to create a binary TFD representation denoted as $B^{(\text{IM})}(t, f)$. In this image, ones represent component crest locations, while zeros the remaining TF points, as follows [95]:

$$B^{(\text{IM})}(t, f) = \begin{cases} 1, & \frac{d}{df}\rho(t, f) = 0 \text{ and } \frac{d^2}{df^2}\rho(t, f) < 0, \\ 0, & \text{otherwise.} \end{cases} \quad (6.5)$$

This stage often produces peaks that are not exclusively associated with the TF ridges of the auto-terms. To extract the IF of signal components, an m -connectivity criterion is applied, which is derived from image processing techniques. In this study, a value of $m = 10$ is employed, as suggested in [14, 95] which specifies a 10-neighborhood for considered point at location (z, q) : $\{(z - 1, q), (z - 1, q - 1), (z - 1, q + 1), (z - 1, q + 2), (z - 1, q - 2), (z + 1, q), (z + 1, q - 1), (z + 1, q + 1), (z + 1, q + 2), (z + 1, q - 2)\}$. In accordance with this criterion, data points positioned below and above the IF curves are disregarded, implying that each signal component is associated with a single frequency value at each time slice [95].

Lastly, it is necessary to establish an optimal threshold for determining the minimum duration of an auto-term in order to provide the resulting TFD, which comprises only components that satisfy the given threshold. In this case, when there is no a priori knowledge of the input signal, the threshold is related to the component time support information obtained from the STRE. The Image-based-STRE method showed high computational efficiency and performance without a need for a priori knowledge about the components' IF laws and amplitude, as shown for real-life signals in [17, 33].

The second approach utilized for IF estimation in the dissertation is the blind source separation (BSS) technique, which is an efficacious procedure for identifying and extracting of components from signals containing multiple sources in the TFD [74]. The expression "blind" indicates that the method is applied without any prior information of the origin or the number of components in the signal mixture, relying solely on the statistical independence assumption among the sources. The version of the method used in this dissertation has been enhanced by the STRE method in [119], namely the BSS-STRE, eliminating the requirement for numerous thresholds needed by the original technique [74]. The BSS method's steps are briefly described as follows.

Initially, the desired TFD of the signal is calculated. From this TFD, the local number of components, $NC_t(t)$, is derived using the STRE method. Then, the method identifies and extracts the most prominent TFD peak at $\rho(t_0, f_0)$, along with its neighboring component

frequency band, $\rho(t_0, f_0 - B_l : f_0 + B_r)$. After the extraction of the component peak and its frequency range, the algorithm sets $\rho(t_0, f_0 - B_l : f_0 + B_r) = 0$ and $NC_t(t_0) = NC_t(t_0) - 1$. Following that, two new subregions are defined in both directions around t_0 as $(t_0 - 1, f_0 - B_l : f_0 + B_r)$ and $(t_0 + 1, f_0 - B_l : f_0 + B_r)$, followed by the most prominent peak identification in both of them. The described bidirectional methodology is iteratively executed until the edges of the component are reached, detected by the $|NC'_t(t)| \neq 0$. If there are any remaining components in the TFD, the previous steps are reiterated.

The application of the BSS method yields multiple TFDS, each encompassing a singular retrieved component, out of which the IF of the respective component is estimated as an individual vector. In this dissertation, all estimated IFs are displayed within $B^{(BSS)}(t, f)$ and $B^{(IM)}(t, f)$ binary TFDS. Note that the LO-ADTFD has been used in the considered IF estimation methods, as its superior performance has proven it to be a suitable underlying TFD in numerous IF estimation algorithms [61, 64, 65, 67].

The precision of IF estimation techniques relies heavily on the STRE method. In the case of the Image-based IF estimation method, an incorrect $NC_t(t)$ can result in either a threshold that is too low, causing interference to be classified as a true signal component, or a threshold that is too high, resulting in the rejection of true signal components. Similarly, with the BSS method, an incorrect $NC_t(t)$ may lead to the incorrect detection of component edges, resulting in incomplete extraction of the signal. Moreover, higher values of $NC_t(t)$ will also cause the BSS method to estimate the IF of interference terms.

Furthermore, inappropriate localization leads to estimated IFs that are inconsistent and displaced from the actual ridge of the signal component. This issue is especially challenging for the Image-based method, as the m -connectivity criterion would need to be significantly increased to connect true signal components. However, it is not advisable to raise the m -connectivity criterion as it may result in the connection of interfering terms, as cautioned in previous studies [14, 95].

6.2.2 Method for Automatic Estimation of Instantaneous Frequency and Group Delay

In this dissertation, the above-mentioned limitations are tackled by presenting a method that blindly estimates component ridges in a TFD by simultaneously estimating IF and GD with the information obtained from the STRE and NBRE, respectively. The presented method consists of the following steps [57]:

1. Firstly, the considered TFD is partitioned into two TFDS using the $\eta_t\{\cdot\}$ and $\eta_f\{\cdot\}$ operators to obtain a TFD suitable for IF estimation based on the time slice procedure, denoted as $\eta_t\{\rho(t, f)\}$, and another TFD suitable for GD estimation based on the frequency slice procedure, denoted as $\eta_f\{\rho(t, f)\}$.

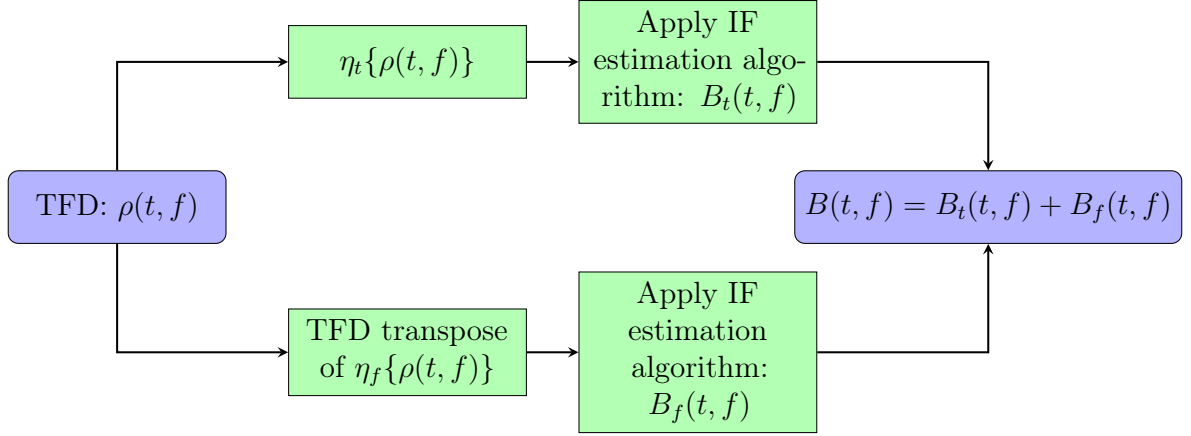


Figure 6.9 A simplified flowchart illustrating the automated estimation of IF and GD for a given TFD.

2. An IF estimation method is then applied to $\eta_t\{\rho(t, f)\}$, resulting in a binary TFD that contains TF ridges of selected components, denoted as $B_t(t, f)$.
3. The discrete version of $\eta_f\{\rho(t, f)\}$ is transposed to enable the use of IF estimation methods that localize in frequency slices and estimate the GD of the remaining components, resulting in a binary TFD, denoted as $B_f(t, f)$.
4. The final binary TFD, denoted as $B(t, f)$, is obtained by summing the IF and GD estimations.

A simplified diagram illustrating the presented method is depicted in Figure 6.9 [57]. The method described above has been incorporated into the existing IF estimation methods, transforming them into IF/GD estimation methods, specifically the BSS-STRE-NBRE and Image-based-STRE-NBRE methods.

6.2.3 Simulation Results

The comparative evaluation of the mutual IF and GD estimation method against the standalone IF estimation approach is performed on three distinct signal: $z_{\text{LFM}}(t)$, $z_{\text{mix}}(t)$, and $z_{\text{grav}}(t)$. The results are depicted in Figures 6.10 and 6.11.

In the case of $z_{\text{LFM}}(t)$, it is observed that the Image-based-STRE method encounters difficulties in establishing connections between TF peaks that exhibit deviations from the time axis. Due to this limitation, all four auto-terms associated with LFM are completely omitted, while interference terms that are almost parallel to the time axis are incorrectly estimated, as illustrated in Figure 6.10a. In contrast, the Image-based-STRE-NBRE method estimates auto-terms with high connectivity, but also interference terms due to imperfect $NC_f(f)$ estimation, as shown in Figure 6.10b. The BSS-STRE method does not have missing components, but produces discontinuous IF estimates that do not belong

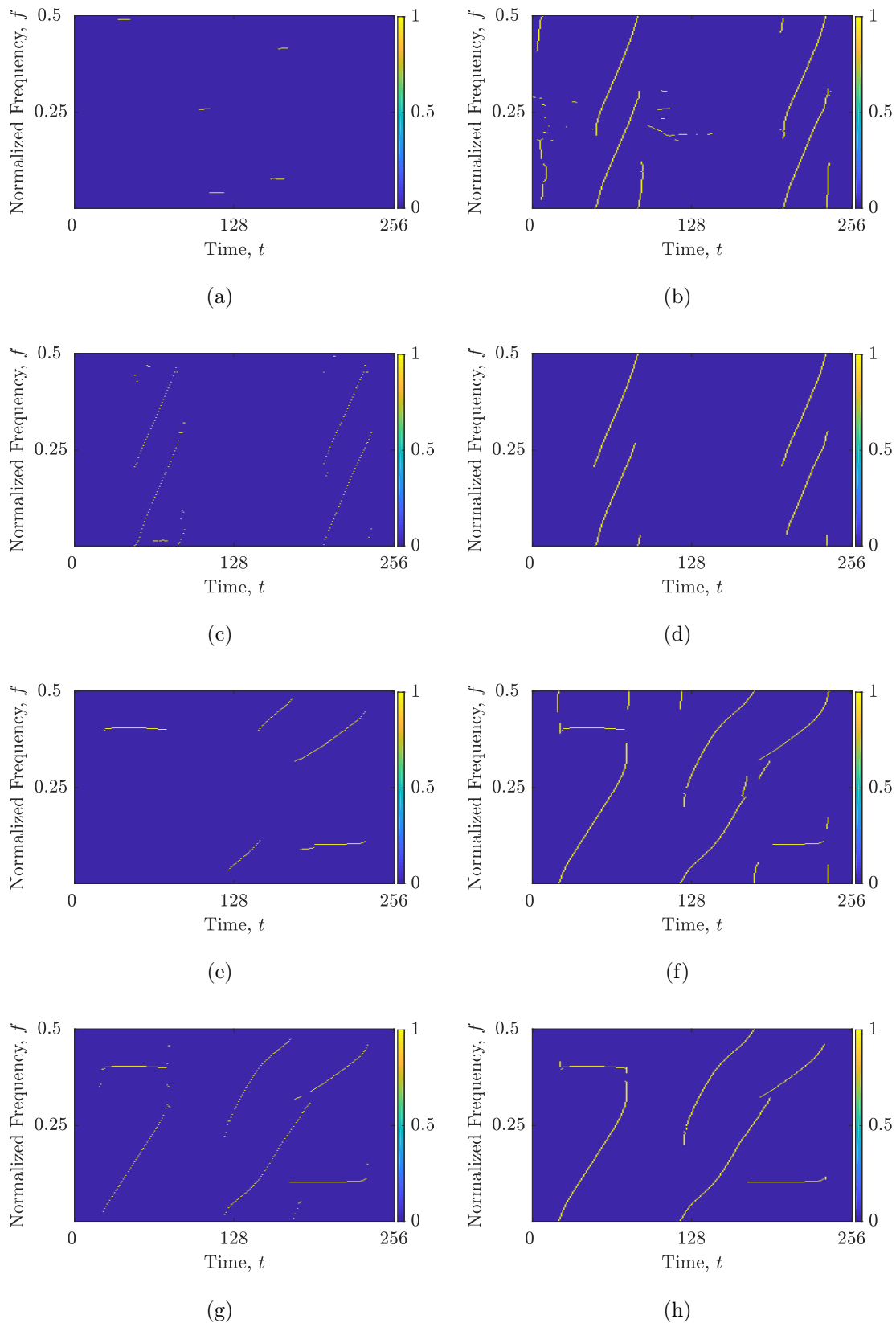


Figure 6.10 IF and GD estimations (in yellow) for the considered signal and method combination: (a) $z_{\text{LFM}}(t)$, the Image-based-STRE; (b) $z_{\text{LFM}}(t)$, the Image-based-STRE-NBRE; (c) $z_{\text{LFM}}(t)$, the BSS-STRE; (d) $z_{\text{LFM}}(t)$, the BSS-STRE-NBRE; (e) $z_{\text{mix}}(t)$, the Image-based-STRE; (f) $z_{\text{mix}}(t)$, the Image-based-STRE-NBRE; (g) $z_{\text{mix}}(t)$, the BSS-STRE; (h) $z_{\text{mix}}(t)$, the BSS-STRE-NBRE.

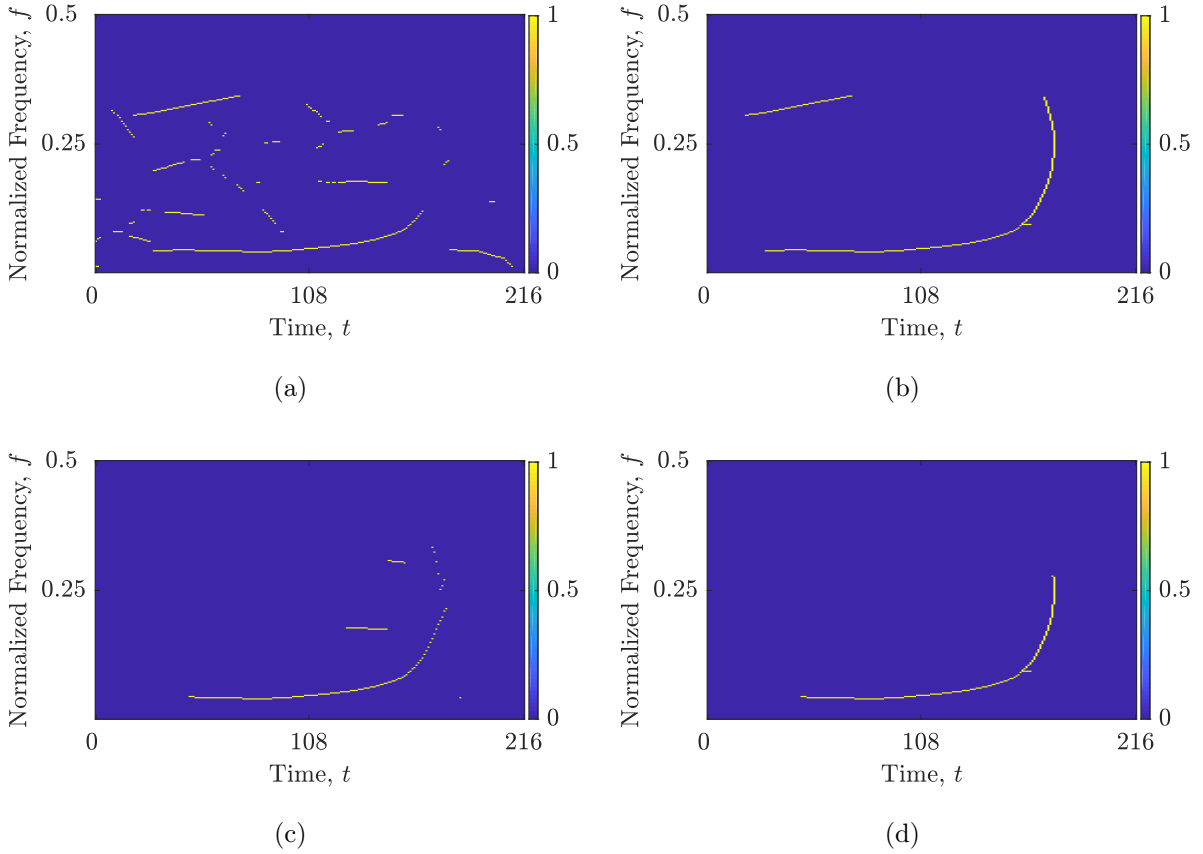


Figure 6.11 IF and GD estimation (in yellow) for the signal $z_{\text{grav}}(t)$ utilizing method: (a) the Image-based-STRE; (b) the Image-based-STRE-NBRE; (c) the BSS-STRE; (d) the BSS-STRE-NBRE.

explicitly to auto-terms, as shown in Figure 6.10c. Figure 6.10d depicts that the mutual IF and GD estimation method provides better auto-term preservation and connectivity.

The same conclusions can be drawn for the signals $z_{\text{mix}}(t)$ and $z_{\text{grav}}(t)$. The Image-based-STRE method misses linking parts or full components that diverge from the time axis and fails to avoid interference samples due to inaccurate $NC_t(t)$, as shown in Figures 6.10e and 6.11a, while the BSS-STRE method produces discontinuous and dislocated estimated IFs, as shown in Figures 6.10g and 6.11c. Again, both methods have been significantly improved by employing combined estimation of IFs and GDs, as shown in Figures 6.10f, 6.10h, 6.11b and 6.11d.

To validate visual observations, the MSE and MAE metrics have been calculated between the local numbers of components in the starting LO-ADTFD and the TFDs with IF and/or GD estimations using (4.4c) and (4.5c). It is assumed that TFDs with discontinuous or missing estimations, as well as those with noise or cross-term-related estimations, would produce larger errors compared to TFDs with continuous and properly-positioned IF and GD estimations. The results given in Table 6.1 show a decrease in the $MSE_{t,f}$ and $MAE_{t,f}$ when mutually estimating IF and GD using the combined STRE

Table 6.1 Comparison of the performance between the mutual IF and GD estimation and the IF estimation for the signals $z_{\text{LFM}}(t)$, $z_{\text{mix}}(t)$ and $z_{\text{grav}}(t)$. Values in bold indicate the best-performing method.

Method	Image-based	Image-based	BSS	BSS	Shrinkage operator
Support information	STRE	STRE and NBRE	STRE	STRE and NBRE	STRE and NBRE
$z_{\text{LFM}}(t)$					
MSE $_{t,f}$	0.2897	0.0425	0.1414	0.0101	0.0107
MAE $_{t,f}$	0.4345	0.1214	0.3002	0.0502	0.0528
$z_{\text{mix}}(t)$					
MSE $_{t,f}$	0.2123	0.0401	0.1301	0.0219	0.0212
MAE $_{t,f}$	0.3925	0.1464	0.3046	0.1064	0.1068
$z_{\text{grav}}(t)$					
MSE $_{t,f}$	0.1260	0.0352	0.0314	0.0129	0.0131
MAE $_{t,f}$	0.2552	0.1123	0.1037	0.0628	0.0635

and NBRE methods with the presented $C_M(t, f)$. Specifically, for the signals $z_{\text{LFM}}(t)$, $z_{\text{mix}}(t)$ and $z_{\text{grav}}(t)$, estimation of the Image-based method is enhanced by 85.33%, 81.11% and 72.06% in terms of MSE $_{t,f}$, and 72.06%, 62.70% and 55.99% in terms of MAE $_{t,f}$, respectively. Equally significant, estimation of the BSS method is enhanced by 92.86%, 83.17% and 58.92% in terms of MSE $_{t,f}$, and 83.82%, 65.07% and 39.44% in terms of MAE $_{t,f}$ for the same signals, respectively.

Furthermore, the findings illustrate that the utilization of the shrinkage operator to derive $B^{(\text{shrink})}(t, f)$ surpasses the BSS-STRE and Image-based-STRE methods' performance. The values of MSE $_{t,f}$ and MAE $_{t,f}$ exhibit improvements of up to 96.31% and 87.85%, respectively, for the signal $z_{\text{LFM}}(t)$, 90.02% and 72.78%, respectively, for the signal $z_{\text{mix}}(t)$, and 89.60% and 75.12%, respectively, for the signal $z_{\text{grav}}(t)$. Furthermore, the findings suggest a close similarity between the derived $B^{(\text{shrink})}(t, f)$ and the $B^{(\text{BSS})}(t, f)$ obtained through the BSS-STRE-NBRE method, with a marginal reduction of 3.20% in MSE $_{t,f}$ for $z_{\text{mix}}(t)$, while the remaining metrics favor the BSS-STRE-NBRE method (up to 5.61%).

Finally, the IF and GD estimation algorithm performances have been tested when embedding the signals $z_{\text{LFM}}(t)$ and $z_{\text{mix}}(t)$ in AWGN with SNR = [0, 10] dB. Figure 6.12 shows the MSE between the $NC_t(t)$ and $NC_f(f)$ for noisy and noise-free signals when using the LO-ADTFD as an underlying TFD for the STRE and NBRE calculation, and it can be observed that the estimations of local numbers of components are stable for SNR > 1 dB. The trends of the F-norm and F1 metrics are observed in Figures 6.13 and 6.14, evidently showing that the Image-based-STRE-NBRE method exhibits greater susceptibility to noise compared to the BSS-STRE-NBRE and shrinkage operator methods.

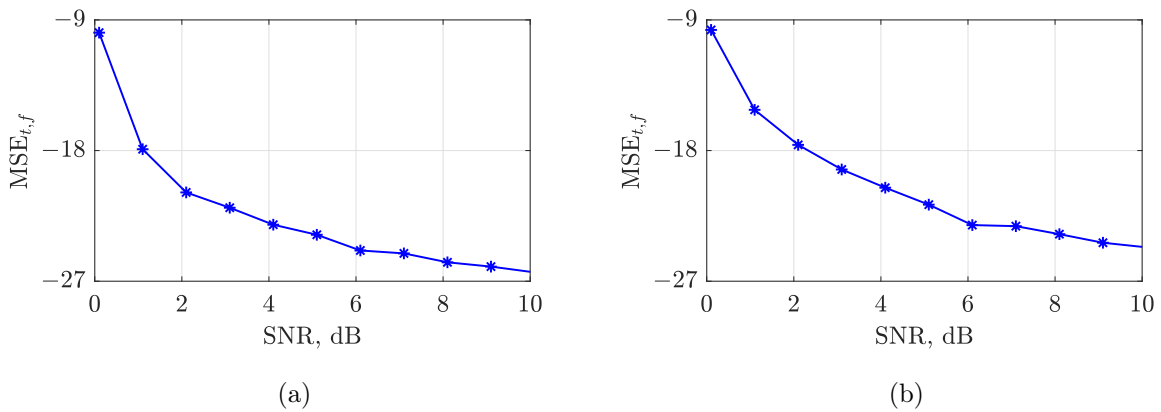


Figure 6.12 The MSE computed between the estimated local number of signal components from noisy and noise-free LO-ADTFDs in AWGN with SNR values ranging from 0 dB to 10 dB for the signals: (a) $z_{\text{LFM}}(t)$; (b) $z_{\text{mix}}(t)$.

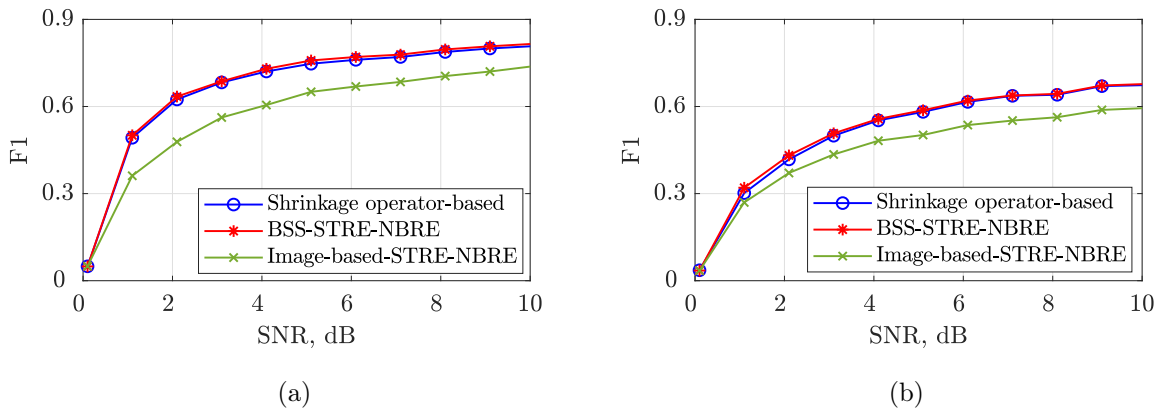


Figure 6.13 F1 values for determining the sensitivity of the considered IF and GD estimation methods to AWGN in SNR values ranging from 0 dB to 10 dB for the signals: (a) $z_{\text{LFM}}(t)$; (b) $z_{\text{mix}}(t)$.

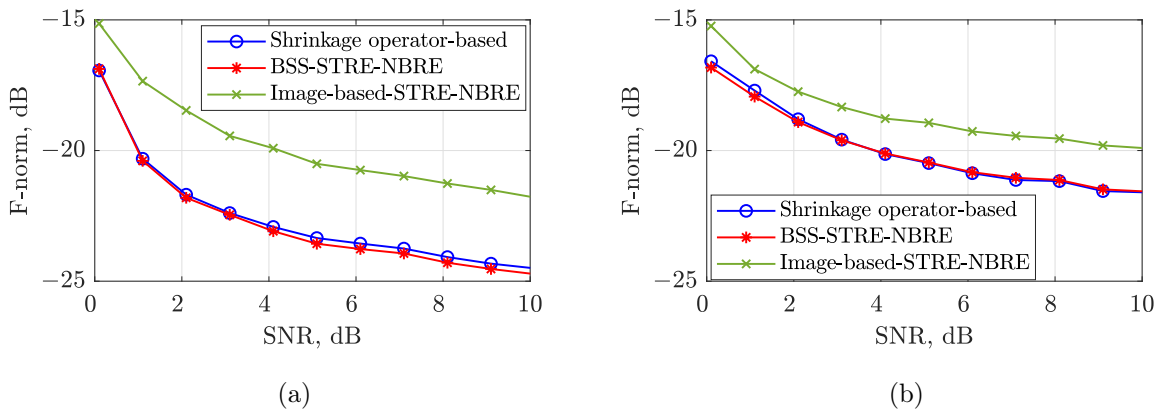


Figure 6.14 F-norm values for determining the sensitivity of the considered IF and GD estimation methods to AWGN in SNR values ranging from 0 dB to 10 dB for the signals: (a) $z_{\text{LFM}}(t)$; (b) $z_{\text{mix}}(t)$.

6.3 Performance Criteria Based on the Instantaneous Frequency and Group Delay Estimation

In this section, performance criteria for measuring TFDS based on estimated IFs and GDs are presented. While MSE metrics based on the LRE method utilize two 1-D information sources (the STRE and NBRE), this approach utilizes 2-D information, which enables precise identification of signal auto-terms in the 2-D TF plane. The criterion is based on the following requirements for a high-performing TFD:

- Preservation of signal auto-terms throughout the TFD, such that their peaks accurately reflect the IF law.
- High resolution of signal auto-terms.
- Absence of energy terms related to cross-terms or noise.

To assess each TFD requirement individually, the IF/GD-based measure is presented, denoted as χ , which is decomposed into three distinct components, denoted as χ_{at} , χ_r , and χ_{ct} . The first component, χ_{at} , evaluates the quality of auto-term preservation in a TFD. Each estimated IF and GD is examined in turn, searching for a signal component that is present within an interval surrounding the estimated IF or GD. The measure penalizes any instance where a signal component is not detected within this interval. The second component, χ_r , evaluates the quality of auto-term resolution. Specifically, it quantifies the width of the detected auto-term's main lobe. The third component, χ_{ct} , evaluates the quality of cross-term suppression by measuring the number of samples unrelated to auto-terms. The steps of this measure are as follows:

1. Initialize the measure components χ_{at} and χ_r to zero: $\chi_{at} = \chi_r = 0$.
2. For each estimated IF point (t_{i_n}, f_{i_n}) of the n -th signal component in the bounded region $B(t, f)$, where $C_M(t, f) = 1$, the frequency f_{m_n} is determined as the first local maximum in the TFD within the frequency range $[f_{i_n} - \Delta_\chi, f_{i_n} + \Delta_\chi]$ that is closest to f_{i_n} :

$$f_{m_n} = \arg \max_{f_{k_n}} \rho(t_{i_n}, f_{k_n}), f_{i_n} - \Delta_\chi \leq f_{k_n} \leq f_{i_n} + \Delta_\chi, \quad (6.6)$$

where Δ_χ represents the maximum allowable range defined by the user, in which a non-negative value in the TFD is considered as auto-term.

3. If no positive maximum is detected, one is added to the χ_{at} measure component to penalize it, $\chi_{at} = \chi_{at} + 1$, and steps 4 and 5 are skipped. Otherwise, the distance between (t_{i_n}, f_{i_n}) and f_{m_n} is calculated using a Gaussian function:

$$D_\chi(t_{i_n}, f_{i_n}) = 1 - \exp\left(-\frac{(f_{i_n} - f_{m_n})^2}{2\sigma_G^2}\right), \quad (6.7)$$

where σ_G is the tuning parameter that controls the width of the Gaussian function, and $D_\chi(t, f)$ is the TFD containing distance values at the positions of estimated IFs and GDs. Add $D_\chi(t_{i_n}, f_{i_n})$ to the χ_{at} measure component: $\chi_{at} = \chi_{at} + D_\chi(t_{i_n}, f_{i_n})$.

4. Locate frequency bins denoted with f_{l_n} and f_{r_n} to the left and right from the observed auto-term maximum at which its amplitude is equal to $\sqrt{2}/2$ of the maximum value and calculate its resolution as $R_\chi(t_{i_n}, f_{i_n}) = \frac{|f_{l_n} - f_{r_n}|}{N_f}$, where $R_\chi(t, f)$ denotes the TFD with resolution values at the positions of estimated IFs and GDs. Add $R_\chi(t_{i_n}, f_{i_n})$ to the χ_r measure component: $\chi_r = \chi_r + R_\chi(t_{i_n}, f_{i_n})$.
5. Remove the considered component from TFD around the detected auto-term maximum $\rho(t_{i_n}, f_{m_n})$.
6. Perform the same procedure for each estimated GD point (t_{j_n}, f_{j_n}) of the n -th component in $B(t, f)$ determined with $C_M(t, f) = 0$. That is, define t_{m_n} as the time of the first local maximum in TFD within the time range $[t_{j_n} - \Delta_\chi, t_{j_n} + \Delta_\chi]$ closest to the time t_{i_n} :

$$t_{m_n} = \arg \max_{t_{k_n}} \rho(t_{k_n}, f_{j_n}), t_{j_n} - \Delta_\chi \leq t_{k_n} \leq t_{j_n} + \Delta_\chi. \quad (6.8)$$

7. If no positive maximum is detected, penalize it by adding one to the χ_{at} measure component, $\chi_{at} = \chi_{at} + 1$, and steps 8 and 9 are skipped. Otherwise, calculate the distance between (t_{j_n}, f_{j_n}) and t_{m_n} using a Gaussian function:

$$D_\chi(t_{j_n}, f_{j_n}) = 1 - \exp\left(-\frac{(t_{j_n} - t_{m_n})^2}{2\sigma_G^2}\right), \quad (6.9)$$

and add $D_\chi(t_{j_n}, f_{j_n})$ to the χ_{at} measure component: $\chi_{at} = \chi_{at} + D_\chi(t_{j_n}, f_{j_n})$.

8. Locate time samples denoted with t_{l_n} and t_{r_n} to the left and right from the observed auto-term maximum at which its amplitude is equal to $\sqrt{2}/2$ of the maximum value and calculate its resolution as $R_\chi(t_{j_n}, f_{j_n}) = \frac{|t_{l_n} - t_{r_n}|}{N_t}$. Add $R_\chi(t_{j_n}, f_{j_n})$ to the χ_r measure component: $\chi_r = \chi_r + R_\chi(t_{j_n}, f_{j_n})$.
9. Remove the considered component from TFD around the detected auto-term maximum $\rho(t_{m_n}, f_{j_n})$.
10. Normalize the measure components χ_{at} by the total number of estimated IF and GD points in $B(t, f)$, and χ_r by the total number of detected auto-term maxima in $R_\chi(t, f)$ as:

$$\chi_{at} = \frac{\chi_{at}}{\|B(t, f)\|_0}, \quad \chi_r = \frac{\chi_r}{\|R_\chi(t, f)\|_0}. \quad (6.10)$$

11. Since the signal auto-terms were removed from a TFD, the amount of cross-terms is determined by calculating the number of non-zero elements in the remaining TFD, denoted as $\rho^{(\text{cross})}(t, f)$:

$$\chi_{ct} = \frac{1}{N_t N_f} \|\rho^{(\text{cross})}(t, f)\|_0. \quad (6.11)$$

12. The overall quality measure, denoted as χ , is calculated as the weighted sum of the three measure components:

$$\chi = \frac{\chi_{at} + \chi_r + \chi_{ct}}{3}. \quad (6.12)$$

Figure 6.15 illustrates the application of the χ measure to two reconstructed TFDS obtained using the TwIST algorithm given in Section 3.2. For the first oversparse reconstructed TFD with $\lambda = 15$, its time slice representative shown in Figure 6.15a reveals that the sinusoidal component in the vicinity of f_{i_1} is missing, which results in a penalty value of one for the χ measure. The analysis focuses on the resolution, $|f_{l_2} - f_{r_2}|$, and bias, $f_{i_2} - f_{m_2}$, of the detected LFM component with respect to the f_{i_2} . In contrast, the second reconstructed TFD (with $\lambda = 0.1$), contains the sinusoidal component ($f_{m_1} > 0$), as shown in Figure 6.15b. However, both auto-terms exhibit low resolution, which is evident from the larger $|f_{l_2} - f_{r_2}|$ compared to the previous TFD. Additionally, the time slice of this TFD contains a significant number of cross-terms compared to the previous TFD.

In the χ_{at} component, the absence of auto-term components is penalized with a value of one, while for the detected auto-terms, a value close to zero is assigned, which depends on the auto-term bias with respect to the estimated IF or GD. This bias is expected to occur when analyzing different TFDS and noise levels [14], hence the inclusion of the parameter Δ_χ . A too large value of Δ_χ may lead to the detection of multiple maxima, which is why the first maximum closest to the estimated IF or GD is considered to belong to the auto-term. Through extensive simulations focused mainly on sparse reconstructed TFDS, $\Delta_\chi = N_t/8$. The degree of penalization of the bias is controlled by the parameter σ_G of the Gaussian function. A larger value of σ_G results in a wider and flatter curve, while a smaller value results in a narrower and taller curve, indicating a stronger penalization of the bias. In this dissertation, $\sigma_G = 10$. Note that when the auto-term maximum exhibits the exact position of the estimated IF or GD of the n -th component, $D_\chi(t_{i_n}, f_{i_n}) = 0$, indicating no penalization is provided. The χ_{at} component is bounded in the range $[0, 1]$, where smaller values indicate better-performing TFDS.

The χ_r component is intended to evaluate the resolution of the signal's auto-terms in both time and frequency slices. In contrast to previous research that used a normalized instantaneous bandwidth to measure resolution [16], this approach normalizes χ_r with respect to N_t or N_f to provide an interpretable measure with respect to both axes equally. As a result, χ_r is bounded within the range $[1/N_{t,f}, 1]$, where smaller values are preferred

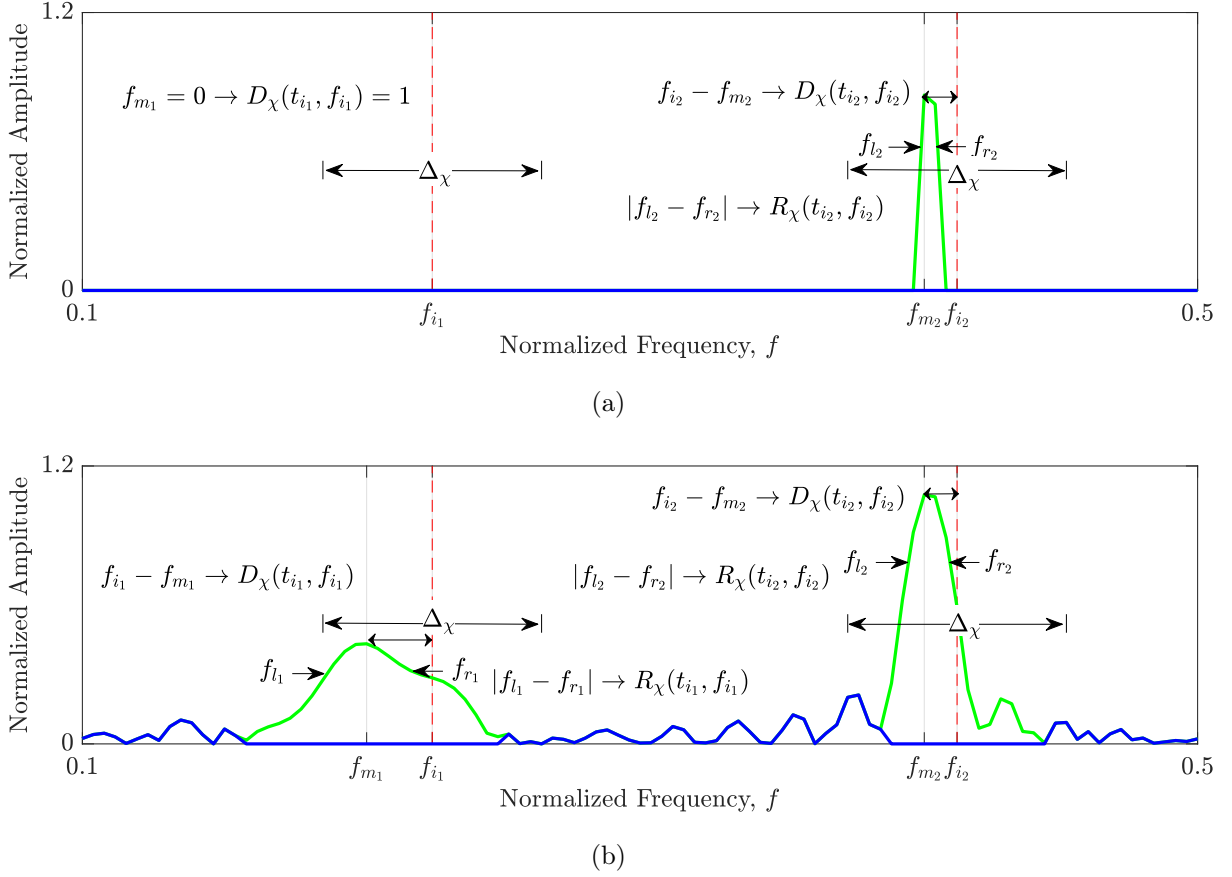


Figure 6.15 A time slice $t = 64$ example analysis of the χ measure for the reconstructed TFDs of the signal $z_{\text{SINLFM}}(t)$ using the TwIST algorithm with: (a) missing auto-term samples (oversparsity), $\lambda = 15$; (b) auto-terms with low-resolution and reconstructed cross-terms, $\lambda = 0.1$. The green line represents the detected auto-terms, while the blue line represents the cross-terms after removing auto-terms.

to indicate higher resolution. When $\chi_r = 1/N_{t,f}$, the auto-term resolution is of one sample or bin, which is considered ideal.

The χ_{ct} component is distinct from the previous measures as it assesses the TFD globally. Since it is normalized by the total number of samples in the TFD, $N_t \times N_f$, the value of χ_{ct} can be interpreted as the percentage of the TFD that is affected by cross-terms. This component is also bounded in the range $[0, 1]$, with smaller values indicating a lower level of cross-term contamination. When $\chi_{ct} = 0$, it means that cross-terms have been entirely eliminated.

It is important to note that the presented measures do not consider the amplitude of auto-terms or cross-terms. This decision was made due to the presence of TFDs that may exhibit amplitudes that are lower than one. Accounting for amplitude would lead to incorrect penalization in the χ_{at} component and insufficient penalization in the χ_{ct} component.

By taking the mean value of χ components, the overall measure treats each component equally. However, in this dissertation, using the measure components independently is

emphasized, as they provide useful insights into each TFD requirement. This approach enables us to gain more information than previous measures based on the LRE.

6.3.1 Validation of Criteria for Reconstructed TFD Evaluation

First, oversparse and low-resolution reconstructed TFDs shown in Figure 3.2 were evaluated, and the results are presented in Table 6.2.

For the signal $z_{\text{SINLFM}}(t)$, the χ_{at} measure component successfully detects that the auto-terms are completely preserved in low-resolution reconstructed TFDs obtained using the TwiST and SALSA algorithms with $\lambda = 0.01$ and $\lambda = 1$, respectively. On the other hand, the worst auto-term preservation is detected in the reconstructed TFD using the TwiST algorithm with $\lambda = 15$. The χ_r component accurately identifies the reconstructed TFDs by the SALSA and TwiST algorithms with $\lambda = 15$ as having superior auto-term resolution than the rest. Additionally, the χ_{ct} component correctly identifies the reconstructed TFDs using the TwiST and SALSA algorithms with low λ values of 0.01 and 1, respectively, as having a significant quantity of reconstructed cross-terms. Overall, the measure χ accurately highlights the TFD obtained using the SALSA algorithm with $\lambda = 15$ as the best-performing, as confirmed by visual inspection and the results given in Table 4.1 using the measure based on the LRE.

The same measure performance is observed for the signal $z_{\text{LFM}}(t)$. The χ_{at} component accurately determines that the auto-terms are better preserved in reconstructed TFDs using lower λ values, specifically the SpaRSA algorithm with $\lambda = 0.01$ and the YALL1 algorithm with $\lambda = 1$. In contrast, oversparse TFDs reconstructed by the SpaRSA and YALL1 algorithms with $\lambda = 15$ exhibit higher auto-term resolution and a lower quantity of reconstructed cross-terms, which are successfully detected by the χ_r and χ_{ct} measure components, respectively. Once again, the measure χ successfully identified the reconstructed TFD using the YALL1 algorithm with $\delta = 1$ as the best-performing TFD.

Table 6.2 Performance results of the IF/GD-based measure for evaluating the oversparse and low-resolution reconstructed TFDs for the signals $z_{\text{SINLFM}}(t)$ and $z_{\text{LFM}}(t)$. Bold values indicate the best-performing algorithm.

	$z_{\text{SINLFM}}(t)$				$z_{\text{LFM}}(t)$			
	TwiST		SALSA		SpaRSA		YALL1	
λ	15	0.01	15	1	15	0.01	15	1
χ_{at}	0.3307	0.0	0.0778	0.0	0.7183	0.0	0.8748	0.2330
χ_r	0.0118	0.0396	0.0104	0.0366	0.0058	0.0274	0.0038	0.0046
χ_{ct}	0.0	0.4194	0.0003	0.1339	0.0	0.5010	0.0	0.0087
χ	0.1142	0.1530	0.0295	0.0568	0.2414	0.1761	0.2929	0.0821

Table 6.3 Performance results of the IF/GD-based measure for evaluating optimized reconstructed TFDs with two different objective functions for the signal $z_{\text{SINLFM}}(t)$. Bold values indicate the best-performing algorithm.

Algorithm	Objectives MSE_t, MSE_f	$z_{\text{SINLFM}}(t)$			
		χ_{at}	χ_r	χ_{ct}	χ
TwIST	M^S	0.0661	0.0159	0.0003	0.0274
	N_r	0.0623	0.0164	0.0005	0.0264
SpaRSA	M^S	0.1440	0.0112	0.0	0.0517
	N_r	0.0624	0.0152	0.0005	0.0260
SALSA	M^S	0.0856	0.0102	0.0003	0.0320
	N_r	0.0700	0.0112	0.0003	0.0272
YALL1	M^S	0.2257	0.0078	0.0	0.0778
	N_r	0.1206	0.0082	0.0012	0.0433
RTwIST	M^S	0.0355	0.0108	0.0010	0.0154
	N_r	0.0191	0.0185	0.0005	0.0127

The reconstructed TFDs obtained using the optimization objective functions based on M^S or N_r measures for the signals $z_{\text{SINLFM}}(t)$ and $z_{\text{LFM}}(t)$, as shown in Figures 4.5, 4.6 and 5.5, have been evaluated using the IF/GD-based measure. The results of the evaluation are presented in Tables 6.3 and 6.4.

For the signal $z_{\text{SINLFM}}(t)$, the χ_{at} component of the measure correctly detects that the TFDs reconstructed by YALL1 and SpaRSA optimized using the objective M^S exhibit the lowest auto-term preservation. Specifically, using the N_r measure as an optimization objective reduces all χ_{at} values by 5.75% to 56.67% compared to when using the M^S measure. In contrast, the χ_r component favors the reconstructed TFDs optimized using the M^S measure, by 3.05% to 41.62%. The same observation applies to the χ_{ct} component, which is equal to or negligibly smaller when using the M^S measure instead of N_r as the optimization objective. The only exception is the RTwIST algorithm, where the reconstructed TF samples related to the sinusoidal FM component that deviated more from its true position are classified as cross-terms, which increases the χ_{ct} value when the M^S objective has been used. According to the χ measure, optimization using the N_r objective achieves reconstructed TFDs with overall higher performance for all considered reconstruction algorithms (by 3.65% up to 49.71%). As the best-performing algorithm, the RTwIST is highlighted, which achieves improvements compared to the considered reconstruction algorithms by 43.80% (TwIST) up to 80.21% (YALL1) and by 51.89% (TwIST) up to 70.67% (YALL1) using objective functions with M^S or N_r , respectively.

The measure reveals similar performance of reconstructed TFDs for the signal $z_{\text{LFM}}(t)$. The lower measure component χ_{at} highlights better auto-term preservation for reconstructed

Table 6.4 Performance results of the IF/GD-based measure for evaluating reconstructed TFDS optimized with objective functions (MSE_t , MSE_f , M^S) and (MSE_t , MSE_f , N_r) for the signal $z_{\text{LFM}}(t)$. Bold values indicate the best-performing algorithm.

$z_{\text{LFM}}(t)$					
Algorithm	Objectives MSE_t, MSE_f	Measure Components			
		χ_{at}	χ_r	χ_{ct}	χ
TwIST	M^S	0.0678	0.0062	0.0050	0.0270
	N_r	0.0675	0.0064	0.0071	0.0263
SpaRSA	M^S	0.1287	0.0082	0.0003	0.0457
	N_r	0.1126	0.0090	0.0004	0.0407
SALSA	M^S	0.0698	0.0068	0.0006	0.0257
	N_r	0.0681	0.0072	0.0009	0.0254
YALL1	M^S	0.3248	0.0042	0.0001	0.1096
	N_r	0.3121	0.0042	0.0001	0.1055
RTwIST	M^S	0.0623	0.0054	0.0005	0.0227
	N_r	0.0572	0.0066	0.0005	0.0214

TFDs optimized with the N_r measure by 0.44% up to 12.51%. The lower components χ_r and χ_{ct} are achieved for reconstructed TFDS optimized with the M^S measure by up to 18.18% and 33.33%, respectively. The RTwIST algorithm is highlighted as the best-performing TFD, with 11.67% (SALSA) up to 79.29% (YALL1) and 15.75% (SALSA) up to 79.72% (YALL1) lower χ measure using objective functions with M^S or N_r , respectively. For this signal example, it can be concluded that using both objective functions resulted in reconstructed TFDS with no significant difference – χ results are slightly in favor when using N_r objective (by 1.17% up to 10.94%).

Based on the findings presented in this section, the conclusions drawn in the preceding chapters can be confirmed. The results indicate that optimizing with the M^S objective function leads to slightly better concentration of auto-terms and suppression of cross-terms. However, there is a higher probability of excluding auto-term samples in this case. On the other hand, the N_r objective function is better at preserving auto-terms by favoring continuous auto-term trajectories, even if the resolution of auto-terms is slightly degraded. Overall, having the N_r objective function ensures slightly better results, as obtained by χ measure components.

Finally, the reconstructed TFDS obtained using two distinct CS-AF area selections for the signals $z_{\text{PFM}}(t)$, shown in Figure 5.10, and $z_{\text{grav}}(t)$, shown in Figure 5.11, were evaluated. The results are presented in Table 6.5.

For the signal $z_{\text{PFM}}(t)$, this measure correctly detects that the biggest improvement has been achieved in the suppression of interference caused by the non-LFM component, as evaluated with a significantly lower χ_{ct} component. Specifically, TwIST, SpaRSA, and

Table 6.5 Performance results of the IF/GD-based measure for evaluating optimized reconstructed TFDs with two different CS-AF area selections for the signals $z_{\text{PFM}}(t)$ and $z_{\text{grav}}(t)$. Bold values indicate the best-performing algorithm.

Γ, Λ	RTwIST		TwIST		SpaRSA		SALSA	
	0, 1	Γ^+, Λ^+	0, 1	Γ^+, Λ^+	0, 1	Γ^+, Λ^+	0, 1	Γ^+, Λ^+
$z_{\text{PFM}}(t)$								
χ_{at}	0.0311	0.0296	0.0536	0.0530	0.1660	0.0589	0.0435	0.0433
χ_r	0.0136	0.0080	0.0092	0.0082	0.0232	0.0060	0.0069	0.0067
χ_{ct}	0.0027	0.0006	0.0025	0.0	0.0826	0.0	0.0042	0.0
χ	0.0158	0.0127	0.0218	0.0204	0.0906	0.0216	0.0182	0.0167
$z_{\text{grav}}(t)$								
χ_{at}	0.2081	0.1468	0.2481	0.2148	0.2666	0.2184	0.2252	0.1918
χ_r	0.0122	0.0076	0.0142	0.0080	0.0124	0.0082	0.0094	0.0070
χ_{ct}	0.0020	0.0012	0.0009	0.0003	0.0005	0.0004	0.0005	0.0014
χ	0.0741	0.0519	0.0877	0.0744	0.0932	0.0757	0.0784	0.0667

SALSA algorithms with presented (Λ^+, Γ^+) completely suppress the interference as seen by $\chi_{ct} = 0$. It is confirmed that the SpaRSA algorithm exhibits the most prominent enhancement, with χ_{at} , χ_r , χ_{ct} and χ values improved by 64.52%, 74.14%, 100% and 76.16%, respectively. It may be noted that χ highlights reconstructed TFDs obtained using the CS-AF area selection presented in this dissertation as better-performing in all reconstruction algorithms. The RTwIST algorithm is highlighted among the considered reconstruction algorithms, with improvements of 13.19% up to 82.56% and 23.95% up to 41.20% using ($\Lambda = 0, \Gamma = 1$) and (Λ^+, Γ^+), respectively.

The results of the measure components χ_{at} and χ_r in the signal $z_{\text{grav}}(t)$ further verifies that the use of the parametrized CS-AF area improves the preservation and resolution of hyperbolic auto-term. Specifically, the use of CS-AF results in improvements of 14.79% to 29.46% and 25.53% to 43.66% for χ_{at} and χ_r , respectively. Similarly to the previous signal example, the presented CS-AF area selection results in improved χ values across all reconstruction algorithms, where the RTwIST shows improvements by 5.48% up to 20.49% and by 22.19% up to 31.44% using ($\Lambda = 0, \Gamma = 1$) and (Λ^+, Γ^+), respectively.

In conclusion, the IF/GD-based measure presented in this study supports the improvement of the RTwIST algorithm over other considered algorithms with respect to the compromise between auto-term resolution and preservation, and the ability to suppress cross-terms. The measure shows that the RTwIST algorithm consistently performs better in preserving auto-terms, as confirmed by the superior performance of the χ_{at} component. However, the ability to suppress cross-terms and resolve auto-terms is competitive with the other algorithms and is signal-dependent.

6.3.2 Evaluating Optimization Performance: Results

This subsection aims to evaluate the suitability and performance of measure components χ_{at} , χ_r , and χ_{ct} as objective functions for optimization purposes in comparison to (MSE_t, MSE_f, M^S) and (MSE_t, MSE_f, N_r) . The RTwIST algorithm is used to address the multi-objective optimization problem presented in (5.5), where χ_{at} , χ_r , and χ_{ct} are formalized as objective functions:

$$\begin{aligned} \text{minimize: } & \chi_{at}, \chi_r, \chi_{ct}(\alpha_{\text{TwIST}}, \beta_{\text{TwIST}}, p, \delta_t, \delta_f) \\ \text{subject to: } & \alpha_{\text{TwIST}} \in \langle 0, 1 \rangle, p \in [0, 1], \beta_{\text{TwIST}} \in \langle 0, 2\alpha \rangle, \delta_t, \delta_f \in [0.6, 1]. \end{aligned} \quad (6.13)$$

The results of the numerical evaluation of the reconstructed TFDs obtained from this optimization process for the signals $z_{\text{SINLFM}}(t)$ and $z_{\text{LFM}}(t)$ is given in Table 6.6, while the obtained reconstructed TFDs are shown in Appendix E.

The findings of this simulation demonstrate that the IF/GD-based measure can be effectively utilized for optimization purposes and provides comparable performance to previously presented objective function formulations. The optimized reconstructed TFDs using the IF/GD-based measure tend to exhibit higher resolution than those optimized

Table 6.6 Reconstructed TFDs obtained using the multi-objective optimization approach with the IF/GD-based measure components χ_{at} , χ_r and χ_{ct} as objective functions for the signals $z_{\text{SINLFM}}(t)$ and $z_{\text{LFM}}(t)$. Bold values indicate the best-performing algorithm.

Algorithm	Measure Components				
		χ_{at}	χ_r	χ_{ct}	χ
$z_{\text{SINLFM}}(t)$					
TwIST	$\lambda^+ = 7.520$	0.0625	0.0163	0.0003	0.0264
SpaRSA	$\lambda^+ = 6.632$	0.0623	0.0150	0.0004	0.0259
SALSA	$\lambda^+ = 12.20$	0.0664	0.0111	0.0003	0.0259
YALL1	$\lambda^+ = 1.581$	0.1208	0.0081	0.0009	0.0433
RTwIST	$(p^+, \delta_t^+, \delta_f^+)$ (0.81, 0.95, 0.86)	0.0161	0.0097	0.0002	0.0087
$z_{\text{LFM}}(t)$					
TwIST	$\lambda^+ = 2.682$	0.0675	0.0064	0.0062	0.0267
SpaRSA	$\lambda^+ = 4.871$	0.0711	0.0095	0.0004	0.0270
SALSA	$\lambda^+ = 12.780$	0.0680	0.0070	0.0006	0.0252
YALL1	$\lambda^+ = 2.970$	0.2787	0.0044	0.0002	0.0944
RTwIST	$(p^+, \delta_t^+, \delta_f^+)$ (0.0, 0.99, 0.96)	0.0559	0.0055	0.0004	0.0206

with the N_r measure and greater preservation of auto-terms than those optimized with the M^S measure. Despite the fact that all reconstruction parameters contribute to the final result, this is particularly evident in the obtained λ^+ values. For the $z_{\text{SINLFM}}(t)$ signal, the λ^+ value lies between the values obtained with the M^S and N_r objectives: $7.947 \rightarrow 7.520 \rightarrow 6.711$ (TwIST), $9.262 \rightarrow 6.632 \rightarrow 6.541$ (SpaRSA), $13.217 \rightarrow 12.20 \rightarrow 11.706$ (SALSA), $5.561 \rightarrow 1.581 \rightarrow 1.480$ (YALL1).

The same trend is observed for the $z_{\text{LFM}}(t)$ signal: $2.701 \rightarrow 2.682 \rightarrow 2.081$ (TwIST) and $13.941 \rightarrow 12.780 \rightarrow 12.180$ (SALSA), except for the SpaRSA and YALL1 algorithms where the λ^+ value is reduced to better preserve auto-terms: $6.145 \rightarrow 5.390 \rightarrow 4.871$ and $4.001 \rightarrow 3.931 \rightarrow 2.970$, respectively. The reconstructed TFDs obtained using the RTwIST algorithm show similar auto-term resolution to the TFDs optimized with M^S measure with better auto-term preservation.

In conclusion, the optimized reconstructed TFDs using the IF/GD-based measure achieve a slightly better trade-off between the χ measure and its components compared to the TFDs presented in Tables 6.3 and 6.4. This is expected since the optimization process directly minimized the χ components.

6.4 Renyi Entropy-Based Algorithm Enhancement

This dissertation has shown that the performance of the RTwIST algorithm relies on the choice of the parameter p , which must be set according to the signal component's alignment along the time or frequency axis. The parameter p operates globally, i.e., the entire TFD is considered. However, signal components may have locally varying directions and shapes, requiring signal components in localized TF regions to have widely divergent p values. This suggests that having a single global parameter, such as p , may be inappropriate.

To address this issue, an alternative approach is presented that leverages the $C_M(t, f)$ map to improve the RTwIST reconstruction algorithm. Specifically, the selection of parameter p can be omitted entirely by modifying (5.4) as:

$$[\zeta_z(t, f)]^{[n+1]} = \text{shrink}_t \{ \eta_t \{ [\zeta'_z(t, f)]^{[n+1]} \} \} + \text{shrink}_f \{ \eta_f \{ [\zeta'_z(t, f)]^{[n+1]} \} \}, \quad (6.14)$$

indicating that the final shrunken TFD $[\zeta_z(t, f)]^{[n+1]}$ is composed of two independent shrinkage operations over time and frequency that do not require any input from a user. That is, the $C_M(t, f)$ determines the TF regions of $\zeta'_z(t, f)$ on which $\text{shrink}_t \{ \cdot \}$ or $\text{shrink}_f \{ \cdot \}$ is performed. Note that the usual inputs to the RTwIST algorithm, $NC_t(t)$ and $NC_t(f)$, have been replaced with more accurate local numbers of components estimated on TFDs with disjoint components, $\eta_t \{ \rho(t, f) \}$ and $\eta_f \{ \rho(t, f) \}$.

The expected advantages with the modified RTwIST algorithm, further denoted with MRTwIST, not having parameter p are numerous. First, a user does not need to know

the signal component behavior to tune the parameter p accordingly. Second, optimization convergence may be quicker with fewer input parameters to optimize. Third, if $p \neq 0$ or $p \neq 1$, multiplication of $\zeta_z^{t,f}(t, f)$ with p or $(1 - p)$ lowers its amplitude and, consequently, the amplitude of the reconstructed TFD.

The performance evaluation of the MRTwIST algorithm was conducted on the signals employed throughout the dissertation, namely $z_{\text{SINLFM}}(t)$, $z_{\text{LFM}}(t)$, $z_{\text{mix}}(t)$, and $z_{\text{grav}}(t)$. A comparison is made between the performance of MRTwIST and the LO-ADTFD. The simulation encompassed all the methods introduced in this dissertation, including the utilization of CS-AF area selection from Chapter 5 and the optimization of reconstruction parameters via multi-objective optimization formalized in (6.13). The IF/GD-based measure employed the IFs and GDs from the BSS-STRE-NBRE method. The remaining parameters pertaining to NSGA-III, reconstruction algorithms, and LRE were consistent with the preceding simulations. The resulting reconstructed TFDs are depicted in Figure 6.16, and their performance evaluated using the χ measure components, is presented in Table 6.7.

The reconstructed TFDs obtained through the MRTwIST algorithm exhibit high resolution and preserved auto-terms, along with effective suppression of cross-terms, across all considered signals. On the one hand, the LO-ADTFD demonstrates superior preservation of auto-terms than the MRTwIST algorithm, as evidenced by the lower χ_{at} component. However, that is expected given that the estimated IFs and GDs are based on the LO-ADTFD. On the other hand, the MRTwIST outperforms the LO-ADTFD in terms of the χ_r and χ_{ct} components. Notably, the MRTwIST achieves a reduction of up to 73.29% in χ_r and up to 99.52% in χ_{ct} . These results prove the superiority of the TFD reconstruction method in terms of auto-term resolution and cross-term suppression over LO-ADTFD. The optimized CS-AF areas for all four signal examples can be found in Appendix F.

It is important to highlight that, except for $z_{\text{SINLFM}}(t)$, all signal examples are found to be optimal with the ideal parameters $\delta_t^+ = 1$ and $\delta_f^+ = 1$. This finding provides further validation for the methods presented in this dissertation, as they collectively enhance various underlying procedures for TFD reconstruction. These improvements facilitate the selection of parameters that yield higher-performing reconstructed TFDs. Additionally, it should be noted that simplifying the MRTwIST by presetting parameters δ_t and δ_f to one and excluding them from the optimization process could potentially be advantageous. However, given the variability of real-life signals, further research is necessary to draw definitive conclusions.

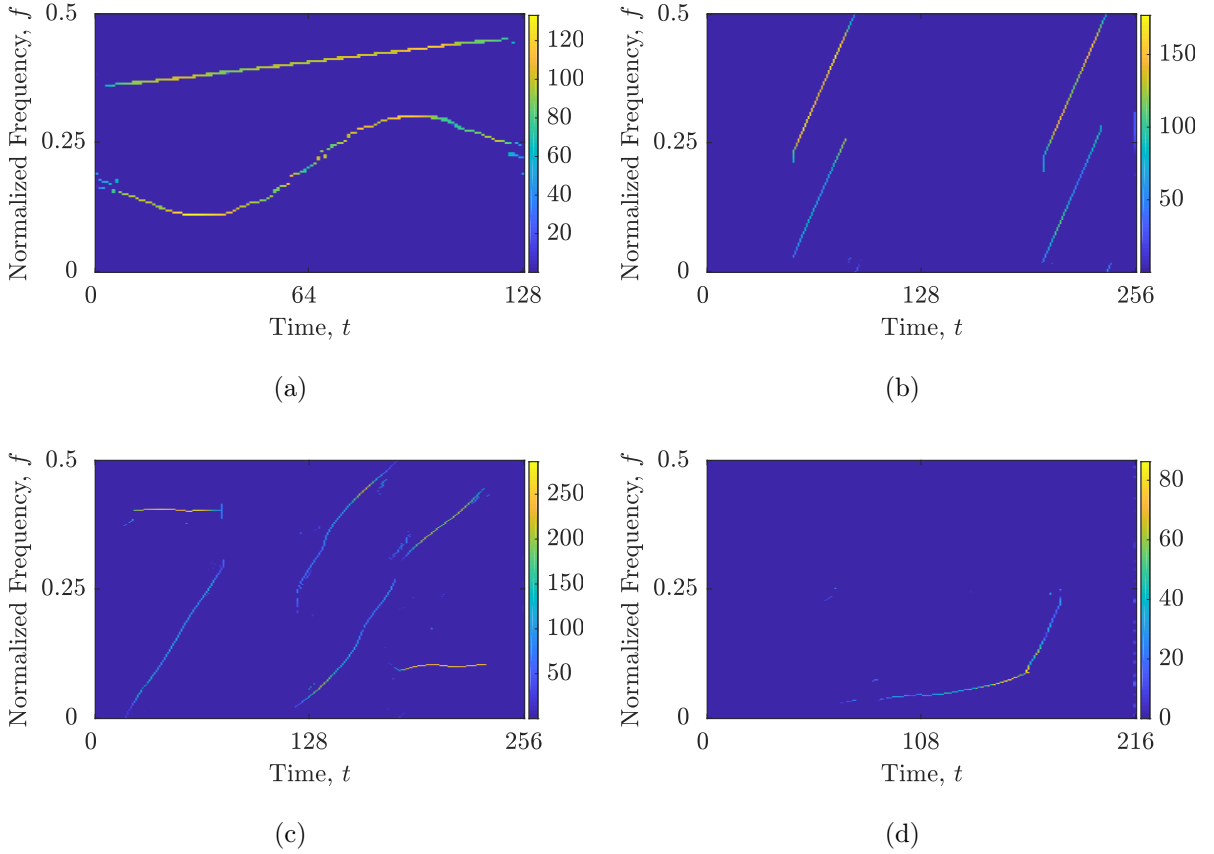


Figure 6.16 Reconstructed TFDs using the MRTwIST algorithm for the considered signals: (a) $z_{\text{SINLFM}}(t)$; (b) $z_{\text{LFM}}(t)$; (c) $z_{\text{mix}}(t)$; (d) $z_{\text{grav}}(t)$.

Table 6.7 Performance evaluation of the reconstructed TFDs obtained using the MRTwIST algorithm versus the LO-ADTFD for the signals $z_{\text{SINLFM}}(t)$, $z_{\text{LFM}}(t)$, $z_{\text{mix}}(t)$ and $z_{\text{grav}}(t)$. Bold values indicate better performing TFD.

		Measure Components			
			χ_{at}	χ_r	χ_{ct}
$z_{\text{SINLFM}}(t)$	$\alpha_{\text{TwIST}}^+, \beta_{\text{TwIST}}^+$	0.912, 0.802	0.0140	0.0094	0.0002
	$\delta_t^+, \Gamma^+, \Lambda^+$	0.97, 0.010, 0.879			
	LO-ADTFD		0.0	0.0238	0.0033
$z_{\text{LFM}}(t)$	$\alpha_{\text{TwIST}}^+, \beta_{\text{TwIST}}^+$	0.870, 0.849	0.0213	0.0039	0.0002
	$\delta_f^+, \Gamma^+, \Lambda^+$	1.0, 0.130, 0.418			
	LO-ADTFD		0.0	0.0098	0.0347
$z_{\text{mix}}(t)$	$\alpha_{\text{TwIST}}^+, \beta_{\text{TwIST}}^+$	0.885, 0.880	0.0829	0.0039	0.0020
	$\delta_{t,f}^+, \Gamma^+, \Lambda^+$	1.0, 0.073, 0.190			
	LO-ADTFD		0.0	0.0146	0.0208
$z_{\text{grav}}(t)$	$\alpha_{\text{TwIST}}^+, \beta_{\text{TwIST}}^+$	0.896, 0.919	0.1148	0.0046	0.0002
	$\delta_{t,f}^+, \Gamma^+, \Lambda^+$	1.0, 0.160, 0.186			
	LO-ADTFD		0.0	0.0128	0.0417

6.5 Summary

In this chapter, several methods have been presented for defining performance measure criteria using estimated IFs and GDs. First, a method has been introduced for automatically defining a binary map that indicates TFD blocks necessitating specific localization. This method exploits the STRE and NBRE methods' imperfections to find local components unsuitable for certain localization approaches. Several applications of the presented binary map have been shown. First, component extraction using the binary map yielded more accurate local component numbers. Second, it allowed the definition of a method for combined IF and GD estimation, which improved Image-based and BSS IF estimation algorithms to estimate GD. Third, the binary map was used to modify the RTwIST algorithm, called MRTwIST, to improve TFD reconstruction without the key parameter defined in the previous chapter.

The presented measure criteria, χ , consisted of three components: the first component, χ_{at} , penalizes missing auto-terms on or near an estimated IF or GD, the second component, χ_r , measures the auto-term main lobe as its resolution, and the third component, χ_{ct} , determines the amount of unresolved cross-terms. The results were measured on synthetic and real-life gravitational signals. The presented measure was more informative than the LRE-based measure and performed satisfactorily as an objective function for the multi-objective optimization approach.

CHAPTER 7

TIME-FREQUENCY ANALYSIS OF ELECTROENCEPHALOGRAM SEIZURE SIGNALS

In this chapter, the presented methods are evaluated for their effectiveness in analyzing a real-life electroencephalogram (EEG) seizure signal in epilepsy, as published by the author in the international peer-reviewed journal [57]. Epilepsy, a common neurological condition, is distinguished by the occurrence of repeated seizures caused by the rapid and excessive firing of nerve cells in the brain, leading to a disruption in normal electrical activity [51, 125]. While EEG recordings are non-invasive and commonly used for identifying these disruptions, manual identification of seizures requires a neurologist in real-time, which is limiting. Therefore, the development of automated seizure detection systems using computers has become an area of significant interest [31, 36, 59, 63, 69, 85, 90, 124, 146].

EEG signals, which exhibit non-stationary properties, are typically analyzed using time-frequency and time-scale representations [11, 58, 109, 146]. However, the analysis of EEG seizure signals exhibits a unique challenge due to their combination of rhythmic and spike characteristics. Previous studies have emphasized the importance of IF in characterizing non-stationary signals in practical applications [19, 59, 75, 84, 90, 95, 117]. Nevertheless, the estimation of IF for EEG seizure signals raises concerns about the suitability of existing approaches, as the spike components require a distinct methodology utilizing the GD technique [62, 66]. Consequently, the main objective of this chapter is to apply the presented method in Chapter 6 to automatically estimate IF and GD for obtaining accurate estimates of both spikes and sinusoidal components.

An alternative avenue for feature extraction involves leveraging the graphical representation of TFDs as images, enabling the application of image analysis techniques such as Haralick features and local binary patterns [6, 23, 69, 149]. Moreover, previous studies have shown the advancements of TFD features in accurately detecting and analyzing

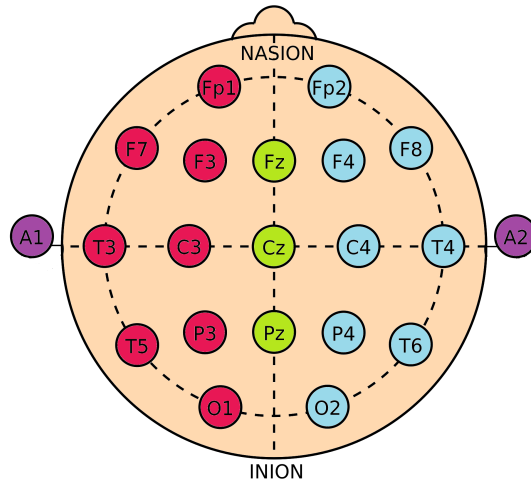


Figure 7.1 The 10-20 EEG electrode placement. $T_4 - T_6$, $F_4 - T_4$, $F_3 - T_3$, $T_5 - O_1$, $T_6 - O_2$, $T_3 - T_5$, $C_4 - P_4$, $F_4 - C_4$, $F_3 - C_3$, $P_4 - O_2$, $C_3 - P_3$, $T_4 - C_4$, $C_4 - C_Z$, $C_Z - C_3$, $P_3 - O_1$, $T_6 - P_4$, $C_3 - T_3$, $P_Z - P_3$, $P_4 - P_Z$, and $P_3 - T_5$ are the channel designations.

seizure activity [17, 60]. However, selecting an appropriate TFD for EEG seizure signals is not a straightforward task. The existence of spikes introduces cross-terms in the TFD, necessitating the application of smoothing along the frequency axis, which can lead to a loss of resolution in the sinusoidal signal component. One commonly employed solution is the LO-ADTFD, which has exhibited high performance in analyzing EEG signals of interest [59, 87]. Therefore, the second objective of this chapter is to apply sparse TFD reconstruction to EEG seizure signals and compare the performance of the MRTwIST algorithm with other reconstruction algorithms utilized in this study, as well as the LO-ADTFD.

7.1 EEG Database Description

In this study, a database comprising 200 EEG seizure signals was employed, which had been previously made available in [17]¹ and utilized in [59, 60, 62, 86]. The EEG signals were obtained from newborns who were admitted to the Royal Women’s Hospital in Brisbane, Australia, and sampled at 256 Hz using the 10-20 international electrode placement method with bipolar montage, as illustrated in Figure 7.1. The electrode locations in this study are denoted by a combination of a letter indicating the lobe and a number (or letter) indicating the hemisphere. Specifically, the lobe letters used are F for Frontal, T for Temporal, C for Central, P for Parietal, and O for Occipital regions of the brain. It is pertinent to highlight that there is an absence of a designated Central lobe. Electrodes bearing even numbers are affiliated with the right hemisphere, whereas those bearing odd numbers are linked to the left hemisphere.

¹Available at: <https://github.com/nabeelalikhani/EEG-Classification-IF-and-GD-features>

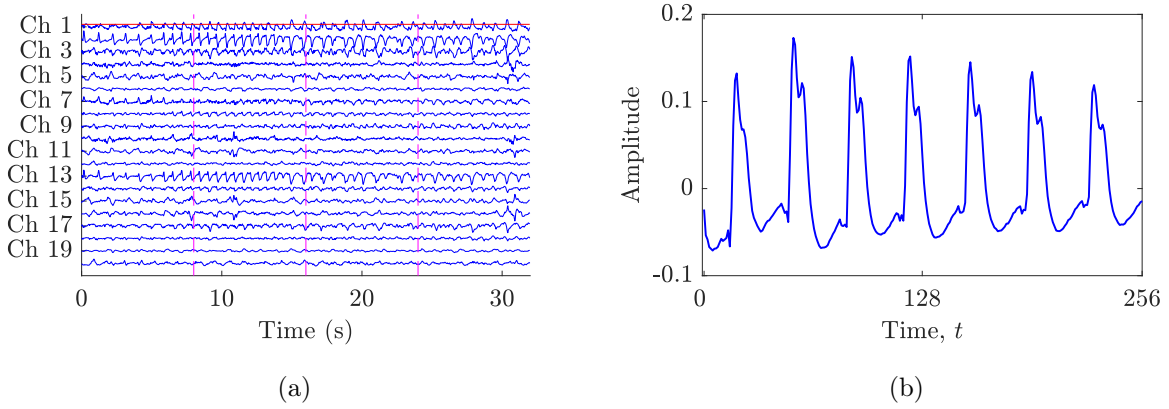


Figure 7.2 For the real-life EEG seizure signal representative, $z_{\text{EEG}}(t)$: (a) recordings over different channels; (b) time-domain representation with pronounced spikes.

The EEG signals were preprocessed to remove noise and interference. Initially, an analog bandpass filter was employed with a frequency range of 0.5 to 70 Hz to eliminate low-frequency noise components. Subsequently, a 50 Hz notch filter was employed to suppress power line interference. The preprocessed signals then progressed through a low-pass filter with a cut-off frequency of 16 Hz. To lower the computational burden, the data were downsampled to 32 Hz. To facilitate analysis, the collected EEG signals were partitioned into non-overlapping intervals of 8 seconds, as illustrated in Figure 7.2a. For this study, one representative of seizure activity has been selected according to the studies [14, 87], which time representation is shown in Figure 7.2b.

7.1.1 EEG Seizure Signal: Mathematical Model

EEG seizure signals are typically represented as amplitude-modulated FM signals with piecewise LFM [59, 60]:

$$s_{\text{EEG}}(t) = \sum_{k=1}^{NC} a_k(t) e^{j2\pi \int f_k(\tau) d\tau}. \quad (7.1)$$

However, the model in (7.1) does not incorporate the presence of spikes or short-duration transients, which are frequently observed in EEG seizure recordings. In order to address this limitation, an updated model has been used in this study, given as follows [59, 60]:

$$s_{\text{EEG}}(t) = \sum_{k=1}^{NC} a_k(t) e^{j2\pi \int f_k(\tau) d\tau} + \sum_{k=1}^{NC} \delta(t - T_k), \quad (7.2)$$

where the second term signifies the spikes in the EEG signal that occur at times T_k . By adding this term, the signal model accounts for both the frequency-modulated components of the signal and the abrupt spikes that can occur during seizures.

Prior investigations have indicated that the utilization of a differential operator (filter) serves to equalize the background of EEG signals and amplify the discernible features of spikes. This technique significantly facilitates the analysis of EEG signals by augmenting the visibility and interpretability of spikes [60, 62, 83, 117]. Hence, this study involves EEG seizure signals without, denoted as $z_{\text{EEG}}(t)$, and with a differentiator filter, denoted as $z_{\text{EEG}_{\text{flt}}}(t)$. Figure 7.3 shows the TFDs of the EEG signals, namely the EMBD and LO-ADTFD, which provide a visualization of the signal's components. The TFDs reveal that the considered signal consists of one dominant sinusoidal component and seven spikes. Moreover, the LO-ADTFD outperforms the EMBD method in terms of component retention and interference suppression. The filtered signal, $z_{\text{EEG}_{\text{flt}}}(t)$, exhibits more pronounced true components and fewer interference terms than the unfiltered signal $z_{\text{EEG}}(t)$. Note that the LRE parameters have been set as $\Theta_t = \Theta_f = 5$ for the purpose of acquiring spike features more rigorously, while the LO-ADTFD has been used as an underlying RID.

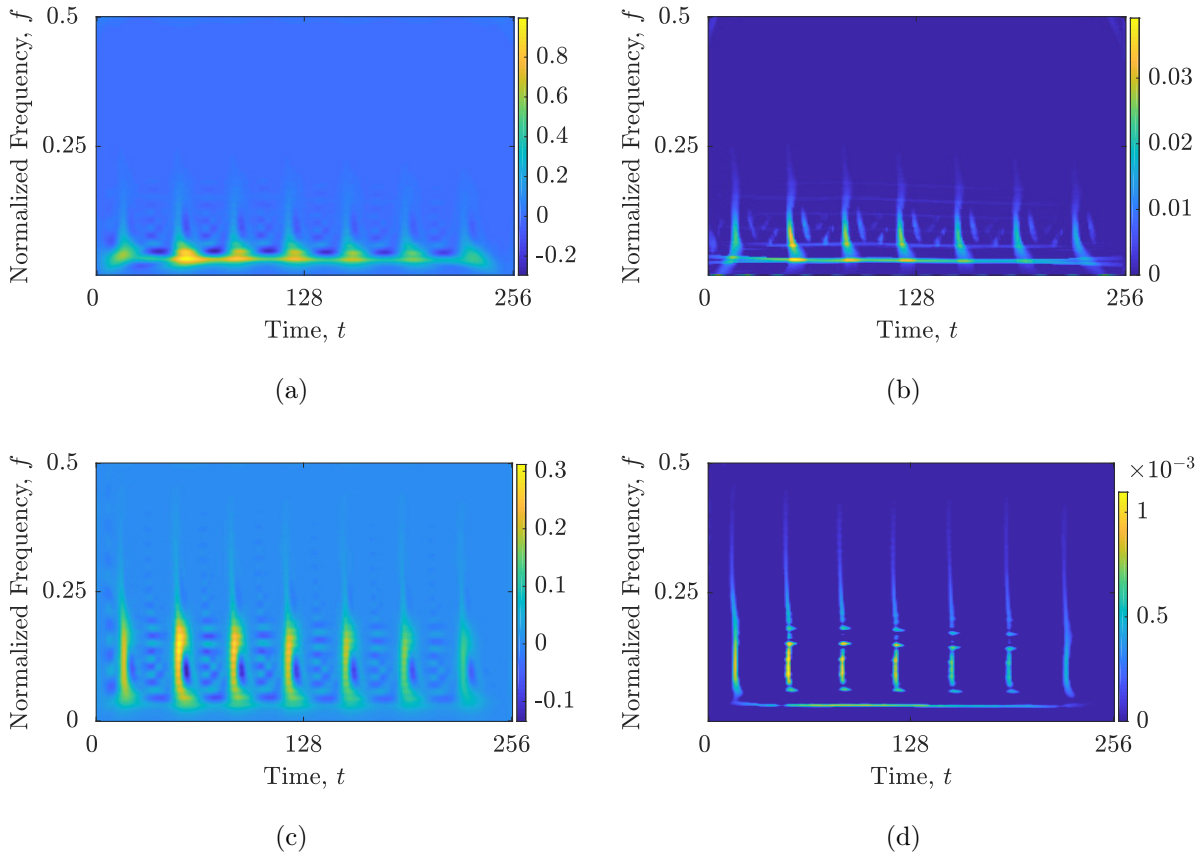


Figure 7.3 (a) EMBD of the signal $z_{\text{EEG}}(t)$, $\alpha_{\text{EMB}} = 0.1$, $\beta_{\text{EMB}} = 0.2$; (b) LO-ADTFD of the signal $z_{\text{EEG}}(t)$; (c) EMBD of the signal $z_{\text{EEG}_{\text{flt}}}(t)$, $\alpha_{\text{EMB}} = 0.08$, $\beta_{\text{EMB}} = 0.3$; (d) LO-ADTFD of the signal $z_{\text{EEG}_{\text{flt}}}(t)$.

7.2 Evaluating Instantaneous Frequency and Group Delay Estimation Performance: Results

Figure 7.4 demonstrates the effectiveness of $C_M(t, f)$ in discerning and separating the sinusoidal and spike components present in both $z_{\text{EEG}}(t)$ and $z_{\text{EEG}_{\text{filt}}}(t)$ signals. The resulting $C_M(t, f)$ successfully associates different localization approaches for spike and sinusoidal components. As a result, separate TFDs for the extracted spike and sinusoidal components are displayed in Figure 7.5. Notably, these TFDs exhibit a substantial reduction in spurious local maxima when compared to the original LO-ADTFD analysis, as evident from the diminished estimated local numbers of components ($NC_t(t)$ and $NC_f(f)$) illustrated in Figure 7.6.

It may be observed that discernible performance variations persist between the two signals, namely $z_{\text{EEG}}(t)$ and $z_{\text{EEG}_{\text{filt}}}(t)$. The LO-ADTFD applied to the unfiltered signal $z_{\text{EEG}}(t)$ does not entirely eliminate cross-terms, leading to slightly diminished performance in estimating $C_M(t, f)$, $NC_t(t)$, and $NC_f(f)$ due to unresolved cross-term interference.

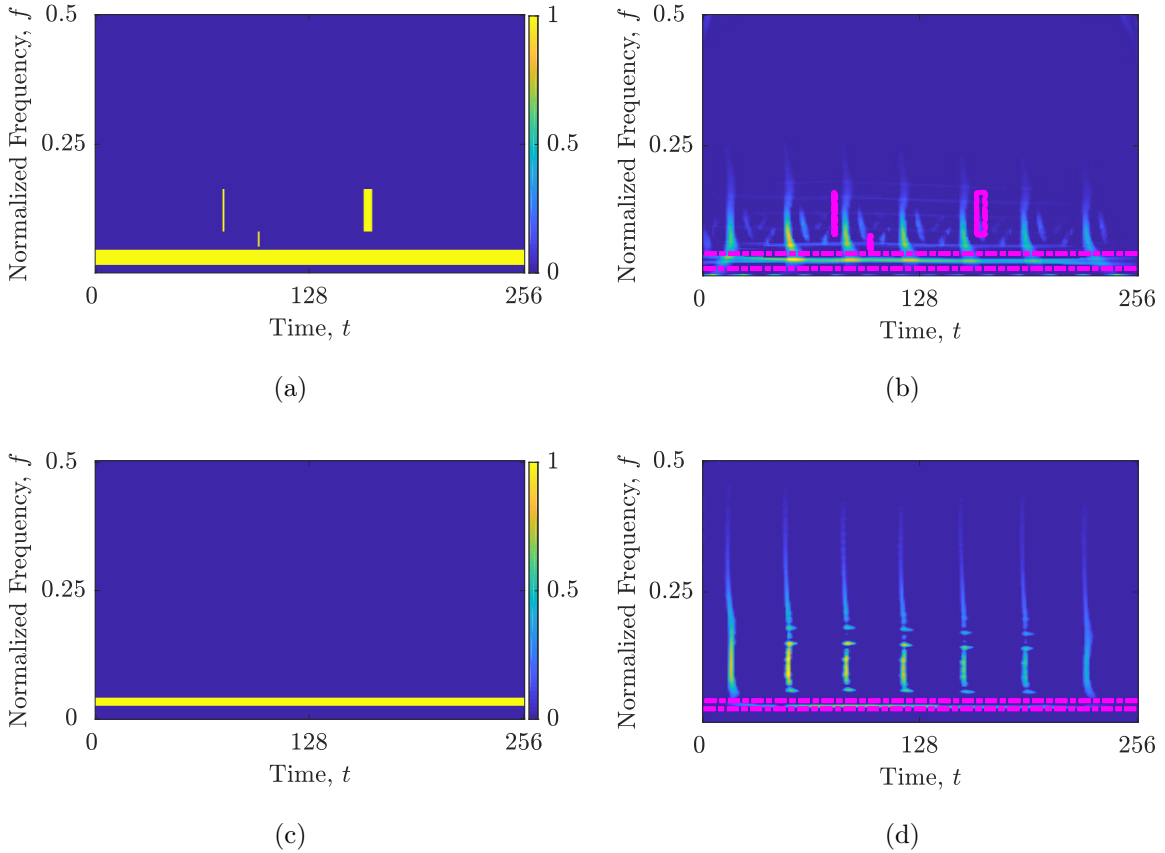


Figure 7.4 The obtained $C_M(t, f)$ for the considered signal: (a) $z_{\text{EEG}}(t)$; (b) $z_{\text{EEG}}(t)$ with its LO-ADTFD; (c) $z_{\text{EEG}_{\text{filt}}}(t)$; (d) $z_{\text{EEG}_{\text{filt}}}(t)$ with its LO-ADTFD. The regions highlighted by yellow and dash-dotted pink rectangles delineate time-based analysis areas, whereas the remaining blue region of the TFD necessitates frequency-based analysis.

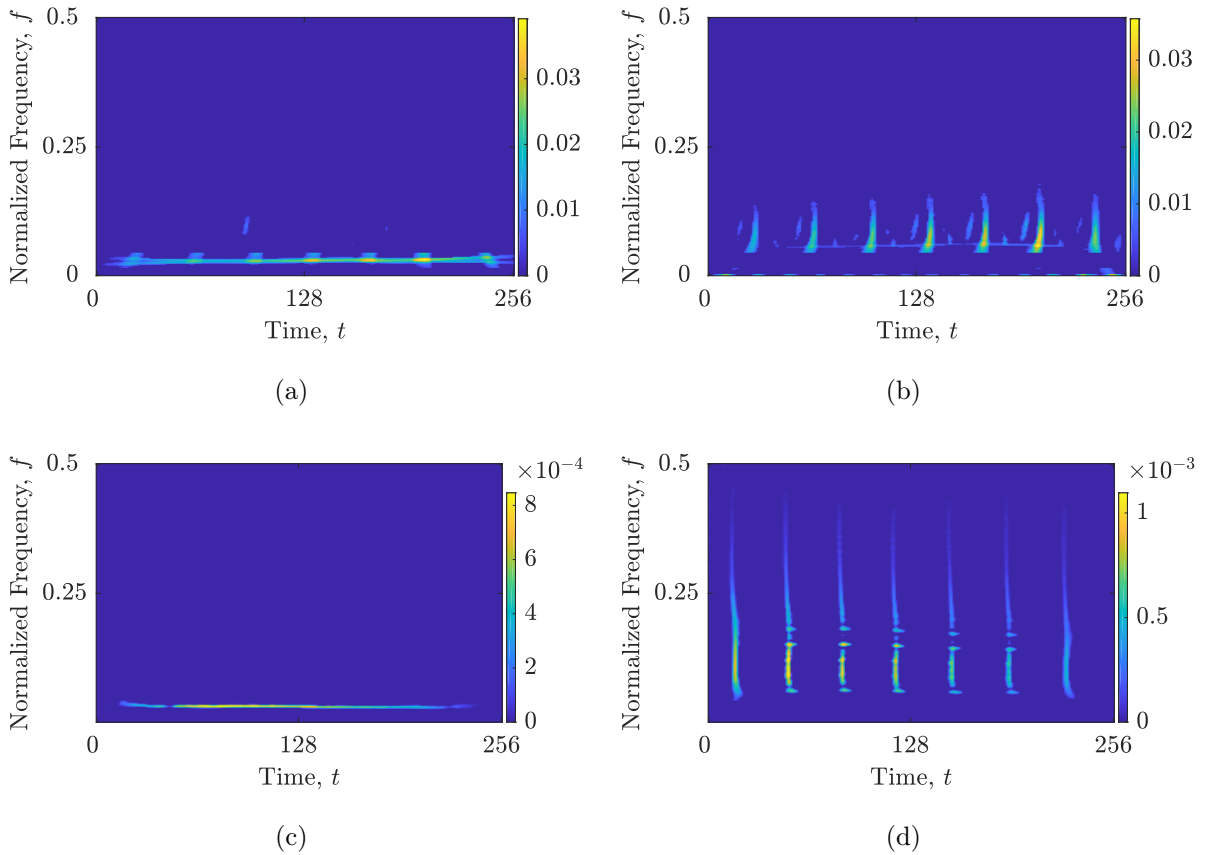


Figure 7.5 Components extracted using different approaches: (a) time-based analysis using $\eta_t\{\rho_{(lo)}(t, f)\}$ for $z_{\text{EEG}}(t)$; (b) frequency-based analysis using $\eta_f\{\rho_{(lo)}(t, f)\}$ for $z_{\text{EEG}}(t)$; (c) time-based analysis using $\eta_t\{\rho_{(lo)}(t, f)\}$ for $z_{\text{EEG}_{\text{flt}}}(t)$; (d) frequency-based analysis using $\eta_f\{\rho_{(lo)}(t, f)\}$ for $z_{\text{EEG}_{\text{flt}}}(t)$.

The obtained results in this study are noteworthy and demonstrate the effectiveness of the presented methodology in extracting and characterizing the targeted components, yielding overall satisfactory outcomes.

Furthermore, it is pertinent to acknowledge that during the process of extracting intersecting components necessitating distinct localization techniques, a minor fraction of components proximate to the point of intersection may inadvertently be captured using an alternative TFD method. This occurrence is exemplified in Figure 7.5a for the unfiltered EEG signal $z_{\text{EEG}}(t)$, wherein minute portions of spike components coexist alongside sinusoidal components. This conduct may be credited to pragmatic considerations in the computation of the NBRE and STRE. The employed sliding window, with a designated size (Θ_t or Θ_f), effectively detects the time or frequency support of a component with a slight extension beyond the ideal range stipulated in [103, 105]. Consequently, the boundaries of the TFD block delineated in the $C_M(t, f)$ exhibit a marginal expansion relative to the actual time or frequency support of the component, accommodating this phenomenon.

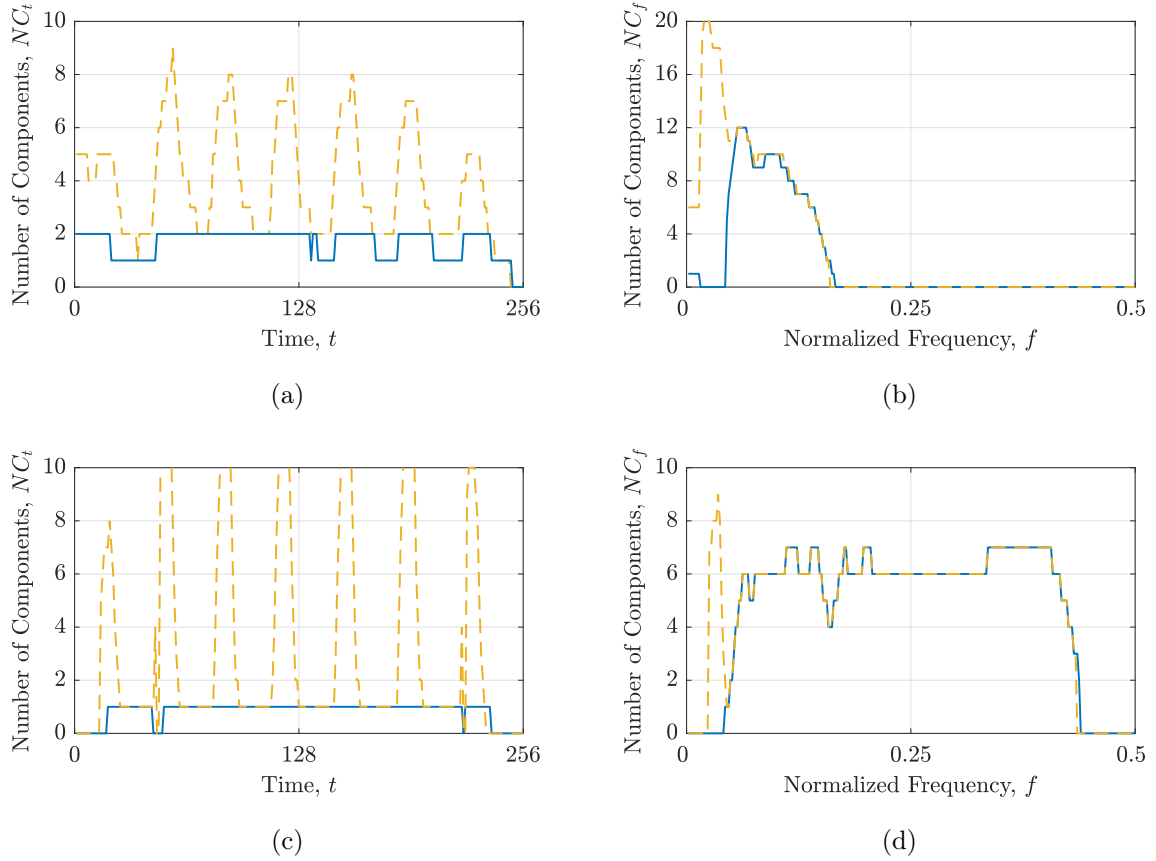


Figure 7.6 Comparison of the local numbers of signal components derived from the application of the STRE and NBRE within the starting TFD (indicated by the yellow dashed line) and subsequent extraction of components employing the presented operators η_t and η_f (represented by the blue solid line) for the respective signals: (a, b) $z_{\text{EEG}}(t)$; (c, d) $z_{\text{EEG}_{\text{filt}}}(t)$.

Figure 7.7 illustrates the IFs and GDs estimated using the method given in [62]² for the EEG signals $z_{\text{EEG}}(t)$ and $z_{\text{EEG}_{\text{filt}}}(t)$. The estimated IFs are computed employing a time-domain approach, whereas the estimated GDs are derived from the signal’s FT using the duality property, which converts vertical signal ridges into horizontal within TFD [62]. The results demonstrate the efficacy of the method in estimating the IFs and GDs for the $z_{\text{EEG}_{\text{filt}}}(t)$, consistent with the research in [62].

Nevertheless, when applied to the unfiltered signal $z_{\text{EEG}}(t)$, the approach has been found to be unsuitable for accurately estimating the GDs, as shown in Figure 7.7d. This constraint arises from the existence of unaddressed background noise and a variable number of components in the TF domain. Note that the user must supply the overall number of components to achieve these estimates, which can pose a functional restriction when dealing with an unfamiliar signal. These findings yield valuable insights into the constraints of the method in [62] and further substantiate the requirement for an automated approach

²Available at: <https://github.com/nabeelalikhani/EEG-Classification-IF-and-GD-features>

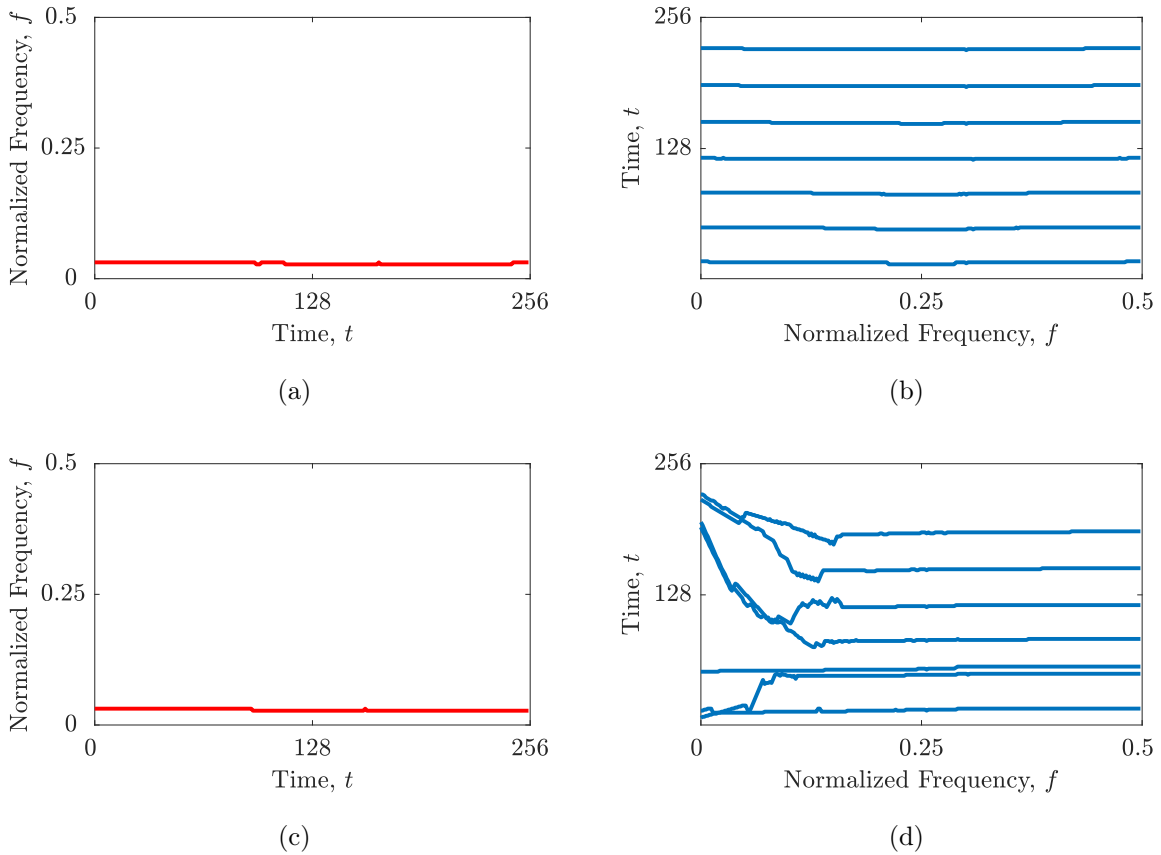


Figure 7.7 For the considered EEG seizure signals: (a) estimated IFs (red line) of $z_{\text{EEG}_{\text{fit}}}(t)$; (b) estimated GDs (blue line) of $z_{\text{EEG}_{\text{fit}}}(t)$; (c) estimated IFs (red line) of $z_{\text{EEG}}(t)$; (d) estimated GDs (blue line) of $z_{\text{EEG}}(t)$. The method proposed in [62] was used.

to IF and GD estimation presented in this dissertation.

Figures 7.8 and 7.9 offer a comparative evaluation of the performance of the presented mutual IF and GD estimation technique against the Image-based and BSS with STRE IF estimation approaches. The findings indicate that the considered IF estimation methods yield accurate estimates when a sinusoidal component is given. However, the estimation of IFs for spike components is characterized by pronounced discontinuities and challenges in distinguishing them from background samples, particularly in the case of the unfiltered signal $z_{\text{EEG}}(t)$. These findings are consistent with previous research that has reported the difficulty of analyzing spike components using IF estimation methods alone [62, 66].

On the contrary, the estimation of GDs for the spike components demonstrates a significant enhancement in their connectivity and overall preservation. The results presented in Figures 7.8 and 7.9 demonstrate that all considered IF and GD estimation methods effectively estimate the mutual IFs and GDs, resulting in improved connectivity and preservation of the spike components. These findings highlight the importance of incorporating GD estimation in the analysis of signals with spike components and provide valuable perspectives on the effectiveness of the mutual IF and GD estimation method.

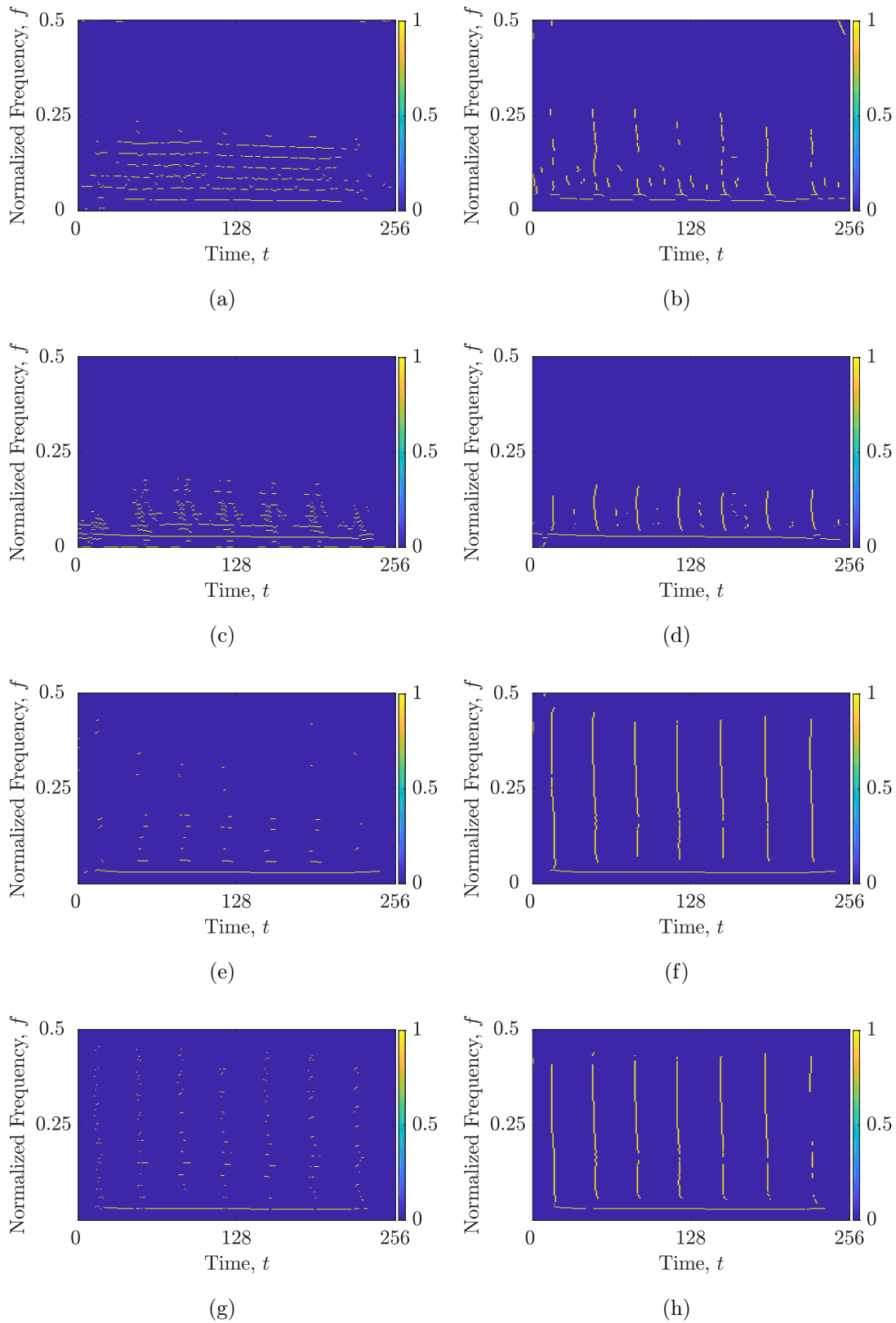


Figure 7.8 IF and GD estimation (in yellow) of EEG seizure signals using various methods: (a) the Image-based-STRE for $z_{\text{EEG}}(t)$; (b) the Image-based-STRE-NBRE for $z_{\text{EEG}}(t)$; (c) the BSS-STRE for $z_{\text{EEG}}(t)$; (d) the BSS-STRE-NBRE for $z_{\text{EEG}}(t)$; (e) the Image-based-STRE for $z_{\text{EEG}_{\text{fit}}}(t)$; (f) the Image-based-STRE-NBRE for $z_{\text{EEG}_{\text{fit}}}(t)$; (g) the BSS-STRE for $z_{\text{EEG}_{\text{fit}}}(t)$; (h) the BSS-STRE-NBRE for $z_{\text{EEG}_{\text{fit}}}(t)$.

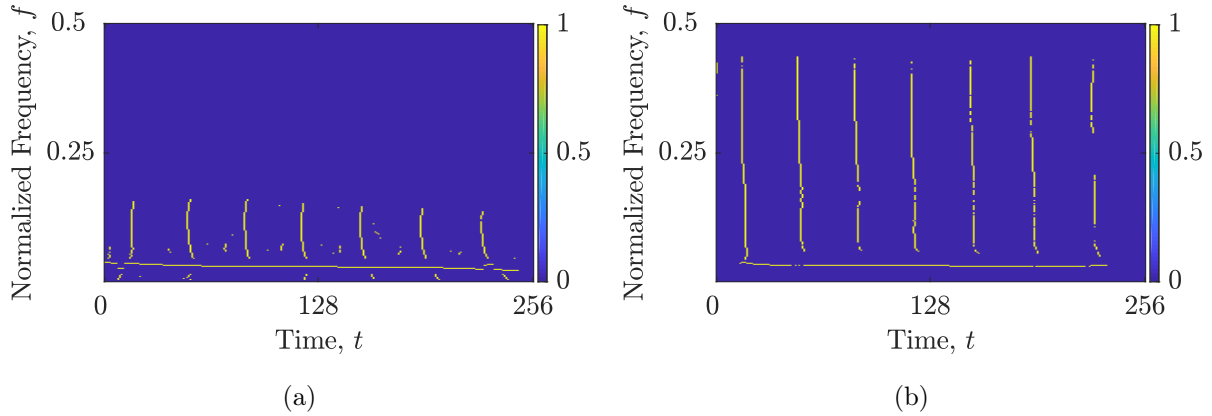


Figure 7.9 $B^{(\text{shrink})}(t, f)$ consisted of estimated IFs and GDs (in yellow) obtained utilizing the shrinkage operator for the EEG seizure signals: (a) $z_{\text{EEG}}(t)$; (b) $z_{\text{EEG}_{\text{filt}}}(t)$.

Table 7.1 Comparison of the performance between the mutual IF and GD estimation and the IF estimation methods for the EEG seizure signals $z_{\text{EEG}}(t)$ and $z_{\text{EEG}_{\text{filt}}}(t)$ database. Values in bold indicate the best-performing algorithm.

Method	Image-based	Image-based	BSS	BSS	Shrinkage operator
Support information	STRE	STRE and NBRE	STRE	STRE and NBRE	STRE and NBRE
Estimation	IF	IF and GD	IF	IF and GD	IF and GD
Database containing 200 examples of $z_{\text{EEG}}(t)$					
$\overline{\text{MSE}}_{t,f}$	0.0522	0.0302	0.0482	0.0287	0.0278
$\overline{\text{MAE}}_{t,f}$	0.1733	0.1212	0.1412	0.1121	0.1097
Database containing 200 examples of $z_{\text{EEG}_{\text{filt}}}(t)$					
$\overline{\text{MSE}}_{t,f}$	0.0729	0.0589	0.0802	0.0522	0.0546
$\overline{\text{MAE}}_{t,f}$	0.3121	0.2311	0.3324	0.2215	0.2317

Table 7.1 summarizes the experimental findings of the IF and GD estimated mutually, which have been averaged over a database consisting of 200 $z_{\text{EEG}}(t)$ signals. The findings provide empirical evidence supporting the effectiveness of the mutual IF and GD strategy compared to IF estimation alone. Explicitly, when applied to the unfiltered $z_{\text{EEG}}(t)$ database, the BSS-STRE-NBRE and Image-based-STRE-NBRE methods demonstrate significant improvements of up to 42.23% and 30.08%, respectively, in terms of the $\overline{\text{MSE}}_{t,f}$ and $\overline{\text{MAE}}_{t,f}$ indicators, when compared to the BSS-STRE and Image-based-STRE methods. Comparable advancements are also observed for the $z_{\text{EEG}_{\text{filt}}}(t)$ database, with reductions of up to 34.96% and 33.41% in the $\overline{\text{MSE}}_{t,f}$ and $\overline{\text{MAE}}_{t,f}$ indicators, respectively, using the BSS-STRE-NBRE and Image-based-STRE-NBRE methods. Furthermore, the outcomes demonstrate the superior performance of the shrinkage operator compared to the BSS-STRE and Image-based-STRE methods. The shrinkage operator-based estimation achieves

improvements of up to 46.45% and 36.61% for the $z_{\text{EEG}}(t)$ database, and up to 31.71% and 30.35% for the $z_{\text{EEG}_{\text{filt}}}(t)$ database, in terms of the $\overline{\text{MSE}}_{t,f}$ and $\overline{\text{MAE}}_{t,f}$ indicators respectively. Notably, the estimation performance of the shrinkage operator exhibits competitiveness comparable to that of the BSS-STRE-NBRE method.

7.3 Evaluating TFD Reconstruction Performance: Results

This section encompasses the evaluation of four distinct algorithms, namely MRTwIST, TwIST, SALSA, and SpaRSA, for the purpose of assessing the reconstruction performance of TFDs on signals $z_{\text{EEG}}(t)$ and $z_{\text{EEG}_{\text{filt}}}(t)$ in conjunction with LO-ADTFD and EMBD. The measure χ components are utilized as a comparative criterion for performance evaluation, serving as the objective functions for optimizing the reconstructed TFD parameters. The parameters of the NSGA-III and reconstruction algorithms remain consistent with those used in previous chapters, while the LRE parameters adhere to the definitions provided in the preceding section.

Figure 7.10 showcases the reconstructed TFDs of the signal $z_{\text{EEG}}(t)$, while the corresponding numerical outcomes are presented in Table 7.2. Upon visual examination, it becomes evident that all reconstruction algorithms encounter challenges in preserving the spike components in comparison to the sinusoidal components. This phenomenon arises due to the complex nature of the signal's AF, where the actual spike components are masked by interference, thereby rendering them more difficult to retain during the application of the CS-based approach. Notably, MRTwIST exhibits improved detection of spike components compared to other algorithms. Nevertheless, the CS-AF approach compromises their consistency, leading to a decrease in overall reconstruction performance manifested by the representation of delta functions.

The obtained results indicate that MRTwIST surpasses the other reconstruction algorithms across a majority of metrics. Particularly, the preservation of auto-terms and improvements in resolution are confirmed by the values of χ_{at} and χ_r , which are reduced by 78.74% and 25.42%, respectively, in comparison to the second-best algorithms, SALSA and SpaRSA. However, inaccuracies in the trajectories of spike components within MRTwIST result in certain samples being misclassified as cross-terms, contributing to a slight increase in the χ_{ct} value when compared to the SpaRSA and SALSA algorithms. Overall, MRTwIST exhibits commendable performance in terms of χ , which surpasses the second-best algorithm, TwIST, by 78.94%.

When comparing MRTwIST to LO-ADTFD, notable enhancements are observed in terms of χ_r , χ_{ct} , and χ , exhibiting improvements of 64.63%, 92.45%, and 25.43%, respectively. However, MRTwIST performs less favorably than LO-ADTFD and EMBD in

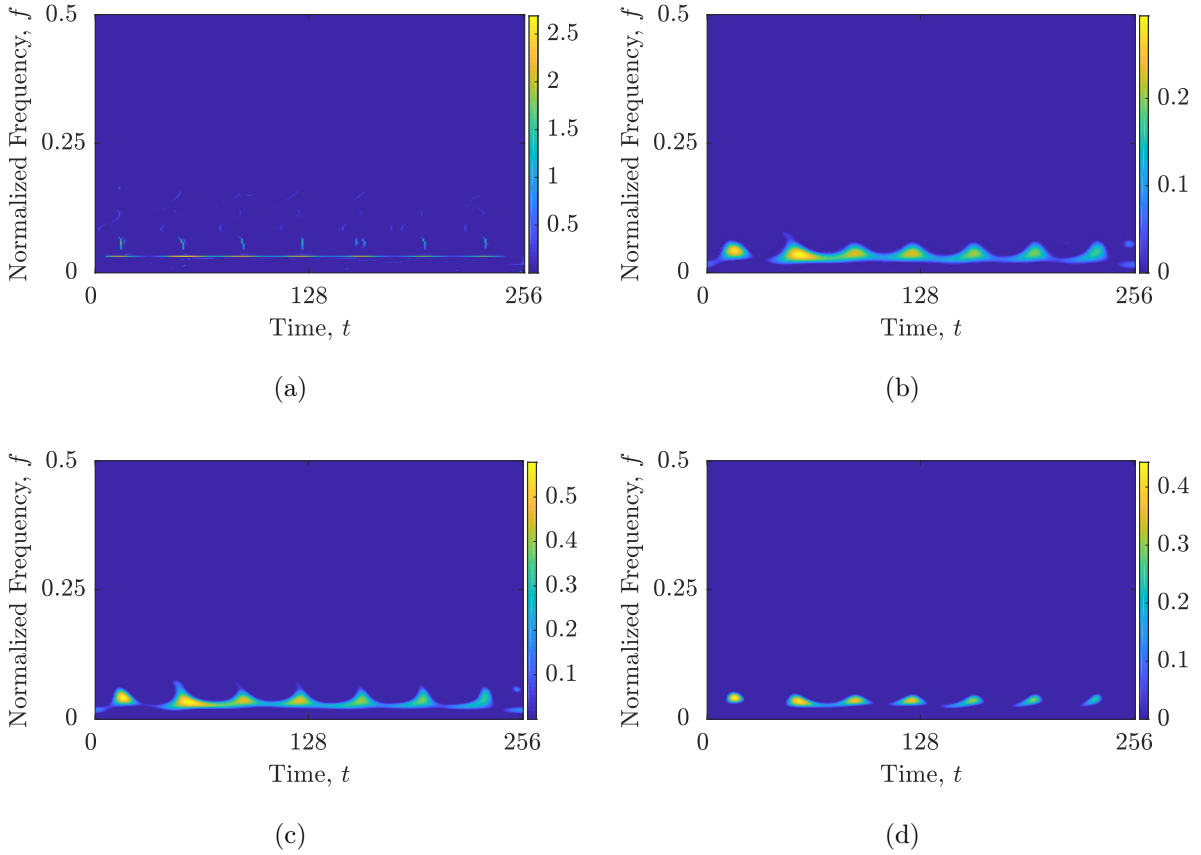


Figure 7.10 Reconstructed TFDs of the unfiltered $z_{\text{EEG}}(t)$ signal obtained using the following reconstruction algorithm: (a) MRTwIST; (b) TwIST; (c) SALSAs; (d) SpaRSA.

Table 7.2 Performance evaluation of the considered TFDs for the unfiltered EEG seizure signal $z_{\text{EEG}}(t)$. Bold values indicate the best-performing TFD.

	$z_{\text{EEG}}(t)$			
	χ_{at}	χ_r	χ_{ct}	χ
MRTwIST	0.0789	0.0044	0.0083	0.0305
TwIST	0.4033	0.0204	0.0095	0.1444
SpaRSA	0.6542	0.0059	0.0013	0.2205
SALSAs	0.3711	0.0160	0.0074	0.1315
EMBD	0.0382	0.0261	0.1691	0.0778
LO-ADTFD	0.0	0.0128	0.1100	0.0409

MRTwIST: $\alpha_{\text{TwIST}}^+ = 0.914$, $\beta_{\text{TwIST}}^+ = 0.804$, $\delta_t^+ = \delta_f^+ = 0.99$, $\Gamma^+ = 0.07$, $\Lambda^+ = 0.40$;

TwIST: $\alpha_{\text{TwIST}}^+ = 0.923$, $\beta_{\text{TwIST}}^+ = 0.801$, $\lambda^+ = 0.022$, $\Gamma^+ = 0.01$, $\Lambda^+ = 0.89$;

SALSAs: $\lambda^+ = 0.03$, $\Gamma^+ = 0.01$, $\Lambda^+ = 0.98$; SpaRSA: $\lambda^+ = 0.06$, $\Gamma^+ = 0.01$, $\Lambda^+ = 0.78$

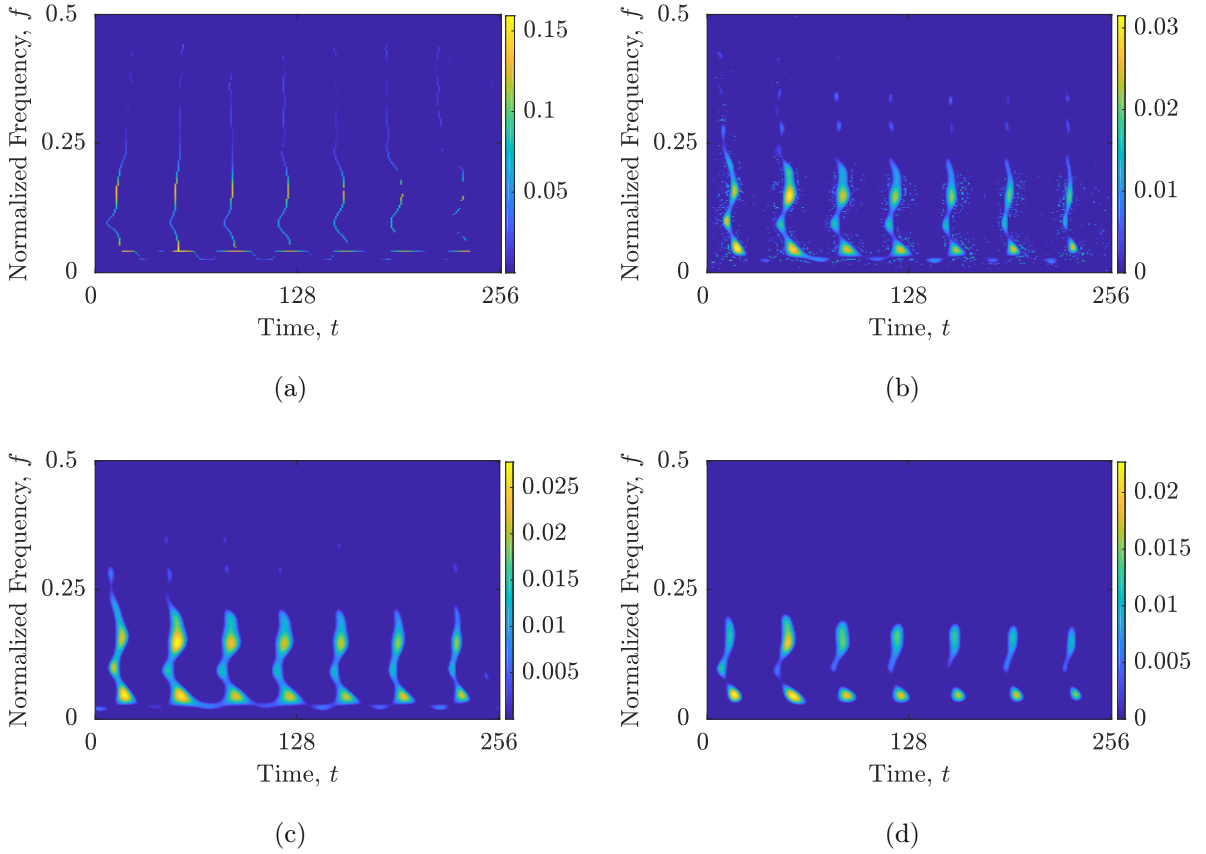


Figure 7.11 Reconstructed TFDs for the filtered $z_{\text{EEG}_{\text{filt}}}(t)$ signal obtained using the following reconstruction algorithm: (a) MRTwIST; (b) TwIST; (c) SALSAs; (d) SpaRSA.

terms of χ_{at} , primarily due to the challenges associated with preserving spike components.

The reconstructed TFDs of the filtered signal $z_{\text{EEG}_{\text{filt}}}(t)$ are presented in Figure 7.11, and the corresponding numerical results are reported in Table 7.3. Visual inspection reveals that all reconstruction algorithms struggled to fully preserve the spike and sinusoidal components. However, due to the lower complexity of the signal’s AF, the spike components are better preserved compared to those in the signal $z_{\text{EEG}}(t)$.

The results show that MRTwIST outperforms other reconstruction algorithms in all metrics for the filtered signal. Specifically, MRTwIST reduces χ_{at} , χ_r , χ_{ct} , and χ values by 19.53%, 18.75%, 75.22%, and 31.97% compared to the second-best algorithms, TwIST, SpaRSA, SpaRSA, and TwIST, respectively. When compared to LO-ADTFD, MRTwIST shows improvements in terms of χ_r and χ_{ct} by 49.35% and 63.64%, respectively. As expected, LO-ADTFD and EMBD achieved better auto-term preservation measured with χ_{at} , due to which LO-ADTFD turns out to be better-performing overall than MRTwIST, with a lower χ value. The complexity of the signals’ AFs and the obtained CS-AF areas for the MRTwIST algorithm are shown in Figure 7.12.

The previously obtained results yield several notable conclusions. Firstly, the MRTwIST algorithm has exhibited superior performance in reconstructing TFDs compared to the

Table 7.3 Performance evaluation of the considered TFDs for the filtered EEG seizure signal $z_{\text{EEG}_{\text{filt}}}(t)$. Bold values indicate the best-performing TFD.

	$z_{\text{EEG}_{\text{filt}}}(t)$			
	χ_{at}	χ_r	χ_{ct}	χ
MRTwIST	0.1879	0.0039	0.0028	0.0649
TwIST	0.2335	0.0081	0.0446	0.0954
SpaRSA	0.6833	0.0048	0.0113	0.2331
SALSA	0.3108	0.0127	0.0212	0.1149
EMBD	0.0	0.0172	0.2062	0.0745
LO-ADTFD	0.0	0.0077	0.0077	0.0051

MRTwIST: $\alpha_{\text{TwIST}}^+ = 0.922$, $\beta_{\text{TwIST}}^+ = 0.812$, $\delta_t^+ = \delta_f^+ = 0.99$, $\Gamma^+ = 0.05$, $\Lambda^+ = 0.51$;

TwIST: $\alpha_{\text{TwIST}}^+ = 0.923$, $\beta_{\text{TwIST}}^+ = 0.801$, $\lambda^+ = 0.001$, $\Gamma^+ = 0.01$, $\Lambda^+ = 0.91$;

SALSA: $\lambda^+ = 0.002$, $\Gamma^+ = 0.01$, $\Lambda^+ = 0.61$; SpaRSA: $\lambda^+ = 0.0026$, $\Gamma^+ = 0.01$, $\Lambda^+ = 0.75$

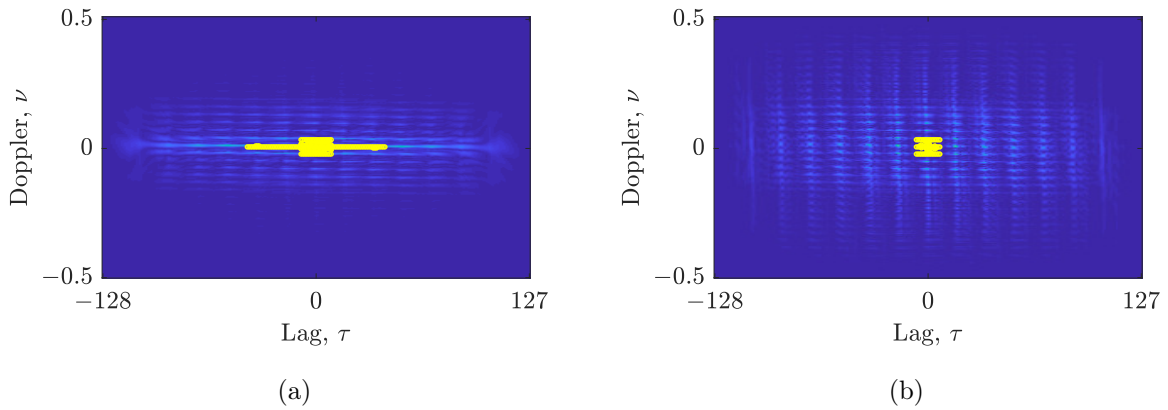


Figure 7.12 AFs with highlighted CS-AF areas in yellow obtained with the MRTwIST algorithm for the considered signal: (a) $z_{\text{EEG}}(t)$; (b) $z_{\text{EEG}_{\text{filt}}}(t)$.

other algorithms under evaluation. Moreover, it has proven to exhibit higher resolution in preserving auto-terms and better suppression of cross-terms in comparison to the highly-performing LO-ADTFD. However, it is important to acknowledge that in practical signal scenarios characterized by closely-spaced multi-components and complex behavior, the selection of the CS-AF area may result in the degradation of actual component trajectories. This observation highlights a potential avenue for future research, where alternative TFDs that incorporate initial interference reduction prior to reconstruction should be explored as potential replacements for the WVD in CS-based method based on the AF. have the potential to pave the way for the advancement of more resilient and accurate TFD reconstruction techniques capable of handling intricate signal characteristics and mitigating the challenges associated with interference and overlapping components.

7.4 Summary

This chapter provided an analysis of EEG seizure signals that were representative of both spike and sinusoidal components. The efficacy of using a differential filter to enhance useful components was examined, and a method for creating $C_M(t, f)$ map was applied that has allowed for the classification of spike and sinusoidal components. Results from the experiments have shown that component extraction was achieved with more accurate local numbers of components.

The study also evaluated the performance of existing BSS-STRE and Image-based estimation methods for estimating EEG seizure signals. The results indicated that mutually estimating the IF and GD significantly enhanced component estimation performance for both unfiltered and filtered EEG seizure signals, as shown using the improved BSS-STRE-NBRE, Image-based-STRE-NBRE, and shrinkage operator-based algorithms.

Additionally, the reconstruction performance of the CS-based method has been examined on EEG data. The experiments showed that using the MRTwIST algorithm resulted in significant improvements in spike reconstruction, auto-term resolution, and cross-term reduction over the other reconstruction algorithms considered. Furthermore, the MRTwIST algorithm achieved better auto-term resolution and cross-term elimination than the LO-ADTFD. However, component consistency as a delta function remained in favor of the LO-ADTFD.

CHAPTER 8

CONCLUSIONS AND FUTURE WORK

8.1 Conclusions

Time-frequency distributions present a notable contribution to the analysis of non-stationary signals as they allow for the visualization of signal energy distribution in joint time-frequency domain. However, TFDs involve a compromise between auto-resolution and cross-term suppression, which makes their interpretation complicated. Advanced methods have introduced another complexity to this trade-off, known as auto-term preservation, which highlights the limitations of existing concentration measures and optimization approaches. Although compressive sensing-based methods have been used to obtain highly concentrated sparse TFDs, their reconstructed TFDs heavily rely on input parameters and underlying procedures, limiting their broad applicability.

The key idea is to define performance criteria that properly evaluate auto-term preservation and penalize its absence. Calculating and comparing the local numbers of components in starting and reconstructed TFDs obtained using the LRE methods accomplishes this. The conducted experiments have shown that when the reconstructed TFDs are evaluated with the proposed criteria, the TFD reconstruction that caused the absence of auto-terms is highlighted as poorly performing, which has not been the case when using traditional global concentration measures. This supports the first hypothesis of this dissertation. The here-proposed criteria have been implemented in a multi-objective meta-heuristic optimization environment as objective functions. The results have shown that the presented optimization approach converges to a high-performing TFD with preserved auto-terms, which has not been achieved using existing optimization approaches.

This research involved further upgrading the LRE method with the introduction of the NBRE approach. Experimental results have shown that the local number of components in

frequency bins obtained using the NBRE exhibits higher accuracy than the one obtained using the STRE for certain signals. This finding supports the second hypothesis of this study. Moreover, the study underscores the importance of considering both time and frequency localizations in TFD analysis, as demonstrated by the different applications presented throughout the dissertation.

The first enhancement of the CS-based method involves the algorithm for the shrinkage operator that locally detects and concentrates on the signal's auto-terms, which exhibit the largest surfaces in each time and frequency slice. The STRE and NBRE methods determine the total number of surfaces to be considered. The proposed LRE-based sparse reconstruction algorithm outperforms all of the tested ℓ_1 norm-based reconstruction algorithms in terms of the here-proposed performance criteria. This finding supports the third hypothesis of this study.

The second enhancement of the CS-based method involves a method that adapts the CS-AF area in the AF on auto-term trajectories with arbitrary shapes. This method uses parameters to reduce the density between samples related to auto-terms or cross-terms, based on which the DBSCAN clustering method extracts a single cluster with auto-term-explicit samples. Experimental results have demonstrated that this method increases the number of auto-term-related samples in the CS-AF area, while simultaneously discarding noise and cross-term-related samples. As a result, TFD reconstruction is improved, with less sensitivity to noise.

In addition to the LRE-based performance criteria described previously, this dissertation presents another set of criteria based on estimated IFs and GDs. The research conducted to establish these criteria has yielded an LRE-based method that automatically delineates TFD regions necessitating specific localization. The ability to seamlessly integrate both localization approaches without requiring any prior knowledge from the user proves advantageous across multiple applications. Firstly, this method facilitates the combined estimation of IF and GD, surpassing the performance of IF estimation alone. Secondly, it achieves an improvement over the previously proposed LRE-based sparse reconstruction algorithm. The performance criteria formulated based on the estimated IFs and GDs independently indicate the quality of auto-term preservation, resolution, and cross-term suppression, which confers an advantage over the LRE-based criterion. Furthermore, the optimization performance based on these criteria demonstrates competitiveness with the LRE-based criterion, resulting in reconstructed TFDs that exhibit preserved auto-terms with high resolution and suppressed cross-terms.

Ultimately, the outcomes elucidated in this dissertation reinforce the efficacy of mutual IF and GD estimations, alongside the here-presented CS-based method's enhancements, in facilitating an enhanced estimation of components and reconstruction of EEG seizure signals. These advancements hold substantial promise for informing future research endeavors in the domain of seizure detection.

8.2 Future Research Directions

The presented optimization methodology holds the potential to be implemented in various TF methods that require auto-term preservation. Further advancements within these methods, similar to the CS-based method in this dissertation, could be achieved.

Although the WVD served as the basis for sparse time-frequency distribution TFD calculation in this dissertation, it would be advantageous to delve into alternative classes of TFDs, involving other QTFDs and higher-order TFDs. QTFDs may introduce fewer cross-terms than the WVD, but may require a higher reconstruction algorithm requirement. On the other hand, higher-order TFDs may require a different approach in the CS-AF area due to the introduction of more cross-terms. The research direction could focus on finding a substitute domain other than the AF since the mathematical by-product of higher-order TFDs introduces artificial auto-terms, which are indistinguishable from true auto-terms in the magnitude plot of the AF.

Another research direction could involve a thorough investigation of how to weight the performance criteria used in this dissertation and combine them into one measure. This could allow for the implementation of single-objective meta-heuristic optimization algorithms, which have some advantages over multi-objective ones.

Finally, future research directions could focus on more application-oriented research in EEG signal processing. Improvements in component estimation and reconstruction obtained in this dissertation could be used in developing a classifier for detecting seizures from background data without specialist intervention. This would require a thorough investigation of existing approaches that are not based on TF analysis and their possible connection with deep learning algorithms. This research direction is not limited to the analysis of EEG seizure signals, but could include other EEG, seismic, radar, and gravitational signals, among others.

BIBLIOGRAPHY

- [1] M. V. Afonso, J. M. Bioucas-Dias, and M. A. T. Figueiredo, “Fast image recovery using variable splitting and constrained optimization,” *IEEE Transactions on Image Processing*, vol. 19, no. 9, pp. 2345–2356, Sep. 2010, doi: 10.1109/TIP.2010.2047910.
- [2] J. Allen, “Short term spectral analysis, synthesis, and modification by discrete Fourier transform,” *IEEE Transactions on Acoustics, Speech, and Signal Processing*, vol. 25, no. 3, pp. 235–238, 1977, doi: 10.1109/TASSP.1977.1162950.
- [3] S. Aviyente and W. J. Williams, “Minimum entropy time-frequency distributions,” *IEEE Signal Processing Letters*, vol. 12, no. 1, pp. 37–40, Jan 2005, doi: 10.1109/LSP.2004.839696.
- [4] M. A. Awal and B. Boashash, “An automatic fast optimization of quadratic time-frequency distribution using the hybrid genetic algorithm,” *Signal Processing*, vol. 131, pp. 134–142, 2017, doi: 10.1016/j.sigpro.2016.08.017.
- [5] J. Bader, K. Deb, and E. Zitzler, “Faster hypervolume-based search using Monte Carlo sampling,” in *Multiple Criteria Decision Making for Sustainable Energy and Transportation Systems*, M. Ehrgott, B. Naujoks, T. J. Stewart, and J. Wallenius, Eds. Berlin, Heidelberg: Springer Berlin Heidelberg, 2010, pp. 313–326, doi: 10.1007/978-3-642-04045-0_27.
- [6] V. Bajaj, K. Rai, A. Kumar, and D. Sharma, “Time-frequency image based features for classification of epileptic seizures from EEG signals,” *Biomedical Physics and Engineering Express*, vol. 3, no. 1, p. 015012, jan 2017, doi: 10.1088/2057-1976/aa5199.
- [7] R. G. Baraniuk, “Compressive sensing [Lecture Notes],” *IEEE Signal Processing Magazine*, vol. 24, no. 4, pp. 118–121, July 2007, doi: 10.1109/MSP.2007.4286571.
- [8] R. G. Baraniuk, P. Flandrin, A. J. E. M. Janssen, and O. J. J. Michel, “Measuring time-frequency information content using the Rényi entropies,” *IEEE Transactions on Information Theory*, vol. 47, no. 4, pp. 1391–1409, May 2001, doi: 10.1109/18.923723.
- [9] G. E. A. P. A. Batista, R. C. Prati, and M. C. Monard, “A study of the behavior of several methods for balancing machine learning training data,” *SIGKDD Explor. Newsl.*, vol. 6, no. 1, p. 20–29, jun 2004. [Online]. Available: <https://doi.org/10.1145/1007730.1007735>, doi: 10.1145/1007730.1007735.
- [10] L. Batistić, J. Lerga, and I. Stanković, “Detection of motor imagery based on short-term entropy of time-frequency representations,” *BioMedical Engineering OnLine*, vol. 22, no. 1, p. 41, 2023, doi: 10.1186/s12938-023-01102-1.
- [11] A. Bhattacharyya, R. B. Pachori, A. Upadhyay, and U. R. Acharya, “Tunable-Q wavelet transform based multiscale entropy measure for automated classification of epileptic EEG signals,” *Applied Sciences*, vol. 7, no. 4, 2017, doi: 10.3390/app7040385.

- [12] X. Bing, H. Xiaojian, L. Xuanda, H. Ziqi, and Z. Hanchang, “Simulation of an NSGA-III based fireball inner-temperature-field reconstructive method,” *IEEE Access*, vol. 8, pp. 43 908–43 919, 2020, doi: 10.1109/ACCESS.2020.2977853.
- [13] J. M. Bioucas-Dias and M. A. T. Figueiredo, “A new TwIST: two-step iterative shrinkage/thresholding algorithms for image restoration,” *IEEE Transactions on Image Processing*, vol. 16, no. 12, pp. 2992–3004, Dec 2007, doi: 10.1109/TIP.2007.909319.
- [14] B. Boashash, *Time-Frequency Signal Analysis and Processing, A Comprehensive Reference*, 2nd ed., ser. EURASIP and Academic Press Series in Signal and Image Processing. London, UK: Elsevier, December 2016.
- [15] B. Boashash and S. Ouelha, “An improved design of high-resolution quadratic time–frequency distributions for the analysis of nonstationary multicomponent signals using directional compact kernels,” *IEEE Transactions on Signal Processing*, vol. 65, no. 10, pp. 2701–2713, May 2017, doi: 10.1109/TSP.2017.2669899.
- [16] B. Boashash and V. Sucic, “Resolution measure criteria for the objective assessment of the performance of quadratic time-frequency distributions,” *IEEE Transactions on Signal Processing*, vol. 51, no. 5, pp. 1253–1263, 2003, doi: 10.1109/TSP.2003.810300.
- [17] B. Boashash, G. Azemi, and N. Ali Khan, “Principles of time–frequency feature extraction for change detection in non-stationary signals: Applications to newborn EEG abnormality detection,” *Pattern Recognition*, vol. 48, no. 3, pp. 616–627, 2015, doi: 10.1016/j.patcog.2014.08.016.
- [18] B. Boashash and T. Ben-Jabeur, “Design of a high-resolution separable-kernel quadratic TFD for improving newborn health outcomes using fetal movement detection,” in *2012 11th International Conference on Information Science, Signal Processing and their Applications (ISSPA)*, 2012, pp. 354–359, doi: 10.1109/ISSPA.2012.6310574.
- [19] B. Boashash, L. Boubchir, and G. Azemi, “A methodology for time-frequency image processing applied to the classification of non-stationary multichannel signals using instantaneous frequency descriptors with application to newborn EEG signals,” *EURASIP Journal on Advances in Signal Processing*, vol. 2012, no. 1, p. 117, 2012, doi: 10.1186/1687-6180-2012-117.
- [20] B. Boashash, B. K. Jawad, and S. Ouelha, “Refining the ambiguity domain characteristics of non-stationary signals for improved time–frequency analysis: test case of multidirectional and multicomponent piecewise LFM and HFM signals,” *Digital Signal Processing*, vol. 83, pp. 367–382, 2018, doi: doi.org/10.1016/j.dsp.2018.05.005.
- [21] P. Borgnat and P. Flandrin, “Time-frequency localization from sparsity constraints,” in *2008 IEEE International Conference on Acoustics, Speech and Signal Processing*, 2008, pp. 3785–3788, doi: 10.1109/ICASSP.2008.4518477.
- [22] M. Born and P. Jordan, “Zur quantenmechanik,” *Zeitschrift fur Physik*, vol. 34, pp. 858–888, 1925.
- [23] L. Boubchir, S. Al-Maadeed, and A. Bouridane, “Haralick feature extraction from time-frequency images for epileptic seizure detection and classification of EEG data,” in *2014 26th International Conference on Microelectronics (ICM)*, 2014, pp. 32–35, doi: 10.1109/ICM.2014.7071799.

- [24] R. J. G. B. Campello, D. Moulavi, and J. Sander, “Density-based clustering based on hierarchical density estimates,” in *Advances in Knowledge Discovery and Data Mining*. Berlin, Heidelberg: Springer Berlin Heidelberg, 2013, pp. 160–172, doi: 10.1007/978-3-642-37456-2_14.
- [25] T.-S. Cao, T.-T.-T. Nguyen, V.-S. Nguyen, V.-H. Truong, and H.-H. Nguyen, “Performance of six metaheuristic algorithms for multi-objective optimization of nonlinear inelastic steel trusses,” *Buildings*, vol. 13, no. 4, 2023, doi: 10.3390/buildings13040868.
- [26] P. Chaudhari, A. K. Thakur, R. Kumar, N. Banerjee, and A. Kumar, “Comparison of NSGA-III with NSGA-II for multi objective optimization of adiabatic styrene reactor,” *Materials Today: Proceedings*, vol. 57, pp. 1509–1514, 2022, international Chemical Engineering Conference 2021 (100 Glorious Years of Chemical Engineering and Technology), doi: 10.1016/j.matpr.2021.12.047.
- [27] H.-I. Choi and W. Williams, “Improved time-frequency representation of multicomponent signals using exponential kernels,” *IEEE Transactions on Acoustics, Speech, and Signal Processing*, vol. 37, no. 6, pp. 862–871, 1989, doi: 10.1109/ASSP.1989.28057.
- [28] C. Coello, G. Pulido, and M. Lechuga, “Handling multiple objectives with particle swarm optimization,” *IEEE Transactions on Evolutionary Computation*, vol. 8, no. 3, pp. 256–279, 2004, doi: 10.1109/TEVC.2004.826067.
- [29] L. Cohen, *Time-Frequency Analysis: Theory and Applications*. USA: Prentice-Hall, Inc., 1995.
- [30] K. Deb and H. Jain, “An evolutionary many-objective optimization algorithm using reference-point-based nondominated sorting approach, part I: solving problems with box constraints,” *IEEE Transactions on Evolutionary Computation*, vol. 18, no. 4, pp. 577–601, 2014, doi: 10.1109/TEVC.2013.2281535.
- [31] M. Deriche, S. Arafat, S. Al-Insaf, and M. Siddiqui, “Eigenspace time frequency based features for accurate seizure detection from EEG data,” *IRBM*, vol. 40, no. 2, pp. 122–132, 2019, doi: 10.1016/j.irbm.2019.02.002.
- [32] J. Dombi, A. Vranković Lacković, and J. Lerga, “A new insight into entropy based on the fuzzy operators, applied to useful information extraction from noisy time-frequency distributions,” *Mathematics*, vol. 11, no. 3, 2023, doi: 10.3390/math11030505.
- [33] S. Dong, B. Boashash, G. Azemi, B. E. Lingwood, and P. B. Colditz, “Automated detection of perinatal hypoxia using time-frequency-based heart rate variability features,” *Medical and Biological Engineering and Computing*, vol. 52, no. 2, pp. 183–191, 2014, doi: 10.1007/s11517-013-1129-3.
- [34] J. J. Durillo, J. García-Nieto, A. J. Nebro, C. A. C. Coello, F. Luna, and E. Alba, “Multi-objective particle swarm optimizers: an experimental comparison,” in *Evolutionary Multi-Criterion Optimization*. Berlin, Heidelberg: Springer Berlin Heidelberg, 2009, pp. 495–509, doi: 10.1007/978-3-642-01020-0_39.
- [35] M. Ester, H.-P. Kriegel, J. Sander, and X. Xu, “A density-based algorithm for discovering clusters in large spatial databases with noise,” in *Proceedings of the Second International Conference on Knowledge Discovery and Data Mining*, ser. KDD’96. Portland, Oregon: AAAI Press, 1996, p. 226–231.

- [36] M. S. Farooq, A. Zulfiqar, and S. Riaz, “Epileptic seizure detection using machine learning: taxonomy, opportunities, and challenges,” *Diagnostics*, vol. 13, no. 6, 2023, doi: 10.3390/diagnostics13061058.
- [37] P. Flandrin and P. Borgnat, “Time-frequency energy distributions meet compressed sensing,” *IEEE Transactions on Signal Processing*, vol. 58, no. 6, pp. 2974–2982, June 2010, doi: 10.1109/TSP.2010.2044839.
- [38] D. Gabor, “Theory of communication,” *Journal of the Institution of Electrical Engineers - Part I: General*, vol. 94, pp. 58–58, 1946.
- [39] A. Gholami, “Sparse time–frequency decomposition and some applications,” *IEEE Transactions on Geoscience and Remote Sensing*, vol. 51, no. 6, pp. 3598–3604, June 2013, doi: 10.1109/TGRS.2012.2220144.
- [40] A. Ghosal, A. Nandy, A. K. Das, S. Goswami, and M. Panday, “A short review on different clustering techniques and their applications,” in *Emerging Technology in Modelling and Graphics*, J. K. Mandal and D. Bhattacharya, Eds. Singapore: Springer Singapore, 2020, pp. 69–83, doi: 10.1007/978-981-13-7403-6_9.
- [41] I. Goodfellow, Y. Bengio, and A. Courville, *Deep Learning*. MIT Press, 2016, <http://www.deeplearningbook.org>.
- [42] A. Gramfort, D. Strohmeier, J. Haueisen, M. S. Hämmäläinen, and M. Kowalski, “Time-frequency mixed-norm estimates: sparse M/EEG imaging with non-stationary source activations,” *NeuroImage*, vol. 70, pp. 410–22, Apr 2013, doi: 10.1016/j.neuroimage.2012.12.051.
- [43] X. He, X. Fu, and Y. Yang, “Energy-efficient trajectory planning algorithm based on multi-objective PSO for the mobile sink in wireless sensor networks,” *IEEE Access*, vol. 7, pp. 176 204–176 217, 2019, doi: 10.1109/ACCESS.2019.2957834.
- [44] F. Hlawatsch and F. Auger, *Time-frequency analysis : concepts and methods*. London, Hoboken, NJ: ISTE ; Wiley, 2008.
- [45] Y. Hua, Q. Liu, K. Hao, and Y. Jin, “A survey of evolutionary algorithms for multi-objective optimization problems with irregular Pareto fronts,” *IEEE/CAA Journal of Automatica Sinica*, vol. 8, no. 2, pp. 303–318, 2021, doi: 10.1109/JAS.2021.1003817.
- [46] Y. Huang, W. Bao, F. Li, and X. Li, “Sparse time-frequency analysis based on instantaneous frequency estimation and fault diagnosis application,” *IEEE Transactions on Instrumentation and Measurement*, vol. 71, pp. 1–9, 2022, doi: 10.1109/TIM.2022.3210987.
- [47] N. Hurley and S. Rickard, “Comparing measures of sparsity,” *IEEE Transactions on Information Theory*, vol. 55, no. 10, pp. 4723–4741, 2009, doi: 10.1109/TIT.2009.2027527.
- [48] Z. Hussain and B. Boashash, “Adaptive instantaneous frequency estimation of multicomponent FM signals using quadratic time-frequency distributions,” *IEEE Transactions on Signal Processing*, vol. 50, no. 8, pp. 1866–1876, 2002, doi: 10.1109/TSP.2002.800406.
- [49] X. Jiang, J. Ma, J. Jiang, and X. Guo, “Robust feature matching using spatial clustering with heavy outliers,” *IEEE Transactions on Image Processing*, vol. 29, pp. 736–746, 2020, doi: 10.1109/TIP.2019.2934572.

- [50] D. Jones and T. Parks, "A high resolution data-adaptive time-frequency representation," *IEEE Transactions on Acoustics, Speech, and Signal Processing*, vol. 38, no. 12, pp. 2127–2135, 1990, doi: 10.1109/29.61539.
- [51] V. Joshi, R. B. Pachori, and A. Vijesh, "Classification of ictal and seizure-free EEG signals using fractional linear prediction," *Biomedical Signal Processing and Control*, vol. 9, pp. 1–5, 2014, doi: 10.1016/j.bspc.2013.08.006.
- [52] V. Jurdana, I. Volaric, and V. Sucic, "The local Rényi entropy based shrinkage algorithm for sparse TFD reconstruction," in *2020 International Conference on Broadband Communications for Next Generation Networks and Multimedia Applications (CoBCom)*, Graz, Austria, July 2020, pp. 1–8, doi: 10.1109/CoBCom49975.2020.9174168.
- [53] V. Jurdana, N. Lopac, and M. Vrankic, "Sparse time-frequency distribution reconstruction using the adaptive compressed sensed area optimized with the multi-objective approach," *Sensors*, vol. 23, no. 8, 2023, doi: 10.3390/s23084148.
- [54] V. Jurdana, I. Volaric, and V. Sucic, "A sparse TFD reconstruction approach using the S-method and local entropies information," in *2021 12th International Symposium on Image and Signal Processing and Analysis (ISPA)*, Zagreb, Croatia, Sep. 2021, pp. 4–9, doi: 10.1109/ISPA52656.2021.9552042.
- [55] —, "Sparse time-frequency distribution reconstruction based on the 2D Rényi entropy shrinkage algorithm," *Digital Signal Processing*, vol. 118, p. 103225, 2021, doi: 10.1016/j.dsp.2021.103225.
- [56] —, "Application of the 2D local entropy information in sparse TFD reconstruction," in *2022 International Conference on Broadband Communications for Next Generation Networks and Multimedia Applications (CoBCom)*, Graz, Austria, Jul. 2022, pp. 1–7, doi: 10.1109/CoBCom55489.2022.9880775.
- [57] V. Jurdana, M. Vrankic, N. Lopac, and G. M. Jadav, "Method for automatic estimation of instantaneous frequency and group delay in time-frequency distributions with application in EEG seizure signals analysis," *Sensors*, vol. 23, no. 10, 2023, doi: 10.3390/s23104680.
- [58] H. Kalbkhani and M. G. Shayesteh, "Stockwell transform for epileptic seizure detection from EEG signals," *Biomedical Signal Processing and Control*, vol. 38, pp. 108–118, 2017, doi: 10.1016/j.bspc.2017.05.008.
- [59] N. A. Khan and S. Ali, "Classification of EEG signals using adaptive time-frequency distributions," *Metrology and Measurement Systems*, vol. 23, no. 2, pp. 251–260, 2016, doi: 10.1515/mms-2016-0021.
- [60] —, "A new feature for the classification of non-stationary signals based on the direction of signal energy in the time–frequency domain," *Computers in Biology and Medicine*, vol. 100, pp. 10–16, 2018, doi: 10.1016/j.compbiomed.2018.06.018.
- [61] —, "A robust and efficient instantaneous frequency estimator of multi-component signals with intersecting time-frequency signatures," *Signal Processing*, vol. 177, p. 107728, 2020, doi: 10.1016/j.sigpro.2020.107728.
- [62] N. A. Khan, S. Ali, and K. Choi, "An instantaneous frequency and group delay based feature for classifying EEG signals," *Biomedical Signal Processing and Control*, vol. 67, p. 102562, 2021, doi: 10.1016/j.bspc.2021.102562.

- [63] —, “Modified time-frequency marginal features for detection of seizures in newborns,” *Sensors*, vol. 22, no. 8, 2022, doi: 10.3390/s22083036.
- [64] N. A. Khan and B. Boashash, “Multi-component instantaneous frequency estimation using locally adaptive directional time frequency distributions,” *International Journal of Adaptive Control and Signal Processing*, vol. 30, no. 3, pp. 429–442, 2016, doi: 10.1002/acs.2583.
- [65] N. A. Khan and I. Djurović, “ADTFD-RANSAC For multi-component IF estimation,” *Signal Processing*, vol. 195, p. 108494, 2022, doi: 10.1016/j.sigpro.2022.108494.
- [66] N. A. Khan, M. Mohammadi, and K. Choi, “A rule-based classifier to detect seizures in EEG signals,” *Circuits, Systems, and Signal Processing*, 2023, doi: 10.1007/s00034-022-02281-3.
- [67] N. A. Khan, M. Mohammadi, and I. Djurović, “A modified viterbi algorithm-based IF estimation algorithm for adaptive directional time-frequency distributions,” *Circuits, Systems, and Signal Processing*, vol. 38, no. 5, pp. 2227–2244, 2019, doi: 10.1007/s00034-018-0960-z.
- [68] N. A. Khan and M. Sandsten, “Time–frequency image enhancement based on interference suppression in Wigner–Ville distribution,” *Signal Processing*, vol. 127, pp. 80–85, 2016, doi: <https://doi.org/10.1016/j.sigpro.2016.02.027>.
- [69] T. S. Kumar, V. Kanhangad, and R. B. Pachori, “Classification of seizure and seizure-free EEG signals using local binary patterns,” *Biomedical Signal Processing and Control*, vol. 15, pp. 33–40, 2015, doi: 10.1016/j.bspc.2014.08.014.
- [70] A. V. Lacković, J. Lerga, and M. Tomić, “Local Shannon, Rényi, and Tsallis entropy for useful content extraction from Choi-Williams and Zhao-Atlas-Marks time-frequency distributions,” in *2022 International Conference on Electrical, Computer, Communications and Mechatronics Engineering (ICECCME)*, 2022, pp. 1–5, doi: 10.1109/ICECCME55909.2022.9988560.
- [71] J. Lerga, N. Saulig, R. Lerga, and I. Štajduhar, “TFD thresholding in estimating the number of EEG components and the dominant if using the short-term Rényi entropy,” in *Proceedings of the 10th International Symposium on Image and Signal Processing and Analysis*, Sep. 2017, pp. 80–85, doi: 10.1109/ISPA.2017.8073573.
- [72] J. Lerga, N. Saulig, and V. Mozetič, “Algorithm based on the short-term Rényi entropy and IF estimation for noisy EEG signals analysis,” *Computers in Biology and Medicine*, vol. 80, pp. 1–13, 2017, doi: 10.1016/j.combiomed.2016.11.002.
- [73] J. Lerga, N. Saulig, L. Stanković, and D. Seršić, “Rule-based EEG classifier utilizing local entropy of time–frequency distributions,” *Mathematics*, vol. 9, no. 4, 2021, doi: 10.3390/math9040451.
- [74] J. Lerga, V. Sucic, and B. Boashash, “An efficient algorithm for instantaneous frequency estimation of nonstationary multicomponent signals in low SNR,” *EURASIP Journal on Advances in Signal Processing*, vol. 2011, no. 1, p. 725189, 2011, doi: 10.1155/2011/725189.
- [75] S. Li, W. Zhou, Q. Yuan, S. Geng, and D. Cai, “Feature extraction and recognition of ictal EEG using EMD and SVM,” *Computers in biology and medicine*, vol. 43, pp. 807–16, Aug 2013, doi: 10.1016/j.combiomed.2013.04.002.

- [76] J. Liang, X. Ban, K. Yu, B. Qu, K. Qiao, C. Yue, K. Chen, and K. C. Tan, "A survey on evolutionary constrained multiobjective optimization," *IEEE Transactions on Evolutionary Computation*, vol. 27, no. 2, pp. 201–221, 2023, doi: 10.1109/TEVC.2022.3155533.
- [77] L. Liu, Y. Xu, F. Zhou, G. Hu, L. Yu, and C. He, "Multiobjective optimization design for a MR damper based on EBFNN and MOPSO," *Applied Sciences*, vol. 12, no. 17, 2022, doi: 10.3390/app12178584.
- [78] Y. Liu, L. Mejias, and Z. Li, "Fast power line detection and localization using steerable filter for active UAV guidance," *The International Archives of the Photogrammetry, Remote Sensing and Spatial Information Sciences*, vol. XXXIX-B3, pp. 491–496, 2012, doi: 10.5194/isprsarchives-XXXIX-B3-491-2012.
- [79] N. Lopac, "Detection of gravitational-wave signals from time-frequency distributions using deep learning," Ph.D. dissertation, University of Rijeka. Faculty of Engineering, 2022.
- [80] N. Lopac, F. Hrzić, I. P. Vuksanović, and J. Lerga, "Detection of non-stationary GW signals in high noise from Cohen's class of time-frequency representations using deep learning," *IEEE Access*, vol. 10, pp. 2408–2428, 2021, doi: 10.1109/ACCESS.2021.3139850.
- [81] N. Lopac, J. Lerga, and E. Cuoco, "Gravitational-wave burst signals denoising based on the adaptive modification of the intersection of confidence intervals rule," *Sensors*, vol. 20, no. 23, p. 6920, 2020, doi: 10.3390/s20236920.
- [82] N. Lopac, J. Lerga, N. Saulig, L. Stanković, and M. Daković, "On optimal parameters for ICI-based adaptive filtering applied to the GWs in high noise," in *2021 6th International Conference on Smart and Sustainable Technologies (SpliTech)*. IEEE, 2021, pp. 1–6, doi: 10.23919/SpliTech52315.2021.9566364.
- [83] K. Majumdar, "Differential operator in seizure detection," *Computers in Biology and Medicine*, vol. 42, no. 1, pp. 70–74, 2012, doi: 10.1016/j.combiomed.2011.10.010.
- [84] A. Mesbah, A. van Deursen, and S. Lenselink, "Crawling ajax-based web applications through dynamic analysis of user interface state changes," *ACM Trans. Web*, vol. 6, no. 1, mar 2012, doi: 10.1145/2109205.2109208.
- [85] W. A. Mir, M. Anjum, Izharuddin, and S. Shahab, "Deep-EEG: an optimized and robust framework and method for EEG-based diagnosis of epileptic seizure," *Diagnostics*, vol. 13, no. 4, 2023, doi: 10.3390/diagnostics13040773.
- [86] M. Mohammadi, N. Ali Khan, H. Hassanpour, and A. Hussien Mohammed, "Spike detection based on the adaptive time-frequency analysis," *Circuits, Systems, and Signal Processing*, vol. 39, no. 11, pp. 5656–5680, 2020, doi: 10.1007/s00034-020-01427-5.
- [87] M. Mohammadi, A. A. Pouyan, N. A. Khan, and V. Abolghasemi, "Locally optimized adaptive directional time-frequency distributions," *Circuits, Systems, and Signal Processing*, vol. 37, no. 8, pp. 3154–3174, 2018, doi: 10.1007/s00034-018-0802-z.
- [88] J. A. Nelder and R. Mead, "A simplex method for function minimization," *The Computer Journal*, vol. 7, no. 4, pp. 308–313, 01 1965, doi: 10.1093/comjnl/7.4.308.

- [89] I. Orović, S. Stanković, and T. Thayaparan, “Time–frequency-based instantaneous frequency estimation of sparse signals from incomplete set of samples,” *IET Signal Processing*, vol. 8, no. 3, pp. 239–245, 2014, doi: 10.1049/iet-spr.2013.0354.
- [90] R. B. Pachori and V. Bajaj, “Analysis of normal and epileptic seizure EEG signals using empirical mode decomposition,” *Computer Methods and Programs in Biomedicine*, vol. 104, no. 3, pp. 373–381, 2011, doi: 10.1016/j.cmpb.2011.03.009.
- [91] A. Papandreou-Suppappola, *Applications in Time-Frequency Signal Processing*. CRC Press, 2002.
- [92] P. Paral, A. Chatterjee, and A. Rakshit, “Vision sensor-based shoe detection for human tracking in a human–robot coexisting environment: A photometric invariant approach using DBSCAN algorithm,” *IEEE Sensors Journal*, vol. 19, no. 12, pp. 4549–4559, June 2019, doi: 10.1109/JSEN.2019.2897989.
- [93] J. Principe, *Information Theoretic Learning: Renyi’s Entropy and Kernel Perspectives*. Springer New York, NY, 01 2010, doi: 10.1007/978-1-4419-1570-2.
- [94] K. Qiu and A. Dogandzic, “Sparse signal reconstruction via ECME hard thresholding,” *IEEE Transactions on Signal Processing*, vol. 60, no. 9, pp. 4551–4569, Sep. 2012, doi: 10.1109/TSP.2012.2203818.
- [95] L. Rankine, M. Mesbah, and B. Boashash, “IF estimation for multicomponent signals using image processing techniques in the time–frequency domain,” *Signal Processing*, vol. 87, no. 6, pp. 1234–1250, 2007, doi: 10.1016/j.sigpro.2006.10.013.
- [96] K. Ren, L. Du, B. Wang, Q. Li, and J. Chen, “Statistical compressive sensing and feature extraction of time–frequency spectrum from narrowband radar,” *IEEE Transactions on Aerospace and Electronic Systems*, vol. 56, no. 1, pp. 326–342, Feb 2020, doi: 10.1109/TAES.2019.2914518.
- [97] A. Sadollah, H. Eskandar, A. Bahreininejad, and J. H. Kim, “Water cycle algorithm for solving multi-objective optimization problems,” *Soft Computing*, vol. 19, no. 9, pp. 2587–2603, 2015, doi: 10.1007/s00500-014-1424-4.
- [98] A. Sadollah, H. Eskandar, and J. H. Kim, “Water cycle algorithm for solving constrained multi-objective optimization problems,” *Applied Soft Computing*, vol. 27, pp. 279–298, 2015, doi: 10.1016/j.asoc.2014.10.042.
- [99] N. Saini and S. Saha, “Multi-objective optimization techniques: a survey of the state-of-the-art and applications,” *The European Physical Journal Special Topics*, vol. 230, no. 10, pp. 2319–2335, 2021, doi: 10.1140/epjs/s11734-021-00206-w.
- [100] J. Sander, M. Ester, H.-P. Kriegel, and X. Xu, “Density-based clustering in spatial databases: The algorithm GDBSCAN and its applications,” *Data Mining and Knowledge Discovery*, vol. 2, no. 2, pp. 169–194, Jun. 1998, doi: 10.1023/A:1009745219419.
- [101] N. Saulig, N. Pustelnik, P. Borgnat, P. Flandrin, and V. Sucic, “Instantaneous counting of components in nonstationary signals,” in *21st European Signal Processing Conference (EUSIPCO 2013)*, 2013, pp. 1–5.
- [102] N. Saulig, J. Lerga, Z. Milanović, and C. Ioana, “Extraction of useful information content from noisy signals based on structural affinity of clustered TFDs’ coefficients,” *IEEE Transactions on Signal Processing*, vol. 67, no. 12, pp. 3154–3167, 2019, doi: 10.1109/TSP.2019.2912134.

- [103] N. Saulig, J. Lerga, S. Miličić, and Z. Tomasović, “Block-adaptive Rényi entropy-based denoising for non-stationary signals,” *Sensors*, vol. 22, no. 21, 2022, doi: 10.3390/s22218251.
- [104] N. Saulig, I. Orović, and V. Sucic, “Optimization of quadratic time–frequency distributions using the local Rényi entropy information,” *Signal Processing*, vol. 129, pp. 17–24, 2016, doi: doi.org/10.1016/j.sigpro.2016.05.025.
- [105] N. Saulig, Željka Milanović, and C. Ioana, “A local entropy-based algorithm for information content extraction from time–frequency distributions of noisy signals,” *Digital Signal Processing*, vol. 70, pp. 155–165, 2017, doi: 10.1016/j.dsp.2017.08.005.
- [106] E. Schubert, J. Sander, M. Ester, H. P. Kriegel, and X. Xu, “DBSCAN Revisited, Revisited: Why and How You Should (Still) Use DBSCAN,” *ACM Trans. Database Syst.*, vol. 42, no. 3, Jul. 2017, doi: 10.1145/3068335.
- [107] E. Sejdić and L. F. Chaparro, “Time-frequency representations based on compressive samples,” in *21st European Signal Processing Conference (EUSIPCO 2013)*, Sep. 2013, pp. 1–4. [Online]. Available: <http://imedlab.org/pdfs/papers/cs-tfr-eusipco.pdf>
- [108] E. Sejdić, I. Orović, and S. Stanković, “Compressive sensing meets time-frequency: An overview of recent advances in time-frequency processing of sparse signals.” *Digital signal processing*, vol. 77, pp. 22–35, Jun 2018, doi: 10.1016/j.dsp.2017.07.016.
- [109] M. Sharma, R. B. Pachori, and U. Rajendra Acharya, “A new approach to characterize epileptic seizures using analytic time-frequency flexible wavelet transform and fractal dimension,” *Pattern Recognition Letters*, vol. 94, pp. 172–179, 2017, doi: 10.1016/j.patrec.2017.03.023.
- [110] S. Sharma and V. Kumar, “A comprehensive review on multi-objective optimization techniques: Past, present and future,” *Archives of Computational Methods in Engineering*, vol. 29, no. 7, pp. 5605–5633, 2022, doi: 10.1007/s11831-022-09778-9.
- [111] J. Shen, X. Hao, Z. Liang, Y. Liu, W. Wang, and L. Shao, “Real-time superpixel segmentation by DBSCAN clustering algorithm,” *IEEE Transactions on Image Processing*, vol. 25, no. 12, pp. 5933–5942, Dec 2016, doi: 10.1109/TIP.2016.2616302.
- [112] A. Soroudi, M. Ehsan, and H. Zareipour, “A practical eco-environmental distribution network planning model including fuel cells and non-renewable distributed energy resources,” *Renewable Energy*, vol. 36, no. 1, pp. 179–188, 2011, doi: 10.1016/j.renene.2010.06.019.
- [113] L. Stankovic, M. Dakovic, and T. Thayaparan, *Time-Frequency Signal Analysis with Applications*. Boston, USA: Artech House Publishers, Feb. 2013.
- [114] L. Stanković, I. Orović, S. Stanković, and M. Amin, “Compressive sensing based separation of nonstationary and stationary signals overlapping in time-frequency,” *IEEE Transactions on Signal Processing*, vol. 61, no. 18, pp. 4562–4572, Sep. 2013, doi: 10.1109/TSP.2013.2271752.
- [115] L. Stanković, S. Stanković, I. Orović, and M. G. Amin, “Robust time-frequency analysis based on the L-estimation and compressive sensing,” *IEEE Signal Processing Letters*, vol. 20, no. 5, pp. 499–502, May 2013, doi: 10.1109/LSP.2013.2252899.
- [116] L. Stanković, “A measure of some time–frequency distributions concentration,” *Signal Processing*, vol. 81, no. 3, pp. 621 – 631, 2001, doi: 10.1016/S0165-1684(00)00236-X.

- [117] N. Stevenson, J. O’Toole, L. Rankine, G. Boylan, and B. Boashash, “A nonparametric feature for neonatal EEG seizure detection based on a representation of pseudo-periodicity,” *Medical Engineering & Physics*, vol. 34, no. 4, pp. 437–446, 2012, doi: 10.1016/j.medengphy.2011.08.001.
- [118] V. Sucic, J. Lerga, and B. Boashash, “Multicomponent noisy signal adaptive instantaneous frequency estimation using components time support information,” *IET Signal Processing*, vol. 8, no. 3, pp. 277–284, 2014, doi: 10.1049/iet-spr.2013.0349.
- [119] —, “Multicomponent noisy signal adaptive instantaneous frequency estimation using components time support information,” *IET Signal Processing*, vol. 8, no. 3, pp. 277–284, 2014, doi: 10.1049/iet-spr.2013.0349.
- [120] V. Sucic, N. Saulig, and B. Boashash, “Estimating the number of components of a multicomponent nonstationary signal using the short-term time-frequency Rényi entropy,” *EURASIP Journal on Advances in Signal Processing*, vol. 2011, no. 1, p. 125, Dec. 2011, doi: 10.1186/1687-6180-2011-125.
- [121] —, “Analysis of local time-frequency entropy features for nonstationary signal components time supports detection,” *Digital Signal Processing*, vol. 34, pp. 56 – 66, 2014, doi: 10.1016/j.dsp.2014.07.013.
- [122] K. Tang, K. Man, S. Kwong, and Q. He, “Genetic algorithms and their applications,” *IEEE Signal Processing Magazine*, vol. 13, no. 6, p. 22 – 37, 1996, cited by: 727, doi: 10.1109/79.543973.
- [123] C. Tong, S. Wang, I. Selesnick, R. Yan, and X. Chen, “Ridge-aware weighted sparse time-frequency representation,” *IEEE Transactions on Signal Processing*, vol. 69, pp. 136–149, 2021, doi: 10.1109/TSP.2020.3039871.
- [124] M. Varli and H. Yilmaz, “Multiple classification of EEG signals and epileptic seizure diagnosis with combined deep learning,” *Journal of Computational Science*, vol. 67, p. 101943, 2023, doi: 10.1016/j.jocs.2023.101943.
- [125] A. Varsavsky, I. Mareels, and M. Cook, *Epileptic seizures and the EEG: measurement, models, detection and prediction*. Taylor & Francis, 2011.
- [126] J. Ville, “Theorie et applications de la notion de signal analytique,” *Cables Transmission*, vol. 2, pp. 61–74, 1948.
- [127] I. Volarić, “Signal concentration enhancement in the time-frequency domain using adaptive compressive sensing,” Ph.D. dissertation, Faculty of Engineering, University of Rijeka, 2017.
- [128] I. Volaric and V. Sucic, “On the noise impact in the L1 based reconstruction of the sparse time-frequency distributions,” in *2016 International Conference on Broadband Communications for Next Generation Networks and Multimedia Applications (CoBCom)*, 2016, pp. 1–6, doi: 10.1109/COBCOM.2016.7593495.
- [129] —, “Localized Rényi entropy based sparse TFD reconstruction,” in *Proceedings of the Second International Balkan Conference on Communications and Networking BalkanCom 2018 Podgorica, Montenegro*, 06 2018, pp. 1–5.
- [130] —, “On the L0-norm based sparse time-frequency distribution reconstruction,” in *2018 International Conference on Broadband Communications for Next Generation Networks and Multimedia Applications (CoBCom)*, 2018, pp. 1–8, doi: 10.1109/COBCOM.2018.8443966.

- [131] I. Volaric, V. Sucic, and S. Stankovic, “A data driven compressive sensing approach for time-frequency signal enhancement,” *Signal Processing*, vol. 141, pp. 229 – 239, 2017, doi: 10.1016/j.sigpro.2017.06.013.
- [132] A. Vranković, I. Ipšić, and J. Lerga, “Entropy-based extraction of useful content from spectrograms of noisy speech signals,” in *2021 International Symposium ELMAR*, 2021, pp. 83–86, doi: 10.1109/ELMAR52657.2021.9550891.
- [133] A. Vranković, J. Lerga, and N. Saulig, “A novel approach to extracting useful information from noisy TFDs using 2D local entropy measures,” *EURASIP Journal on Advances in Signal Processing*, vol. 2020, no. 1, p. 18, Apr. 2020, doi: 10.1186/s13634-020-00679-2.
- [134] H. Wang, S. Yang, Y. Liu, and Q. Li, “Compressive sensing reconstruction for rolling bearing vibration signal based on improved iterative soft thresholding algorithm,” *Measurement*, vol. 210, p. 112528, 2023, doi: 10.1016/j.measurement.2023.112528.
- [135] P. Wang, E. Cetin, A. G. Dempster, Y. Wang, and S. Wu, “Improved characterization of GNSS jammers using short-term time-frequency Rényi entropy,” *IEEE Transactions on Aerospace and Electronic Systems*, vol. 54, no. 4, pp. 1918–1930, Aug 2018, doi: 10.1109/TAES.2018.2805195.
- [136] Z. Wang, S. Wang, Q. Wang, Z. Zhan, W. Zhao, and S. Huang, “Bayesian compressive sensing for recovering the time-frequency representation of under-sampled Lamb wave signals,” *Applied Acoustics*, vol. 187, p. 108480, 2022, doi: 10.1016/j.apacoust.2021.108480.
- [137] E. Wigner, “On the quantum correction for thermodynamic equilibrium,” *Phys. Rev.*, vol. 40, pp. 749–759, Jun 1932, doi: 10.1103/PhysRev.40.749.
- [138] W. Williams and T. Sang, “Adaptive RID kernels which minimize time-frequency uncertainty,” in *Proceedings of IEEE-SP International Symposium on Time-Frequency and Time-Scale Analysis*, 1994, pp. 96–99, doi: 10.1109/TFSA.1994.467355.
- [139] S. J. Wright, R. D. Nowak, and M. A. T. Figueiredo, “Sparse reconstruction by separable approximation,” *IEEE Transactions on Signal Processing*, vol. 57, no. 7, pp. 2479–2493, July 2009, doi: 10.1109/TSP.2009.2016892.
- [140] L. Xing, Y. Wen, S. Xiao, J. Zhang, and D. Zhang, “Compressed-sensing-based time–frequency representation for disturbance characterization of Maglev on-board distribution systems,” *Electronics*, vol. 9, no. 11, 2020, doi: 10.3390/electronics9111909.
- [141] D. Xu and Y. Tian, “A comprehensive survey of clustering algorithms,” *Annals of Data Science*, vol. 2, no. 2, pp. 165–193, 2015, doi: 10.1007/s40745-015-0040-1.
- [142] R. Xu and D. Wunsch, “Survey of clustering algorithms,” *IEEE Transactions on Neural Networks*, vol. 16, no. 3, pp. 645–678, 2005, doi: 10.1109/TNN.2005.845141.
- [143] J. Yang and Y. Zhang, “Alternating direction algorithms for ℓ_1 -problems in compressive sensing,” *SIAM J. Sci. Comput.*, vol. 33, pp. 250–278, 2011, doi: 10.1137/090777761.
- [144] K. Yang, K. Yu, and H. Wang, “A hybrid method of multi-objective particle swarm optimization and k-means clustering and its application to modal parameter estimation in the time–frequency domain,” *Journal of Vibration and Control*, vol. 26, no. 9-10, pp. 769–778, 2020, doi: 10.1177/1077546319889787.

- [145] Y. Yang, M. Suliang, W. Jianwen, J. Bowen, L. Weixin, and L. Xiaowu, “Fault diagnosis in gas insulated switchgear based on genetic algorithm and density-based spatial clustering of applications with noise,” *IEEE Sensors Journal*, vol. 21, no. 2, pp. 965–973, Jan 2021, doi: 10.1109/JSEN.2019.2942618.
- [146] Q. Yuan, W. Zhou, L. Zhang, F. Zhang, F. Xu, Y. Leng, D. Wei, and M. Chen, “Epileptic seizure detection based on imbalanced classification and wavelet packet transform,” *Seizure*, vol. 50, pp. 99–108, 2017, doi: 10.1016/j.seizure.2017.05.018.
- [147] Z. Zhang, Y. Xu, J. Yang, X. Li, and D. Zhang, “A survey of sparse representation: algorithms and applications,” *IEEE Access*, vol. 3, pp. 490–530, 2015, doi: 10.1109/ACCESS.2015.2430359.
- [148] X. Zhu and T. Fujii, “A novel modulation classification method in cognitive radios based on features clustering of time-frequency,” in *2016 IEEE Radio and Wireless Symposium (RWS)*, 2016, pp. 45–47, doi: 10.1109/RWS.2016.7444364.
- [149] A. Şengür, Y. Guo, and Y. Akbulut, “Time-frequency texture descriptors of EEG signals for efficient detection of epileptic seizure,” *Brain Informatics*, vol. 3, no. 2, pp. 101–108, 2016, doi: 10.1007/s40708-015-0029-8.

LIST OF ABBREVIATIONS

ADTFD	adaptive directional time-frequency distribution
AF	ambiguity function
AWGN	additive white Gaussian noise
BJD	Born-Jordan distribution
BSS	blind-source separation
BSS-STRE	blind source separation method with the short-term Rényi entropy
BSS-STRE-NBRE	blind source separation method with the short-term and narrow-band Rényi entropies
CS	compressive sensing
CS-AF	compressive sensed ambiguity function
CWD	Choi-Williams distribution
DBSCAN	density-based spatial clustering of applications with noise
DGF	double-derivative directional Gaussian filter
EEG	electroencephalogram
EMBD	extended modified B distribution
FSM	fuzzy-satisfying method
FT	Fourier transform
GA	genetic algorithm
GD	group delay
GDM	gradient-descent method
HGA	hybrid generic algorithm
IACF	instantaneous auto-correlation function
IF	instantaneous frequency
Image-based-STRE	image-based method with the short-term Rényi entropy
Image-based-STRE-NBRE	image-based method with the short-term and narrow-band Rényi entropies
LFM	linear frequency modulated
LO-ADTFD	locally optimized adaptive directional time-frequency distribution
LRE	localized Rényi entropy
MAE	mean absolute error
MAX	maximum absolute error
MBD	modified B distribution
MOPSO	multi-objective particle swarm optimization

MOWCA	multi-objective water cycle algorithm
MSE	mean squared error
NBRE	narrow-band Rényi entropy
NSGA-III	non-dominated sorting genetic algorithm III
PFM	parabolic frequency modulated
PSO	particle-swarm optimization
QTFD	quadratic time-frequency distribution
RID	reduced-interference distribution
SALSA	split augmented Lagrangian shrinkage algorithm
SNR	signal-to-noise ratio
SD	spectral delay
SpaRSA	sparse reconstruction by separable approximation
SPEC	spectrogram
STFT	short-time Fourier transform
STRE	short-term Rényi entropy
TF	time-frequency
TFD	time-frequency distribution
TwIST	two-step iterative shrinkage/thresholding
WVD	Wigner-Ville distribution
YALL1	your augmented Lagrangian algorithm for ℓ_1

LIST OF SYMBOLS

Latin symbols:

$\{\cdot\}^+$	optimal value
$[\cdot]^{[n]}$	solution of the n -th algorithm iteration
$\{\cdot\}^f$	shrinkage conducted on frequency slices using the narrow-band Rényi entropy
$\{\cdot\}^t$	shrinkage conducted on time slices using the short-term Rényi entropy
a, b, WL	parameters of the adaptive directional time-frequency distribution
$a_i(t)$	instantaneous amplitude of the i -th signal component
$A_z(\nu, \tau)$	ambiguity function of $z(t)$
$\mathcal{A}_z(\nu, \tau)$	filtered ambiguity function of $z(t)$
$\mathbf{A}_z(\nu, \tau)$	matrix representation of $A_z(\nu, \tau)$
$\mathbf{A}_z^M(\nu, \tau)$	compressive sensed $\mathbf{A}_z(\nu, \tau)$, i.e., CS-AF area
$\mathbf{A}_{z_\Gamma}(\nu, \tau)$	$N'_\tau \times N'_\nu$ area parametrized with Γ
$\mathbf{A}_{z_\Lambda}(\nu, \tau)$	AF area outside the $N'_\tau \times N'_\nu$ parametrized with Λ
$B(t, f)$	binary TFD consisted of estimated IFs and GDs
$B_f(t, f)$	binary TFD consisted of estimated GDs
B_r, B_l	frequency band of signal's component in the blind source separation method
$B_t(t, f)$	binary TFD consisted of estimated IFs
$B^{(\text{BSS})}(t, f)$	binary TFD consisted of estimated IFs and/or GDs obtained using the blind source separation method
$B^{(\text{IM})}(t, f)$	binary TFD consisted of estimated IFs and/or GDs obtained using the image-based estimation method
$B^{(\text{shrink})}(t, f)$	binary TFD consisted of estimated IFs and/or GDs obtained using the shrinkage operator
$c(\Upsilon_z(t, f))$	generalized regularization function
$C_M(t, f)$	component alignment binary map
C_Ω	index set of CS-AF samples in the AF
d	Euclidean distance
d_{\max}, N_{sr}	parameters of the multi-objective water cycle algorithm
$D_\chi(t, f)$	TFD containing distance values at the positions of estimated IFs and GDs
E_z	total energy of signal $z(t)$

f	continuous frequency
f_0	frequency slice
$f_{0_i}(t)$	instantaneous frequency of the i -th signal component
F-norm	Frobenius norm
$F_z(t, f)$	short-time Fourier transform of $z(t)$
\mathcal{F}	Fourier transform
FN	false negatives
FP	false positives
$g(\nu, \tau)$	kernel in the ambiguity domain
$G(t, \tau)$	kernel in the time-lag domain
\mathcal{H}	Hilbert transform
H	parameter of the M^H
HV	hypervolume
$K_z(t, \tau)$	instantaneous auto-correlation function of $z(t)$
$minPts$	minimum number of samples inside the \mathcal{N}_ε of the DBSCAN
m_r, p_c, p_m	parameters of the non-dominated sorting genetic algorithm III
M^H	Hoyer concentration measure
M^{RN}	ratio-of-norms concentration measure
M^S	concentration measure proposed by Stanković
$MAE_{t,f},$ $MAX_{t,f}, MSE_{t,f}$	mean absolute, maximum absolute and mean squared errors between the local number of components in the starting and reconstructed TFD obtained from the STRE (notation t) and NBRE (notation f) methods
N_{dom}	number of dominated solutions involved in hypervolume analysis
N_f	number of available frequency samples
N_{it}	maximum number of iterations for sparse reconstruction algorithms
N_{obj}	number of objective functions in multi-objective meta-heuristic optimization
N_{par}	number of Pareto optimal solutions in the repository
N_{pop}	number of particles in multi-objective meta-heuristic algorithm (population size)
N_r	number of regions with continuously-connected TFD samples
N_t	number of available time samples
N_{tot}	number of randomly-inserted solutions in hypervolume analysis
NC	total number of signal components
$NC_f(f)$	number of signal components in narrow band obtained using the NBRE
$NC_t(t)$	instantaneous number of signal components obtained using the STRE
N'_ν	number of Doppler bins in $N'_\tau \times N'_\nu$
N'_τ	number of lag bins in $N'_\tau \times N'_\nu$
$N'_\tau \times N'_\nu$	rectangular adaptive CS-AF area
\mathcal{N}_ε	ε -neighborhood

p	weighting parameter of the Rényi entropy-based shrinkage algorithm
p_s	parameter of the M^S
R	Rényi entropy
$R_\chi(t, f)$	TFD with resolution values at the positions of estimated IFs and GDs
$s(t)$	real signal
$s_{\text{EEG}}(t)$	real-life EEG seizure signal
$S_z(t, f)$	spectrogram of $z(t)$
t	continuous time
t_0	time slice
T_k	time at which the k -th spike component of EEG seizure signal occurs
T_{max}	number of iterations of multi-objective meta-heuristic algorithm
TN	true negatives
TP	true positives
$z(t)$	analytic associate of $s(t)$
$z_{\text{EEG}}(t)$	analytic associate of a real-life EEG seizure signal
$z_{\text{EEG}_{\text{fit}}}(t)$	analytic associate of a real-life EEG seizure signal with a differentiator filter
$z_{\text{grav}}(t)$	analytic associate of a real-life gravitational signal
$z_{\text{LFM}}(t)$	synthetic signal consisted of four LFM components embedded in AWGN with SNR = 5 dB
$z_{\text{mix}}(t)$	synthetic signal consisted of two constant FM and four non-LFM components
$z_{\text{PFM}}(t)$	synthetic signal consisted of two parabolic FM components embedded in AWGN with SNR = 6 dB
$z_{\text{SINLFM}}(t)$	synthetic signal consisted of one LFM component and one sinusoidal component
$Z(f)$	Fourier transform of $z(t)$
$Z_{\text{SINLFM}}(f)$	Fourier transform of $z_{\text{SINLFM}}(t)$
v_j	j -th objective function of the fuzzy-satisfying method
w, m_r, c_1, c_2	parameters of the multi-objective particle swarm optimization algorithm
$W_z(t, f)$	Wigner-Ville distribution of $z(t)$

Greek symbols:

α_{BJ}	kernel parameter of the Born-Jordan distribution
$\alpha_{\text{EMB}}, \beta_{\text{EMB}}$	kernel parameters of the extended modified B distribution
α_{R}	order of the Rényi entropy
$\alpha_{\text{SpaRSA}}, \beta_{\text{SpaRSA}}$	parameters of the sparse reconstruction by separable approximation algorithm

$\alpha_{\text{TWIST}}, \beta_{\text{TWIST}}$	parameters of the two-step iterative shrinkage/thresholding algorithm
$\alpha_{\text{YALL1}}, \beta_{\text{YALL1}}, \gamma_{\text{YALL}}, \mu_{\text{YALL}}$	parameters of the your augmented Lagrangian algorithm for ℓ_1
β_{MB}	kernel parameter of the modified B distribution
$\gamma(t, f)$	kernel in the time-frequency domain
$\gamma_{\theta}(t, f)$	adaptive directional kernel in the time-frequency domain
Γ	minimum normalized magnitude of the AF sample selected from the $\mathbf{A}_{z_{\Gamma}}(\nu, \tau)$
δ_f, δ_t	parameters of the Rényi entropy-based shrinkage algorithm
Δ_{f_0}	operator which denotes that all TFD samples are set to zero, except those in the vicinity of $f = f_0$
Δ_{t_0}	operator which denotes that all TFD samples are set to zero, except those in the vicinity of $t = t_0$
Δ_{NC}	difference in the number of local components between the observed maximum and the minima to the left and right
Δ_x	maximum allowable range in a time or frequency slice in which a non-negative TFD value is considered as auto-term
ϵ	accuracy of the $\Upsilon_z(t, f)$ reconstruction
ε	radius parameter of the DBSCAN
$\eta_t\{\cdot\}$	operator that retains in the TFD only those TF regions that are defined by $C_M(t, f) = 1$
$\eta_f\{\cdot\}$	operator that retains in the TFD only those TF regions that are defined by $C_M(t, f) = 0$
θ	parameter controlling direction of kernel $\gamma_{\theta}(t, f)$
Θ_f	window length at f_0
Θ_t	window length at t_0
λ	regularization parameter
Λ	minimum normalized magnitude of the AF sample selected from the $\mathbf{A}_{z_{\Lambda}}(\nu, \tau)$
ν	Doppler variable
ξ_j^k	linear membership function for the k -th solution of the j -th objective function of the fuzzy-satisfying method
$\hat{\rho}(t, f)$	ideal time-frequency distribution
$\rho(t, f)$	generalized Quadratic time-frequency distribution
$\rho_{(ad)}(t, f)$	adaptive directional time-frequency distribution
$\rho_{(lo)}(t, f)$	locally adaptive directional time-frequency distribution
$\rho_{\text{ref}}(t, f)$	generalized Quadratic TFD of the local Rényi entropy reference signal
σ_{CW}	kernel parameter of the Choi-Williams distribution
σ_G	width of the Gaussian function
$\mathfrak{s}_z(t, f)$	soft-thresholding result
$\mathfrak{s}'_z(t, f)$	argument of the soft-thresholding operator
τ	lag variable

$\tau_{d_i}(f)$	spectral delay of the i -th signal component
$\Upsilon_z(t, f)$	reconstructed time-frequency distribution
$\Upsilon_z(t, f)$	matrix representation of the reconstructed time-frequency distribution
$\hat{\Upsilon}_z(t, f)$	optimal $\Upsilon_z(t, f)$
$\Upsilon_z^{\ell_0}(t, f)$	$\hat{\Upsilon}_z(t, f)$ obtained with the ℓ_0 minimization
$\Upsilon_z^{\ell_1}(t, f)$	$\hat{\Upsilon}_z(t, f)$ obtained with the ℓ_1 minimization
$\phi_i(t)$	instantaneous phase of the i -th signal component
χ	IF/GD-based measure calculated as the mean value of its components
χ_{at}	IF/GD-based measure component determining the auto-term preservation quality of a TFD
χ_{ct}	IF/GD-based measure component determining the cross-term suppression quality of a TFD
χ_r	IF/GD-based measure component determining the auto-term resolution quality of a TFD
Ψ	domain transformation matrix representing the 2D Fourier transform
Ω	database matrix consisted of AF samples from $\mathbf{A}_{z_T}(\nu, \tau)$ and $\mathbf{A}_{z_\Lambda}(\nu, \tau)$

LIST OF FIGURES

Figure 2.1	Example of a stationary signal $z(t)$ with a constant frequency spectrum: (a) the signal's instantaneous power, $ z(t) ^2$; (b) the signal's energy spectrum, $ Z(f) ^2$	8
Figure 2.2	Example of a two-component non-stationary signal $z_{\text{SINLFM}}(t)$ with a linear and sinusoidal frequency modulated component: (a) the signal's instantaneous power, $ z_{\text{SINLFM}}(t) ^2$; (b) the signal's energy spectrum, $ Z_{\text{SINLFM}}(f) ^2$	9
Figure 2.3	Ideal TFDs of the considered examples of: (a) a stationary signal; (b) a non-stationary signal with a linear and sinusoidal frequency modulated component, $z_{\text{SINLFM}}(t)$	11
Figure 2.4	Ambiguity function of the considered examples of: (a) a stationary signal with two constant frequency modulated components; (b) a non-stationary signal with a linear and sinusoidal frequency modulated component, $z_{\text{SINLFM}}(t)$	16
Figure 2.5	Considered QTFDs of the signal $z_{\text{SINLFM}}(t)$: (a) WVD; (b) SPEC (<i>Hamming</i> , $N_w = 32$); (c) CWD ($\sigma_{\text{CW}} = 1$), (d) BJD ($\alpha_{\text{BJ}} = 0.4$), (e) MBD ($\beta_{\text{MB}} = 0.2$); (f) EMBD ($\alpha_{\text{EMB}} = 0.3, \beta_{\text{EMB}} = 0.12$.) . . .	17
Figure 2.6	LO-ADTFD of the signal $z_{\text{SINLFM}}(t)$	19
Figure 3.1	Ambiguity functions with the static CS-AF area, $\sqrt{N_t} \times \sqrt{N_t}$, (red rectangle) versus the automatically obtained adaptive CS-AF area, N'_τ and N'_ν , (black rectangle): (a) $z_{\text{SINLFM}}(t)$, $\sqrt{N_t} \cong 11$ (static), $N'_\tau = 25, N'_\nu = 11$ (adaptive); (b) $z_{\text{LFM}}(t)$, $\sqrt{N_t} \cong 15$ (static), $N'_\tau = 17, N'_\nu = 31$ (adaptive).	25
Figure 3.2	Reconstructed TFDs for the following signal, reconstruction algorithm and parameter λ : (a) $z_{\text{SINFM}}(t)$, TwIST, $\lambda = 15$; (b) $z_{\text{SINFM}}(t)$, TwIST, $\lambda = 0.01$; (c) $z_{\text{SINFM}}(t)$, SALSA, $\lambda = 15$; (d) $z_{\text{SINFM}}(t)$, SALSA, $\lambda = 1$; (e) $z_{\text{LFM}}(t)$, SpaRSA, $\lambda = 15$; (b) $z_{\text{LFM}}(t)$, SpaRSA, $\lambda = 0.01$; (c) $z_{\text{LFM}}(t)$, YALL1, $\lambda = 15$; (d) $z_{\text{LFM}}(t)$, YALL1, $\lambda = 1$	29
Figure 4.1	Extracted components (in red) taken at time slice $t_0 = 71$: (a) the STRE method's reference signal; (b) the signal $z_{\text{LFM}}(t)$, $NC_t(71) = 6.1777 \gg 2$	36
Figure 4.2	Extracted components (in red) taken at frequency slice $f_0 = 200$ of: (a) the NBRE method's reference signal; (b) the signal $z_{\text{LFM}}(t)$, $NC_f(200) = 1.9058 \cong 2$	37

Figure 4.3	The ideal (red dashed line) and obtained (blue solid line) local numbers of components for the considered signals: (a, b) $z_{\text{SINLFM}}(t)$ with $\alpha_{\text{R}} = 3$ and $\Theta_t = \Theta_f = 5$; (c, d) $z_{\text{LFM}}(t)$ with $\alpha_{\text{R}} = 3$ and $\Theta_t = \Theta_f = 11$	37
Figure 4.4	The local numbers of components in starting (depicted with a solid blue line) and reconstructed TFD obtained by the TwIST algorithm (depicted with a dashed red line) for the signal $z_{\text{SINLFM}}(t)$ with: (a, b) $\lambda = 15$; (c, d) $\lambda = 0.01$	40
Figure 4.5	Reconstructed TFDs for the signal $z_{\text{SINLFM}}(t)$ optimized with two objective function formalizations: (a) TwIST, M^{S} ; (b) TwIST, N_r ; (c) SpaRSA, M^{S} ; (d) SpaRSA, N_r ; (e) SALSA, M^{S} ; (f) SALSA, N_r ; (g) YALL1, M^{S} ; (h) YALL1, N_r	47
Figure 4.6	Reconstructed TFDs for the signal $z_{\text{LFM}}(t)$ optimized with two objective function formalizations: (a) TwIST, M^{S} ; (b) TwIST, N_r ; (c) SpaRSA, M^{S} ; (d) SpaRSA, N_r ; (e) SALSA, M^{S} ; (f) SALSA, N_r ; (g) YALL1, M^{S} ; (h) YALL1, N_r	48
Figure 5.1	The obtained TFDs from the filtered AFs with the CS-AF area for the considered signals: (a) $z_{\text{SINLFM}}(t)$; (b) $z_{\text{LFM}}(t)$. Red dashed lines represent an arbitrarily chosen time slice at sample $t = 100$ for the signal $z_{\text{SINLFM}}(t)$ in (a), and a frequency slice at frequency bin $f = 120$ for the signal $z_{\text{LFM}}(t)$ in (b).	54
Figure 5.2	(a) A time slice at sample $t_0 = 100$ for the signal $z_{\text{SINLFM}}(t)$ with $p = 0.9$ and $NC_t(t_0) = 2$; (b) a frequency slice at frequency bin $f_0 = 120$ for the signal $z_{\text{SINLFM}}(t)$ with $p = 0.1$ and $NC_f(f_0) = 4$. The RTwIST parameters $\delta_t = \delta_f$ have been randomly set to 0.5 (black dashed line) and 0.95 (red dashed line).	54
Figure 5.3	Reconstructed TFDs obtained using the RTwIST algorithm with parameters $\alpha_{\text{TwIST}} = 0.91$, $\beta_{\text{TwIST}} = 0.8$ and $\delta_t = \delta_f = 0.85$: (a) signal $z_{\text{SINLFM}}(t)$ with $p = 0.1$; (b) signal $z_{\text{SINLFM}}(t)$ with $p = 0.9$; (c) signal $z_{\text{LFM}}(t)$ with $p = 0.1$; (d) signal $z_{\text{LFM}}(t)$ with $p = 0.9$. . .	55
Figure 5.4	Reconstructed TFDs obtained using the RTwIST algorithm with parameters $\alpha_{\text{EMB}} = 0.91$, $\beta_{\text{EMB}} = 0.8$: (a) signal $z_{\text{SINLFM}}(t)$, $p = 0.9$ and $\delta_t = \delta_f = 0.5$; (b) signal $z_{\text{SINLFM}}(t)$, $p = 0.9$ and $\delta_t = \delta_f = 0.95$; (c) signal $z_{\text{LFM}}(t)$, $p = 0.1$ and $\delta_t = \delta_f = 0.5$; (d) signal $z_{\text{LFM}}(t)$, $p = 0.1$ and $\delta_t = \delta_f = 0.95$	57
Figure 5.5	Reconstructed TFDs obtained by the RTwIST algorithm with objective functions formalized as $\text{MSE}_t, \text{MSE}_f$ and: (a) signal $z_{\text{SINLFM}}(t)$, M^{S} ; (b) signal $z_{\text{SINLFM}}(t)$, N_r ; (c) signal $z_{\text{LFM}}(t)$, M^{S} ; (d) signal $z_{\text{LFM}}(t)$, N_r	59
Figure 5.6	Reconstructed TFDs obtained by the RTwIST algorithm for the considered signals embedded in AWGN: (a) $z_{\text{SINLFM}}(t)$, SNR = 1 dB; (b) $z_{\text{SINLFM}}(t)$, SNR = 3 dB; (c) $z_{\text{LFM}}(t)$, SNR = 1 dB; (d) $z_{\text{LFM}}(t)$, SNR = 3 dB.	65

- Figure 5.7 (a) the WVD of $z_{\text{PFM}}(t)$; (b) the AF of $z_{\text{PFM}}(t)$, $N'_\tau \times N'_\nu = 49 \times 53$; (c) the WVD of $z_{\text{grav}}(t)$; (d) the AF of $z_{\text{grav}}(t)$, $N'_\tau \times N'_\nu = 35 \times 15$. The automatically selected $N'_\tau \times N'_\nu$ area is marked by the rectangle. 69
- Figure 5.8 Clustered CS-AF area, denoted as C_Ω , for: (a) signal $z_{\text{PFM}}(t)$, with $(\Gamma, \Lambda) = (0.06, 0.5)$; (b) signal $z_{\text{grav}}(t)$ with $(\Gamma, \Lambda) = (0.15, 0.18)$. The green circles represent the samples within the cluster, while the red circles indicate the outlier samples. The blue rectangle corresponds to the automatically selected $N'_\tau \times N'_\nu$ area. 69
- Figure 5.9 TFDs obtained from filtered AFs for: (a) signal $z_{\text{PFM}}(t)$ with a full $N'_\tau \times N'_\nu$ area; (b) signal $z_{\text{PFM}}(t)$ with the presented CS-AF area, $(\Gamma, \Lambda) = (0.06, 0.5)$; (c) signal $z_{\text{grav}}(t)$ with a full $N'_\tau \times N'_\nu$ area; (d) signal $z_{\text{grav}}(t)$ with the presented CS-AF area, $(\Gamma, \Lambda) = (0.15, 0.18)$. 70
- Figure 5.10 Reconstructed TFDs obtained using the following reconstruction algorithm and CS-AF area with (Γ, Λ) for the signal $z_{\text{PFM}}(t)$: (a) RTwIST, (0, 1); (b) RTwIST, (0.046, 0.426); (c) TwIST, (0, 1); (d) TwIST, (0.043, 0.520); (e) SpaRSA, (0, 1); (f) SpaRSA, (0.029, 0.515); (g) SALSA, (0, 1); (h) SALSA, (0.070, 0.350). 72
- Figure 5.11 Reconstructed TFDs obtained using the following reconstruction algorithm and CS-AF area with (Γ, Λ) for the signal $z_{\text{grav}}(t)$: (a) RTwIST, (0, 1); (b) RTwIST, (0.142, 0.189); (c) TwIST, (0, 1); (d) TwIST, (0.300, 0.179); (e) SpaRSA, (0, 1); (f) SpaRSA, (0.080, 0.195); (g) SALSA, (0, 1); (h) SALSA, (0.098, 0.195). 74
- Figure 6.1 Considering the signal $z_{\text{mix}}(t)$: (a) $\rho_{(lo)}(t, f)$; (b) the estimated IFs (yellow) in $\rho_{(lo)}^t(t, f)$; (c) the estimated GDs (yellow) in $\rho_{(lo)}^f(t, f)$. . 83
- Figure 6.2 Considering the signal $z_{\text{mix}}(t)$: (a) the local number of components, $NC_f(f)$; (b) LO-ADTFD. The red dashed lines delineate the initial segment $[f_1, f_2]$ chosen from $NC_f(f)$, where a substantial augmentation in $NC_f(f)$ is observed. 84
- Figure 6.3 Considering the signal $z_{\text{mix}}(t)$: (a) detected components in extracted LO-ADTFD; (b) the $NC_t(t)$ calculated on extracted LO-ADTFD; (c) $\rho_{(lo)}^t(t, f)$; (d) $\rho_{(lo)}^f(t, f)$. Detected segments, evaluated using the N_r measure in $\rho_{(lo)}^t(t, f)$ and $\rho_{(lo)}^f(t, f)$, are indicated by red dashed lines. A segment that contains components suitable for the current time localization approach is highlighted by green dashed lines. . . 85
- Figure 6.4 Considering the signal $z_{\text{mix}}(t)$: (a) $C_M(t, f)$; (b) LO-ADTFD with $C_M(t, f)$. The yellow and dash-dotted pink rectangles highlight the specific regions within the TFD that are suitable for analysis using time slices. The remaining portion of the TFD, indicated by the blue color, should be analyzed using frequency slices. 86

Figure 6.5	Considering the real-life gravitational signal $z_{\text{grav}}(t)$: (a) $\rho_{(lo)}^t(t, f)$; (b) $\rho_{(lo)}^f(t, f)$; (c) $C_M(t, f)$; (d) LO-ADTFD with $C_M(t, f)$. The yellow and dashed red rectangles highlight the specific regions within the TFD that are suitable for analysis using time slices. In contrast, the remaining portion of the TFD, indicated by the blue color, should be analyzed using frequency slices.	87
Figure 6.6	Considering the signal $z_{\text{mix}}(t)$: (a) $\eta_t\{\rho_{(lo)}(t, f)\}$; (b) $\eta_f\{\rho_{(lo)}(t, f)\}$; (c) the $NC_t(t)$ estimates obtained utilizing the STRE in starting TFD and $\eta_t\{\rho_{(lo)}(t, f)\}$; (d) the $NC_f(f)$ estimates obtained utilizing the NBRE in starting TFD and $\eta_f\{\rho_{(lo)}(t, f)\}$. The estimates are represented with yellow dashed lines for starting TFD, and blue solid lines for $\eta_t\{\rho_{(lo)}(t, f)\}$ and $\eta_f\{\rho_{(lo)}(t, f)\}$	88
Figure 6.7	Considering the signal $z_{\text{grav}}(t)$: (a) $\eta_t\{\rho_{(lo)}(t, f)\}$; (b) $\eta_f\{\rho_{(lo)}(t, f)\}$; (c) the $NC_t(t)$ estimates obtained utilizing the STRE in starting TFD and $\eta_t\{\rho_{(lo)}(t, f)\}$; (d) the $NC_f(f)$ estimates obtained utilizing the NBRE in starting TFD and $\eta_f\{\rho_{(lo)}(t, f)\}$. The estimates are represented with red dashed lines for starting TFD, and blue solid lines for $\eta_t\{\rho_{(lo)}(t, f)\}$ and $\eta_f\{\rho_{(lo)}(t, f)\}$	89
Figure 6.8	$B^{(\text{shrink})}(t, f)$ with IF and GD estimations (in yellow) utilizing the shrinkage operator for the signals: (a) $z_{\text{LFM}}(t)$; (b) $z_{\text{mix}}(t)$; (c) $z_{\text{grav}}(t)$	90
Figure 6.9	A simplified flowchart illustrating the automated estimation of IF and GD for a given TFD.	93
Figure 6.10	IF and GD estimations (in yellow) for the considered signal and method combination: (a) $z_{\text{LFM}}(t)$, the Image-based-STRE; (b) $z_{\text{LFM}}(t)$, the Image-based-STRE-NBRE; (c) $z_{\text{LFM}}(t)$, the BSS-STRE; (d) $z_{\text{LFM}}(t)$, the BSS-STRE-NBRE; (e) $z_{\text{mix}}(t)$, the Image-based-STRE; (f) $z_{\text{mix}}(t)$, the Image-based-STRE-NBRE; (g) $z_{\text{mix}}(t)$, the BSS-STRE; (h) $z_{\text{mix}}(t)$, the BSS-STRE-NBRE.	94
Figure 6.11	IF and GD estimation (in yellow) for the signal $z_{\text{grav}}(t)$ utilizing method: (a) the Image-based-STRE; (b) the Image-based-STRE-NBRE; (c) the BSS-STRE; (d) the BSS-STRE-NBRE.	95
Figure 6.12	The MSE computed between the estimated local number of signal components from noisy and noise-free LO-ADTFDs in AWGN with SNR values ranging from 0 dB to 10 dB for the signals: (a) $z_{\text{LFM}}(t)$; (b) $z_{\text{mix}}(t)$	97
Figure 6.13	F1 values for determining the sensitivity of the considered IF and GD estimation methods to AWGN in SNR values ranging from 0 dB to 10 dB for the signals: (a) $z_{\text{LFM}}(t)$; (b) $z_{\text{mix}}(t)$	97
Figure 6.14	F-norm values for determining the sensitivity of the considered IF and GD estimation methods to AWGN in SNR values ranging from 0 dB to 10 dB for the signals: (a) $z_{\text{LFM}}(t)$; (b) $z_{\text{mix}}(t)$	97

Figure 6.15	A time slice $t = 64$ example analysis of the χ measure for the reconstructed TFDs of the signal $z_{\text{SINLFM}}(t)$ using the TwIST algorithm with: (a) missing auto-term samples (oversparsity), $\lambda = 15$; (b) auto-terms with low-resolution and reconstructed cross-terms, $\lambda = 0.1$. The green line represents the detected auto-terms, while the blue line represents the cross-terms after removing auto-terms.	101
Figure 6.16	Reconstructed TFDs using the MRTwIST algorithm for the considered signals: (a) $z_{\text{SINLFM}}(t)$; (b) $z_{\text{LFM}}(t)$; (c) $z_{\text{mix}}(t)$; (d) $z_{\text{grav}}(t)$	109
Figure 7.1	The 10-20 EEG electrode placement. $T_4 - T_6$, $F_4 - T_4$, $F_3 - T_3$, $T_5 - O_1$, $T_6 - O_2$, $T_3 - T_5$, $C_4 - P_4$, $F_4 - C_4$, $F_3 - C_3$, $P_4 - O_2$, $C_3 - P_3$, $T_4 - C_4$, $C_4 - C_Z$, $C_Z - C_3$, $P_3 - O_1$, $T_6 - P_4$, $C_3 - T_3$, $P_Z - P_3$, $P_4 - P_Z$, and $P_3 - T_5$ are the channel designations.	112
Figure 7.2	For the real-life EEG seizure signal representative, $z_{\text{EEG}}(t)$: (a) recordings over different channels; (b) time-domain representation with pronounced spikes.	113
Figure 7.3	(a) EMBD of the signal $z_{\text{EEG}}(t)$, $\alpha_{\text{EMB}} = 0.1$, $\beta_{\text{EMB}} = 0.2$; (b) LO-ADTFD of the signal $z_{\text{EEG}}(t)$; (c) EMBD of the signal $z_{\text{EEG}_{\text{filt}}}(t)$, $\alpha_{\text{EMB}} = 0.08$, $\beta_{\text{EMB}} = 0.3$; (d) LO-ADTFD of the signal $z_{\text{EEG}_{\text{filt}}}(t)$	114
Figure 7.4	The obtained $C_M(t, f)$ for the considered signal: (a) $z_{\text{EEG}}(t)$; (b) $z_{\text{EEG}}(t)$ with its LO-ADTFD; (c) $z_{\text{EEG}_{\text{filt}}}(t)$; (d) $z_{\text{EEG}_{\text{filt}}}(t)$ with its LO-ADTFD. The regions highlighted by yellow and dash-dotted pink rectangles delineate time-based analysis areas, whereas the remaining blue region of the TFD necessitates frequency-based analysis.	115
Figure 7.5	Components extracted using different approaches: (a) time-based analysis using $\eta_t\{\rho_{(l_o)}(t, f)\}$ for $z_{\text{EEG}}(t)$; (b) frequency-based analysis using $\eta_f\{\rho_{(l_o)}(t, f)\}$ for $z_{\text{EEG}}(t)$; (c) time-based analysis using $\eta_t\{\rho_{(l_o)}(t, f)\}$ for $z_{\text{EEG}_{\text{filt}}}(t)$; (d) frequency-based analysis using $\eta_f\{\rho_{(l_o)}(t, f)\}$ for $z_{\text{EEG}_{\text{filt}}}(t)$	116
Figure 7.6	Comparison of the local numbers of signal components derived from the application of the STRE and NBRE within the starting TFD (indicated by the yellow dashed line) and subsequent extraction of components employing the presented operators η_t and η_f (represented by the blue solid line) for the respective signals: (a, b) $z_{\text{EEG}}(t)$; (c, d) $z_{\text{EEG}_{\text{filt}}}(t)$	117
Figure 7.7	For the considered EEG seizure signals: (a) estimated IFs (red line) of $z_{\text{EEG}_{\text{filt}}}(t)$; (b) estimated GDs (blue line) of $z_{\text{EEG}_{\text{filt}}}(t)$; (c) estimated IFs (red line) of $z_{\text{EEG}}(t)$; (d) estimated GDs (blue line) of $z_{\text{EEG}}(t)$. The method proposed in [62] was used.	118

Figure 7.8	IF and GD estimation (in yellow) of EEG seizure signals using various methods: (a) the Image-based-STRE for $z_{\text{EEG}}(t)$; (b) the Image-based-STRE-NBRE for $z_{\text{EEG}}(t)$; (c) the BSS-STRE for $z_{\text{EEG}}(t)$; (d) the BSS-STRE-NBRE for $z_{\text{EEG}}(t)$; (e) the Image-based-STRE for $z_{\text{EEG}_{\text{filt}}}(t)$; (f) the Image-based-STRE-NBRE for $z_{\text{EEG}_{\text{filt}}}(t)$; (g) the BSS-STRE for $z_{\text{EEG}_{\text{filt}}}(t)$; (h) the BSS-STRE-NBRE for $z_{\text{EEG}_{\text{filt}}}(t)$.	119
Figure 7.9	$B^{(\text{shrink})}(t, f)$ consisted of estimated IFs and GDs (in yellow) obtained utilizing the shrinkage operator for the EEG seizure signals: (a) $z_{\text{EEG}}(t)$; (b) $z_{\text{EEG}_{\text{filt}}}(t)$.	120
Figure 7.10	Reconstructed TFDs of the unfiltered $z_{\text{EEG}}(t)$ signal obtained using the following reconstruction algorithm: (a) MRTwIST; (b) TwIST; (c) SALSAs; (d) SpaRSA.	122
Figure 7.11	Reconstructed TFDs for the filtered $z_{\text{EEG}_{\text{filt}}}(t)$ signal obtained using the following reconstruction algorithm: (a) MRTwIST; (b) TwIST; (c) SALSAs; (d) SpaRSA.	123
Figure 7.12	AFs with highlighted CS-AF areas in yellow obtained with the MRTwIST algorithm for the considered signal: (a) $z_{\text{EEG}}(t)$; (b) $z_{\text{EEG}_{\text{filt}}}(t)$.	124
Figure C.1	Pareto fronts (blue circles) and ξ^{best} (red triangle) for the signal $z_{\text{SINLFM}}(t)$ and reconstruction algorithm: (a) SALSAs; (b) YALL1; (c) SALSAs; (d) TwIST.	169
Figure C.2	Pareto fronts (blue circles) and ξ^{best} (red triangle) for the signal $z_{\text{LFM}}(t)$ and reconstruction algorithm: (a) SpaRSA; (b) YALL1; (c) SALSAs; (d) SpaRSA.	170
Figure D.1	Clustered CS-AF area for the signal $z_{\text{PFM}}(t)$ and reconstruction algorithms: (a) RTwIST; (b) TwIST; (c) SpaRSA; (d) SALSAs. The black circles represent the samples within the cluster, while the red circles indicate the outlier samples. The black rectangle corresponds to the automatically selected $N'_\tau \times N'_\nu$ area.	171
Figure D.2	Clustered CS-AF area for the signal $z_{\text{grav}}(t)$ and reconstruction algorithms: (a) RTwIST; (b) TwIST; (c) SpaRSA; (d) SALSAs. The black circles represent the samples within the cluster, while the red circles indicate the outlier samples. The black rectangle corresponds to the automatically selected $N'_\tau \times N'_\nu$ area.	172
Figure E.1	Reconstructed TFDs optimized with $(\chi_{at}, \chi_r, \chi_{ct})$ objective functions for the considered signals obtained using the RTwIST reconstruction algorithm: (a) $z_{\text{SINLFM}}(t)$; (b) $z_{\text{LFM}}(t)$.	173

Figure E.2 Reconstructed TFDs optimized with $(\chi_{at}, \chi_r, \chi_{ct})$ objective functions for the considered signals obtained using the following reconstruction algorithm: (a) $z_{\text{SINLFM}}(t)$, TwIST; (b) $z_{\text{SINLFM}}(t)$, SpaRSA; (c) $z_{\text{SINLFM}}(t)$, SALSA; (d) $z_{\text{SINLFM}}(t)$, YALL1; (e) $z_{\text{LFM}}(t)$, TwIST; (f) $z_{\text{LFM}}(t)$, SpaRSA; (g) $z_{\text{LFM}}(t)$, SALSA; (h) $z_{\text{LFM}}(t)$, YALL1. 174

Figure F.1 AFs with highlighted CS-AF areas in yellow obtained using the MRTwIST algorithm for the signal: (a) $z_{\text{SINLFM}}(t)$; (b) $z_{\text{LFM}}(t)$; (c) $z_{\text{mix}}(t)$; (d) $z_{\text{grav}}(t)$ 175

LIST OF TABLES

Table 2.1	Time-lag and Doppler-lag selected QTFD kernels.	18
Table 2.2	Concentration measures of the considered QTFDs, SPEC and LO-ADTFD for the signal $z_{\text{SINLFM}}(t)$. Values in bold indicate the best-performing TFD according to the respective measure.	21
Table 3.1	Performance measures of the considered ℓ_1 norm-based reconstruction algorithms with an arbitrarily chosen regulation parameter λ . According to the respective measure, values in bold indicate the best-performing reconstruction algorithm for the signals $z_{\text{SINLFM}}(t)$ and $z_{\text{LFM}}(t)$	30
Table 4.1	LRE-based metrics, MSE_t , MSE_f , and N_r of the considered ℓ_1 norm-based reconstruction algorithms with arbitrarily chosen regulation parameter λ . According to the respective measure, values in bold indicate the best-performing reconstruction algorithm for the signals $z_{\text{SINLFM}}(t)$ and $z_{\text{LFM}}(t)$	41
Table 4.2	Fixed parameters for the MOPSO, NSGA-III and MOWCA meta-heuristic optimization algorithms.	45
Table 4.3	Performance comparison of the reconstructed TFDs obtained using the TwIST, SpaRSA, SALSA and YALL1 algorithms optimized with $(M^S, \text{MSE}_t, \text{MSE}_f)$ versus $(N_r, \text{MSE}_t, \text{MSE}_f)$ objective functions for the signal $z_{\text{SINLFM}}(t)$. Values in bold indicate the best-performing and the fastest algorithm.	46
Table 4.4	Performance comparison of the reconstructed TFDs obtained using the TwIST, SpaRSA, SALSA and YALL1 algorithms optimized with $(M^S, \text{MSE}_t, \text{MSE}_f)$ versus $(N_r, \text{MSE}_t, \text{MSE}_f)$ objective functions for the signal $z_{\text{LFM}}(t)$. Values in bold indicate the best-performing and the fastest algorithm.	49
Table 5.1	Performance comparison of the RTwIST algorithm with different parameters p selection for the signals $z_{\text{SINLFM}}(t)$ and $z_{\text{LFM}}(t)$. Bold values indicate the superior performing algorithm.	56
Table 5.2	Performance of the RTwIST algorithm with different parameters δ_t and δ_f selection for the signals $z_{\text{SINLFM}}(t)$ and $z_{\text{LFM}}(t)$. Bold values indicate the superior performing algorithm.	58

Table 5.3	Performance of the RTwIST algorithm optimized with the NSGA-III and objective functions formalized as (MSE_t, MSE_f, M^S) versus (MSE_t, MSE_f, N_r) for the signals $z_{\text{SINLFM}}(t)$ and $z_{\text{LFM}}(t)$. Bold values indicate the superior performing algorithm.	60
Table 5.4	Hypervolume values (best, average, worst) of five reconstruction algorithms, including RTwIST, TwIST, SALSA, SpaRSA, and YALL1, for the signals $z_{\text{SINLFM}}(t)$ and $z_{\text{LFM}}(t)$ with objective functions using the M^S or N_r measures. Values in bold indicate the best-performing algorithm with the highest hypervolume values.	61
Table 5.5	Confusion matrices for evaluating the RTwIST algorithm's sensitivity to noise for $\text{SNR} = (1, 3, 5, 7, 9)$ dB for the signals $z_{\text{SINLFM}}(t)$ and $z_{\text{LFM}}(t)$. Values in bold indicate the true negative and true positive indices.	64
Table 5.6	Statistical measures for evaluating the RTwIST algorithm's sensitivity to noise for $\text{SNR} = (1, 3, 5, 7, 9)$ dB for the signals $z_{\text{SINLFM}}(t)$ and $z_{\text{LFM}}(t)$	65
Table 5.7	Performance comparison of considered reconstruction algorithms using the full $N'_r \times N'_v$ area $((\Gamma, \Lambda) = (0, 1))$ versus the presented CS-AF area with optimized (Γ^+, Λ^+) for the signal $z_{\text{PFM}}(t)$. Bold values represent the best-performing or the fastest algorithm. . . .	73
Table 5.8	Performance comparison of considered reconstruction algorithms using the full $N'_r \times N'_v$ area $((\Gamma, \Lambda) = (0, 1))$ versus the presented CS-AF area with optimized (Γ^+, Λ^+) for the signal $z_{\text{grav}}(t)$. Values in bold represent the best-performing or the fastest algorithm. . . .	75
Table 5.9	Comparison of the performance between the RTwIST algorithm using the full $N'_r \times N'_v$ area $((\Gamma, \Lambda) = (0, 1))$ and the presented CS-AF area (Γ^+, Λ^+) for the signal $z_{\text{PFM}}(t)$ in the presence of noise at various SNR levels.	76
Table 5.10	Confusion matrices and statistical measures for evaluating the RTwIST algorithm's sensitivity to noise for $\text{SNR} = (1, 5, 9)$ dB with the full $N'_r \times N'_v$ area versus the presented CS-AF area selection (Γ^+, Λ^+) for the signal $z_{\text{PFM}}(t)$. Values in bold indicate the true negative and true positive indices.	77
Table 5.11	Confusion matrices for evaluating the RTwIST algorithm's sensitivity to noise for $\text{SNR} = (1, 5, 9)$ dB with the presented CS-AF area selection (Γ^+, Λ^+) for the signals $z_{\text{SINLFM}}(t)$ and $z_{\text{LFM}}(t)$. Values in bold indicate the true negative and true positive indices.	78
Table 5.12	Statistical measures for evaluating the RTwIST algorithm's sensitivity to noise for $\text{SNR} = (1, 5, 9)$ dB with the presented CS-AF area selection (Γ^+, Λ^+) for the signals $z_{\text{SINLFM}}(t)$ and $z_{\text{LFM}}(t)$	78
Table 6.1	Comparison of the performance between the mutual IF and GD estimation and the IF estimation for the signals $z_{\text{LFM}}(t)$, $z_{\text{mix}}(t)$ and $z_{\text{grav}}(t)$. Values in bold indicate the best-performing method. . . .	96

Table 6.2	Performance results of the IF/GD-based measure for evaluating the oversparse and low-resolution reconstructed TFDs for the signals $z_{\text{SINLFM}}(t)$ and $z_{\text{LFM}}(t)$. Bold values indicate the best-performing algorithm.	102
Table 6.3	Performance results of the IF/GD-based measure for evaluating optimized reconstructed TFDs with two different objective functions for the signal $z_{\text{SINLFM}}(t)$. Bold values indicate the best-performing algorithm.	103
Table 6.4	Performance results of the IF/GD-based measure for evaluating reconstructed TFDs optimized with objective functions ($\text{MSE}_t, \text{MSE}_f, M^{\text{S}}$) and ($\text{MSE}_t, \text{MSE}_f, N_r$) for the signal $z_{\text{LFM}}(t)$. Bold values indicate the best-performing algorithm.	104
Table 6.5	Performance results of the IF/GD-based measure for evaluating optimized reconstructed TFDs with two different CS-AF area selections for the signals $z_{\text{PFM}}(t)$ and $z_{\text{grav}}(t)$. Bold values indicate the best-performing algorithm.	105
Table 6.6	Reconstructed TFDs obtained using the multi-objective optimization approach with the IF/GD-based measure components χ_{at}, χ_r and χ_{ct} as objective functions for the signals $z_{\text{SINLFM}}(t)$ and $z_{\text{LFM}}(t)$. Bold values indicate the best-performing algorithm.	106
Table 6.7	Performance evaluation of the reconstructed TFDs obtained using the MRTwIST algorithm versus the LO-ADTFD for the signals $z_{\text{SINLFM}}(t), z_{\text{LFM}}(t), z_{\text{mix}}(t)$ and $z_{\text{grav}}(t)$. Bold values indicate better performing TFD.	109
Table 7.1	Comparison of the performance between the mutual IF and GD estimation and the IF estimation methods for the EEG seizure signals $z_{\text{EEG}}(t)$ and $z_{\text{EEG}_{\text{fit}}}(t)$ database. Values in bold indicate the best-performing algorithm.	120
Table 7.2	Performance evaluation of the considered TFDs for the unfiltered EEG seizure signal $z_{\text{EEG}}(t)$. Bold values indicate the best-performing TFD.	122
Table 7.3	Performance evaluation of the considered TFDs for the filtered EEG seizure signal $z_{\text{EEG}_{\text{fit}}}(t)$. Bold values indicate the best-performing TFD.	124
Table B.1	Hypervolume values (best, average, worst) of the TwIST algorithm optimized with objective functions using the M^{S} or N_r measures for the signals $z_{\text{SINLFM}}(t)$ and $z_{\text{LFM}}(t)$. Values in bold indicate the highest hypervolume values.	167

APPENDICES

Appendix A

PSEUDOCODE OF MULTI-OBJECTIVE META-HEURISTIC ALGORITHMS

This appendix presents the pseudocode of the multi-objective meta-heuristic algorithms used in this dissertation.

Algorithm 3 MOPSO Pseudocode

Require: $w, c_1, c_2, m_r, N_{\text{par}}, N_{\text{pop}}$ and T_{max} .

Ensure: a set of Pareto-optimal solutions that are non-dominated.

- 1: Randomly initialize the particle population.
 - 2: Evaluate the objective functions of each particle.
 - 3: Set each particle's personal best position to its current position.
 - 4: Identify the non-dominated solutions within the initial population and store them in the Pareto archive.
 - 5: **while** termination criterion not met **do**
 - 6: Compute the updated velocity of a particle by considering its current velocity, personal best position, and global best position with c_1, c_2 and w .
 - 7: Calculate the position of a particle by considering its current position and velocity.
 - 8: Evaluate the objective functions of the new position.
 - 9: Update the personal best position.
 - 10: If the objective function values of the new position are better than the personal best position, update the personal best position.
 - 11: Update the global best position.
 - 12: If the objective function values of the new position are better than the global best position, update the global best position with the non-dominated set of solutions.
 - 13: Apply mutation to some particles with probability m_r .
 - 14: Evaluate the objective function of mutated particles.
 - 15: Update personal best position for mutated particles.
 - 16: Determine new non-dominated solutions and store them in the Pareto archive.
 - 17: Increment current iteration.
 - 18: **end while**
-

Algorithm 4 NSGA-III Pseudocode

Require: p_c , p_m , m_r , N_{par} , N_{pop} and T_{max} .

Ensure: a set of Pareto-optimal solutions that are non-dominated.

- 1: Initialize the population of individuals randomly.
 - 2: Evaluate the objective functions of each individual.
 - 3: Assign each individual to a rank based on dominance.
 - 4: Calculate the probability of crossover and mutation for the next generation.
 - 5: Identify the non-dominated solutions within the initial population and store them in the Pareto archive.
 - 6: **while** termination criterion not met **do**
 - 7: Generate offspring population using crossover and mutation operators with probabilities p_c and p_m , respectively.
 - 8: Evaluate the objective functions of the offspring population.
 - 9: Merge parent and offspring populations.
 - 10: Assign each individual to a rank based on dominance.
 - 11: Truncate the population to its original size using non-dominated sorting.
 - 12: Determine new non-dominated solutions and store them in the Pareto archive.
 - 13: Increment current iteration.
 - 14: **end while**
-

Algorithm 5 MOWCA Pseudocode

Require: N_{sr} , d_{max} , N_{par} , N_{pop} and T_{max} .

Ensure: a set of Pareto-optimal solutions that are non-dominated.

- 1: Initialize the population of individuals randomly and get the starting streams, rivers, and sea using N_{sr} .
 - 2: Evaluate the objective functions of each stream.
 - 3: Identify the non-dominated solutions within the initial population and store them in the Pareto archive.
 - 4: Determine the flow intensity for rivers and seas based on the computed crowding distance values.
 - 5: **while** termination criterion not met **do**
 - 6: Compute the flow of streams into rivers and swap the positions of a river with a stream that yields the best solution.
 - 7: Compute the flow of rivers into the sea and exchange the positions of the sea with a river that yields the best solution.
 - 8: Check the evaporation condition and reduce the value of d_{max} .
 - 9: Generate new feasible solutions for the population.
 - 10: Evaluate the objective functions of new solutions, determine new non-dominated solutions, and store them in the Pareto archive.
 - 11: Compute the crowding distance value for each member of the Pareto archive and eliminate the members with the lowest crowding distance value as required.
 - 12: Calculate the crowding distance value for each member of the Pareto archive in order to determine the selection of new seas and rivers.
 - 13: Increment current iteration.
 - 14: **end while**
-

Appendix B

RESULTS OF THE HYPERVOLUME TEST ON META-HEURISTIC ALGORITHMS IN CHAPTER 4

This appendix presents the results of the hypervolume test performed on the Pareto front obtained using the TwIST algorithm optimized with the MOPSO, NSGA-III, and MOWCA meta-heuristic algorithms. Table B.1 reveals that the NSGA-III achieved the overall best Pareto front among the considered algorithms.

Table B.1 Hypervolume values (best, average, worst) of the TwIST algorithm optimized with objective functions using the M^S or N_r measures for the signals $z_{\text{SINLFM}}(t)$ and $z_{\text{LFM}}(t)$. Values in bold indicate the highest hypervolume values.

Objectives	$z_{\text{SINLFM}}(t)$		$z_{\text{LFM}}(t)$	
	M^S MSE _t , MSE _f	N_r MSE _t , MSE _f	M^S MSE _t , MSE _f	N_r MSE _t , MSE _f
MOPSO	53.8745	73.0021	88.1478	84.8888
	52.8899	71.8987	87.7896	83.6987
	51.1112	70.4587	85.7896	81.9873
NSGA-III	54.8777	73.7778	89.9354	85.1254
	54.2589	73.1054	88.3698	84.3698
	53.7896	72.2365	87.4587	83.5698
MOWCA	54.6587	74.1125	88.4587	84.8878
	53.8987	73.3654	87.9887	84.0125
	52.2222	72.1254	86.9878	83.0021

Appendix C

RESULTS OF THE PARETO FRONT IN CHAPTER 4

This appendix presents examples of the Pareto front obtained using the NSGA-III for the signals $z_{\text{SINLFM}}(t)$ and $z_{\text{LFM}}(t)$, and arbitrarily chosen reconstruction algorithms in Figures C.1 and C.2, respectively.

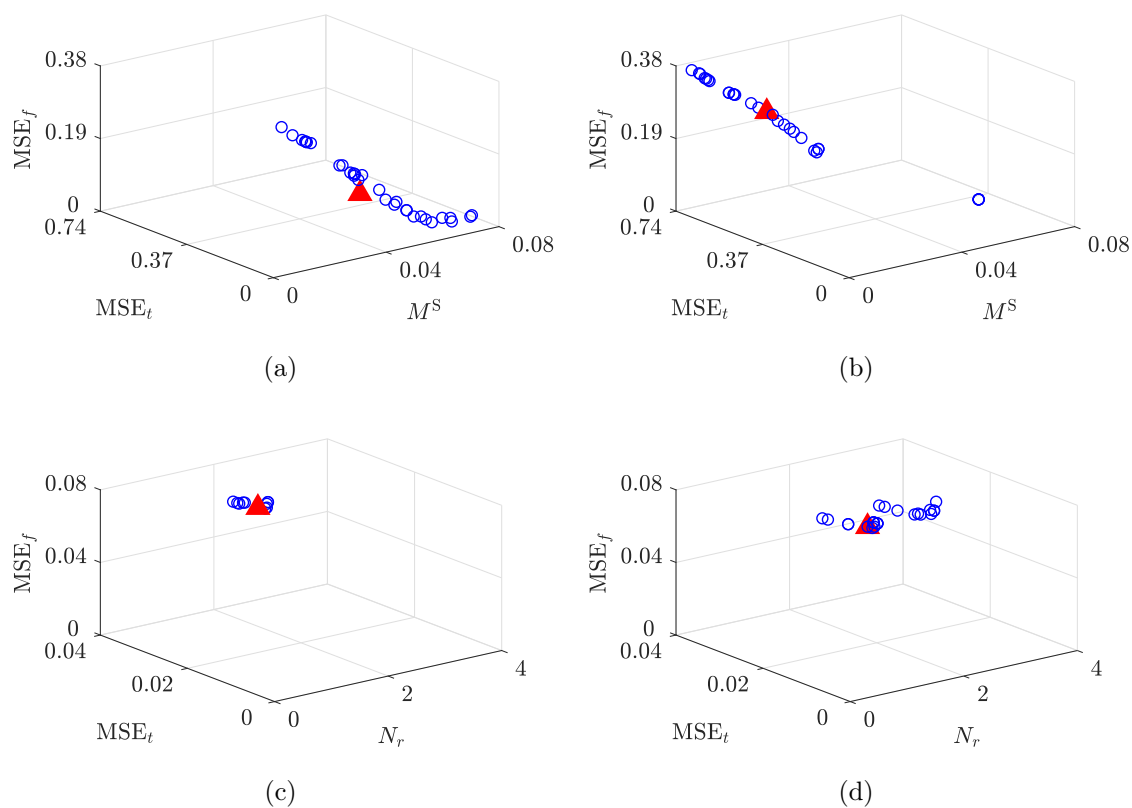


Figure C.1 Pareto fronts (blue circles) and ξ^{best} (red triangle) for the signal $z_{\text{SINLFM}}(t)$ and reconstruction algorithm: (a) SALSA; (b) YALL1; (c) SALSA; (d) TwIST.

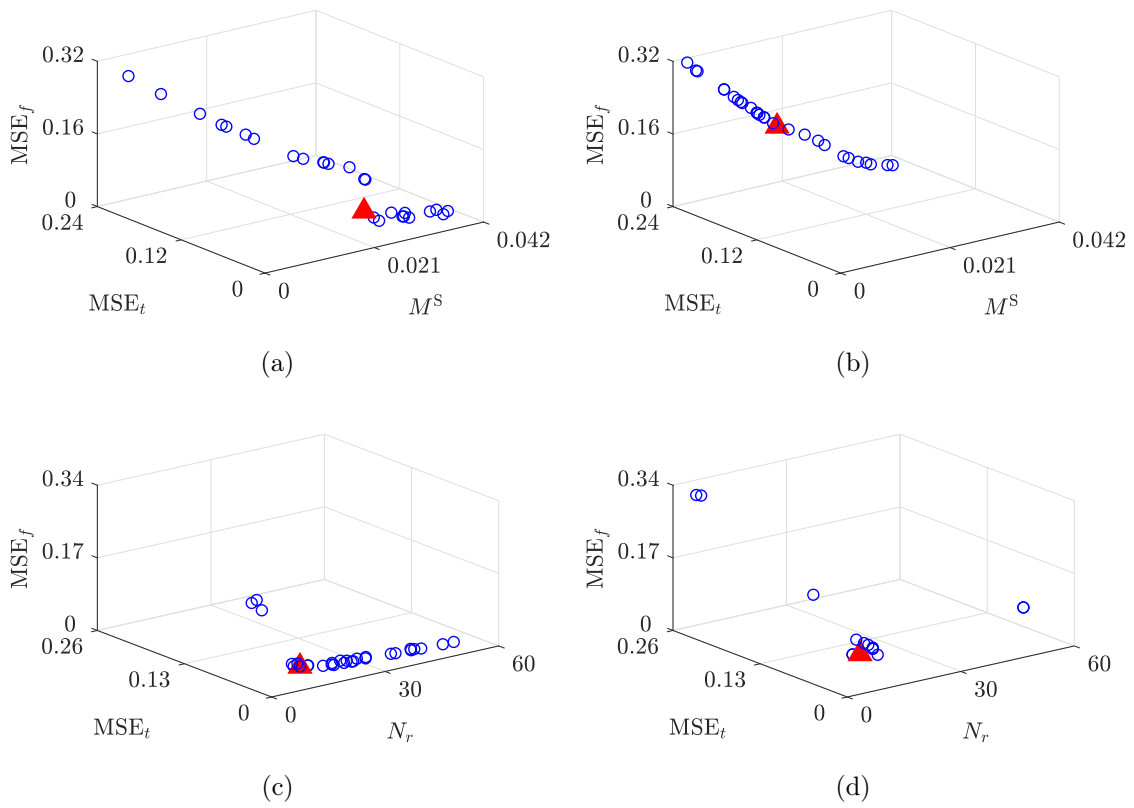


Figure C.2 Pareto fronts (blue circles) and ξ^{best} (red triangle) for the signal $z_{\text{LFM}}(t)$ and reconstruction algorithm: (a) SpaRSA; (b) YALL1; (c) SALSA; (d) SpaRSA.

Appendix D

RESULTS OF THE OPTIMIZED COMPRESSIVE SENSING AREAS IN CHAPTER 5

This appendix presents the optimized CS-AF areas obtained from the reconstruction algorithms for signals $z_{\text{PFM}}(t)$ and $z_{\text{grav}}(t)$ (Figures D.1 and D.2).

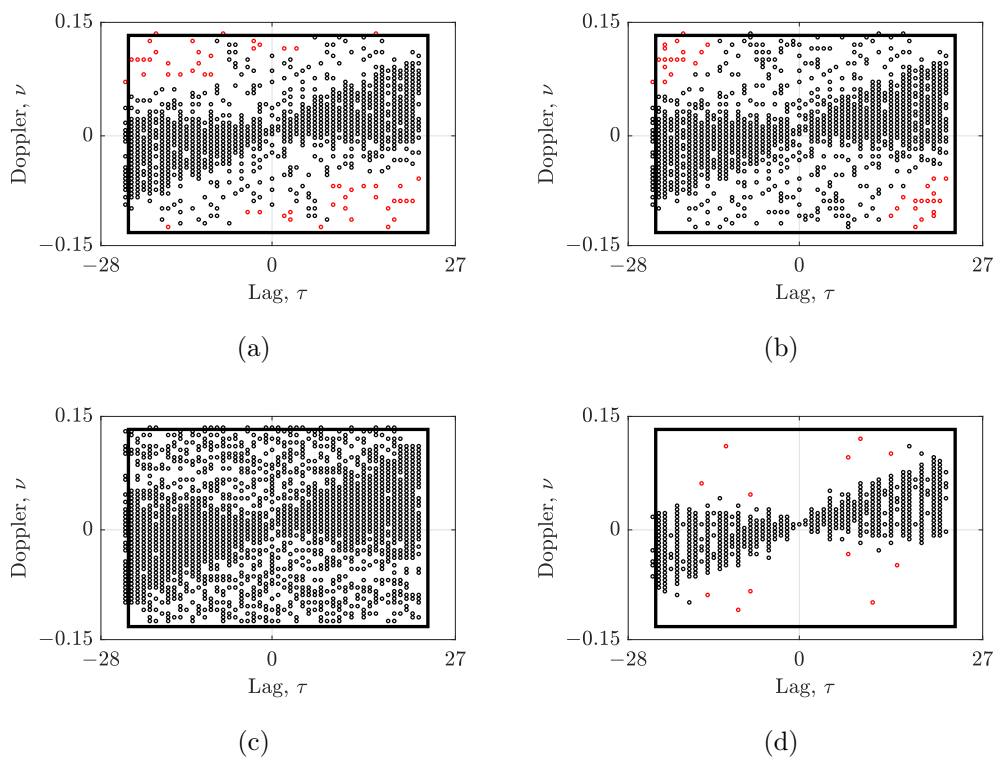


Figure D.1 Clustered CS-AF area for the signal $z_{\text{PFM}}(t)$ and reconstruction algorithms: (a) RTwIST; (b) TwIST; (c) SpaRSA; (d) SALSA. The black circles represent the samples within the cluster, while the red circles indicate the outlier samples. The black rectangle corresponds to the automatically selected $N'_\tau \times N'_\nu$ area.

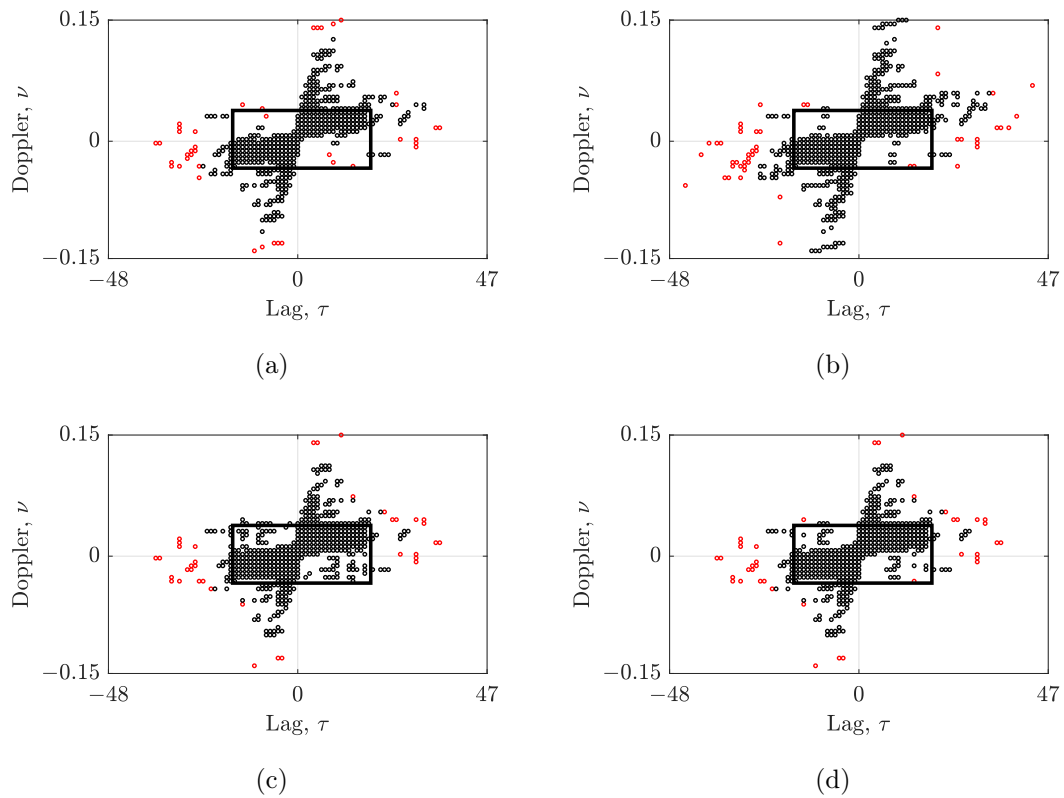


Figure D.2 Clustered CS-AF area for the signal $z_{\text{grav}}(t)$ and reconstruction algorithms: (a) RTwIST; (b) TwIST; (c) SpaRSA; (d) SALSAs. The black circles represent the samples within the cluster, while the red circles indicate the outlier samples. The black rectangle corresponds to the automatically selected $N'_\tau \times N'_\nu$ area.

Appendix E

RESULTS OF THE RECONSTRUCTED TFDS OPTIMIZED WITH THE IF/GD-BASED CRITERIA IN CHAPTER 6

This appendix presents the reconstructed TFDS obtained using the RTwIST (Figure E.1) and TwIST, SpaRSA, SALSA, and YALL1 reconstruction algorithms (Figure E.2) for the signals $z_{\text{SINLFM}}(t)$ and $z_{\text{LFM}}(t)$, whose parameters have been optimized with $(\chi_{at}, \chi_r, \chi_{ct})$ objective functions.

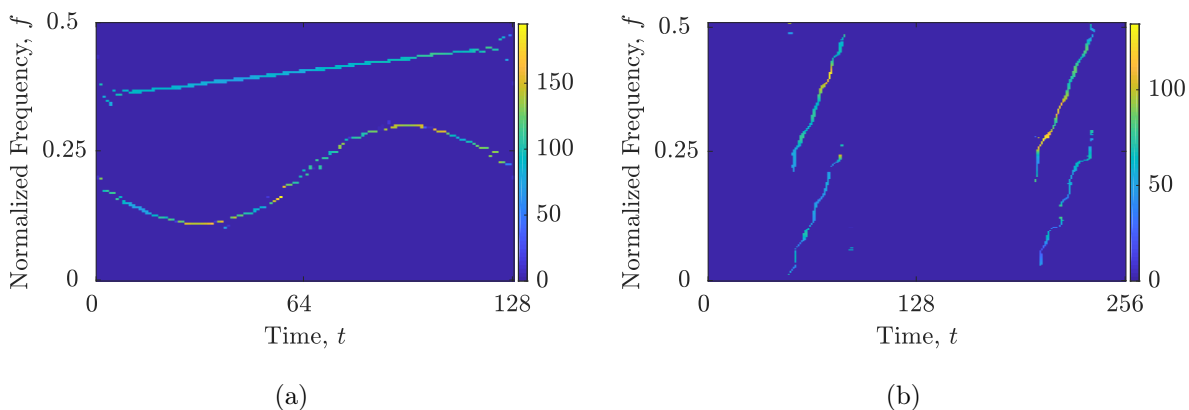


Figure E.1 Reconstructed TFDS optimized with $(\chi_{at}, \chi_r, \chi_{ct})$ objective functions for the considered signals obtained using the RTwIST reconstruction algorithm: (a) $z_{\text{SINLFM}}(t)$; (b) $z_{\text{LFM}}(t)$.

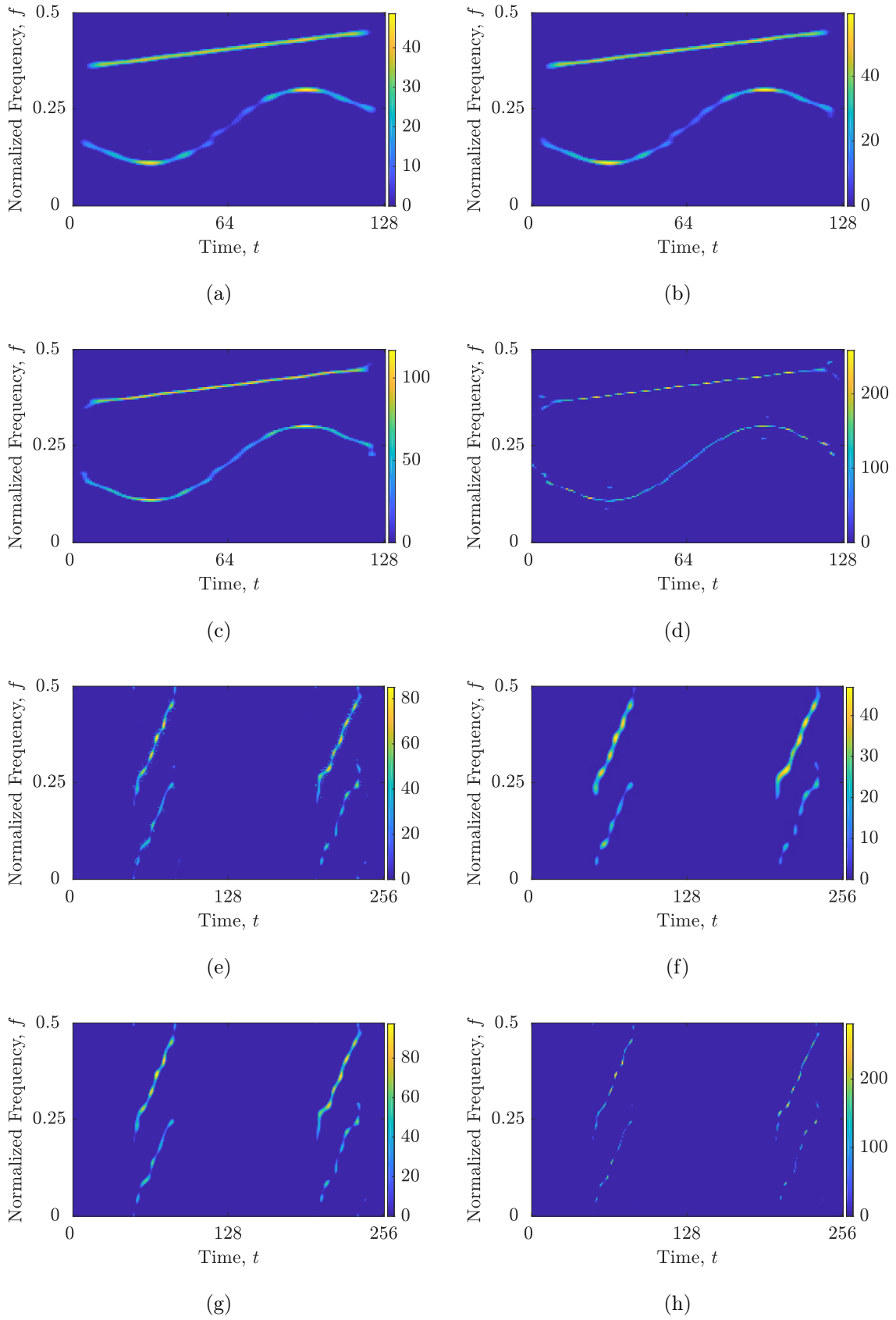


Figure E.2 Reconstructed TFDs optimized with $(\chi_{at}, \chi_r, \chi_{ct})$ objective functions for the considered signals obtained using the following reconstruction algorithm: (a) $z_{\text{SINLFM}}(t)$, TwIST; (b) $z_{\text{SINLFM}}(t)$, SpARSA; (c) $z_{\text{SINLFM}}(t)$, SALSA; (d) $z_{\text{SINLFM}}(t)$, YALL1; (e) $z_{\text{LFM}}(t)$, TwIST; (f) $z_{\text{LFM}}(t)$, SpARSA; (g) $z_{\text{LFM}}(t)$, SALSA; (h) $z_{\text{LFM}}(t)$, YALL1.

Appendix F

RESULTS OF THE OPTIMIZED COMPRESSIVE SENSING AREAS IN CHAPTER 6

This appendix presents the optimized CS-AF areas obtained using the MRTwIST algorithm for the signals $z_{\text{SINLFM}}(t)$, $z_{\text{LFM}}(t)$, $z_{\text{mix}}(t)$, $z_{\text{grav}}(t)$ in Figure F.1.

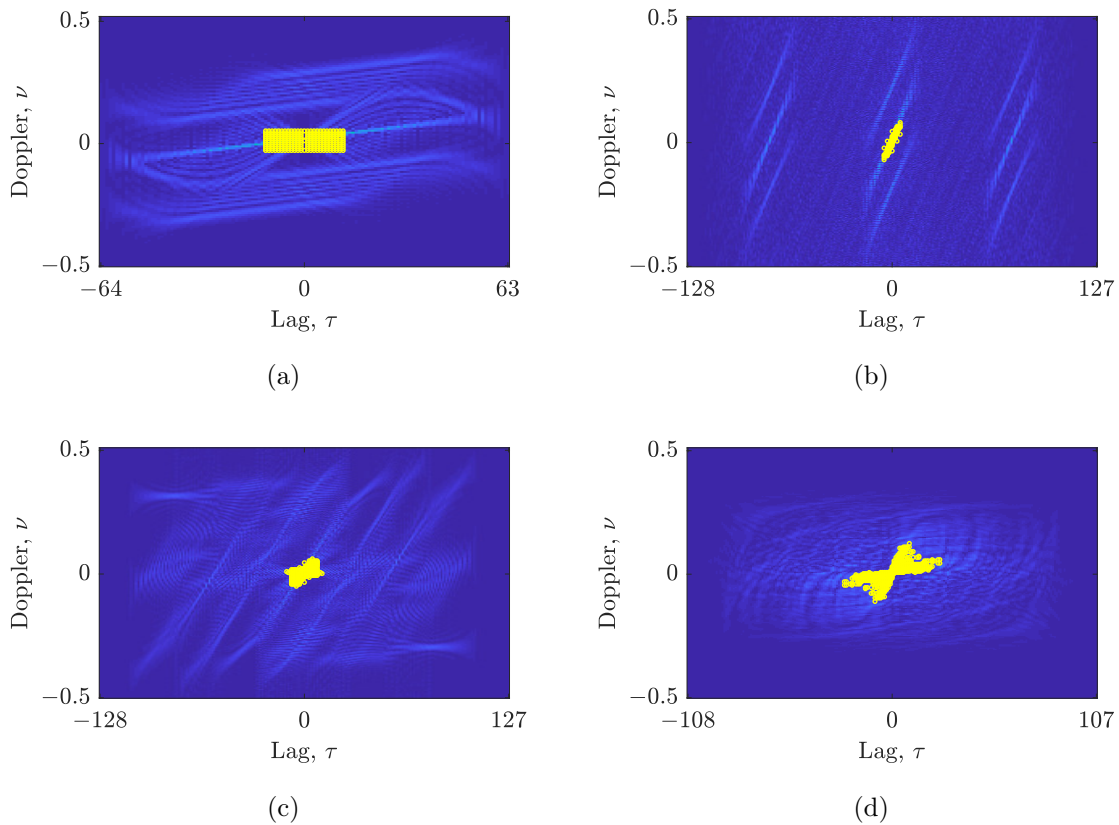


Figure F.1 AFs with highlighted CS-AF areas in yellow obtained using the MRTwIST algorithm for the signal: (a) $z_{\text{SINLFM}}(t)$; (b) $z_{\text{LFM}}(t)$; (c) $z_{\text{mix}}(t)$; (d) $z_{\text{grav}}(t)$.

CURRICULUM VITAE

Vedran Jurdana, born on December 9, 1992, in Rijeka, Croatia, began his academic journey at the University of Rijeka, Faculty of Engineering, in 2011. He completed his undergraduate studies in electrical engineering in 2015, earning a bachelor's degree (B. Sc.). Subsequently, he enrolled in the graduate program in electrical engineering at the same institution and obtained his master's degree (M. Sc.) with cum laude honors in 2017. His master's thesis, titled "Optimization of bearingless motor structure without permanent magnets on rotor with combined windings," was conducted in collaboration with the Institute for Electrical Drives and Power Electronics at Johannes Kepler University Linz, Austria.

In 2017, he joined the Faculty of Engineering for postgraduate doctoral study in the field of electrical engineering. Following his graduation, he took on the role of a research and teaching assistant at the University of Rijeka, Faculty of Engineering, Department of Automation and Electronics.

As a teaching assistant, he has contributed to various courses, including Digital Electronics and Signals and Systems in the undergraduate program of electrical engineering, Signals and Systems in the undergraduate program of computer engineering, Digital Signal Processing and Statistical Signal Analysis in the graduate program of electrical engineering, and Signals and Systems in the Lifelong Learning Programs of Electrical and Computer Engineering.

He has actively participated in several scientific projects and collaborated with research groups at national and international academic institutions. He has authored four scientific articles as the first author in international peer-reviewed journals indexed in the Current Contents (CC) database, published four scientific papers in conference proceedings, and presented one professional paper. Additionally, he has served as a reviewer for 12 international journals, reviewing 24 scientific articles in his research field. He has expanded his research experience by spending research visits at prestigious institutions such as the Institute for Electrical Drives and Power Electronics at Johannes Kepler University Linz (Austria), the Institute of Microwave and Photonic Engineering at Graz University of Technology (Austria), the Faculty of Engineering and Computer Science at the University of Maribor (Slovenia), and the Faculty of Informatics at Eötvös Loránd University Budapest

(Hungary).

His current research interests encompass various areas, including signal processing, time-frequency signal analysis, compressive sensing, information theory, and electroencephalogram data processing.

LIST OF PUBLICATIONS

Scientific articles in peer-reviewed journals indexed in Current Contents (CC) database

1. V. Jurdana, M. Vrankic, N. Lopac, and G. M. Jadav, “Method for automatic estimation of instantaneous frequency and group delay in time–frequency distributions with application in EEG seizure signals analysis,” *Sensors*, vol. 23, no. 10, May 2023, Art. no. 4680, doi: 10.3390/s23104680.
2. V. Jurdana, N. Lopac, and M. Vrankic, “Sparse time-frequency distribution reconstruction using the adaptive compressed sensed area optimized with the multi-objective approach,” *Sensors*, vol. 23, no. 8, April 2023, Art. no. 4148, doi: 10.3390/s23084148.
3. V. Jurdana, I. Volaric, and V. Sucic, “Sparse time-frequency distribution reconstruction based on the 2D Rényi entropy shrinkage algorithm,” *Digital Signal Processing*, vol. 118, p. 103225, Nov. 2021, doi: 10.1016/j.dsp.2021.103225.
4. V. Jurdana, N. Bulić, and W. Gruber, “Topology choice and optimization of a bearingless flux-switching motor with a combined winding set,” *Machines*, vol. 6, no. 4, Nov. 2018, Art. no. 57, doi: 10.3390/machines6040057.

Scientific papers in proceedings of international conferences

1. V. Jurdana, I. Volaric, and V. Sucic, "Application of the 2D local entropy information in sparse TFD reconstruction," in *2022 International Conference on Broadband Communications for Next Generation Networks and Multimedia Applications (CoBCom)*. Graz, Austria: IEEE, July 2022, pp. 1–7., doi: 10.1109/CoBCom55489.2022.9880775.
2. V. Jurdana, I. Volaric, and V. Sucic, "A sparse TFD reconstruction approach using the S-method and local entropies information," in *2021 12th International Symposium on Image and Signal Processing and Analysis (ISPA)*. Zagreb, Croatia: IEEE, Sep. 2021, pp. 4–9., doi: 10.1109/ISPA52656.2021.9552042.
3. V. Jurdana, I. Volaric, and V. Sucic, "The local Rényi entropy based shrinkage algorithm for sparse TFD reconstruction," in *2020 International Conference on Broadband Communications for Next Generation Networks and Multimedia Applications (CoBCom)*. Graz, Austria: IEEE, July 2020, pp. 1–8., doi: 10.1109/CoBCom49975.2020.9174168.
4. V. Jurdana, and S. Sladić, "Green energy for low power ships," in *2015 57th International Symposium ELMAR (ELMAR)*. Zadar, Croatia: IEEE, Sep. 2015, pp. 197–200., doi: 10.1109/ELMAR.2015.7334529.

Professional papers

1. V. Jurdana, "Optimization of bearingless motor structure without permanent magnets on rotor with combined windings," in *12th Days of Electrical Engineers*. Vodice, Croatia: Croatian Chamber of Electrical Engineers, Oct. 2019, pp. 265–274.